Developing a 3D full-thickness skin model based on thiol-norbornene chemistry

Angela Cirulli

Doctoral Thesis

“Developing a 3D full-thickness skin model based on thiol-norbornene chemistry”

Angela Cirulli

UNIVERSITAT DE BARCELONA

"Developing a 3D full-thickness skin model based on thiol-norbornene chemistry"

Programa de doctorat en Nanociencias

Autor: **Angela Cirulli**

Director: **Elena Martínez Fraiz**

Tutor: **Josep Samitier Martí**

Angela Cirulli

UNIVERSITAT DE BARCELONA

Index of contents

4. Results …………………………………………………………………………………………… 94

Summary in English

Collagen-based gels are widely used as the standard for *in vitro* skin tissue models due to their biocompatibility and structural similarity to natural skin. However, they have notable drawbacks, such as batch-to-batch variability and gel contraction, which can affect the consistency and reliability of experimental results. To address these issues, various alternatives have been proposed. However, developing a 3D model capable of mimicking the morphology and physiology of the *in vivo* tissue still represents a challenge.

In this thesis, we focused on developing a 3D full-thickness skin model using photocrosslinking gels based on thiol-norbornene chemistry to overcome these limitations. Our initial approach involved creating RGD-functionalized norbornene-pullulan-based gels. The incorporation of the RGD peptide, which is known for enhancing cell adhesion, was aimed at improving cell-matrix interactions to support the development of a functional epithelial layer. The results were promising, as the epithelized-dermal skin models formed successfully, indicating that the norbornene-pullulan gels provided an adequate substrate for skin cell attachment and proliferation. This success laid the groundwork for developing more complex and physiologically relevant skin models.

To further refine our model, we investigated single (SN) and interpenetrating network (IPN) systems, based on norbornene dextran (+/- agarose) resulting in robust full-thickness skin models. The norbornene dextran-based gels provided a stable and supportive dermal compartment, where a well-differentiated epidermis on top was observed. A key advantage of our norbornene-based gel systems is their ability to be finely tuned and customized through photocrosslinking. This method allows for precise control over gel properties such as stiffness, which is critical for replicating the mechanical environment of skin tissue. Additionally, the thiol-norbornene chemistry used in our gels is known for its rapid and efficient crosslinking, minimizing the potential for cytotoxicity and preserving cell viability during the gelation process.

One of the most significant outcomes of our research was demonstrating the potential to vascularize these gel systems. Vascularization is crucial for *in vitro* skin models as it facilitates nutrients and oxygen delivery to the tissue, promoting cell survival and function. By incorporating endothelial cells, we successfully induced the formation of capillary-like structures within the gel matrix. This advancement not only enhances the physiological relevance of our skin model but also opens new possibilities for studying skin-related diseases and drug testing in a more realistic *in vitro* environment.

Finally, we also developed a method for the creation of hydrogels with gradients of stiffness, for strategically favoring the incorporation of different cell types depending on the matrix's stiffness.

In conclusion, this thesis presents a significant advancement in developing *in vitro* skin tissue models. By using photocrosslinking gels based on thiol-norbornene chemistry, we addressed key limitations associated with traditional collagen-based gels. The RGD-functionalized norbornene-pullulan gels supported the formation of epithelized-dermal skin models, while the norbornene dextran-based IPN systems provided robust and more reliable full-thickness skin models with a well-differentiated epidermis. Furthermore, the ability to vascularize these gels enhances their potential for *in vitro* applications, making our model a competitive alternative for studying skin biology, disease mechanisms, and drug testing.

Our findings underscore the importance of developing customizable and valid gel systems for tissue engineering applications. The versatility and tunability of thiol-norbornene-based gels make them a promising platform for creating various tissue models beyond the skin, potentially advancing the field of regenerative medicine and *in vitro* testing. Future research should focus on further optimizing these gels and exploring their applications in other tissue types, paving the way for more accurate and functional *in vitro* models.

Resume en Castellano

Los geles basados en colágeno se usan ampliamente como estándar para modelos de tejido cutáneo in vitro debido a su biocompatibilidad y similitud estructural con la piel natural. Sin embargo, tienen desventajas como la variabilidad entre lotes y la contracción del gel. Se han propuesto varias alternativas, pero desarrollar un modelo 3D que imite la morfología y fisiología del tejido in vivo sigue siendo un desafío.

En esta tesis, desarrollamos un modelo tridimensional de piel de grosor completo utilizando geles de entrecruzamiento por luz basados en la química tiol-norborneno. Inicialmente, creamos geles de norborneno-pululano funcionalizados con RGD, un péptido que mejora la adhesión celular, las interacciones célula-matriz y apoyar el desarrollo de una capa epitelial funcional. Los resultados fueron prometedores, logrando formar modelos de piel dermoepitelizados con éxito.

Para refinar nuestro modelo, investigamos sistemas de red única y interpenetrante (IPN), basados en dextrano de norborneno (+/- agarosa), y creamos modelos de piel robustos. Estos geles proporcionaron un compartimento dérmico estable y de apoyo, observándose una epidermis bien diferenciada en la parte superior. Una ventaja clave de nuestros geles es su capacidad para ser ajustados mediante entrecruzamiento por luz, permitiendo un control preciso sobre propiedades como la rigidez, crucial para replicar el entorno mecánico del tejido cutáneo. Además, la química utilizada minimiza la citotoxicidad y preserva la viabilidad celular.

Un resultado significativo fue demostrar el potencial para vascularizar estos sistemas. La vascularización es crucial para facilitar la entrega de nutrientes y oxígeno al tejido. Al incorporar células endoteliales, logramos formar estructuras capilares dentro de la matriz del gel, mejorando la relevancia fisiológica y abriendo nuevas posibilidades para estudiar enfermedades, y pruebas de medicamentos. También desarrollamos hidrogeles con gradientes de rigidez, favoreciendo la incorporación de diferentes tipos de células según la rigidez de la matriz.

Esta tesis presenta un avance significativo en el desarrollo de modelos de tejido cutáneo in vitro. Los geles basados en tiol-norborneno abordan las limitaciones de los geles de colágeno tradicionales, proporcionando modelos de piel dermoepitelizados y de grosor completo más robustos y confiables. La capacidad de vascularizar estos geles mejora su potencial para aplicaciones in vitro, siendo una alternativa competitiva.

Abbreviations

2D	Two Dimensional
3D	Three Dimensional
AFM	Atomic Force Microscopy
AJ	Adherens junctions
ALI	Air-Liquid-Interface
ANOVA	Analysis of Variance
BSA	Bovine Serum Albumin
CD	Cell-degradable
CDI	Carbonyl diimidazole
CD-Link	Cell-degradable crosslinker
CD-Hy-Link	Cell-degradable hyaluronic acid crosslinker
DAPI	4’, 6-diamidino-2-phenilindole
DEX	Dextran
DLP-SLA	Digital Light Stereolithography
DMEM	Dulbecco’s Modified Eagle Medium
DMSO	Dimethyl sulfoxide
DLW	Direct Laser Writing
E-cadherin	Epithelial cadherin
ECM	Extracellular matrix
F-actin	Filamentous Actin
FBS	Fetal Bovine Serum
FLG	Filaggrin

HaCaT	Human immortalized keratinocytes
HEKn	Primary Epidermal Keratinocytes: Normal, Human, Neonatal Foreskin
Hy	Hyaluronic acid
Hs-27	Human foreskin fibroblasts
HUVEC	Human Umbilical Vein Endothelial Cells
IPN	Interpenetrated network
K5	Keratin 5
K10	Keratin 10
K14	Keratin 14
KDM	Keratinocytes differentiation medium
KGF	Keratinocytes growth factor
KGM	Keratinocytes growth medium
KMM	Keratinocytes maintenance medium
LAP	Lithium phenyl-2,4,6-trimethylbenzoyl phosphinate
LMP	Low-Melting-Point
LOR	Loricrin
MMP	Matrix metalloproteinase
N-DEX	Norbornene-dextran
N-PLN	Norbornene-pullulan
N-PVA	Norbornene-polyvinyl alcohol
NIH-3T3	Mouse fibroblasts
PBS	Phosphate Buffered Saline
PDMS	Polydimethylsiloxane
PEG	Polyethylene Glycol

PLN	Pullulan
P/S	Penicillin/Streptomycin
PSA	Pressure sensitive adhesive
PVA	Polyvinyl alcohol
RGD	Arginine-glycine-aspartate
RPM	Revolutions per minute
RT	Room temperature
SB	Stratum basale
SC	Stratum corneum
SD	Standard Deviation
SG	Stratum granulosum
SS	Stratum spinosum
SEM	Standard Error of the Mean
TEER	Transepithelial Electrical Resistance
TGF ß	Transforming Growth Factor Beta
TJ	Tight junctions
UV	Ultraviolet light

1. Introduction

1.1. Fundamentals of skin tissue: anatomy and physiology

The skin is the first interface between the individual and the external environment. It is one of the most important and largest organs in the body comprising 16% of the human body weight.[1,2] Its importance resides in the pivotal functions that it performs, including protection against external chemical, physical, and biological assailants, wound healing, as well as its role in thermoregulation, or preventing excess water loss from the body,[3] and into the vitamin D synthesis or providing sensation. Besides the fundamental role of the skin as a barrier against external agents or attacks, it also covered the role of route of access for drug transportation and/or blood circulation.[4,5] The skin, and more in general the integumentary system, comprises the epidermis, dermis, hypodermis (or subcutaneous tissue), and skin appendages, including the hair follicle and sebaceous gland.[6,7]

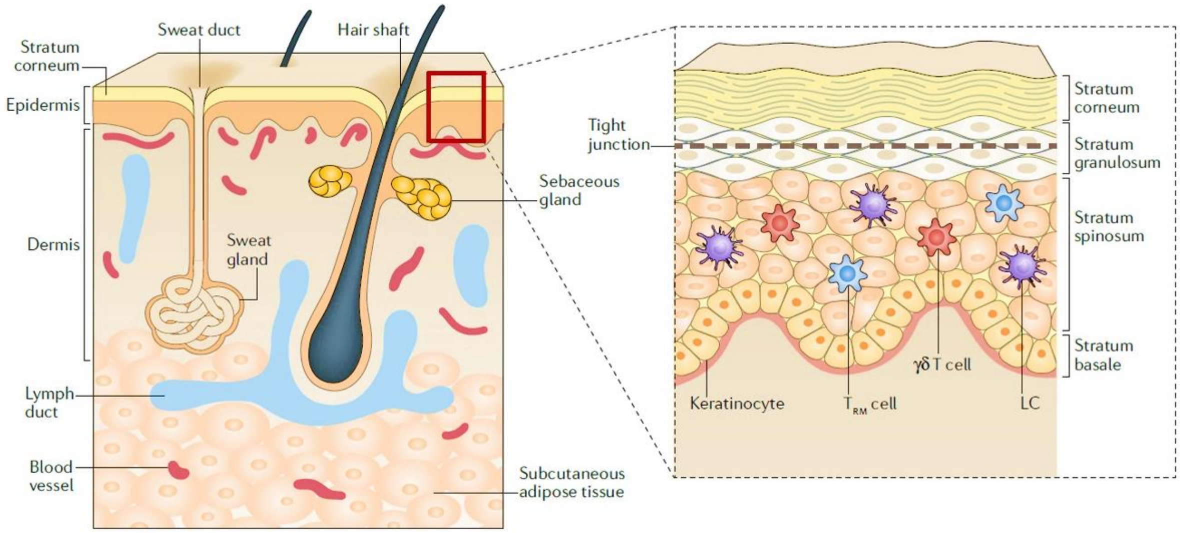

Figure 1.1. Skin anatomy representation. The main layers are presented: the epidermis, dermis, and hypodermis. A zoom view is also depicted, showing the tight junctions formed in the epidermis, underneath the stratum corneum and the single layers of the epidermis compartment, together with three types of immune cell populations: Langerhans cells (LCs), γδ T cells, and the resident memory T (TRM) cells, which reside between keratinocytes. Readapted from Kabashima et al.[8]

The epidermis is the outermost layer of the skin barrier, and its thickness can vary in a range between 50 and 150 μm, depending on the body location and individual.[9,10] Its thickness is critical for skin health, and it is in a state of continuous cell turnover, which is completely renovated every 4 weeks.[11,12]

The epidermis is organized into layers or strata: stratum corneum, stratum granulosum, stratum spinosum, and stratum basale[13] (Figure 1.1). It is mainly composed of sheets of keratinocytes, also including non-epithelial cells- such as Langerhans cells or melanocytes and Merkel cells.[14]

Among them, Langerhans cells and melanocytes are dendritic cells. The Langerhans cells, located in the stratum spinosum, are mainly responsible for immune protection, acting as antigen-presenting cells and engulfing pathogens.[15] Melanocytes, mainly distributed in the basal layer, are responsible for the synthesis of melanin, a pigment for the absorption of UV radiation and protection from its negative effects.[16] Merkel cells, which represent almost 5% of the total number of cells in the epidermis, have a pivotal role in sensory discernment and are considered conductors of physical stimuli.[17,18] Keratinocytes represent the major percentage of cell types in the epidermis and ensure keratinization by differentiating, starting from the basal layer.[19] During the differentiation process, cells migrate towards the skin surface becoming anucleate and clustering keratin in the stratum granulosum. Finally, they flatten and die in the apical strata-stratum corneum. The corneocytes, which are the differentiated keratinocytes, cover an important role since they present tight junctions that prevent water evaporation.[20]

Between the epidermis and the dermis, a semi-permeable membrane is located: the basement membrane, mainly formed by the ECM components, such as collagen type IV, laminin, and nidogen.[21,22] Beneath the epidermis, there is the dermis, mainly composed of fibroblasts, and rich in blood and lymphatic vessels, including nerve endings.

In the dermis compartment, two regions can be distinguished: the papillary dermis and the deeper reticular dermis. The first one is thin and includes collagen (mostly type III) fibers and capillaries.[23] The reticular one, mostly acellular and rich in extracellular components is fundamental in conferring physical strength, flexibility, and support to the skin.[24,25] Various growth factors are also secreted here, such as TGF-ß, cytokine (TNF-α), together with matrix metalloproteinases, which are fundamental to guarantee the formation of ECM and to promote keratinocyte proliferation and differentiation.[26]

The inner compartment is the hypodermis, which protects the internal organs and tissues from cold and trauma, providing energy and participating in hormone synthesis.[27] It is formed by adipocytes structured in lobules, containing nerves, and lymphatic and microvascular networks, ensuring oxygen and nutrient delivery.[28]

As mentioned before, the integumentary system also counts on skin appendages e.g., nails, hair follicles, sweat glands, and sebaceous glands. Nails are composed of keratinized and dead cells.[28] Hair follicles, which are responsible for body temperature control and mechanic perception, are composed of basal cells in the basement membrane.[13]

Then, the sebaceous glands, placed at the bottom of the hair follicles are responsible for the secretion of sebum for the skin, hair lubrification, and waterproofness.[29] Sweat glands are also part of this complex system, secreting sweat into the skin's surface.[30] Sebaceous glands, usually associated with hair follicles, provide several functions such as antioxidant and antibacterial effects, and transport of pheromones. They are also responsible for producing the lipids involved in the pathogenesis of acne.[31] Recent studies have shown that skin has stem cells that can be differentiated into distinct subtypes: epidermal, hematopoietic, melanocytes, follicular, mesenchymal stem cells, neuronal progenitor cells, and sebaceous gland stem.[13,32]

The establishment of the skin barrier is regulated by the viable cells that must connect by intercellular junctions, such as tight junctions, desmosomes, and adherence junctions, as shown in Figure 1.2.[33] Their pivotal role is due to their contribution either in the viable epidermal barrier or in the correct formation and maintenance of the stratum corneum.

The tight junctions (TJ) which are the occluding junctions, are the most apical structure demarcating the border between apical and basolateral membrane domains.[34] TJs are cell-cell junctions that are both present in simple and multi-layered epithelia as well as in endothelia. Mainly composed of transmembrane proteins, proteins of the claudin (Cldn), TJ-associated marvel proteins (e.g. occludin (Ocln)), and junctional adhesion molecules (JAMs)), as well as TJ plaque proteins (e.g. zonula occludens (ZO) proteins 1-3, MUPP-1 and cingulin). Their role is sealing the paracellular pathway to restrict the movement of molecules within the intercellular space. Furthermore, TJs are also involved in the differentiation, proliferation, cell polarity, and signal transduction processes of cells.[35–39]

Immediately below tight junctions, adherens junctions (AJ) are positioned. AJ are dynamic entities that are responsible for creating a transcellular network that coordinates the behavior of a cell population. Their functionalities cover distinct cellular processes such as cell shape, division, growth, barrier function, and apoptosis. Two cell adhesion receptor complexes, normally the cadherin/catenin complex and the nectin/afadin complex, represent the molecular basis of the adherens junctions.[40] Among the classical cadherins expressed in the epidermis, there are P-cadherin (mainly expressed in the basal layer) and E-cadherin, which is found in all the epidermis layers.[41]

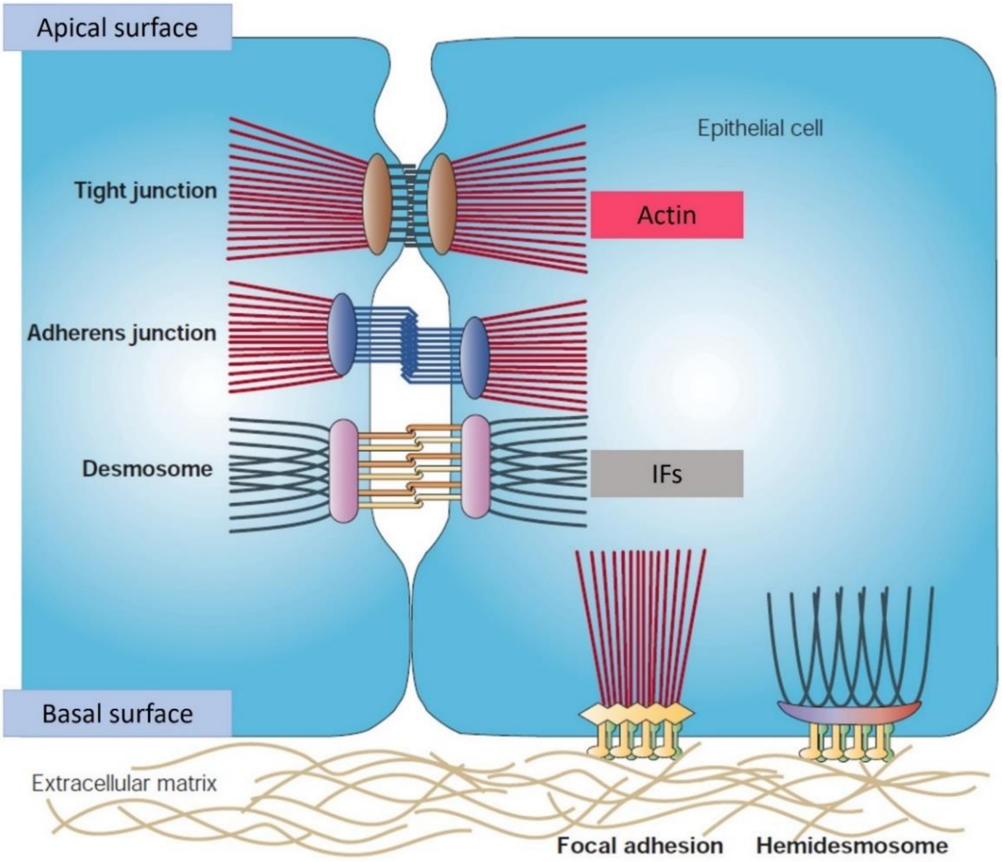

Figure 1.2. Cell-adhesion complexes in mammals. Adhesion complexes are especially abundant in epithelial tissues. The apical surface of the epithelium is exposed to the environment, whereas the basal surface faces the extracellular matrix (ECM). Five different types of junctions are shown here. First, tight junctions or zona occludens (ZO) seal adjacent cells together and function as selective permeability barriers. The transmembrane proteins that form tight junctions, (claudins and occludins) are linked to the actin cytoskeleton through ZO proteins. Second, adherens junctions are cell–cell junctions, formed by classical cadherins that are linked to the actin cytoskeleton through adaptor proteins (catenins and vinculin). Third, desmosomes are cell–cell junctions that are formed by desmosomal cadherins called desmocollins and desmogleins, and that are linked to intermediate filaments (IFs) through desmoplakin. Fourth, focal adhesions are cell–matrix junctions. Finally, hemidesmosomes are cell–matrix junctions, formed by α6 β4 -integrins and BPAG2 (bullous pemphigoid antigen-2). Readapted from Jefferson et al.[42]

Desmosomes are considered the “mechanical” junctions and are mainly involved in cell cohesion.[43] Among the desmosomal cadherins that compose the desmosomes, desmogleins 1-4 and desmocollins 1-3 are mostly found in the human epidermis.

Finally, epithelial cells are connected to the extracellular matrix through the focal adhesions, which are cell-matrix junctions, linked to actin filaments by adaptor proteins such as talin, filamin, and vinculin, and the hemidesmosomes, specialized junctions, associated with keratin intermediate filaments.[42]

1.2. The importance of developing a skin model

Burns endure as one of the most common injuries worldwide, causing more than one million patients in the USA per year.[44] Damaged skin led to an enormous loss of body fluids, followed by several issues such as dehydration, electrolyte imbalance, and renal and circulatory failures. Moreover, several complications can happen, since the burned skin is extremely susceptible, and it can be subjected to bacteria or other pathogens attacks.[23] Hence, covering a burn injury with the appropriate approach is considered a challenge.

Autologous skin replacements are largely used, despite their limitations, especially for patients with limited donor site area.[45,46] Besides the burns issue and the consequent wound repair, several skin disorders can occur for distinct reasons, such as infections, neoplastic transformation, or an imbalance in molecular events that regulate communication between cells. Therefore, the need of a therapeutic intervention is necessary. Three-dimensional *in vitro* tissue models of human skin represent the solution to cover this gap. Nowadays, a huge variety of 3D skin models have been developed in response to scientific and or technical demands.

From drug delivery systems to the cosmetic industry, these systems allow for the replacement of the animal model, overcoming their drawbacks, such as the prediction of drug responses in humans because of species differences. As an alternative, *ex vivo* skin tissues have been also used for testing the dermal toxic effects of chemicals. Also in this case, many issues have been faced, due to the limited sources of skin explants, especially if it is important to consider variations linked to the age, the body sites, and the gender of the samples collected.[47] Hence, *in vitro* skin models represent the appropriate method for drug development. Specifically, for the application of systematically acting drugs, to overcome the skin barrier and to vehiculate the drug into vessels or adipose tissue; or for efficacy testing of drugs (disease models).[48]

Models of skin diseases have been developed to recapitulate the complex microenvironment of human skin and supply an efficacious platform for investigating diseases.[49] Generally, skin diseases are based on inflammatory reactions, as in the case of psoriasis or atopic dermatitis, damage (such as wounding, burns, or photodamage), and abnormal cell behavior, such as melanoma or squamous cell carcinoma.[48] All these diseases have been simulated in approximated models, where cells were harvested from affected patients or preconditioned by certain cytokines.[50,51] For example, different models have been studied to investigate Epidermolysis bullosa (EB), a hereditary skin disease characterized by structural fragility of the skin.[52,53]

Common autoimmune diseases, such as psoriasis, are characterized by chronically red patches, and irritated scaling, caused by altered differentiation of keratinocytes,[54] or atopic dermatitis (AD) characterized by a disruption of the barrier function of the epidermis,[55] have been also explored through 3D models.[56–60]

Currently, skin models are widely applied to test product safety and efficacy both for entire cosmetic formulations and for raw materials, such as active ingredients. Since there is a huge variety of efficacy tests and *in vitro/ex vivo* models for claim substantiation in cosmetics and they are not regulated, the resulting degree of freedom in the selection of the models and the assays is very high.[61–64] However, the use of these alternative skin models is still not completely exploited due to the regulatory issues, depending on the guidelines; for example, in the case of the Asian market, which is quite demanding on this issue, either only clinical studies or, in some cases, animal testing are accepted.[65] Also in the chemical industry, the development of alternative skin models to investigate the toxicity of chemicals, and pesticides or to identify skin irritants, allergens, or sensitizers, is becoming attractive. The ECHA requires alternative methods to animal testing for the registration of chemicals.[66]

1.3. 2D-models: a general overview

To study the complex skin tissue structure, numerous models, either *in vitro* or *in vivo* have been developed, including 2D cell cultures, and 3D models. The design of two-dimensional *in vitro* models mainly consists of four steps, in which the cell movement can be investigated under a controlled *in vitro* environment.[67,68]

As a first step, a cell culture preparation, representing the *in vivo* conditions, is cultured on a specific substrate (as a plastic-bottomed multiwell plate). Cell types are normally used for this purpose, such as keratinocytes, fibroblasts, or endothelial cells,[69] to generate a monolayer. Subsequently, after reaching the confluency, the time-lapse images and videos or the study of the expression of specific proteins and molecules allow for the study of the culture progression and cells' behavior.

Finally, a data analysis step allows to get a qualitative and quantitative analysis. By using this procedure, it is possible to simulate and measure the distance between the edges of the wound or the rate to change a covered area, by a scratch assay, which involves scraping the cell mat into a straight line and measuring the rate of cell migration to fill the gap.[70]

However, this easy, fast, and cheap method presents a big issue which is the manual execution, which reduces the repeatability of the experiment.

One of the big drawbacks of *in vitro* 2D assays, which are essential for understanding the angiogenesis and re-epithelialization process,[71,72] by studying cell migration and proliferation, is the impossibility of recapitulating the complex conditions of a wound. These models, normally involve just one cell type; they also lose the reproducibility of the extracellular scaffolding matrix, which is fundamental for establishing intercellular signals.

1.4. 3D-skin model classification

Based on the previous considerations and the absence of a dermis featuring in the 2D models, 3D models have been developed to mimic the potential of the wound healing process *in vivo*[73–77] and to reproduce a properly functional and structural dermal compartment, built on a three-dimensional scaffold, analogous to ECM, able to support cell adhesion, growth, and differentiation.

According to the traditional perspective, the skin model categorization is based on the model components and their origin. First, as an initial proof of concept in dermatology, cell models were used, which included primary, or cell-line models based on fibroblasts, keratinocytes, or melanocytes. Unfortunately, these models lacked in terms of reproducibility of the skin's complex structure and its functionalities.[78] Then, 3D reconstructed skin models were shown in this classification. These models allow the reconstruction of both the human epidermis (RHE) and the skin (RHS) and are built by combining different cell types in a three-dimensional structure.[79]

For testing the effects of different treatments, *ex vivo* skin models are adopted. Normally, these models are made by taking a small piece of skin tissue from a donor and kept in culture.[80] Besides that, skin-on-a-chip models have been recently studied as complex models. They are microfluidic devices consisting of a chamber containing a layer of cells cultured in specific conditions to mimic the *in vivo* environment, connecting the chamber to channels that guarantee nutrients and oxygen flow.[81]

Lastly, skin-*in-silico* models are the recent ones. These are computational models that allow to simulate and predict some mechanisms and behavior under certain conditions. The challenge point here is to analyze heterogenous data which need to be reliable and standardized.[64,82]

1.5. Commercial products

For skin regeneration, hydrogel models are extensively used in wound dressings, in different forms, such as amorphous gel, films, sheets, or hydrogel-impregnated gauze.
These systems allow to cover a wide spectrum of skin wounds, like skin lacerations, abrasions, and minor burn wounds.[4,83]

Many of the solutions available in the market are based on natural components such as alginate or collagen.[83,84] For instance, ActivHeal® hydrogel, based on alginate, is used as a primary wound dressing, for dry wounds. It promotes the moist wound healing and the growth of epithelial cells.

Other examples are AquaDerm® and DermaSyn®, which are respectively a hydrogel sheet dressing and a hydrogel wound dressing.[84]

Cellular skin models are also present on the market and are mainly distinguished in reconstructed human epidermis models (RHE) which mimic just the epidermis, and the full-thickness reconstructed human skin equivalents which simulate the full human skin.[79,85]

Among the epidermis models, we can find: Episkin (L'Oreal, France), which is composed of stratified human keratinocytes cultured on a collagen-based matrix[86]; SkinEthic® (SkinEthics, France) and EpiDerm® (MatTek Corporation, USA), consisting of epidermal keratinocytes cultured on polycarbonate membrane, Holoderm®, and Kaloderm®.[87–89]

Among the full-thickness reconstructed human skin models, some well-recognized constructs are GraftSkin®, EpiDermFT®, and Pheninon®.[86,90] In particular, Phenion® consists of a multilayered equivalent of the human skin, composed of keratinocytes and fibroblasts from the same human donor, and is gaining popularity for its applications in the testing of cosmetics and pharmaceuticals. The tissue pieces can be produced in a cell culture insert (Figure 1.3 a) with different size options or on a filter disc (Figure 1.3b-c).

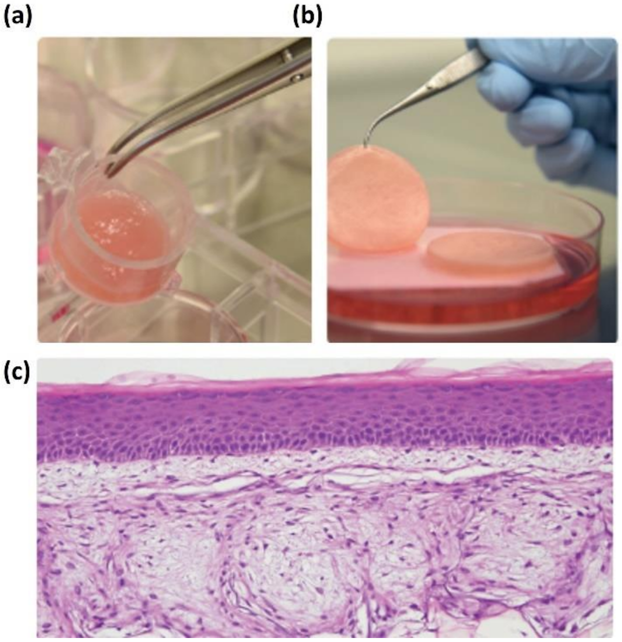

Figure 1.3. Phenion® Full-thickness (FT) skin models available on the market. (a) Phenion® FT Small- Epidermis+ dermis construct (Ø= 0.9 cm), available in insert or on filter disc. **(b)** Phenion® FT Large- Epidermis+ dermis construct (Ø= 3.1 cm), available only on filter disc. **(c)** Histology example of Phenion® Full-thickness (FT) skin model on the day of receipt.

1.6. Hydrogels as scaffolds for regenerative medicine: general overview

Hydrogels are among the most important and used biomaterials for tissue engineering. Mostly due to their similarities with the native extracellular matrix of tissue, their use in regenerative medicine has grown exponentially in recent years. Predominantly used for their different applications in the biomedical field, encompassing drug and cell delivery devices,[91,92] microfluidics,[93–95] tissue engineering,[96,97] and wound treatment,[98–100] these polymeric biomaterials present intrinsic characteristics that make them the perfect candidates to replace organs and tissues.

Hydrogels are defined as hydrophilic polymers, with a three-dimensional network structure. Thanks to the hydrophilic functional groups (-OH, -CONH-, COOH, -$CONH_2$, -SO_3H, NH_2) present in their structure, they possess the peculiar capacity to absorb a large content of water, which fills the space between macromolecules, inducing hydrogel expansion (hydrogel swelling).[84,101] Hence, by properly modifying the molecular weight, the porosity, or the numbers of crosslinking, either the mechanical strength and the degradation rate of these scaffolds can be tuned.[102]

Among their properties, flexibility, porosity, stimuli-responsive and soft structures, permit them to resemble living tissue.[103] For example, the porosity of the tunable hydrogel is important to leverage limited access to chemicals within the gel phase (e.g. selective bio-sensing, xenograft cell encapsulation), regulating the release of entrapped cargoes (drug delivery). All these characteristics, together with biocompatibility and biodegradation, make hydrogels attractive.[104,105]

1.6.1. Hydrogels classification

Hydrogel scaffolds can be classified depending on several factors, such as source, crosslinking, composition, configuration, and ionic charge (Figure 1.4).[106]

Depending on their source, hydrogels can be distinguished into natural, synthetic, and semi-synthetic.[107] Hydrogels from natural sources present of course higher biocompatibility, compared to the synthetic ones, even though they lose in terms of mechanical properties and stability.[108] Among the natural polymers, are collagen, gelatin, alginate, hyaluronic acid, pullulan, dextran, agarose, and chitosan.

Collagen is considered the gold standard as a biomaterial for skin regeneration since it is one of the fundamental proteins of the skin and connective tissue, and the most abundant in the extracellular matrix.[109–111]

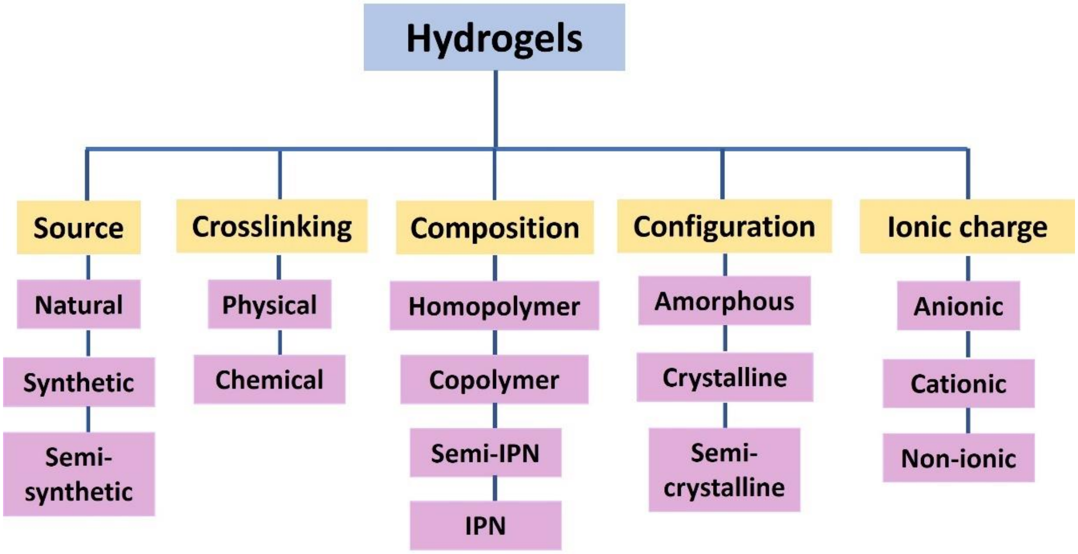

Figure 1.4. Schematic representation of hydrogels' classification.

Collagen is derived from raw materials such as porcine or bovine tissue.[112] Its mechanical properties can be regulated by different factors, such as pH, ionic strength, and temperature.[113,114] However, when fibroblasts are encapsulated within these scaffolds causes a structure's contraction, resulting in the eventual loss of the skin barrier function.[115] To address this issue, different approaches were used, for instance using physical and chemical modifications that allow to minimize collagen's contraction, such as plastic compression or crosslinking the collagen matrix.[116,117]

Gelatin-based hydrogels are largely used in skin regeneration.[118–120] Gelatin is obtained after hydrolysis and denaturation of collagen. Recent studies from Zhao et al.[121] proved that the mechanical and degradation properties of these scaffolds can be tuned by modifying the hydrogel concentration. In the study by Tahri et al.[122], it was shown how gelatin serves as an effective platform to support culture systems, resulting in a promising strategy towards a more accurate 3D *in vitro* model. Gelatin methacrylate is also used for *in vitro* models, as an alternative. Khademhosseini group has compared different gelatin methacrylate concentrations to create the epidermis from keratinocytes, showing that higher concentrations correspond to higher mechanical stiffness, which guarantees better keratinocyte adhesion.[121,123]

Among the natural polymers, alginate also stands as a promising alternative. Alginate is a natural polymer of marine origin and can be used alone or in combination with other natural or synthetic polymers.

Due to its versatility, biocompatibility, nontoxicity, economic affordability, ease of handling, mild gelation properties, and structural mimicry, it is an optimal candidate for living tissue replacement.[124–135] It can be found in different forms, with low, medium, or high viscosity and low or high molecular weight. As a natural polysaccharide, it shows a pH-dependent anionic character and interacts with cationic polyelectrolytes, resulting in a convenient approach to cell loading.[124–135]

Hyaluronic acid (HA) is a non-sulfated glycosaminoglycan present in the extracellular matrix of many soft connective tissues. It is an attractive biomaterial for the construction of scaffolds with desired morphology, stiffness, and bioactivity since it is biocompatible, biodegradable, and non-immunogenic.[136] It plays a fundamental role in distinct biological processes, including cell growth, migration, and differentiation.[137] HA hydrogels are usually prepared through chemical crosslinking to enhance their stability.[138,139] To avoid the organic solvents or toxic agents during the preparation via chemical modification in solution, alternative methods have been explored, as in the study of Calò et al.[140]

Pullulan is a linear, neutral, and non-ionic glucose homopolysaccharide, with physicochemical properties that lead to a multitude of advantages, such as elasticity, thermal stability, and high barrier properties toward oxygen. It is composed of maltotriose units that are interconnected by α-1,6, and α-1,4 glycosidic bonds, with a chemical formula $(C_6H_{10}O_5)_n$.[141]

The biosynthesis of pullulan can be defined as a multistep biological reaction undertaken by *Aureobasidium pullulans*. The specific method for the pullulan biosynthetic pathways is still not clear.[142,143] Its use is mainly due to its good structural flexibility (caused by the regular alternation of glycosidic bonds), elastic properties, and thermal stability, resulting to withstand high temperatures (≥ 250ºC).[144]

Curiously, variations in terms of pH, heat, and the presence of metal ions do not affect the viscosity of the pullulan solution.[145] Moreover, pullulan-based scaffolds protect the wound from infection[146] and accelerate fibroblast proliferation, collagen synthesis, and epithelization, resulting fundamental in wound healing promotion, and shortening the healing period.[147] One of the major inconveniences is related to the costs since it is three times more expensive than other polysaccharides.[148]

As an alternative, dextran is largely employed in tissue regeneration. Dextran is a highly water-soluble polymer. It's a bacterial polysaccharide composed essentially of α-1,6 linked D-glucopyranose residues.[149] Dextran-based hydrogels can be modified by incorporating functional groups, -specifically amino groups- to enhance biocompatibility and integration with the host tissue;[150]

An example is the study proposed by Sun et al., which focused on tailoring the properties of chemically modified dextran gels to promote functional neovascularization *in vivo*.[151]

Agarose is a natural polysaccharide obtained from agar, which is extracted from red seaweed, highly compatible with 3D bioprinting applications to create a thermal-reversible gel.[152] It shows high water uptake capacity and demonstrates notable significant mechanical strength.

Among the polysaccharides that have attracted attention recently, is chitosan. Chitosan is a deacetylated derivative of chitin, a natural polysaccharide that mainly composes exoskeletons of some fungi and arthropods.[153,154] Thanks to its characteristics of biocompatibility, biodegradability, and pH sensitivity, is becoming particularly attractive to study drugs and biomolecule delivery.[155,156]

All the advantages mentioned before, underline the importance of choosing a natural polymer to create an appropriate hydrogel formulation. However, the use of these polymers presents some drawbacks related to the poor control of batch-to-batch variations, degradation rate, short supply, costs, risk of disease transmission, and immunogenicity.[157] Thus, synthetic polymers are also used to overcome these issues. The most used are poly (ethylene oxide) (PEO), polyvinyl alcohol (PVA), poly (ethylene glycol) (PEG), poly (acrylic acid), poly (2-hydroxyethyl methacrylate).[105]

Compared to the natural ones, these polymers offer more controllable mechanical properties, (especially the strength and viscoelasticity), implementing degradation rate and water adsorption capacity, allow to reduce the batch-to-batch variability, and guaranteeing a higher degree of control during the fabrication process.[158]

Despite the several advantages, they lack in terms of specific ECM components, such as growth factors or peptides,[159,160] which can provoke the release of polymer degradation products, leading to adverse effects,[161] and normally require the use of organic solvents during the synthesis.[162]

These are the reasons why hybrid (or semi-synthetic) polymers are often used recently. In fact, by combining natural and synthetic polymers is possible to tune some mechanical properties and reduce the collateral effects caused by the synthetic polymers alone, creating a more friendly environment for cells. Based on the interaction among the polymers' chains, the crosslinking is generally classified as physical or chemical. In the physical gel formation, the forces involved are hydrophobic, electrostatic, and hydrogen bonding between the polymer chain.[163,164] In this network formation, the nature of all these interactions is purely physical, hence the gel formation is reversed. Specifically, these gels are characterized by weak bonds and are prepared without the use of crosslinking entities or chemical modification.

Although physical crosslinked gels are less stable against degradation, showing poor mechanical properties because of the reversible physical interactions, these gels are of great interest for the incorporation of bioactive substances. However, they are inflexible towards variables such as gelation time, gel pore size, degradation or dissolution, and chemical functionalization, making their performance *in vivo* inconsistent.[165] For instance, the mechanism behind the sol-gel and gel-sol conversion of thermal-reversible gel is based on physical crosslinking. These types of gels, present both hydrophilic and hydrophobic domains and are defined as amphiphiles. Amphiphile polymers are water soluble at low temperatures.

The gelation temperature depends on various factors, such as the polymer's concentration, the length of the hydrophobic block, and the chemical structure of the polymer.[166] Electrostatic interactions are also involved in the formation of physical crosslinked gels; in this case, the reaction occurs when two polymers are ionized, they have opposite charges and the pH values are close to the pKa interval of the two polymers.[163]

In contrast, the chemical crosslinking method is based on covalent bonding between polymer chains forming a permanent or irreversible hydrogel, due to the strong nature of these bonds. Contrary to the physical crosslinking, the chemical one is stable against degradation, and it is flexible concerning gelation time, as well as gel pore size or chemical functionalization. In addition, chemical-based hydrogels present domains of high crosslink density, and show higher mechanical properties compared to the physically crosslinked gels.[165]

The establishment of the chemical crosslinking is due to the addition of small crosslinker molecules, photosensitive agents, by polymer-polymer conjugation or by enzyme-catalyzed reaction.[167] Crosslinkers are essential molecules with at least two reactive functional groups that provide the formation of bridges between polymeric chains.[168]

Photocrosslinking is also a chemical crosslinking that depends on the presence of photo-sensitive functional groups. Hence, upon irradiation with light (UV or visible light) the photo-sensitive functional group can be linked to the polymer enabling the crosslinking. These gels present a stronger mechanical strength and stability compared to physically crosslinked gels.[169] Among the advantages of this approach, are the speedy and easy formation of the gels, guaranteeing safety and low-cost preparation compared to the chemical methods which count in the addition of different reactive species. Although the prolonged irradiation required for the crosslinking of the gels, causing a temperature rise which damaged cells and tissue,[170] this approach is largely used in tissue engineering by minimizing the side effects.

To form *in situ* hydrogel, enzyme-catalyzed reactions are also employed. Transglutaminases (TG), peroxidases, and tyrosinase have been studied to be used as catalysts.[171–176] The main advantage of this approach resides in the mild conditions used during the crosslinking, potentially avoiding side reactions, predicting the crosslinking kinetics, and controlling the crosslinking rate.[177]

Hydrogels can be also classified on their composition. Homopolymer hydrogels are made up of single monomer species,[178] while co-polymeric gels are formed by two or more monomer species, of which one is hydrophilic. Their arrangement can be random, block-wise, or alternate along the network chain.[179] Interpenetrated polymer networks (IPN) are the combination of two or more polymers in the network form, in which one polymer is crosslinked in the presence of the other.[180] They are considered as "polymer alloys" since they are topologically interlocked and interlaced at a molecular level, but are not covalently bonded to each other. The network components cannot be separated unless the chemical bonds are broken. [181–183]

One of the peculiar characteristics of IPNs is that the two networks are distinct, so the properties and functions of the single components can be integrated.[184] Their formation normally occurs by a sequential approach or simultaneous approach.[185] In the first case, a hydrophilic network is formed and swelled in a solution of monomers; after that, the monomers are polymerized to create a secondary network. This first approach results in better control of the mechanical properties and hydrogel's morphology;[186] nevertheless, it is usually time-consuming and not adapted to create complex-shaped gels. Against, the simultaneous method is a one-pot process, hence the single precursors are crosslinked at the same time via independent routes, such as free-radical polymerization or physical/chemical gelation. This method drastically reduces the time-consuming and the ratio of the components, although the polymerization kinetics of the single components are required to lead interpenetration other than phase separation. [187]

A further classification is also distinguishable for this class of materials. Specifically, IPN gels can be divided into full-IPN and Semi-IPN hydrogels. In the full-IPN, two networks are crosslinked, in the semi-IPN systems linear polymers are incorporated into a primary crosslinked single network, which is previously synthesized by polymerizing monomers to form linear polymers within the primary network or forming the primary network in the presence of linear polymers. Semi-IPN gels can rapidly respond to external stimuli since there are no network restrictions.[184]

Based on the configuration, hydrogels are also divided into amorphous, crystalline, and semi-crystalline. Semicrystalline hydrogels have been developed by chemical crosslinking, resulting in structures that include both amorphous and crystalline regions. When they are prepared with physical crosslinking can easily change from a solid state to a liquid state and *vice versa*, resulting in suitable injectable hydrogels.[84,188]

Depending on the network electrical charge, the hydrogels can be also classified as anionic, cationic, or non-ionic/neutral gels. The ionic groups that are attached to the polymer monomer can form polyelectrolyte gels, well-known as ionic gels.[189]
This category of gels could be positive, negative, or present simultaneously with both negative and positive ends along the polymer chain. Occasionally, cationic, or anionic gels can result in ampholytic macromolecules.[190] Several properties can depend on the cationic or anionic nature, such as the significant swelling capability shown by the anionic gels, responding to a change in terms of pH environment.[191] For the neutral ones, instead, no charge groups are involved in the crosslinking, and variations in the system's temperature can cause the neutral hydrogels to swell or shrink.[192] The advantage of these gels is that in their polymer organizations, they feature ultra-durable and permanent connections that are irreversible, making them more stable.[193]
Apart from the conventional classification, there are other types of gels called "smart hydrogels", which respond to various stimuli, like temperature, pH, ionic strength, and light, causing changes in terms of structural and mechanical properties.[107]

1.6.2. Hydrogel formation

Thinking about the applications of hydrogels for regenerative medicine, one of the crucial parameters to consider is biocompatibility. To model bio-safe hydrogels, the biomaterials that must be used should encourage simultaneously desired cellular functions, such as adherence, proliferation, and differentiation, and avoid undesirable side effects.[194]

Thus, the materials required to form the gels must have no severe and chronic inflammatory response, mutagenesis and/or carcinogenesis, and cytotoxicity.[195] For optimal tissue regeneration, a proper and controllable biodegradation rate must be controlled, ideally like the degradation rate of tissue growth. It is often required that hydrogels can restore the load, and function of the tissue and then degrade, as in the case of targeted drug and cell delivery or tissue regeneration. At the same time, the degradation process cannot cause the loss of the mechanical properties, which must be preserved. Considering all the aspects, hydrogel formation has a crucial role.

As mentioned before, chemical crosslinking allows to get permanent and highly stable structures compared to the ones obtained through physical crosslinking. Thus, to achieve chemically stabilized hydrogels, commonly, crosslinker molecules that react with hydrophilic groups are employed. This is the case, for example, of the crosslinking reaction of the amino groups with aldehydes and di-hydrazide (e.g. glutaraldehyde) to form Schiff-base, or the example of the Michael addition which occurs between a nucleophile, as a thiol group or an amine, and an electrophile, such as vinyl, acrylates groups, or a condensation reaction.[105] Often, other strategies are also applied, such as crosslinking by UV light, exposing to photo-irradiation acrylates groups, and polymerizing through free radical chain-growth mechanism; or the free-radical polymerization (when free radicals on low-molecular-weight monomers are formed and react with a crosslinker). [196]

Thus, covalent hydrogels can be formed via either radical-mediated polymerization or via bio-orthogonal click reactions.[197–199] The radical-mediated reactions are precisely initiated by radicals, which are generated from initiators excited or decomposed by using an energy source, (e.g. photons, heat, redox potential), or enzyme activity. The resulting chain-growth polymer networks are heterogeneous, presenting high-molecular weight crosslinks. With these reactions, which occur quite fast, sometimes, it is also possible to control the reaction kinetics spatiotemporally. To overcome the heterogeneity of these network systems, different approaches are also possible: copper-catalyzed azide-alkyne cycloaddition[200], thiol-based Michael-type conjugation[201–204], norbornene-tetrazine click reaction[205], and Diels-Alder reaction.[206] These mechanisms are defined as step-growth polymerization, which guarantees no heterogeneous crosslinks within the networks on one side but cannot allow spatiotemporally controls on the crosslinking reactions. For this reason, to enable easy control of the polymerization kinetics, photopolymerization can be considered, by modulating the light irradiation.

In this scenario, Anseth et al.[207] developed a light- and radical-mediated step-growth polymerization scheme based on the orthogonal reaction between thiol and norbornene. This specific chemistry combines the advantages of random chain polymerization while keeping the photochemistry benefits. Recently, thiol-ene photo click hydrogels have emerged in the tissue engineering panorama for developing systems with applications in regenerative medicine. Thiol-ene norbornene-based gels are becoming attractive due to their high cytocompatibility, and biocompatibility, and because they are diverse in gelation.

1.6. 3. Thiol-ene norbornene reaction

Thiol-ene norbornene-based hydrogels are usually created under physiological conditions, with a lower radical concentration in the initial steps compared to the chain-growth polymerization approach.[208] One of the crucial points that make this process different, is the minimization of the chemical toxicity, and the consequent reduction of the biological components damage, present in the pre-gel solution.

The lower radical concentration, together with the possibility to modulate either the biophysical and the biochemical properties of these gels, by tuning the light irradiation, make this process unique.[207] The gelation mechanism of the radical-mediated thiol-ene norbornene reaction and the factors influenced by this novel approach will be examined in depth, respectively:

- Thiol-norbornene photopolymerization mechanism of gelation.
- Network structure: a comparison between the step-growth process and thiol-ene click chemistry.
- Effects of the macromer concentration.
- Defects during the photopolymerization.
- Kinetics and degradation induced by hydrolysis.
- Effect of the initial crosslinking density on the degradation.
- Effect of the crosslinker sequence on the network properties.
- MMPs influence.
- Enzymatic degradation.

The mechanism of reaction occurs in a stoichiometric ratio.[207] The gelation process and the *in-situ* cell encapsulation of thiol-ene norbornene-based hydrogels were reported for the first time by using a long wave UV-light irradiation and by employing photoinitiator of the first type- type I- (cleavage type) as lithium phenyl phosphinate (LAP) or Irgacure-2959.[209]

As depicted in Figure 1.5, upon UV light irradiation, the LAP photoinitiator is decomposed into radicals. The later abstracts protons from sulfhydryl groups (-SH) to form thyl-radicals, that react with strained vinyl bonds in the norbornene moiety on functionalized norbornene-polymer (R_2). The reaction creates a thiol-ether bond and a carbon-centered radical capable of generating another thiyl radical. This mechanism of thiol-norbornene coupling and consequent thiyl radical formation proceeds until the limited moiety (thiol or norbornene) is depleted (Figure 1.5-b).[210]

Since no homopolymerization occurs between norbornene groups, as in the case of acrylate-based hydrogels, the resulting networks only possess orthogonal crosslinks and an idealized structure.[207] Moreover, the degree of network heterogeneity is minimal, compared to random chain-growth polymerization.[211]Another important aspect is that the gelation can be achieved faster (order of seconds), compared to acrylate-based chain growth polymerization[212], without the use of a high concentration of photoinitiator or macromer[208], drastically reducing the reagents consumed.

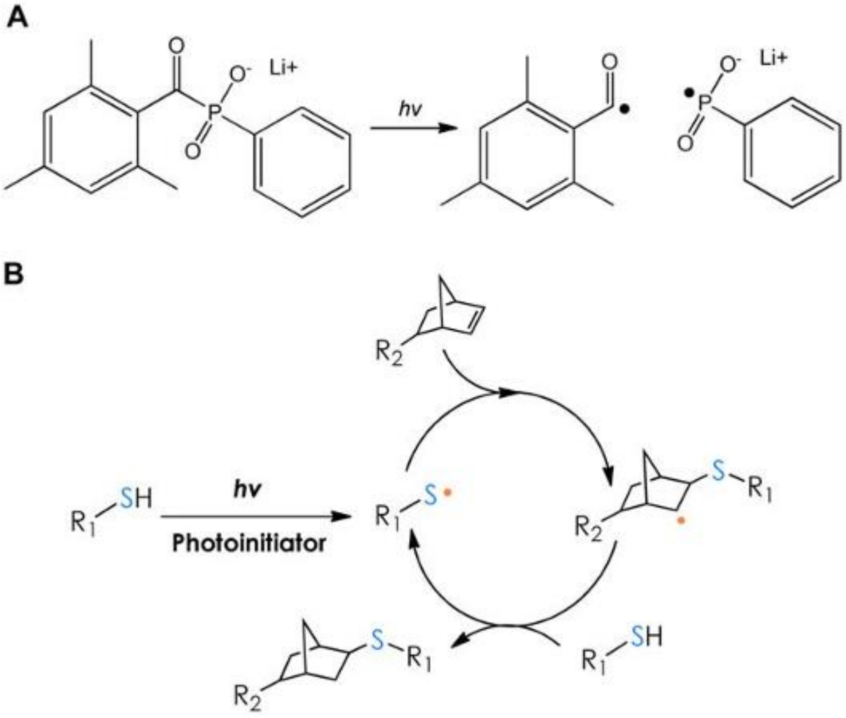

Figure 1.5. Thiol-ene mechanism of reaction. (A) Photocleavage of the LAP (type I) photoinitiator into radicals. **(B)** Schematic representation of radical-mediated step-growth thiol-norbornene photoclick reaction triggered by light irradiation (hν), between a thiol-containing molecule (R_1-SH) and norbornene-functionalized macromer (R_2-norbornene). Adapted from C.C. Lin et al.[210]

Thiol-norbornene mechanism reaction is not oxygen-inhibited, facilitating the cell encapsulation. Visible light can be also used to trigger the reaction, normally in the presence of a type II photoinitiator (non-cleavage type) and a co-initiator.[210] The visible light efficiency is not so high compared to UV-light exposure but can result in more appropriate conditions, especially when cells are involved in the photopolymerization process. The hydrogel network can be estimated through hydrogel equilibrium swelling.[213] Ideally, a "perfect crosslinked" hydrogel, thiol-ene-based gel, or Michael-type hydrogel network should not present defects in the structure.

Thus, from structural information as the molecular weight of the macromer and crosslinker, and functionality, the average molecular weight between crosslinks can be defined as:

$$\bar{M}_c = 2\left(\frac{MW_A}{f_A} + \frac{MW_B}{f_B}\right)$$

Where MW_A and MW_B respectively, are the molecular weight of macromer-norbornene and crosslinker, whereas f_A and f_B are the number of reactive functionalities for macromer-norbornene and crosslinker. Hence, knowing $\bar{M}_c$, the ideal network crosslinking density (v_c) and the polymer volume fraction (v_2) can be calculated by the Flory-Rehner theory:

$$v_c = \frac{V_1}{\overline{M_c}\,\overline{v_2}} = \frac{-\left[ln(1-v_2)+v_2+\chi_{12}\ v_2^2\right]}{v_2^{1/3}-\frac{2v_2}{f_A}}$$

Where $\overline{v_2}$ is the specific volume of the monomer at 37 ºC, V_1 is the molar volume of the water, and χ_{12} is the Flory-Huggins interaction parameter for the macromer and the water system. Consequently, by obtaining v_2, the ideal hydrogel mass swelling ratio q can be calculated by using the following equation:

$$v_2 = \frac{\bar{v}_2}{(q-1)\,\bar{v}_1 + \bar{v}_2}$$

Where v_1 is the specific volume of water (1.006 cm^3/g at 37 ºC).

Another important parameter to consider is the macromer concentration on the thiol-ene hydrogel network. As reported by Shih et al.[214], an ideal step-growth network, without defects and with a fixed macromer composition, should only possess a single equilibrium swelling. The swelling ratio should be totally independent of the macromer concentration in a situation of equilibrium. In their study, they enhanced how the equilibrium mass swelling ratio showed a dependency on the macromer concentration. Hence, when the macromer concentration was increased, the swelling ratios decreased, being closer to the ideal equilibrium swelling ratio (dashed lines- Figure 1.6).

On the other side, low swelling ratios (which means higher macromer contents) correspond to higher values of Elastic Modulus. This inverse relationship was also observed in chemically crosslinked networks, including PEGDA hydrogels based on chain growth reactions. Therefore, macromer concentration-dependent hydrogel swelling is observed experimentally.[214]

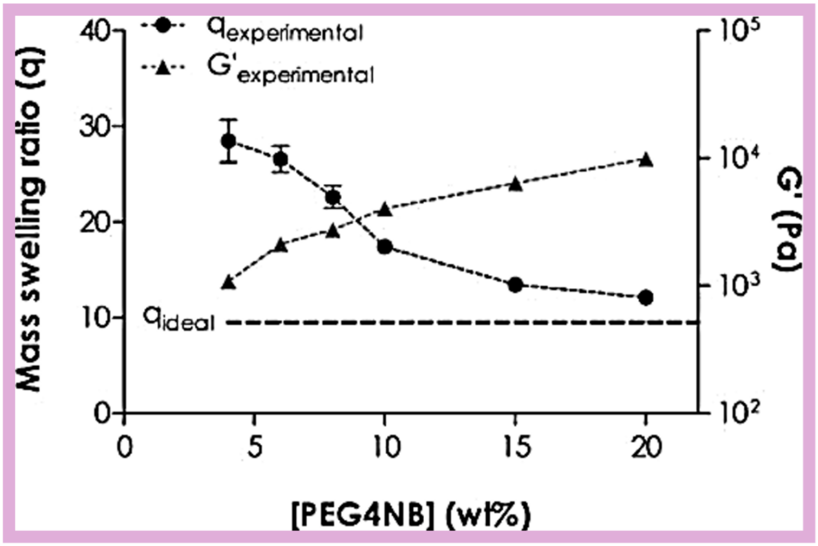

Figure 1.6. Effect of macromer concentration. Effect on the hydrogel equilibrium swelling-**left axis**- and elastic modulus – **right axis.** Adapted from Shih et al.[214]

This strong correlation resulted in beneficial for tuning the physical properties of gels, depending on the biological application. The trend observed in Figure 1.6 can be also attributed to a higher tendency of cyclization at lower macromer contents. In this case, a higher extent of intramolecular reactions provokes more primary cycles. So, as proved in the work of Shih et al,[214] a lower degree of intermolecular crosslinking resulted in increased gel swelling and vice versa.[215] The correlation between the experimental swelling trend and the macromer contents is strictly linked to another aspect: the network defects, mainly caused by different degrees of intramolecular and intermolecular reactions.[215]

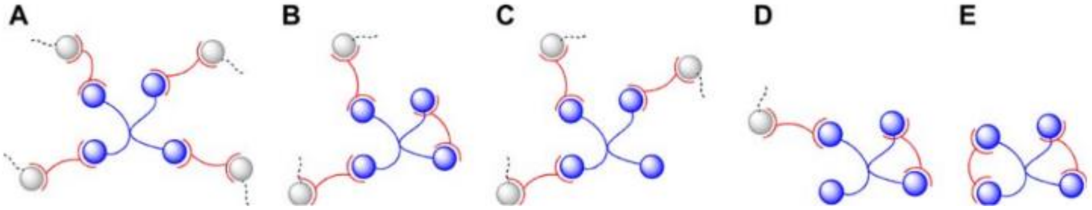

Figure 1.7. Schematics of the potential products after step-growth thiol–norbornene reactions between tetra functional PEGNB and bifunctional DTT. **(A)** defect-free, fully crosslinked thiol–norbornene network; **(B)** fully reacted thiol–ene network with a primary cycle; **(C)** partially crosslinked thiol–ene network with an unreacted, dangling PEGNB arm; **(D)** dangling polymer with a primary cycle and an unreacted PEGNB arm; and **(E)** soluble polymer with fully reacted functional groups. D and E did not contribute to network crosslinking.

The main difference between chain-growth hydrogel networks, such as PEGDA or GelMA, and the radical-mediated thiol-norbornene hydrogels resides in crosslinks. In the first case, they are mainly composed of a random number of homopolymerized (meth)acrylates; instead in the thiol-norbornene-based gels, the crosslinks are thioether bonds. Furthermore, due to the orthogonal thiol-norbornene reaction, the network ideality is very high. Although these systems appear closer to an ideal network Figure 1.7 (A), practically, network defects can occur. As represented in Figure 1.7, in a thiol-norbornene reaction between PEG-tetra-norbornene and a bifunctional crosslinker DTT (dithiothreitol), the existence of unreacted functionality Figure 1.7 (B), primary cycles Figure 1.7 (C), and/or dangling polymers Figure 1.7 (D) reduces the overall crosslinking density of thiol–norbornene hydrogels. These phenomena are more likely to occur at lower macromer concentrations. Anyway, network defects do not contribute to crosslinking density; hence the degree of network heterogeneity is at a minimum when it is compared to random chain-growth polymerization (acrylate-based).

To better examine the advantages of thiol-ene chemistry, it is noteworthy the comparative study reported in the literature and conducted on the gelation kinetics of two-step-growth polymerization, respectively: thiol-ene photo click polymerization and Michael-type addition. It has been observed that, at the same molecular weight of the two distinct macromers used (PEG4NB and PEG4A) and functionalities, the gel point of the photo click reaction was 230-fold faster than that of the Michael-type addition reaction. Furthermore, the time necessary to complete the entire process was almost 10 times faster in the case of thiol-ene polymerization, showing higher final shear Modules, indicating improved network connectivity in thiol-ene hydrogels.[211]

Analysis of the hydrolytic degradation of these hydrogels was also investigated, by varying the macromer concentrations and at different pH values, respectively: pH 7.4 (Figure 1.8-left) and pH 8.0 (Figure 1.8-right). Hydrogels prepared to contain lower weight content of macromer degraded at a slightly faster rate regardless of pH value. Model prediction also followed the same trend. This study suggested that the effect of macromer concentration affected not only the initial network cross-linking (i.e., network ideality) but also the rate of network hydrolytic degradation.

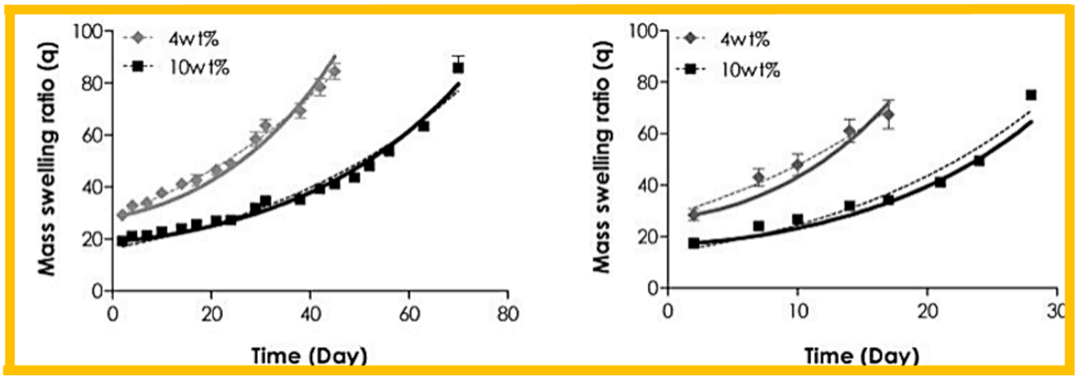

Figure 1.8. Hydrolytic degradation of PEG4NB-DTT hydrogels. Different macromer concentrations in (left) pH 7.4 and (right) pH 8.0 PBS. Symbols represent experimental data, dashed curves represent exponential fit, and solid curves represent model prediction.

Some studies also revealed a correlation between the initial crosslinking density on the gels' properties and degradation. In fact, by keeping constant the macromer concentration, and by altering the crosslinker concentration, it was shown that decreasing the initial network crosslink (the ratio between macromer concentration and crosslinker concentration), resulted in an increased hydrogel swelling since there was an increase in network non-ideality. Results also enhanced that faster degradation rates were observed in this case, as a function of non-ideality.[214]

While the degradation of thiol-ene hydrogels was mediated by ester bond hydrolysis, data suggested that it was also affected by other environmental and structural factors (such as the presence of norbornene groups connecting the thioether and ester bonds).

The degradation of thiol-ene hydrogels appeared slower than the reported degradation of thiol-acrylate Michael-addition hydrogels at comparable macromer concentrations. This was due to the hydrophobic norbornene groups connecting the thioether and ester bonds. In thiol-acrylate Michael-addition hydrogels, this linkage is a less hydrophobic ethylene group. The general trend observed from these studies was that thiol-ene hydrogels with a higher degree of cross-linking degraded at a slower rate than gels with a lower degree of crosslinking.

As an alternative approach, recently it has been observed that PEG hydrogels can be crosslinked by peptide crosslinker, which results in suitable biomimetic systems for creating proper extracellular matrix microenvironments.[216,217] Varying only one amino acid on the peptide sequence crosslinkers, enhanced different behaviors in terms of network properties.

Interestingly, hydrogels cross-linked by peptides containing aromatic (e.g., CGGYC) or hydrophobic (e.g., CGGLC) residues reported slower degradation rates compared to gels cross-linked by simple CGGGC linker. The cause can be potentially correlated with the steric hindrance and hydrophobic effect of tyrosine and leucine residues that retarded degradation. Among the advantages of the thiol-ene norbornene hydrogels employ, there is the study of the influence of the local matrix environment on the cell fate processes, since many processes such as growth, and differentiation, require a protease-induced matrix cleavage, as the matrix metalloproteinase (MMP). This influence can be examined by preparing thiol-norbornene hydrogels, with an MMP-sensitive peptide linker.[209,218] It has been observed that when cells are encapsulated within hydrogels containing an MMP-sensitive linker, they can remodel their local microenvironment, resulting in the accommodation of some cellular activities, such as migration, proliferation, and matrix deposition.[217] Due to the short-range action of proteases, the subsequent degradation of thiol-norbornene-based hydrogels caused by cell-secreted proteases is mostly a local event. These activities led to a reduction in terms of crosslinking density and consequently of the bulk gel mechanical properties.[219]

Last, thiol-norbornene gels can be also degraded by exogenously applied stimuli such as enzymes, or additional light exposure. When the protease-sensitive peptides are used in the crosslinker formulation, gels are degraded enzymatically by placing them in a solution containing the protease of interest. If protease diffuses faster than its enzymatic reaction, the hydrogel will mainly degrade throughout its structure when the protease is introduced externally. However, if the peptide linkages break down quicker than the protease can penetrate the hydrogel, erosion would start from the surface. Since most proteases are relatively large molecules, they typically do not diffuse into hydrogels faster than the molecules they break down. Hence, when a protease is added from outside to degrade the hydrogel, surface erosion is the likely mode of degradation. [220]

1.7 Fabrication methods

The imperative resolution of skin and appendage regeneration stands as a pressing quandary within the domain of tissue engineering (TE) and regenerative medicine. Therefore, it is essential to ascertain a suitable approach for the fabrication of skin-like models. Within the conventional artificial deposition techniques, notable methodologies include electrospinning, fiber deposition, freeze drying, and salt-leaching.[221,222] Electrospinning emerges as the most versatile fabrication method within the context of skin-like models.

When compared to conventional dressings and hydrogels, electrospun nanofibrous materials exhibit notable properties as dermal substitutes owing to their ability to mimic the intricate architecture of the native extracellular matrix (ECM) of the skin. This resemblance facilitates cell adhesion, proliferation, and subsequent dermis regeneration.[223,224] Recently, the application of hand-held electrospinning devices for the *in-situ* deposition of electrospun fibers has gained traction as a promising alternative to traditional electrospinning techniques.[225,226] This approach entails the direct deposition of fibers onto impaired tissue, thereby facilitating tissue repair and regeneration. Moreover, the utilization of 3D nanofiber structures fabricated through wet electrospinning and multilayering confers the advantage of morphological control, enabling tunability of scaffold porosity and fiber size.[227]

In contrast to traditional artificial deposition methods, 3D bioprinting offers several advantages in the preparation of tissue-engineered scaffolds (TES), which include: (1) computer scanning imaging technology enables the rapid production of skin grafts tailored to the shape and depth of the wound surface, characterized by timeliness, high throughput, and repeatability.[228,229] (2) Versatility with multiple available bioinks, facilitating precise deposition of various biological agents such as living cells, nucleic acids, growth factors, and pregelatinized solutions. This capability allows for the construction of tissue structures exhibiting morphology and physiology akin to normal skin.[230](3) Utilizing the layer-by-layer deposition principle, 3D bioprinting could enable the *in-situ* printing of skin tissue directly onto the wound surface.[231] (4) 3D bioprinted constructs feature interconnected pores and large surface areas, supporting vital cellular processes including attachment, growth, intercellular communication, and exchange of gas and nutrients. This stands as a notable advantage over traditional techniques, such as solvent casting, phase separation, and melt molding.[232] Over the past decades, 3D bioprinting technology has found widespread application in the fabrication of biological tissues across various domains, including vascular systems, heart, bone, cartilage, skin, and liver.[233]

Presently, 3D bioprinting technology has garnered escalating interest owing to its considerable potential for the advancement of tissue-engineered scaffolds (TES), as depicted in Figure 1.9.[234] 3D bioprinting entails the application of rapid prototyping technologies to systematically deposit cells, growth factors, and assorted biomaterials in a layer-by-layer manner, intending to generate biomedical components that closely emulate the characteristics of natural tissues and organs.[235]

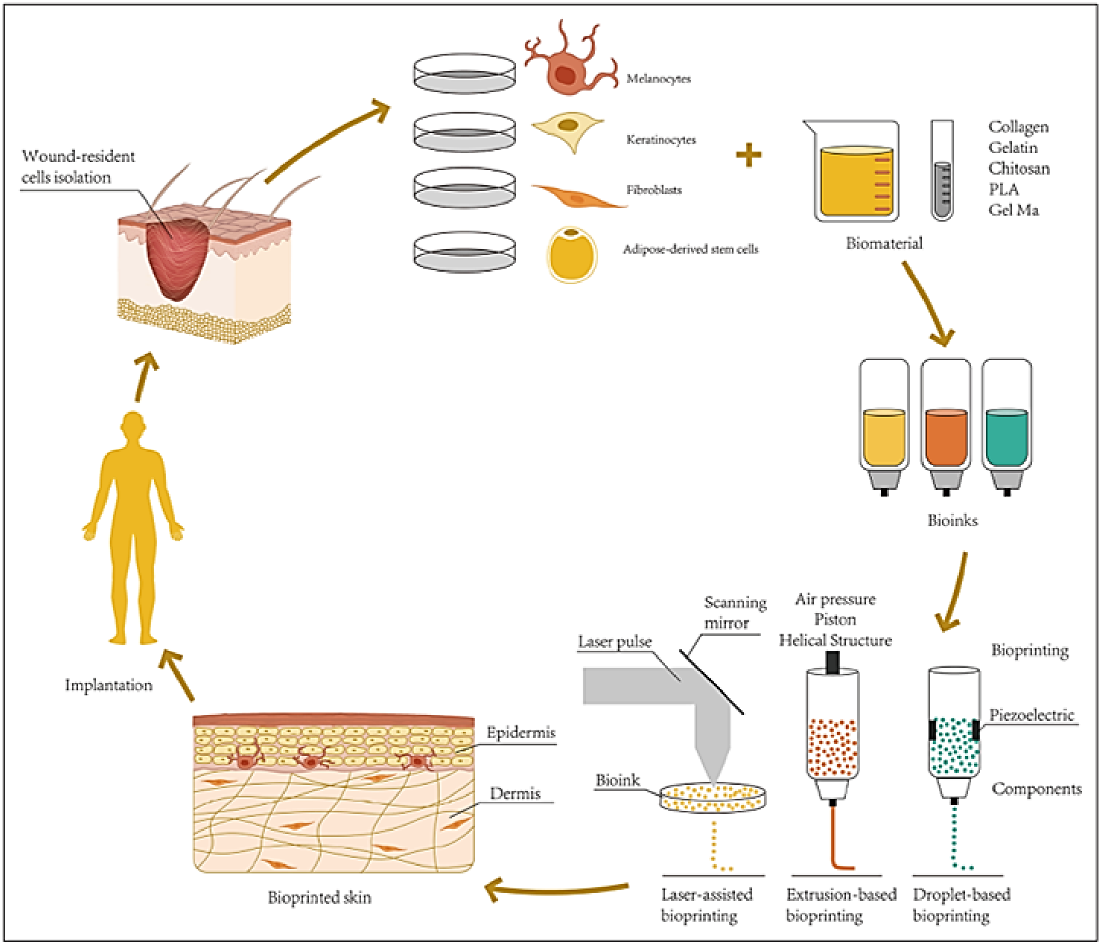

Figure 1.9. Schematic representation of skin 3D bioprinting.[234]

This method serves as an extension of rapid prototyping, also known as additive manufacturing (AM) techniques, which enables the automated fabrication of complex 3D biocompatible structures through the computer-controlled deposition of biological substances onto a substrate, utilizing computer-aided design/computer-aided manufacturing (CAD/CAM) technology.[236] 3D bioprinting technologies, classified based on different molding principles and printing materials, encompass droplet-based bioprinting (DBB), extrusion-based bioprinting (EBB), and photocuring-based bioprinting (PBB).[237]

Droplet-based bioprinting (DBB) technology primarily comprises Inkjet bioprinting (IJB), Electrohydrodynamic (EHD) jetting bioprinting, and Laser-assisted bioprinting (LAB). Inkjet-based bioprinting represents a non-contact process facilitated by 2D desktop inkjet printers. Broadly, these printers are categorized into thermal inkjet bioprinting, electrostatic inkjet bioprinting, and piezoelectric inkjet bioprinting.[237–241] Piezoelectric inkjet bioprinters utilize a piezoelectric actuator to generate acoustic waves within the bioink chamber.[242]

Conversely, electrostatic inkjet bioprinters produce droplets through the application of voltage pulses between a pressure plate and an electrode, while in thermal inkjet bioprinting, heat generation within the bioink chamber induces pressure.[237,239] Despite the commonality in generating ink droplets, the demand for these technologies has surged due to their cost-effectiveness, compatibility with living materials, and rapid fabrication speed of droplet bioinks.[243,244]

Electrohydrodynamic (EHD) jetting bioprinting employs an electric field to draw bioink droplets through an orifice, resulting in the ejection of bioink droplets.[245] Consequently, parameters such as electric field strength (applied voltage), bioink flow rate, and bioink characteristics (such as cell type and concentration) play pivotal roles in determining printing methodologies and subsequently influencing cell viability.[246–248] EHD jetting bioprinting is particularly well-suited for the deposition of highly concentrated bioink formulations, with volume weights of up to 20%.[249]

Laser-assisted bioprinting (LAB) technique, initially devised for metal writing applications, has been effectively adapted for the bioprinting of nucleic acids such as DNA or organ cells.[250,251] The inaugural laser-assisted bioprinter was engineered in 2004 to facilitate the transfer of biological patterns onto substrates, thereby enabling the precise printing of biomaterials with enhanced resolution.[252,253] The LAB technology operates by emitting laser light from a pulsed laser source. This light is directed onto a metal film situated on the back of a silicate glass substrate, where local heating occurs, leading to the rapid evaporation of the bioink deposited on the glass and its subsequent dispersion onto the substrate in the form of liquid drops. LAB predominantly utilizes a nanosecond laser with ultraviolet or near-ultraviolet wavelengths as an energy source, achieving printing resolutions at the picogram level.[254–256] A significant milestone in the Laser-assisted bioprinting field was achieved by Michael et al,[257] who successfully developed a Graftskin® skin substitute using this technology. Moreover, Koch et al,[258] used laser printing based on laser-induced forward transfer (LIFT) to print various cell types, including skin cell lines (FBs-NIH-3T3- and KCs-HaCaT-) and human mesenchymal stem cells (hMSCs), all of which maintained their proliferative capabilities post-LIFT, with high cell survival rates.

Notably, Laser-assisted bioprinting equipment (Figure 1.10) lacks a nozzle, enabling non-contact printing of cells with high activity and resolution.[259–261] However, a notable limitation of LAB resides in its absence of a suitable rapid gelation mechanism, thereby constraining its potential for high-throughput printing applications.

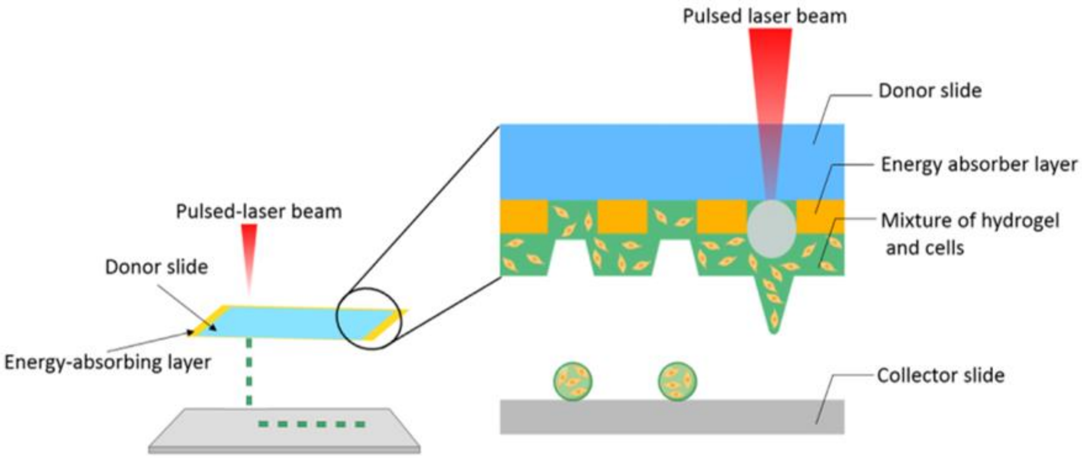

Figure 1.10. Schematic representation of Laser-assisted bioprinting. Adapted from Vanaei et al.[262]

Extrusion-based bioprinting (EBB) technology enables precise printing control through fluid distribution systems and automated machinery.[263] Under computer guidance, bioink that contain cells are propelled through a micro-nozzle in continuous filaments utilizing pneumatic, piston, or screw drive methodologies. Upon layer-by-layer deposition, a comprehensive 3D construct is generated.[264] Notably, hydrogels with shear-thinning properties exhibit optimal performance in pneumatic-based extrusion bioprinting, retaining filament integrity post-extrusion. Conversely, screw-driven systems facilitate the printing of high-viscosity bioinks, conducive to the production of more structurally stable 3D bioprinted tissues.[265] Contemporary extrusion bioprinters are equipped with multiple printer heads, enabling the simultaneous deposition of diverse bioinks while minimizing cross-contamination.[266] Additionally, they afford enhanced control over porosity, shape, and cell distribution within the printed construct. Relative to droplet-based bioprinting (DBB) and laser-assisted bioprinting (LAB), EBB offers advantages such as increased printing speed, compatibility with various types of bioink (including cell clusters, high-viscosity hydrogels, microcarriers, and acellular matrix components), and augmented mechanical strength of printed products. Moreover, EBB facilitates the fabrication of porous grid structures, promoting nutrient and metabolite circulation and achieving biomimetic effects. It also stands as a highly adaptable method, particularly suited to produce scaffolds or prosthetic implants for tissue engineering applications. However, it is associated with lower resolution, typically exceeding 100 µm.[266–268]

Stereolithography (SL), is a bioprinting method employing photopolymers that undergo photopolymerization under precisely controlled light to solidify and form structures.[269] In comparison to alternative bioprinting approaches, stereolithography offers notable advantages such as high precision and rapid processing capabilities.

The principal operational mechanism of this technique relies on the use of a UV laser and a directed mirror array to project a light beam onto the surface of the liquid photocurable resin. This process is iterated in each layer along the Z-direction to construct the 3D parts. However, a significant drawback of SL is its reliance on a UV light source, which poses risks to cells and has been associated with the onset of skin cancer.[270] Within the domain of biology, this method finds application in the fabrication of controllable geometric shapes, including high-precision tissue scaffolds with porous architectures.[271] Stereolithography facilitates the attainment of elevated cell viability by circumventing the application of shear force to cells, coupled with the ability to achieve fast bioprinting of structures with high resolution (approximately 1 μm). Nonetheless, a primary limitation of SL resides in the necessity for transparency in the liquid medium; failure to meet this requirement results in nonuniform light penetration and crosslinking. Consequently, the cell density in the bioink is constrained to approximately 10^8 cells/ml.[272] Currently, stereolithography technology finds extensive application in scaffold printing, yet its utilization in cell-based printing remains infrequent.

Digital Light Processing (DLP)-based bioprinting technology has recently garnered considerable attention as a method for delivering biomedical materials and/or specific cells to create intricate structures for diverse tissue modeling and regeneration purposes.[273] Digital Light Processing (DLP)-based 3D bioprinting facilitates the fabrication of intricate three-dimensional structures by employing digitalized light sources such as ultraviolet (UV) light, blue light, near-infrared (NIR) light, or other visible light spectra to induce *in situ* photopolymerization. This process transforms liquid polymer materials into solid three-dimensional structures characterized by high resolution and structural complexity.[274,275] DLP bioprinting emerges as an efficacious method for fabricating intricate constructs, utilizing a light-based printing approach to solidify an entire layer of monomer simultaneously.

This process is facilitated by light emitted from a digital micromirror device (DMD) projector, as illustrated in Figure 1.11. Consequently, DLP technology offers significantly faster printing and production speeds compared to extrusion-based bioprinting methods, thereby presenting a novel strategy for attaining complex structures.

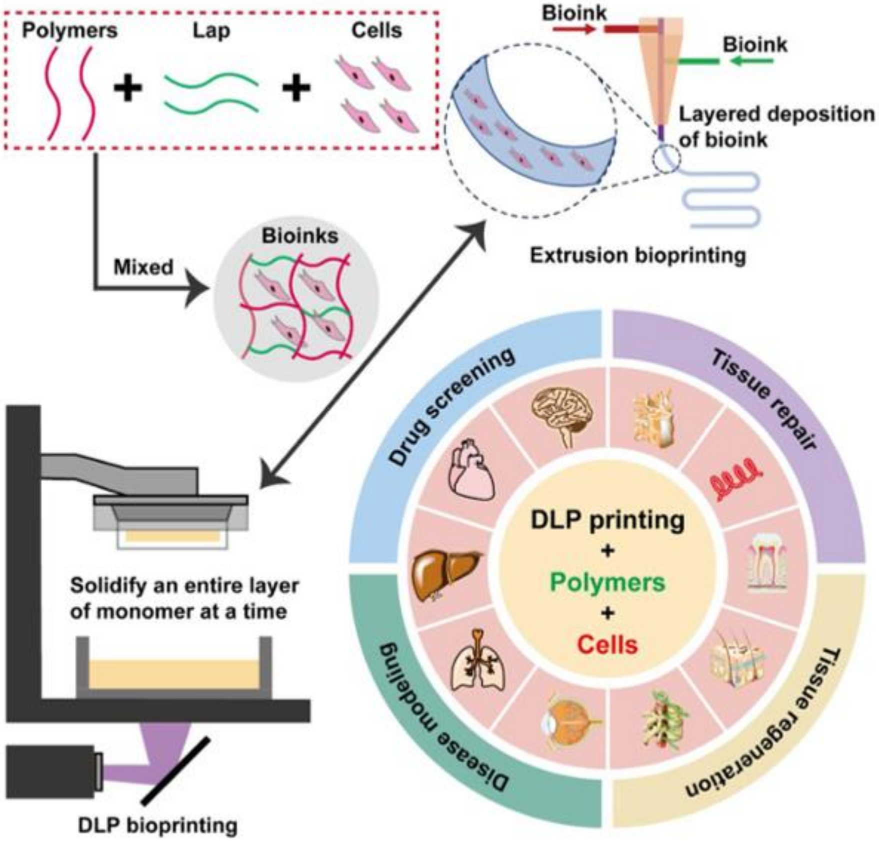

Figure 1.11. 3D extrusion-based bioprinting vs. digital light processing (DLP)-based bioprinting. A brief comparison of 3D extrusion-based bioprinting and digital light processing (DLP)-based bioprinting, and the representative applications of the DLP bioprinting strategies for tissue model. Adapted from Li et al.[273]

1.8. Regeneration of skin tissue model with 3D bioprinting technique

1.8.1. Bioprinting of full-layered skin

Various investigations documented in the literature have elucidated the congruence between 3D-printed skin models and native skin tissue upon attaining maturity. Illustrative of this assertion, Lee et al.[276] conducted a study wherein collagen served as the foundational material for fabricating the dermal skin matrix, while keratinocytes (KCs) and fibroblasts (FBs) were employed as seed cells for the printing of skin tissue.

In this study, the optimization of printing parameters was undertaken with the primary objective of attaining peak cell viability, while concurrently adjusting cell densities within the epidermis to emulate essential physiological characteristics inherent to human skin.

Histological and immunofluorescence methodologies were employed to substantiate the assertion that the 3D-printed skin tissue exhibited a faithful representation both morphologically and biologically akin to the *in vivo* models under investigation.

Cubo et al.[277] used bioinks comprising human plasma alongside primary human fibroblasts (FBs) and keratinocytes (KCs) derived from skin biopsies to print a bilayer human skin construct. Subsequent histological and immunohistochemical evaluations conducted both *in vitro* and *in vivo* corroborated the structural and compositional likeness of the engineered skin model to native human skin tissue.

Wang et al[278] introduced a novel methodology aimed at addressing the challenges associated with the inadequate printability and prolonged crosslinking kinetics characteristic of collagen-based biomaterials. They created a bilayer membrane (BLM) scaffold with an outer PLGA membrane mimicking the epidermis and a lower alginate hydrogel layer representing the dermis. The porous alginate hydrogel enhanced cell adhesion and growth, while PLGA prevented bacterial infiltration and maintained gel moisture. Consequently, the BLM scaffold facilitated significant skin regeneration by fostering neovascularization and increasing collagen I and collagen III deposition. They employed a solid free-form fabrication technique to modify extrusion-based bioprinting, enabling the creation of multi-layered tissue composites. Collagen-based hydrogel bioink was deposited layer by layer, resulting in distinct inner layers of fibroblasts (FBs) and outer layers of keratinocytes (KCs). Robust cell proliferation was evident on both planar and non-planar surfaces.

In situ bioprinting offers a straightforward solution: direct printing of pre-cultured cells onto the wound site, promoting wound closure and skin regeneration. This method simplifies the process, avoiding costly and time-consuming *in vitro* cell differentiation and reducing the need for multiple surgeries.[279]

Albanna et al[280] pioneered a portable skin-in situ bioprinting system. Using a 3D laser scanner, they continuously scanned the entire wound area, generating a precise wound model. Fibrin/collagen served as the hydrogel carrier, facilitating the transportation of allogeneic or autologous dermal fibroblasts (FBs) and keratinocytes (KCs) to the skin defect, ultimately forming a layered skin structure (Figure 1.12). Remarkably, this *in situ* bioprinting system achieved complete wound closure in a murine full-thickness wound model within three weeks post-surgery.

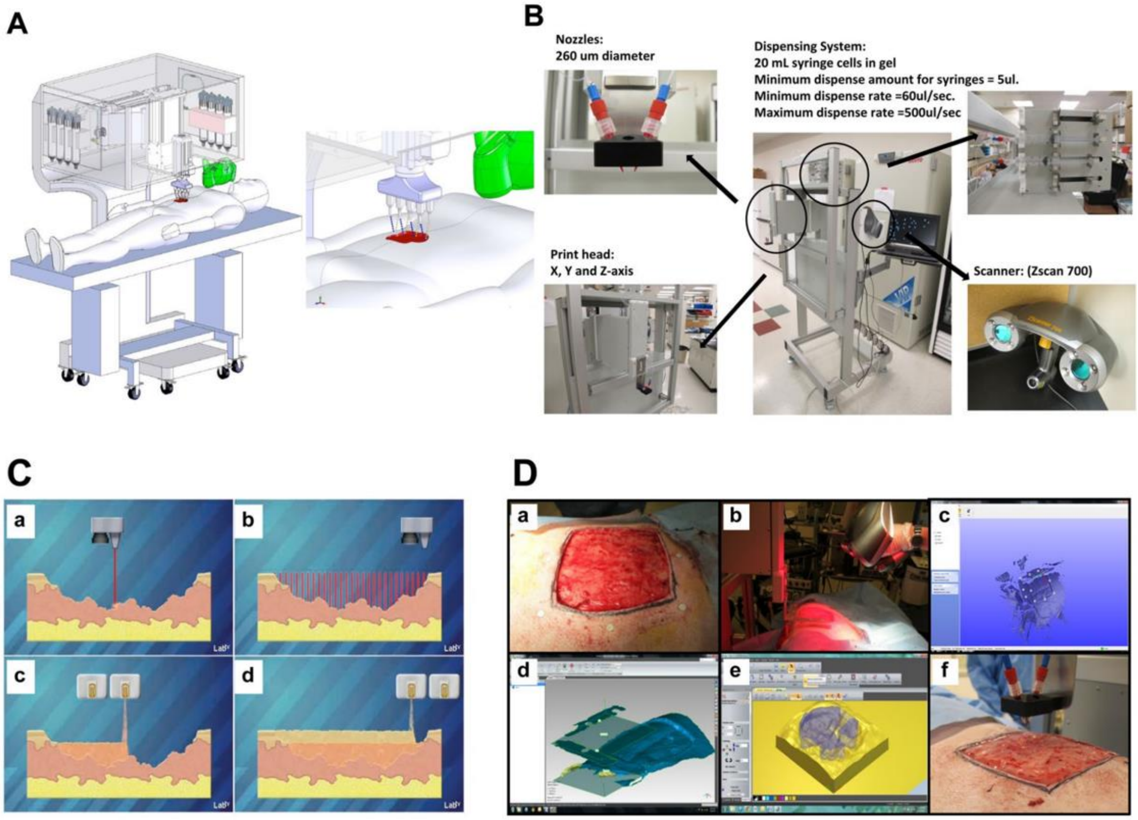

Figure 1.12. Skin bioprinter prototype and *in situ* bioprinting concept. (A) Schematic demonstrating scale, design, and components of the skin bioprinter. **(B)** The main components of the system consist of 260 µm diameter nozzles, driven by up to 8 independent dispensing systems connected to a print-head with an XYZ movement system, and a 3D wound scanner. All components are mounted on a frame small enough to be mobile in the operating room. **(C)** Skin bioprinting concept. Wounds are first scanned to obtain precise information on wound topography, which then guides the print heads to deposit specified materials and cell types in appropriate locations. **(D)** Example of the skin bioprinting process, where markers that are placed around the wound area are used as reference points **(a)** before scanning with a hand-held ZScanner™ Z700 scanner **(b)**. Geometric information obtained via scanning is then inputted in the form of an STL file to orient the scanned images to the standard coordinate system **(c)**. The scanned data with its coordinate system is used to generate the fill volume and the path points for the nozzle head to travel to print the fill volume **(d)**. Output code is then provided to the custom bioprinter control interface for the generation of the nozzle path needed to print fill volume **(e,f).** Adapted from Albanna et al.[280]

1.8.2 Bioprinting of blood-vessel-containing skin.

A critical factor for the survival of 3D-printed skin grafts is timely vascularization post-transplantation. Research indicates that without a network of blood vessels, the maximum distance for effective nutrient diffusion to ensure cell viability is established at 100-200 µm.[281] Thus, tissue constructs exceeding this range necessitate the presence of a network of blood vessels for adequate nutrient supply and cell survival. Yanez et al.[282] enhanced vascularization in printed skin tissues using inkjet printing technology.

They employed collagen type I and fibrinogen as a matrix, with newborn dermal fibroblasts (FBs), keratinocytes (KCs), and human umbilical vascular endothelial cells (HUVECs) as seed cells, demonstrating neovascularization in the 3D-printed skin grafts transplanted onto the back wounds of thymus-free nude mice, two weeks post-surgery.

Abaci et al.[283] introduced an innovative method for micropatterning spatially controlled and perfusable vascular networks in 3D human skin equivalents (Figure 1.13), using both primary and induced pluripotent stem cell (iPSC)-derived endothelial cells. This approach leverages 3D printing technology to precisely control the geometry of the micropatterned vascular networks. Their findings demonstrated that vascularized human skin equivalents (vHSEs) facilitated and directed neovascularization in the wound-healing process.

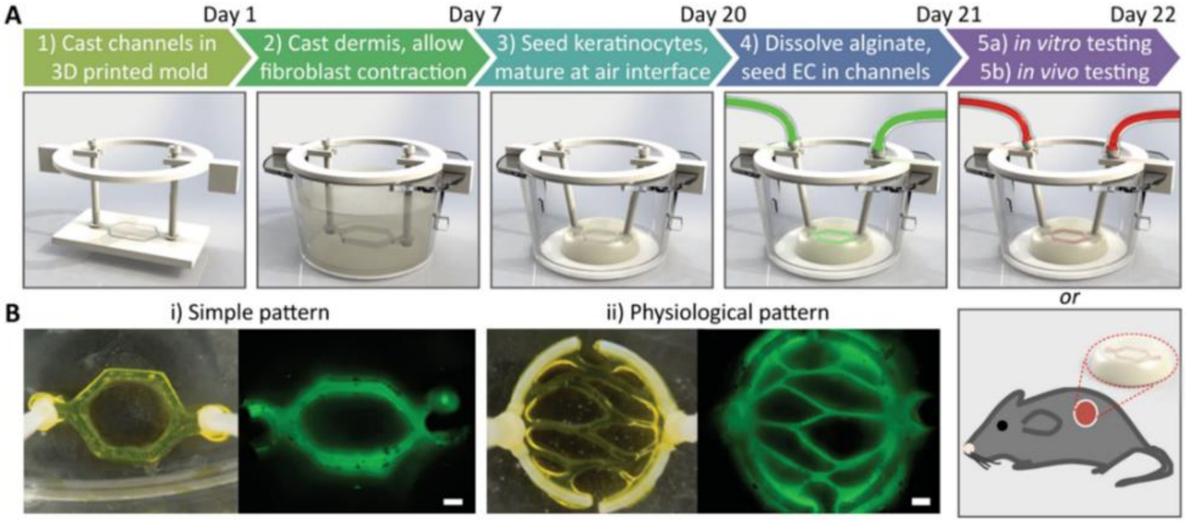

Figure 1.13. Development of vascularized HSEs. A) Schematic description of the protocol to develop vascularized human skin equivalents (vHSEs). A sacrificial layer of alginate microchannels was created in 3D-printed molds, with the desired vasculature pattern. The dermal compartment, consisting of dermal fibroblasts and collagen gel was formed around the sacrificial layer, and suspended in the Transwell inserts using a ring-shaped holder. After the keratinocytes' seeding over the dermal compartment, the construct underwent epidermalization and cornification accompanied by a significant contraction. The sacrificial layer was dissolved by sodium citrate treatment through the inlet/outlet ports followed by EC seeding through the same ports. The vHSEs were used either for grafting or *in vitro* perfusion experiments. **B)** Two different vasculature patterns were used and generated using fluorescently tagged alginate. Scale bar: 600 µm. Adapted from Abaci et al.[283]

In the investigation led by Kerouredan et al.[284], they devised a biofabrication approach using a laser-assisted bioprinting (LAB) system to pattern lines of td-Tomato-labeled endothelial cells co-cultured with MSCs onto a collagen hydrogel substrate. To enhance capillary-like structure formation and maintain the printed pattern, they overlaid the construct with a collagen I hydrogel containing VEGF.

Additionally, the selection of biomaterials such as fibrin and hyaluronic acid (HA) was crucial for promoting angiogenesis. Consequently, the resulting 3D constructs facilitated the development of vascular networks within the printed channels, replacing the original hollow structures.[285]

Mori et al.[286], introduced an alternative model, where they created a perfusable vascular channel within the skin substitute. They coated endothelial cells along the channel and secured them onto a culture device connected to an external pump and tubes. This method yielded robust vascular channels with endothelial cells forming tight junctions along the channel walls.

Kolesky et al.[287] proposed an alternative approach, employing an aqueous bioink consisting of Pluronic F127 to print channels. The outer ring structure was then formed using GelMA loaded with fibroblasts (FBs), followed by cooling the entire construct to 4 ºC to liquefy the Pluronic F127. Subsequent endothelialization of the vessel was achieved by extracting the liquefied Pluronic F127 through a syringe and injecting human umbilical vein endothelial cells (HUVECs) into the channel.

1.8.3. Bioprinting of skin model melanocytes-containing

One of the primary objectives of tissue regeneration is the fabrication of skin tissues endowed with the functionality of skin pigmentation, aiming to address the needs of patients for the restoration of normal skin coloration. Noteworthy advancements have been achieved, wherein a comprehensive skin model, inclusive of pigment, was successfully fabricated utilizing 3D bioprinting methodologies. Specifically, Min et al.[288] have documented a 3D bioprinting methodology proficient in generating a comprehensive skin model featuring full-thickness dimensions and incorporating pigmentation.

Fibroblast-laden collagen hydrogel precursors were systematically deposited and crosslinked via neutralization utilizing sodium bicarbonate, thereby forming the dermal layer. Subsequently, melanocytes (MCs) and keratinocytes (KCs) were sequentially printed upon the dermal layer, aiming to instigate skin pigmentation by applying air-liquid interface culture conditions. Observations revealed that the MC-containing epidermal layer exhibited freckle-like pigmentations localized at the dermal-epidermal junction. Ng et al.[289] have demonstrated the viability of employing a two-step bioprinting methodology for the fabrication of 3D *in vitro* pigmented human skin constructs, incorporating KCs, MCs, and fibroblasts (FBs) derived from distinct skin donors. This approach, characterized by a two-step Drop-on-Demand (DOD) bioprinting strategy, facilitated the controlled deposition of cellular droplets to mimic the epidermal melanin units, while concurrently enabling manipulation of the microenvironment to resemble 3D biomimetic hierarchical porous structures as in the native skin tissue architecture. A well-formed epidermal construct with a uniform distribution of melanin granules was reached, and the presence of specific biomarkers such as collagen VII, Keratin I, and Keratin 6, was also proved.

1.8.4. Bioprinting of hair follicles

Hair follicle reconstruction has become particularly attractive in recent years, and it serves as the foundational prerequisite for the development of tissue-engineered skin endowed with the capacity for hair formation. Central to the endeavor of hair follicle reconstruction lies the identification or enhancement of the follicular seed cells' capacity to elicit hair formation. Presently, the most promising candidates for hair follicle seed cells manifest as hair follicle stem cells (HFSCs) and hair follicle progenitor cells (HPCs). The anatomical localization of these cellular populations within the hair follicles is comparatively elucidated, and the methodologies for their isolation have attained a level of maturity.

Research findings have demonstrated that the combination of newly isolated HFSCs with dermal cells, or HPCs with epidermal cells, can effectively induce hair follicle regeneration. In the study by Wu et al,[290] dermal papilla cells (DPCs), hair follicle epithelial cells, dermal sheath cells, and collagen were mixed to create dermal constructs. These constructs were then transplanted beneath the subcutaneous tissue of nude mice, resulting in the observation of hair fiber formation. In the context of clinical applications, a fundamental requirement for successful hair follicle regeneration is the use of cells originating from the same ethnic background as the recipient. Despite this, limited studies have indicated the potential of human HPCs to regenerate fully functional hair follicles when cultured *in vitro*. Nevertheless, a significant obstacle arises due to the rapid loss of inductive capacity observed in human HPCs within *in vitro* settings.

In summary, the central challenge in hair follicle regeneration lies in enhancing the conditions of *in vitro* 3D culture. This improvement is crucial to emulate the natural growth environment of hair follicles *in vivo* while maintaining the essential biological properties of HPCs and HFSCs. The goal is to achieve the reconstruction of fully developed hair follicles *in vitro*. Abaci et al.[291] devised a biomimetic strategy to generate human hair follicles within human skin constructs. This approach involved the emulation of the physiological three-dimensional (3D) cellular organization found within the microenvironment of hair follicles, accomplished through the utilization of 3D bioprinting technology (Figure 1.14 – a,b, c). This results in the expression of specific differentiation markers of KCs and HSCs, as reported in Figure 1.14 – d-i.

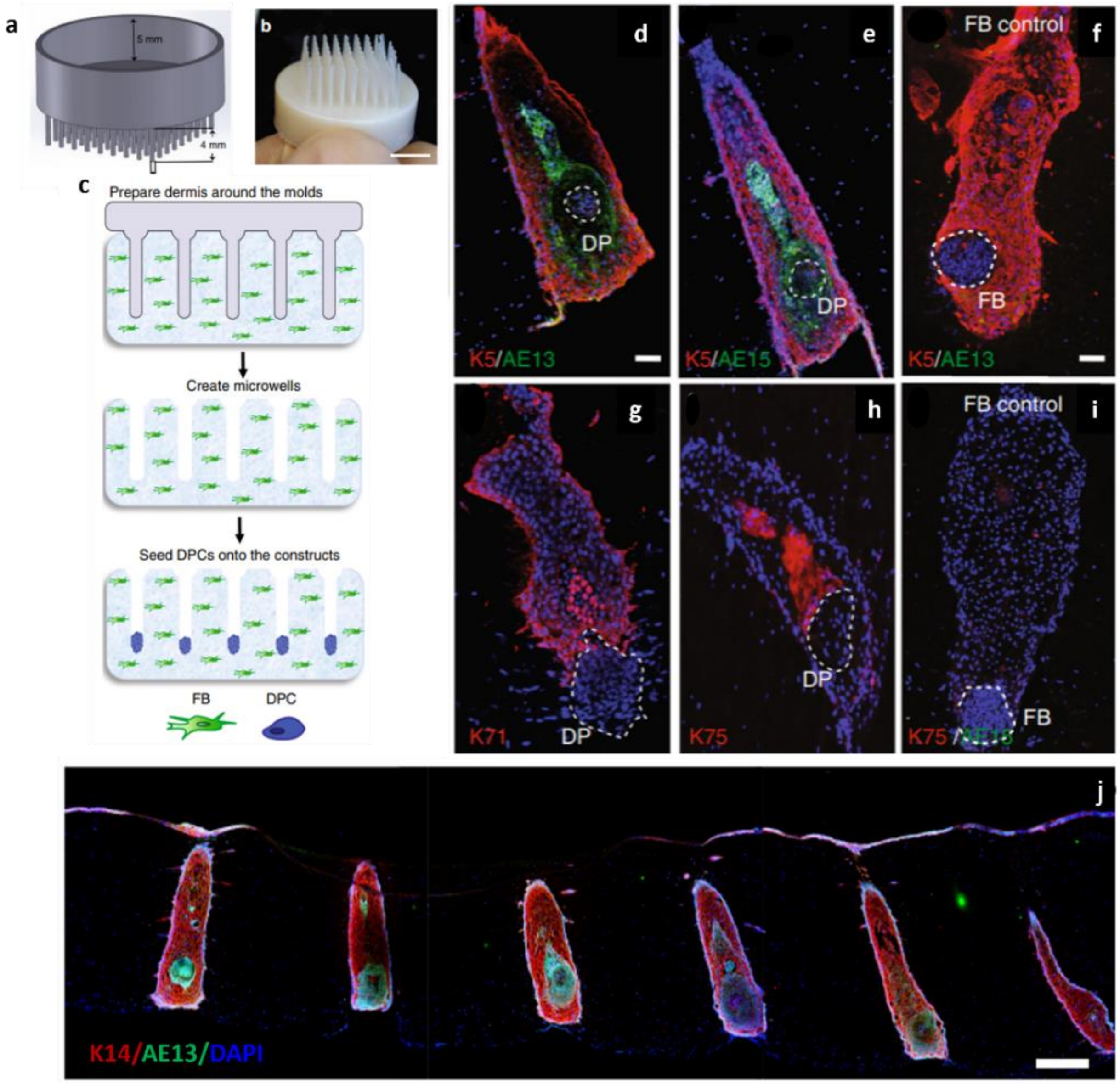

Figure 1.14. Hair follicle development. Hair follicle molds were designed **(a)** and 3D-printed **(b)** to have HF-like extensions and a 5-mm-deep cavity that allows the molds to float on collagen gel. Scale bar = 5 mm **(c)** The collagen gel containing dermal fibroblasts was allowed to solidify around the HF-like extensions to create an array of microwells in which the DPCs formed spontaneous aggregates. **(d-i)** KCs in the HSCs expressed specific hair lineage and differentiation markers K5 and AE13 **(d),** AE15 **(e)**, K71 **(g)**, and K75 **(h)**, which was not observed in HSCs with FB aggregates **(f,i)** after a week of culture. Scale bars = 100 µm. **(j)** Low magnification image demonstrating expression of AE13 in HSCs generated using Lef-1-transfected DPCs and the high efficiency in HF lineage differentiation. Scale bar = 300 µm. Adapted from Abaci et al.[291]

Notably, the application of 3D bioprinting technology facilitated the fabrication of human hair follicle structures characterized by elevated aspect ratios, a feat unattainable via preceding microfabrication methodologies. The overexpression of Lef-1 in dermal papilla cells (DPCs) reinstates the comprehensive transcriptional profile characteristic of intact DPCs and markedly amplifies the efficacy of hair follicle differentiation within human skin constructs (Figure 1.14-j).

Vascularization studies by using hair follicle-density HSCs were also conducted, resulting in the capillary-like network formation and the expression of keratin 14 in the HF structures (Figure 1.15 – a-e), before the engraftment onto immune-deficient mice (Figure 1.15-f).

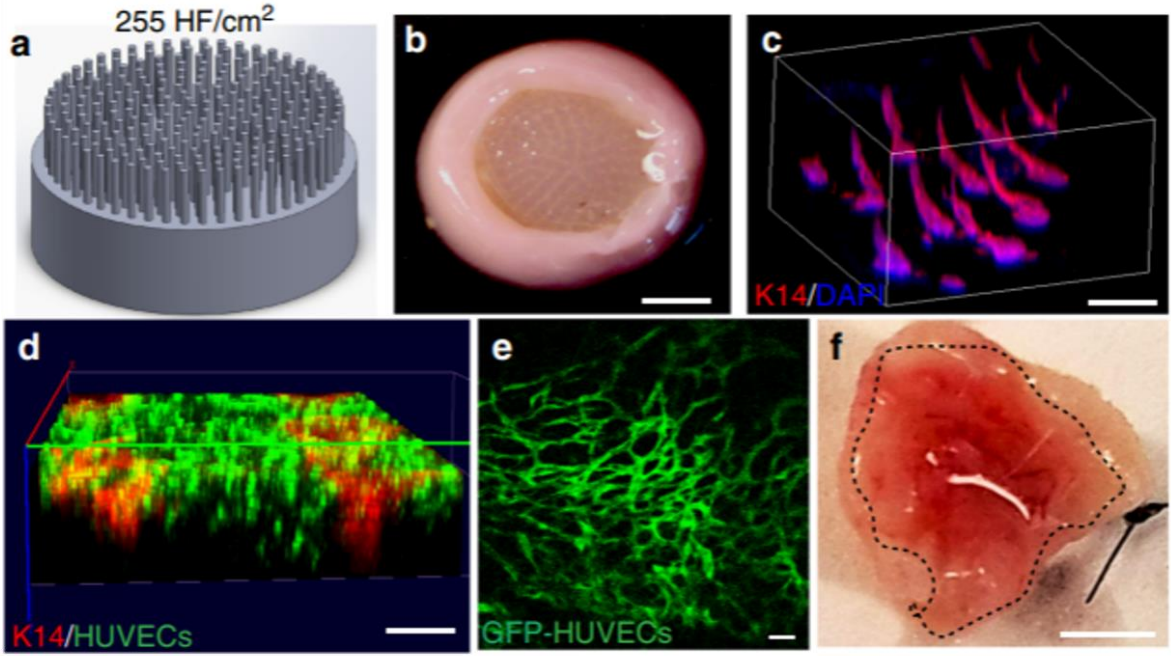

Figure 1.15. Vascularization of high hair follicle-density HSCs for efficient engraftment. (a, b) HSCs were generated using molds that have 255 HF per cm^2 to promote hair growth in grafts. **(c)** 3D-reconstructed wholemount image of the HSCs showing 3D conformation of K14-positive cells at the high hair follicle density. GFP-tagged HUVECs that were encapsulated in the dermal compartment with the fibroblasts closely surrounded the K14-positive cells in the hair follicle structures **(d)** and formed capillary-like networks after 3 days of culture **(e)**. **(f)** Bottom view of the explanted pre-vascularized HSCs (dashed circle) with GFP-HUVECs showing promoted host vascularization and blood supply to the grafts. Adapted from Abaci et al.[291]

Miao et al.[292] undertook the preparation of 3D-structured hair follicle progenitor cell (HPC) spheres using a Matrigel scaffold. The HPC spheres exhibited the characteristic expression of marker genes associated with hair papillae, such as Versican, and α-smooth muscle actin (α-SMA). These marker expressions were notably absent in conventional 2D culture environments. Zhang et al.[293] employed a hair follicle regeneration model to assess the hair follicle-inducing efficacy of dermal papilla multicellular spheroids forming nanofiber sponge substrates. Dermal papilla microtissues suspended in phosphate buffer solution (PBS) were introduced via injection into the dorsal hypodermis of nude mice for evaluation purposes. Experimental findings elucidated that cultured dermal papilla multicellular spheroids exhibited a pronounced capacity to significantly augment the hair follicle-inducing capability.

1.8.5. Bioprinting of complex skin-like models

A recent breakthrough in extrusion bioprinting unveiled the fabrication of multilayered biomimetic skin structures, incorporating six types of human cells: epidermal keratinocytes, melanocytes, dermal fibroblasts, follicular dermal papilla cells (FDPCs), dermal microvascular endothelial cells (DMECs), and adipocytes.[294] In this study, the cells were suspended in three fibrinogen-based hydrogel bioinks and printed using a layer-by-layer deposition method to create a 3 cm–by–3 cm tri-layer biomimetic skin construct, consisting of human-like epidermis, dermis, and hypodermis.

Despite notable advancements in skin bioengineering, contemporary constructs predominantly manifest as planar tissues with exposed boundaries, thus presenting limitations in effectively enveloping anatomically intricate bodily regions, such as the hands. In response to this prevalent paradigm, Pappalardo et al.[295] propose a conceptual shift towards the conception of three-dimensional (3D) enclosed continuous skin constructs, poised to serve as seamlessly transplantable biological integuments adaptable to diverse bodily locales. Central to their innovative approach is the use of a three-dimensional laser scanning technique to generate computer-aided design (CAD) representations of the targeted anatomical region. After CAD model acquisition, a bespoke hollow scaffold architecture, characterized by a permeable porous structure, supplemented by inlet and outlet conduits for medium perfusion, is devised following the anatomical specifications delineated by the CAD model. Employing the Carbon Digital Light Synthesis (DLS) methodology, the scaffold is fabricated, affording precise realization of the envisioned architecture.

The ensuing procedural step entails the fabrication of the dermal layer, realized through the deposition of a primary fibroblast suspension intermingled with collagen I onto the external surface of the scaffold, facilitated by a polydimethylsiloxane (PDMS) negative mold. A requisite maturation period of 14 days within submerged conditions ensues, facilitating extracellular matrix (ECM) remodeling. Concomitantly, human primary keratinocytes are introduced into the interstitial space between the dermal construct and the negative mold, thereby establishing a functional epidermal layer. The air-liquid-interface conditions were applied by suspending the construct in a glass bottle exposing it to the air and perfusing it through the inlet/outlet system. The inner 3D-printed scaffold serves to support the tissue that is wrapped around it, instead, the PDMS mold is removed after each specific phase (Figure 1.16)

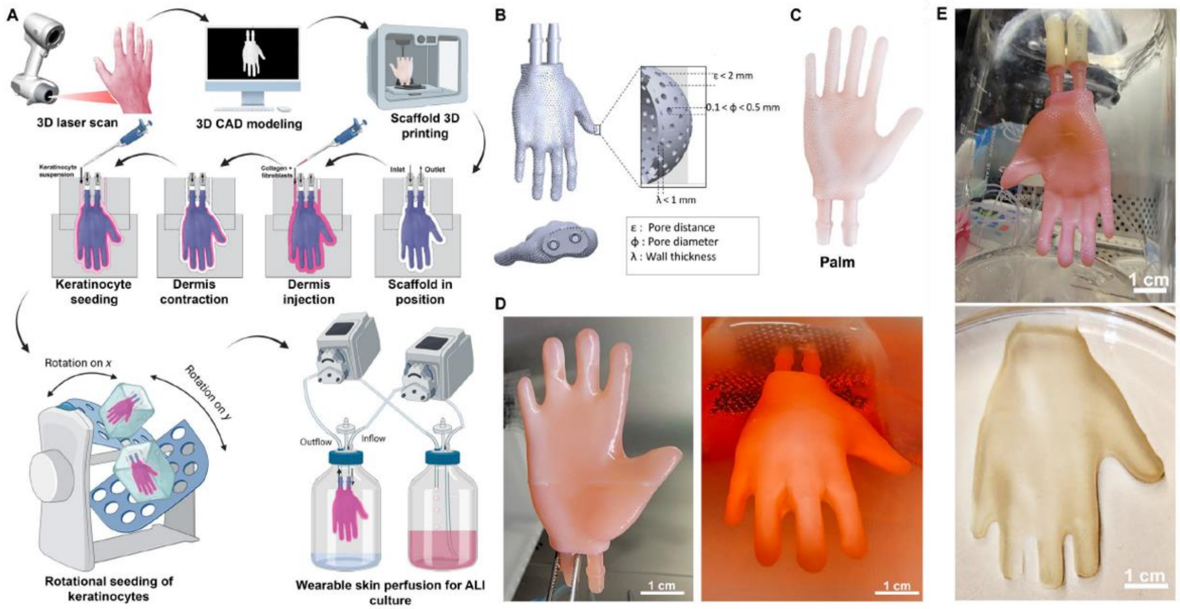

Figure 1.16. A pipeline of the WESC fabrication. (A) A CAD model of an anatomical region is generated through laser scanning and used as a template to design and 3D-print a hollow, perfusable, and porous scaffold through DLS printing. The dermis is cast on the scaffold using a PDMS negative mold. After 14 days of submerging in culture, the dermis contracts, and remodels; currently, KCs are seeded on the surface of the dermis, injecting them as a single-cell suspension on the offset between the dermis and the PDMS mold. A rocking platform ensures that the KCs attach to the dermis surface evenly. After up to 7 days of additional submerging in culture, the scaffold is connected to the fluidic system, and the WESC is cultured inside a glass bottle at the ALI. (**B**) CAD model of the hand scaffold with technical specifics. (**C**) Photograph of a 3D-printed hand scaffold. (**D**) Hand-shaped dermis after 14 days of remodeling. (**E**) WESC on day 7 of ALI culture (up) and after being removed from the scaffold as a skin glove. Scale bars, 1 cm (D and E). Part of the illustration (A) was designed with Biorender. Adapted from Pappalardo et al.[295]

The scaffolds were also vascularized to improve the graft viability, by perfusing human dermal blood endothelial cells (HDBECs) and letting them attach within the walls of the dermis, through the pores surface of the scaffold, before their engraftment onto mice hindlimbs. Hence, the vascularized wearable skin model was removed as a single piece and implanted in the left hindlimb of nude mice. After 4 weeks post-surgery, the graft appeared integrated with the mouse skin, showing full functionality reacquired (Figure 1.17). Immunofluorescence studies and immunohistochemistry corroborated the *in vivo* results.

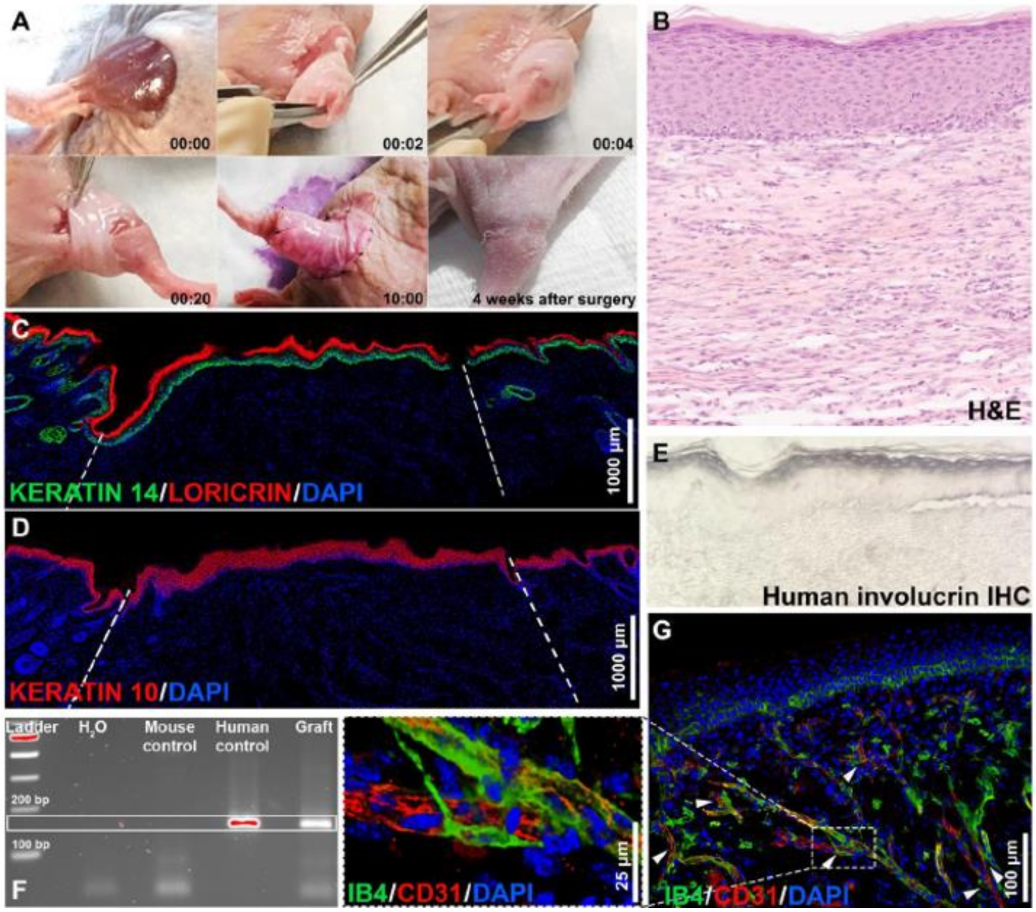

Figure 1.17. Transplantation of the vascularized WESCs onto mouse hindlimbs. (**A**) Time-lapse pictures of the grafting surgery and the integration after 4 weeks; the WESC is easily positioned as a sleeve and sutured to the adjacent mouse skin. The bottom right shows the integration of the graft after 4 weeks. (**B**) H&E staining shows the graft; the human epidermis is fully developed and cornified. (**C** and **D**) IF staining of the graft shows layer-specific epidermal markers of differentiation; Keratin 14, Keratin 10, and loricrin—markers of basal, suprabasal, and cornified layers, respectively—are expressed throughout the epidermis without major interruptions. (**E**) IHC staining for human-specific involucrin, demonstrating the presence of human skin tissue. (**F**) PCR for human-specific β-actin further confirms the survival of human cells in the graft. (**G**) IF staining showing the human (CD31+ IB4−) and mouse (CD31+ and IB4+) vasculature interaction and possible anastomosis sites (arrows). A total of 11 mice were used for grafting. Scale bars, 1000 µm (C and D), 100 µm (G), and 25 µm (G) (magnified). Adapted from Pappalardo et al.[295]

1.9. BRIGHTER technology

The PhD project is in the framework of the BRIGHTER project (European Union's Horizon 2020 research and innovation program under No.828931) which aims to develop a new generation of bioprinting technologies able to produce tissue surrogates (skin models) in an ultrafast, highly precise, and cost-efficient manner.

It involves partners from different countries, respectively from Goethe University (Germany), MYCRONIC company (Sweden), IBEC (Spain), Cellendes company (Germany), and Technion University (Haifa, Israel) and it counts on Light-sheet illumination from two directions combined with high-resolution digital photomasks used to produce the localized crosslinking of cell-laden materials, creating 3D structures in a top-down lithography process (Figure 1.18). The present innovative methodology affords a high-resolution capability that is fully congruent with rapidity in the bioprinting process, yielding constructs that authentically emulate the heterogeneous architectural, biochemical, and mechanical characteristics inherent to the cellular microenvironment within tissues, while concurrently safeguarding cell viability against compromise stemming from prolonged bioprinting durations. Briefly, Cellendes company oversaw the synthesis and development of gel solution' precursors, based on thiol-ene norbornene chemistry. Our group contributed by testing the materials to create proper gel structures either to sustain cell viability and to reconstruct a skin model. Goethe University in collaboration with MYCRONIC company was developing the light-sheet system. Technion University played a part in accomplishing a suitable cell microenvironment, based on cell biology knowledge.

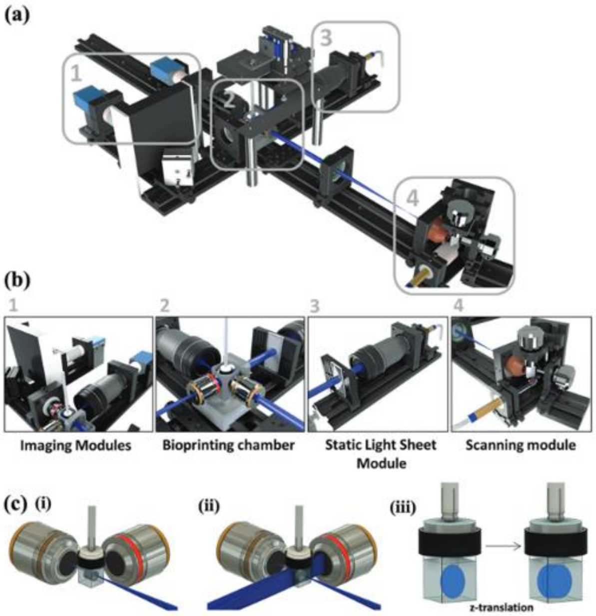

Figure 1.18. Overview of the light sheet bioprinter setup. **a)** Overview of the light sheet patterning bioprinter optical setup. **b)** The bioprinter consists of four distinctive modules. The imaging module (1) can capture patterns during the bioprinting process as well as fluorescence images in situ before and after bioprinting. (2) The bioprinting chamber keeps deionized water steady at 37°C to guarantee optimal conditions for cell culture and bioprinting. (3) The static light sheet is generated by a laser coupled with a beam expander and a cylindrical lens. (4) The scanning module consists of three mirrors, one 45°mirror to inject the laser beam into a galvanometric mirror pair, each one dedicated to scanning the beam in a single axis (x and y). **c)** At the crossing of the (scanned) laser beam and the static light sheet, a cuvette made of FEP-foil contains the bioink (hydrogel and cells) for the photocrosslinking process and imaging. (i) A single laser beam or (ii) double illumination crosslinking is possible for different printing requirements. (iii) Rendering of the layer-by-layer crosslinking process using xy-patterning followed by z-translation.

2. Objectives

Despite considerable advancements in recent years, the development of a physiologically relevant reconstructed human skin model remains a major challenge in tissue engineering. The current gold standard involves the use of collagen-based hydrogels, typically derived from bovine or rat-tail sources[296,297]. These hydrogels are preferred for supporting the formation of a differentiated epidermis. However, they are susceptible to fibroblast-mediated contraction during culture, leading to excessive deformation and making them unsuitable for long-term studies[115,286]. This study aims to find a valid alternative material to fabricate an *in vitro* skin model that shows suitable mechanical and biochemical characteristics that resemble a tissue as much as possible to the *in vivo* one. The **hypothesis** is to address the limitations of collagen-based hydrogels, using alternative polymers, and thiol-ene click chemistry to recreate full-thickness skin models. The specific objectives of the research are summarized as follows:

1. Develop and characterize photocrosslinkable hydrogel systems not toxic to cells, supporting cell adhesion, and amenable to be bioprinted.

2. Adapt a commercial 3D-bioprinting system to create hydrogels with reproducible physicochemical characteristics, based on an interpenetrated network system, establishing single dermis and epidermis compartments.

3. Increase the physiological relevance of the developed skin model for supporting the culture of specific cells (primary keratinocytes, endothelial cells, etc.) that mimic the *in vivo* epidermis and form an intrinsic vasculature system.

3. Materials and Methods

3.1. Hydrogel formulations

3.1.1. Thiol-ene Norbornene chemistry

Hydrogels designed to resemble skin tissue models were prepared by photopolymerization based on thiol-ene Norbornene click chemistry. Preliminary studies were performed to determine the suitable formulation for this process. Thiol-ene click chemistry consists of the reaction between thiol groups (from a crosslinker) and carbon-carbon double bonds. Among the various reactive double bonds available such as acrylate, vinyl carbonate, vinyl ester, vinyl ether, and norbornene, norbornene has been shown as the most reactive (Figure 3.1).

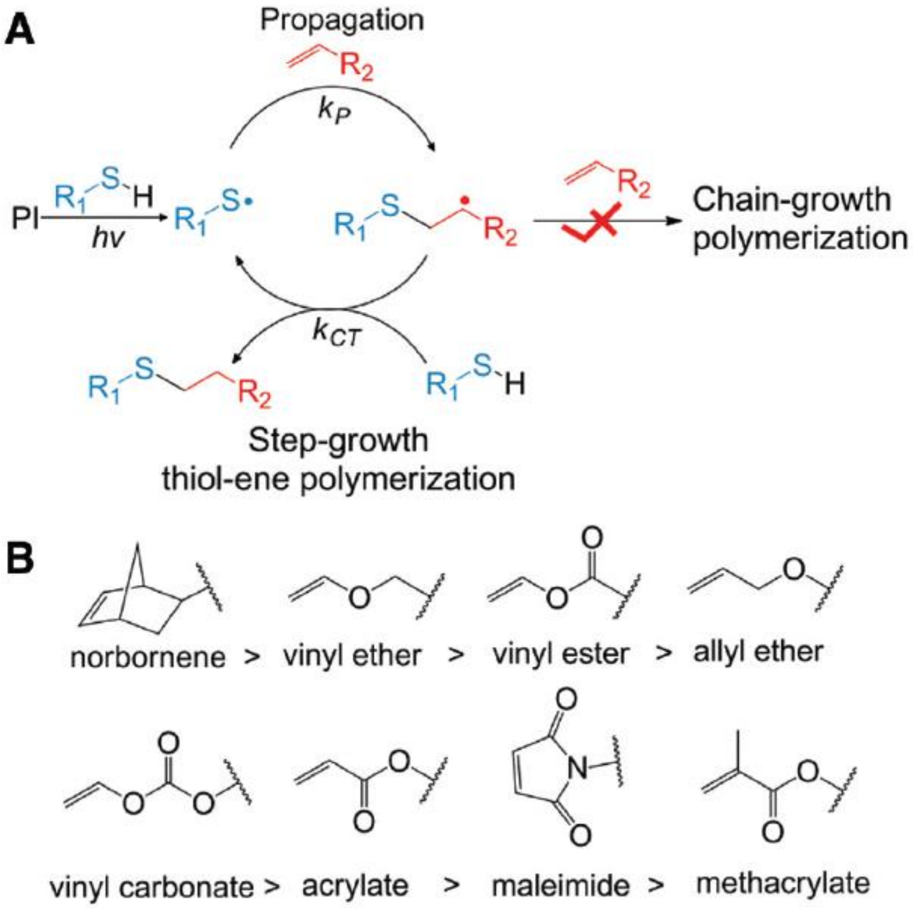

Figure 3.1. (A) Proposed mechanism of radical-mediated thiol-ene photopolymerization and **(B)** reactivity sequence of variable "ene" groups (R2 group in A) towards thiol-ene conjugation.[298]

Upon light irradiation, in the presence of a photoinitiator, a hydrogel can be formed if the norbornene groups are coupled with a first water-soluble polymer, R_2, combined with another water-soluble polymer, R_1, with attached thiol groups (Figure 3.2).

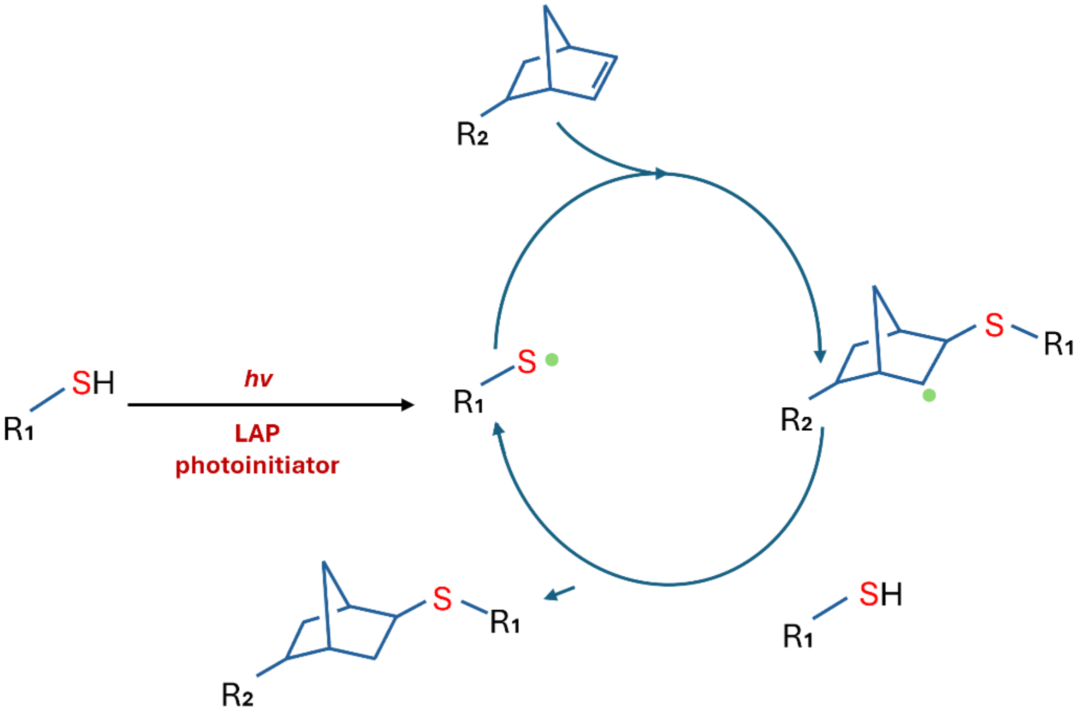

Figure 3.2 Mechanism of reaction behind hydrogel photopolymerization.[210]

All the polymers and the crosslinkers used within this PhD project were prepared and provided by Cellendes, GMbH, Germany. For the preliminary experiments, Polyvinyl alcohol, (PVA- Cellendes GmbH, Germany), a water-soluble polymer, was chosen due to its good cell compatibility and frequent use in hydrogel composition.[299] PVA was functionalized with norbornene using carbonyl diimidazole (CDI), as an activating reagent in dimethyl sulfoxide (DMSO) as a solvent. A fully water-soluble polymer can be obtained only in the presence of a carboxyl group, which provides a negative charge, in physiological conditions, reducing the polymer's hydrophobicity. By adjusting the ratio between PVA and CDI, the degree of substitution can be controlled. CDI-activation of the hydroxyls allows the formation of carbamate bonds between a tri-ethylene oxide diamine linker as well as amine-modified norbornene (norbornene-methylamine). Consequently, the resulting amine functionalized PVA can react with carboxylate norbornene or with norbornene which contains an anhydride group. After amine-functionalization or the functionalization of norbornene groups, an extensive dialysis cycle is necessary to purify the polymers. Unfortunately, the norbornene attachment to the PVA (A) resulted in polymers with limited solubility (B) or completely insoluble polymers (C) (Figure 3.3).

A fully water-soluble polymer can be achieved only in the presence of a carboxyl group, which provides a negative charge at physiological pH, thereby reducing the polymer's hydrophobicity (D). Consequently, Norbornene-PVA (N-PVA) was selected as one of the components to create photopolymerizable hydrogels.

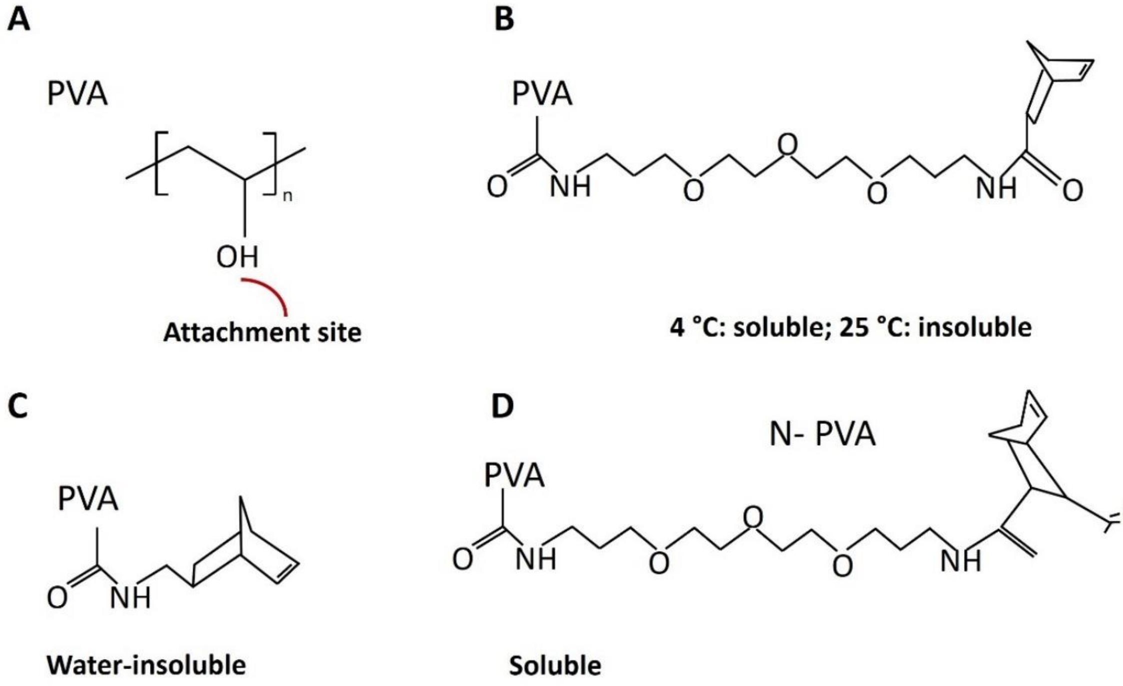

Figure 3.3. **(A)** Structure of PVA with the reactive hydroxyl group. **(B)** Structure after attachment of norbornene carboxylate to hydroxyl groups of PVA using a triethylene glycol linker. **(C)** Structure after attachment of norbornene methylamine directly to the hydroxyl group of PVA, using CDI as a linker. **(D** Structure after attachment of 5-Norbornene-2,3-dicarbonic anhydride using a triethylene glycol linker**.**

In addition to N-PVA, another water-soluble polymer, Pullulan (Cellendes GmbH, Germany) was also examined. Pullulan is a linear polysaccharide composed of maltotriose subunits linked by ɑ-1-6 glycosidic bonds with molecular mass between 10 - 400 kDa, which enhanced its cell compatibility[300]. Pullulan can be functionalized with norbornene using the same chemistry illustrated in Figure 3.3-C, resulting in a water-soluble polymer (Figure 3.4).

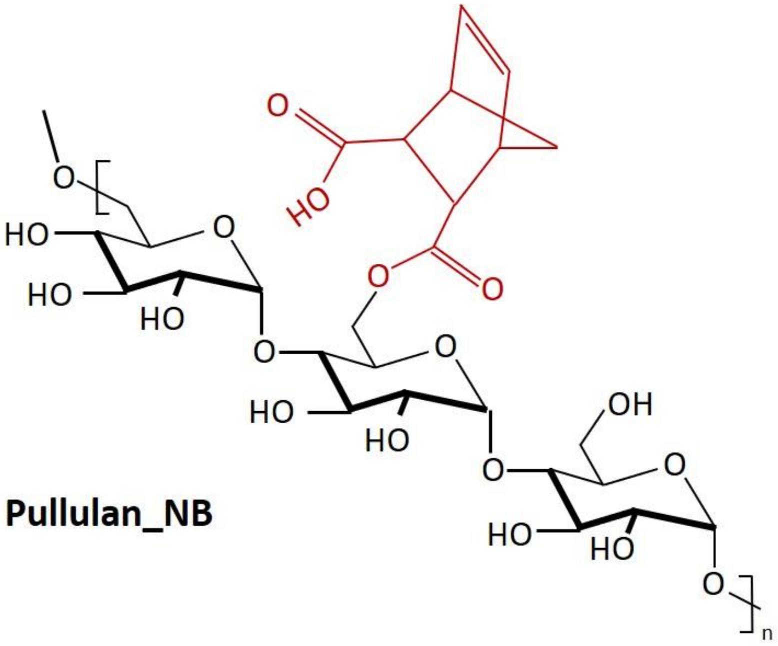

Figure 3.4 The structure of Pullulan polymer functionalized with norbornene.

Once the norbornene-functionalized polymers were defined, different thiol-modified crosslinkers were also investigated. Polyethylene glycol (PEG), (L50-3 3-D Life PEG Link, Cellendes GmbH, Germany) was first evaluated for its unique properties, such as its inability to interact with cells. PEG presents thiol groups attached to both ends and it is normally used in base-catalyzed Michael addition reactions. [301,302]

Subsequently, hyaluronic acid (Hy-Link) (L70-3 3-D Life Hy Link, Cellendes GmbH, Germany) with thiols attached along its backbone was considered. Hyaluronic acid is a polymer based on disaccharides, namely D-glucuronic acid, and N-acetyl-D-glucosamine, both linked via alternating β-(1→4) and β-(1→3) glycosidic bonds and it is a major component of the extracellular matrix in mammalian tissues. [302]

For the addition of the thiol groups to norbornene groups, lithium phenyl-2,4,6-trimethylbenzoylphosphinate (LAP) (TCI Chemicals), (Figure 3.5-left), a blue light photoinitiator was used. LAP was chosen for its water solubility, high biocompatibility, and ability to facilitate good cell encapsulation when used at low concentrations with longer light wavelengths (365–405 nm) (Figure 3.5-right)[303,304]. Upon light irradiation, the photoinitiator can form thiyl groups from thiol groups.

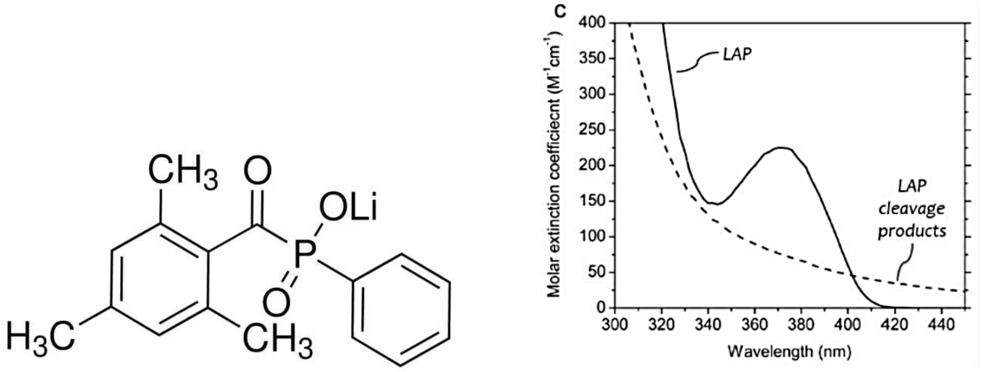

Figure 3.5. ***Left-*** LAP structure and ***Right-*** Absorbance spectra of LAP and LAP photocleavage products[209].

Once the polymers and the crosslinkers were selected, three distinct combinations of norbornene-polymer together with the crosslinkers were considered for the initial photopolymerization tests (Table 3.1).

Table 3.1: Combinations tested for the preliminary trials with the corresponding molar contents.

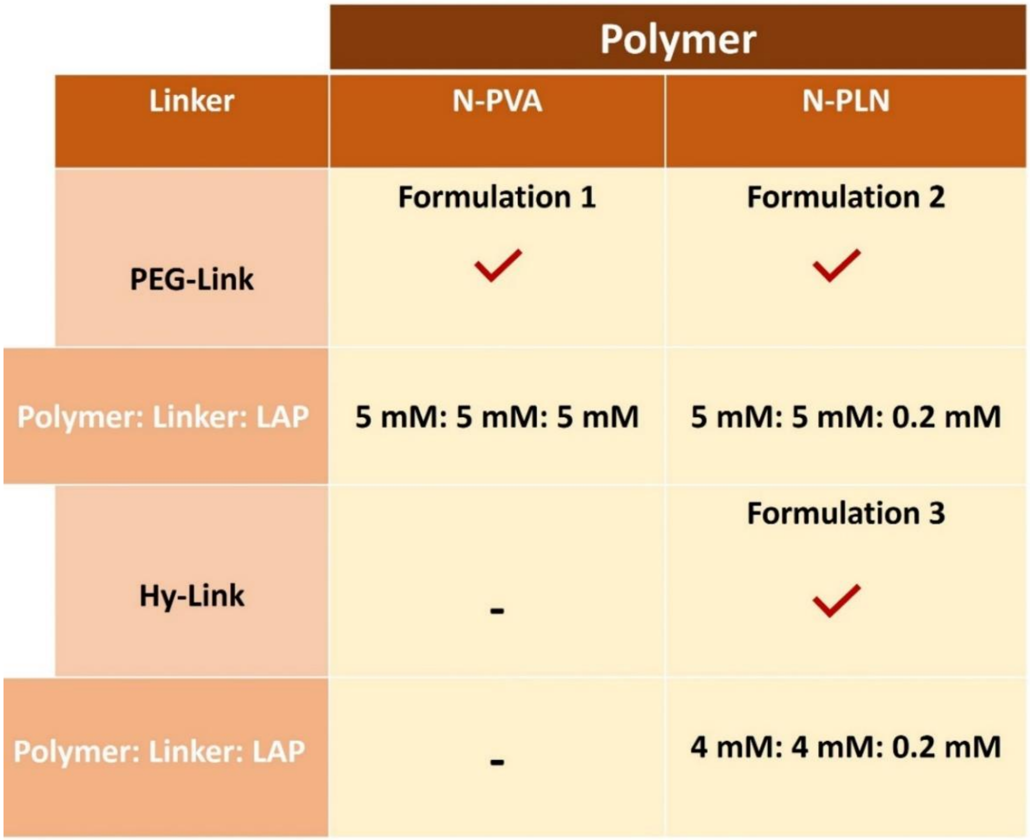

	Polymer	
Linker	N-PVA	N-PLN
PEG-Link	Formulation 1 ✓	Formulation 2 ✓
Polymer: Linker: LAP	5 mM: 5 mM: 5 mM	5 mM: 5 mM: 0.2 mM
Hy-Link	-	Formulation 3 ✓
Polymer: Linker: LAP	-	4 mM: 4 mM: 0.2 mM

To create the scaffolds, a pre-gel solution was prepared (~ 2 ml) by dissolving polymer/linker combination, (Formulation 1, 2, or 3) in Milli Q water (room temperature and stirring conditions) in the presence of LAP. The polymers Norbornene-poly vinyl alcohol (N-PVA) and Norbornene-pullulan (N-PLN), and the crosslinkers PEG-link and HY-link were provided lyophilized or in solution.

When in powder form, preliminary preparation was necessary. First, polymers and crosslinkers were centrifuged, and a specific amount of Milli Q water was added to resuspend the lyophilized powder to reach a certain concentration of the norbornene and thiol groups, followed by a quick vortex. Polymers were then incubated at room temperature for at least 1 hour, without stirring. For PEG-link, 5 min of incubation on ice followed by a brief vortex and centrifugation were necessary. For Hy-link, 1-2h of incubation at RT, followed by a brief vortex and a short centrifugation was required. Once ready, the pre-gel solutions were either used immediately to fabricate the gels or stored at -20ºC until further use. The final molar ratio was established based on the protocols provided by Cellendes GmbH, (Germany).

3.1.2. Introduction of RGD-adhesion peptide motifs

Subsequently, to enhance the adhesion and proliferation of cells seeded on top of the scaffolds or embedded within the norbornene-polymeric matrices, an adhesion peptide motif (the amino acid sequence Arginine-Glycine-Aspartic acid -RGD) was introduced. These RGD motifs were already present in the extracellular matrix such as vitronectin and fibronectin and can induce the formation of adhesion sites by interacting with cell surface proteins (integrins), guaranteeing the worthy conditions for cell types to show a closer phenotype to the *in vivo* ones[305,306]. The RGD motifs attachment was performed by Cellendes GmbH. A direct attachment approach was tested, resulting in an incomplete thiol-ene reaction. Later, a base-catalyzed Michael addition reaction was tried out. Based on the polymerization tests, which will be illustrated later, norbornene-pullulan was selected as a suitable one. Hence, first, a vinyl sulfone group attachment to norbornene-pullulan was operated; after that, thiol-modified RGD-peptide motifs were attached to these already functionalized vinyl sulfones-norbornene-pullulan polymers. Alkaline conditions were applied to insert vinyl sulfone groups into the hydroxyl groups of norbornene-pullulan (Figure 3.6). To enable a sufficient portion of divinyl sulfone to react with only one of the two vinyl sulfone groups, a short incubation in alkaline conditions was required, resulting in a polymer (VS-N-PLN) with a ratio of vinyl sulfone groups to norbornene groups of 0.47:1.

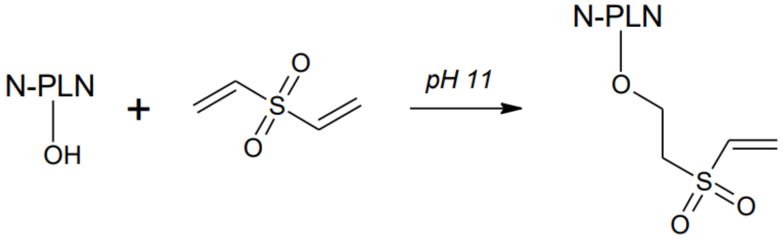

Figure 3.6 Base-catalyzed Michael Addition reaction between hydroxyl groups of Pullulan and Divinyl sulfone.

In the second phase, a constant number of norbornene-pullulan groups were incubated with different amounts of thiol-modified RGD peptides (Figure 3.7), thus the RGD-motifs percentage attached to the polymers was measured. As depicted in Figure 3.7, in the presence of an excess of vinyl sulfone groups, a higher percentage of RGD peptides (60% -70%) can be attached to the polymer.

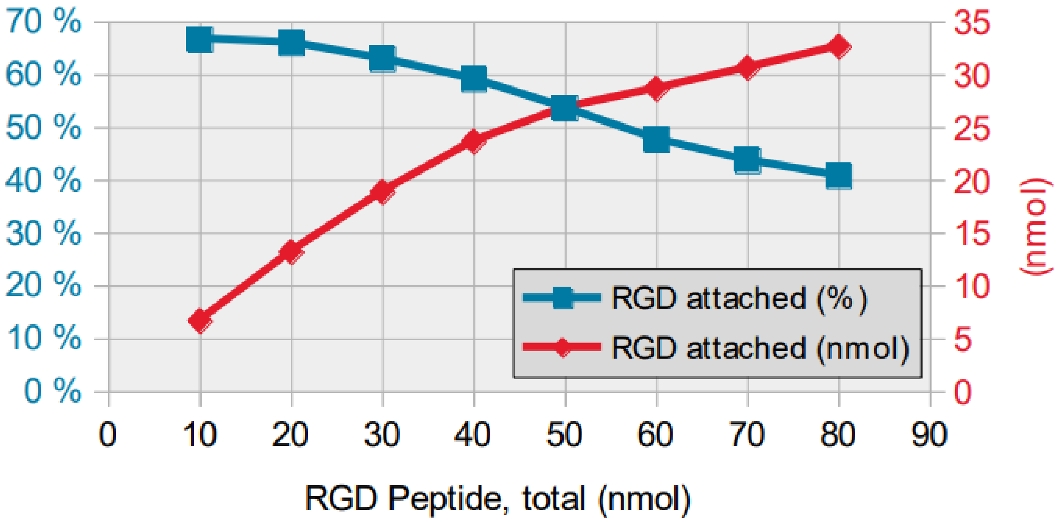

Figure 3.7. 40 nmol pullulan-attached Norbornene groups were incubated with different amounts of thiol-modified RGD peptide at pH 7.4 in a volume of 100 µl for 16 hours at room temperature. Picture provided by Cellendes, GmbH, Germany.

Instead, under an excess of RGD motifs, the percentage of the attached peptides decreased, while the molar amount of bound peptide still increased. Based on these observations, RGD motifs were attached to VS-N-PLN in a bulk reaction. The unreacted peptide was extracted by dialysis and the resulting purified product was employed for the experimental work.

Norbornene-pullulan polymer functionalized with RGD sequences, Formulation 2-RGD functionalized or (RGD-N-PLN: PEG Link: LAP) represented the first advance toward a hydrogel scaffold prone to mimic a skin model. Some experiments were performed to evaluate the influence of the RGD content on the structure of the hydrogel post-swelling together with the cell viability. By following the same procedure described above, fresh pre-gel solutions (RGD-N-PLN: PEG-Link: LAP; 0.5 mM:4 mM: 4 mM: 0.25 mM) and (RGD-N-PLN: PEG-Link: LAP; 1 mM:4 mM: 4 mM: 0.25 mM), respectively, were prepared. Therefore, the first part of the thesis will be dedicated to these formulations.

3.1.3. Introduction of a cell-degradable (CD) cleavable peptide

Later, to raise the hydrogel’s properties, in terms of supporting cells, two new crosslinkers were considered, based on the ones previously cited, -polyethylene glycol- and hyaluronic acid-based linkers. CD linker and CD-Hy linker, (Cellendes GmbH, Germany) respectively, were produced by introducing a peptide portion (CD-cell degradable) containing the Pro-Leu-Gly-Leu-Trp-Ala sequence.

The peculiarity of this peptide portion resides in the possibility of cells cleaving this crosslinker when certain metalloproteases are produced, promoting cell migration, and spreading inside a covalently crosslinked hydrogel. So, the specific sequence was added to test its potentiality on fibroblasts' growth, encouraging their spreading within the extracellular matrix.

After the preliminary investigations, new compositions were also considered. Thus, the introduction of the cell-degradable (CD) peptide indicated the beginning of the study of a new formulation. The new pre-gel composition counted on Norbornene-Pullulan, including the RGD attachment motifs and the CD-Hy linker, -RGD-N-PLN: CD-Hy linker- (Formulation 4). Hydrogels based on this formulation represented a key point of investigation, either analyzing the mechanical properties or examining their support in terms of cell microenvironment biocompatibility, cell sustenance, and growth. The materials, provided by Cellendes GmbH, Germany, required for the preparation included: RGD-N-PLN (with a norbornene concentration of 10 mM/L and an RGD concentration of 2.8 mM/L), CD-Hy Link (with a thiol concentration of 8.11 mM/L), a conjugation buffer (3D-Life 10x CB Buffer- pH 7.2, B20-3, Cellendes GmbH, Germany) and thioglycerol (20 mM/L).

By keeping constant the LAP photoinitiator content (0.5 mM), and the ratio norbornene: thiol groups (1:1), different crosslinking molar contents (norbornene-thiol) were explored (e.g., 1 mM: 1 mM or 2 mM: 2 mM, etc.). To test different concentrations, and simultaneously keep the ratio Norbornene-polymer: crosslinker (1:1), RGD-functionalized norbornene-pullulan and norbornene pullulan alone were combined. Depending on the final molar contents desired, thioglycerol was used to block the excess of Norbornene groups on RGD-N-PLN to react with the CD-Hy link. After several printing trials, the optimal pre-gel solution was prepared by mixing RGD: N-PLN: CD-Hy link: LAP (0.92 mM: 2.5 mM: 2.5 mM: 0.5 mM) in an aqueous environment complemented with CB- Buffer (1x) to provide a cell compatible environment pH 7.2.

3.1.4. A new class of hydrogels: Interpenetrated Network (IPNs) systems

Besides the norbornene-pullulan structures fabricated during this project, a new class of hydrogels was also explored. As aforementioned, recently, it has become of interest to develop scaffold systems based on the combination of two or more different polymers to enhance the physical-chemical characteristics of the final polymer system, taking advantage of the peculiar characteristics of every single component. In this context, norbornene-dextran polymer combinations (Figure 3.8) were selected together with Low Melting Point (LMP) Agarose.

The choice of dextran was correlated with its huge use as a gel component for cell culture applications[307], due to its biocompatibility. It is a natural polysaccharide produced by many different species such as yeast and bacteria. Composed by α-1-6- linked glucose subunits with occasionally branching α-1-4 bonds, it was functionalized with norbornene-methylamine at its hydroxyl groups, using the same mechanism described in Figure 3.3-C, resulting in a water-soluble polymer.

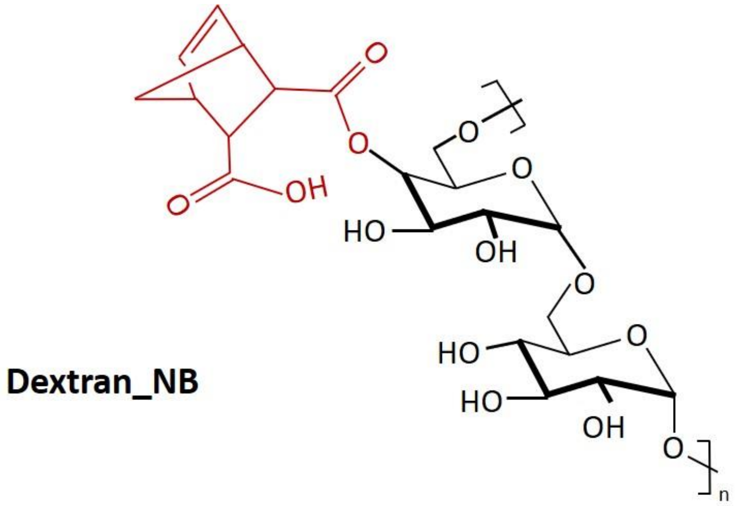

Figure 3.8 Structure of Dextran polymer functionalized with norbornene.

Combinations based on the norbornene-dextran polymer with and without including LMP-Agarose (Figure 3.9) were studied simultaneously, to get hydrogels with reverse gelation properties. Agarose, which is a polysaccharide, mostly extracted from red seaweed, is a linear polymer constituted by agorobiose subunits with a molecular weight of 120 kDa.

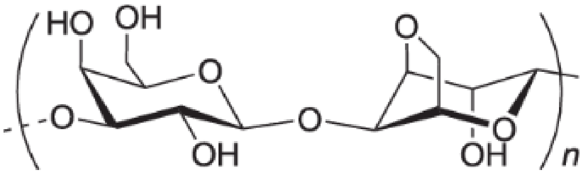

Figure 3.9 The repeating unit of Agarose, consisting of D-galactose and 3,6- anhydro-L-galactopyranose.

It was proved that low concentrations of LMP-Agarose help to prevent the sinking of the cells during the photopolymerization process, as illustrated in Figure 3.10. Gels with different agarose concentrations were tested with this aim. It was observed that from 0.1% to 0.2% content of agarose, the particles’ sinking was prevented for at least 24 hours.

In contrast, when agarose was not added - 0% - or in a control sample with 0.2% agarose, that was still in liquid form (by omitting the cooling step), the beads rapidly sank to the bottom within a few minutes.

On the other side, in a sample with 0.05% agarose gel, most of the beads had sunken to the bottom after 24 hours, but some were still floating above the bottom.

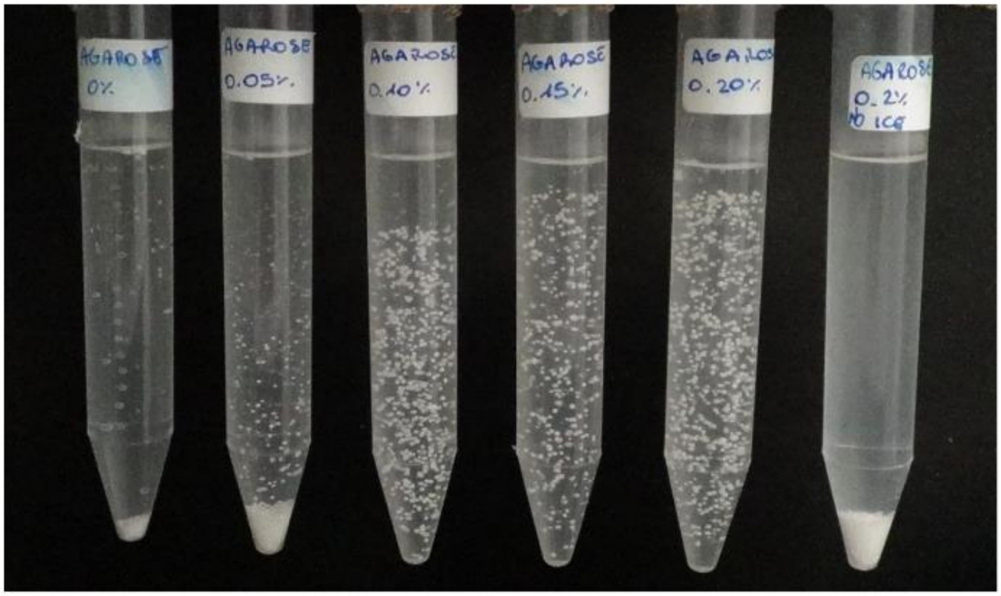

Figure 3.10 Suspension of particles in dilute LMP-Agarose gels, with different concentrations (0-0.2% LMP-Agarose). The figure, provided by Cellendes, GmbH, Germany, shows the samples after sitting still for 24 hours at room temperature.

The LMP-Agarose at different concentrations was prepared by first heating the agarose suspension to 70°C to dissolve the agarose. Later, 5 samples were cooled on ice to induce gel formation. One Sample (0.2% -LMP-Agarose- right one) was not cooled on ice. Then, samples were mixed with chromatography beads (Amberlite FPA98 Cl; Dow Chemical Company). These white particles were used to test if their precipitation could be prevented (Figure 3.10).

As it was observed, for LMP-Agarose concentrations between 0.1 % and 0.2% the beads were homogenously distributed; instead for lower concentrations and in the case of 0.2% of agarose not cooled on ice, the particles precipitated.

One of the peculiarities of agarose resides in the possibility of suspending and dissolving it by heating it in an aqueous solution. Agarose forms a hydrogel when is cooled and it melts and liquefies when is re-heated. The gel formation is caused by inter-molecular hydrogen bonding between the hydroxyl groups of the polymer.

Agarose solution can change its status depending on whether it is cooled down from higher temperatures or heated from lower ones and is either a liquid or a gel at intermediate temperatures, such as 20-55 °C (Figure 3.11). At room temperature, the hysteresis effect allows keeping the agarose either as a gel or as a liquid.

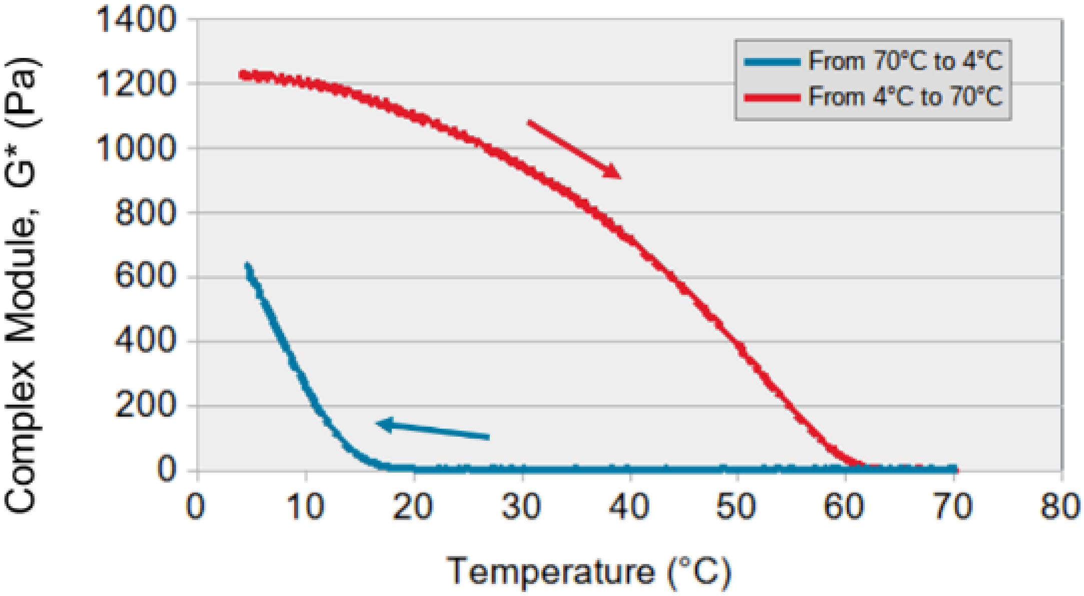

Figure 3.11 Gel stiffness of 0.5% LMP Agarose during temperature ramps (2.2°C/min). Blue: LMP-Agarose was cooled from 70°C to 4°C. Red: LMP-Agarose was heated from 4°C to 70°C. The chart was provided by Cellendes, GmbH, Germany.

The performances of RGD-norbornene-dextran-based hydrogels (+/- agarose) were evaluated in combination with two different crosslinkers, CD-Link (**Formulation 5**) and CD-Hy Link (**Formulation 6**), respectively. Fresh pre-gels solutions were prepared for both formulations and some preliminary tests were conducted to select the working parameters. Therefore, studies on **Formulation 5** (RGD-N-DEX: CD- Link: LAP ~ 0.5 mM: 5 mM: 5 mM: 0.5 mM) and **Formulation 6** (RGD-N-DEX: CD-Hy Link: LAP ~ 0.5 mM: 3.5 mM: 3.5 mM: 0.5 mM) were settled either in the presence and absence of Low-Melting-Point (LMP) Agarose (0.1 w/v %). All the combinations tested during the project are reported in Table 3.2 below.

Table 3.2 List of hydrogel compositions tested during the PhD project. All the compositions are based on norbornene-thiol-ene chemistry, forming Single network (SN) systems and Interpenetrated network (IPN) systems.

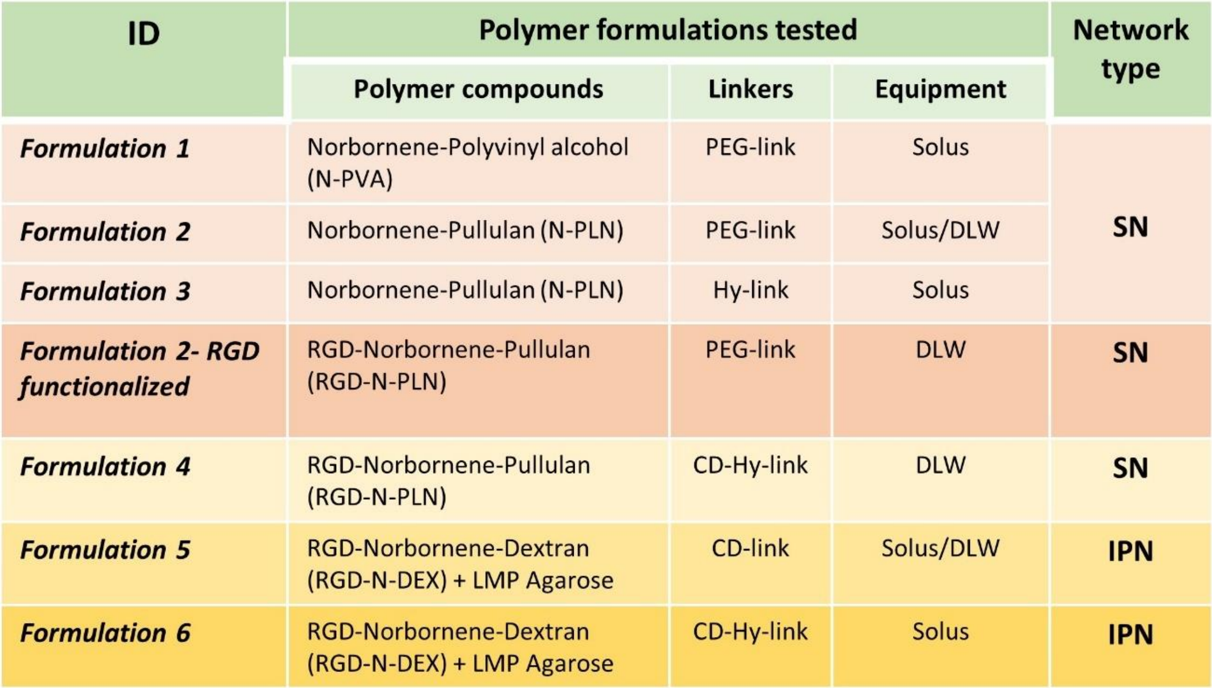

ID	Polymer formulations tested			Network type
	Polymer compounds	Linkers	Equipment	
Formulation 1	Norbornene-Polyvinyl alcohol (N-PVA)	PEG-link	Solus	**SN**
Formulation 2	Norbornene-Pullulan (N-PLN)	PEG-link	Solus/DLW	
Formulation 3	Norbornene-Pullulan (N-PLN)	Hy-link	Solus	
Formulation 2- RGD functionalized	RGD-Norbornene-Pullulan (RGD-N-PLN)	PEG-link	DLW	**SN**
Formulation 4	RGD-Norbornene-Pullulan (RGD-N-PLN)	CD-Hy-link	DLW	**SN**
Formulation 5	RGD-Norbornene-Dextran (RGD-N-DEX) + LMP Agarose	CD-link	Solus/DLW	**IPN**
Formulation 6	RGD-Norbornene-Dextran (RGD-N-DEX) + LMP Agarose	CD-Hy-link	Solus	**IPN**

3. 2. Fabrication

3. 2. 1. Fabrication setups

Hydrogel photocrosslinking mediated by the light was realized through different setups:

1. Digital Light Processing Stereolithography (DLP-SLA) 3D bioprinter system

2. Direct Laser Writing (DLW)

3.2.1.1. Digital light processing Stereolithography (DLP-SLA)

A customized digital light processing stereolithography (DLP-SLA) 3D bioprinting system was built in our facilities, modifying a commercial and low-cost SOLUS bioprinter (Junction 3D), originally designed to print hard resins.

In synthesis, the system depicted in Figure 3.12 consists of (i) a printing support coupled with a Z-axis motor, (ii) a vat that shows a transparent window and is coupled with (iii) a heater to control the temperature at 37 °C, when the pre-gel solution is mixed with a cell suspension and (iv) a beam projector with 1080p in resolution (Vivitek). To protect the cells from IR damage, a short pass heat protection filter (Schott) was employed for the output of the projector.

The process behind the DLP-system operation is called layer-by-layer since it allows the formation of the 3D structure following the vertical direction by printing one layer at a time. A series of white and black patterns, which constitutes the 3D CAD design, is first divided into layers of a certain x µm thickness. Hence, the z motor allows the printing support to go down until the VAT, where the pre-gel solution is contained. Through the transparent window collocated at the bottom of the vat, the first layer of the 3D CAD model is projected onto the pre-gel solution and can be crosslinked. Raising the printing support through the z motor and repeating the process for the next layers, the entire structure can be printed. For the first preliminary tests, our bioink or pre-gel solution was based on the **Formulation 1**-5 mM of Norbornene-poly vinyl alcohol, 5 mM of PEG-Link, and 0.5 mM visible light lithium phenyl-2,4,6- trymethylbenzoylphosphinate LAP photoinitiator (TCI Europe). The solution was prepared by dissolving the components in Milli Q water, protecting the bioink from light.

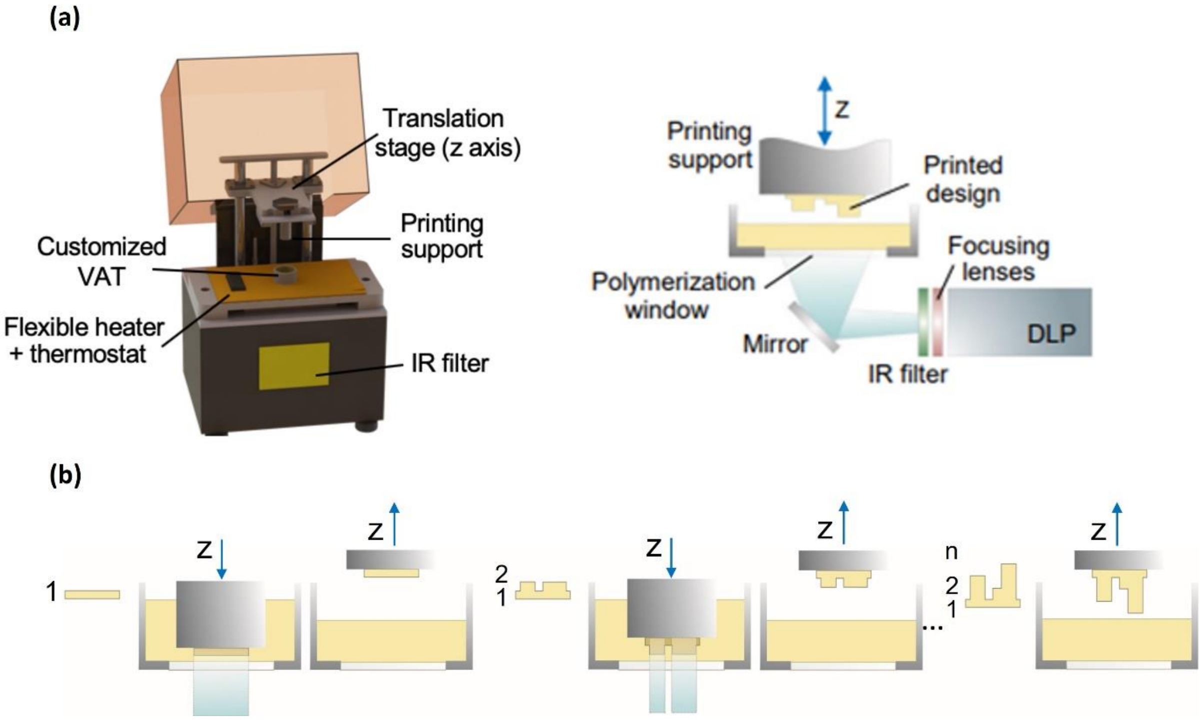

Figure 3.12 Customized 3D bioprinting system: **(a)** 3D CAD model of the 3D bioprinter system (left) with a detailed view of the main components (right). **(b)** Mechanism of action of the SOLUS system. Figures adapted with permission from Torras et al.[308]

The pre-gel solution was allocated into the VAT. The hydrogel design was developed previously by CAD and the different working parameters, as illustrated in Table 3.3, were introduced in the software. With PSA pieces, the silanized membranes (it4ip) were attached to the printing support, for the printing (Figure 3.13). Right after the photopolymerization, the hydrogels were rinsed with warmed PBS, to remove the non-crosslinked polymer, and placed in a 24-well plate with PBS, at 4 ºC. The CAD design consists of a disc-like sample with a diameter of 3 mm and a thickness of 0.5 mm.

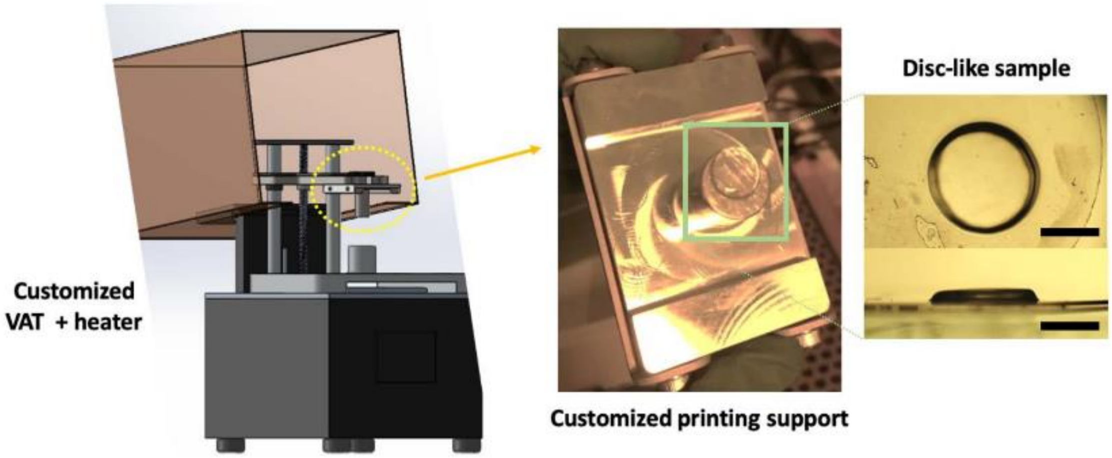

Figure 3.13 Schematics of the DLP-SLA 3D bioprinting system available at IBEC facilities. The printing support and the polymer cuvette (VAT) were customized for printing structures using lower sample volumes. Example of a disc-like printed sample of 3 mm in diameter and 300 µm in thickness (right).

Table 3.3 Printing working parameters used to fabricate Norbornene-poly vinyl alcohol: PEG Link: LAP hydrogels-Formulation 1.

Layer thickness (µm)	Bottom layer exposure time (s)	Normal layer exposure time (s)	Number of bottom layers
10	5	5	2
20		10	
20	5	5	2
	30	10	
20	2	5	2
		2	

To elect the appropriate hydrogel composition in terms of printability, other bioinks were also investigated, changing either the crosslinker or the polymer. Bioinks based first on **Formulation 2 -** 5 mM of Norbornene-pullulan, 5 mM of PEG-Link, and 0.2 mM of LAP photoinitiator and then, on **Formulation 3 -** 4 mM of Norbornene-pullulan, 4 mM of Hyaluronic acid linker (Hy-Link), and 0.2 mM of LAP photoinitiator were also studied. By using the same procedure illustrated before, both compositions were prepared and tested, changing the working conditions as mentioned in the tables below (Table 3.4 and Table 3.5).

Table 3.4 Printing working parameters used to fabricate Norbornene-pullulan: PEG Link: LAP hydrogels- Formulation 2.

Layer thickness (µm)	Bottom layer exposure time (s)	Normal layer exposure time (s)	Number of bottom layers	Number of layers
10	10	5	2	50
				100
20	10	5	2	100
	5			

Table 3.5 Printing working parameters used to fabricate Norbornene-pullulan: Hy Link: LAP hydrogels-Formulation 3.

Layer thickness (µm)	Bottom layer exposure time (s)	Normal layer exposure time (s)	Number of bottom layers
20	5	5	2
10			
20	5	10	2
	10	15	

3.2.1.2. Digital light processing Stereolithography (DLP-SLA) -modified.

As described in the previous section, preliminary tests were conducted to verify the materials' printability, by varying multiple working parameters. Although the adequacy of this system was proved in terms of producing hydrogel scaffolds, some modifications were necessary. One of the big issues faced with this bioprinting setup concerned the required pre-gel volume solutions (2 ml), which were not sustainable. First, to drastically decrease the amount of the pre-gel solution needed, another system-Direct Laser Writing (DLW)- which will be described in the next section, was adopted.

Unfortunately, due to some limitations observed in terms of sample dimensions and superficial area, it was necessary to move again to the Digital Light Stereolithography (DLP-SLA) setup.

This commercial 3D printer (SOLUS) works with a power density of the light source (a full HD projector) adjustable between 3.1 mW/cm^2 and 12.3 mW/cm^2, within a spectral range from 320 nm and 1000 nm.

Considering that, some modifications were applied to make the DLW system and the SOLUS one comparable, either in terms of power density or wavelength irradiation. With this aim, two optical filters were coupled at the output of the projector to narrow the wavelength spectra. A KG3 SCHOTT short pass heat protection filter (ITOS, Edmund Optics) (315-660 nm), and a BG3 band pass filter (Thorlabs), (315-445 nm and 715-1095 nm), were adopted respectively, resulting in a wavelength window ranging from 315 nm and 445 nm, and an output power of 3.24 mW/cm^2.

Briefly, instead of the layer-by-layer process illustrated before, this time, the hydrogels photocrosslinking was performed by illuminating the bioink (containing or not the cells), allocated in a transparent cuvette, from the bottom, passing by a transparent glass window.

Specifical cuvettes were used to minimize the pre-gel solution volumes and were fabricated in poly dimethyl siloxane (PDMS), as a conventional transparent silicone, in a circular shape- (Ø: 6 mm, thickness: 0.5 mm). More than 2 samples can be printed at a time, also minimizing the time-consuming. For each set of experiments, an initial volume between 200 µl and 300 µl was prepared. Depending on the combination of polymer/crosslinker, the components were dissolved in Milli Q water, in the presence of LAP, with a specific molar ratio. All these tests were performed in sterile conditions, in a clean room environment. Again, after the photopolymerization, the scaffolds can be rinsed with warm PBS or warm medium, depending on the cells' presence, and finally kept at 4ºC or 37ºC.

3.2.1.3 Direct Laser Writing (DLW) system

As reported before, after some preliminary tests with the DLP-SLA system, another fabrication setup was considered, mainly due to the big volumes required (2 ml). To minimize this initial volume, another 3D printing system was adopted (Figure 3.14 a-b). A custom-made direct laser writing (DLW) system, previously assembled in our laboratory, was employed to create soft and transparent hydrogels, and test their crosslinking capabilities, starting from easy geometries as depicted in Figure 3.15. The system consists of a 405 nm wavelength laser diode (DL5146-101S, Thorlabs) coupled with a motorized DC servo actuator (Z axis) (Z-series, Thorlabs) and a motorized translational stage, movable in the x-y plane (Z-series, Thorlabs). By way of a collimator (LTN330-A, Thorlabs), and a lens tube with a 10x objective (Edmund Optics), the laser beam can be controlled and directed on the surface of movable printing support, to "write" the 3D structure into the photopolymer. Normally, to do this is necessary to move either the beam focus or the sample. In the first case, galvanometric scanners are required, resulting in a generated structure polymerized in layer-by-layer format. However, as the beam moves, it can be distorted as objective, not providing a completely flat field of view. In our case, instead, of using x-y-z stages for writing structures, is not necessary to slice the design, as the stages can move along all the directions.[309]

The entire equipment is connected to a computer from which it is possible to control either the writing velocity and the x-y-z stage through LabView Interface software. Printable hydrogels can be obtained by modulating different working parameters.

One of these is the z-distance between the objective and the printable support (expressed in nº of steps). The default distance (nº of steps = 0) corresponds to a z-distance of 1 cm. Starting from this value, the z-distance can be varied in a range between 1 and 25 steps, with a jog step size of 0.1 mm. The z-distance is correlated with the energy dosage per superficial area, which is higher when the z-distance decreases. Different movable printable supports, presenting different heights can be used, as Petri dishes or well plates. By varying the x-y distance one at a time, stripped-like gels can be crosslinked, along the desired direction.

Other two important parameters to consider are the speed of the translational stage and the optical power. By using the LabView software, the speed can be modulated: for instance, in our experiments, 0.15 mm/s and 0.3 mm/s speeds have been used, while the optical power can be tuned in a range between 1- 41 mW. As reported in the literature, both working parameters have an impact on the hydrogel line width. Increasing the stage velocity or decreasing the optical power leads to a decreased gel' width. This phenomenon can be explained as a reduced optical influence, meaning a reduced accumulated optical energy per unit area.[310]

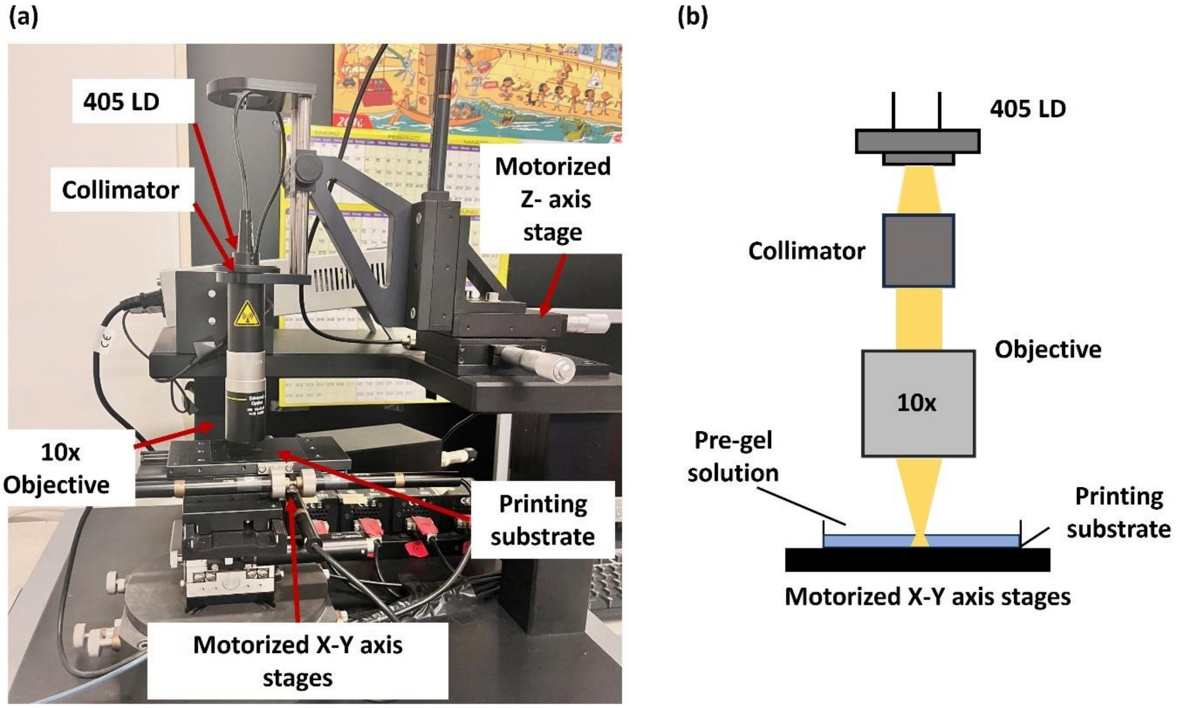

Figure 3.14 The Direct Laser Writing (DLW) equipment. (a) Custom-made real system and its main components. **(b)** Schematic representation of the 405 nm wavelength system.

Several tests were performed by varying the z-distance in a range between 10-25 (nº of steps), the power between 13 mW and 30 mW, and a speed between 0.15 mm/s and 0.3 mm/s, using an initial volume ranging from 0.3 ml to 1 ml. By pipetting the bioink solution on top of silanized glass coverslips (12 or 13 mm in diameter) or silanized PET membranes (0.4 mm pore size), allocated inside of a Petri dish or a well-plate (24-well plates or 6 well-plates), rectangular shaped- hydrogels can be printed within few seconds (10-15 s).

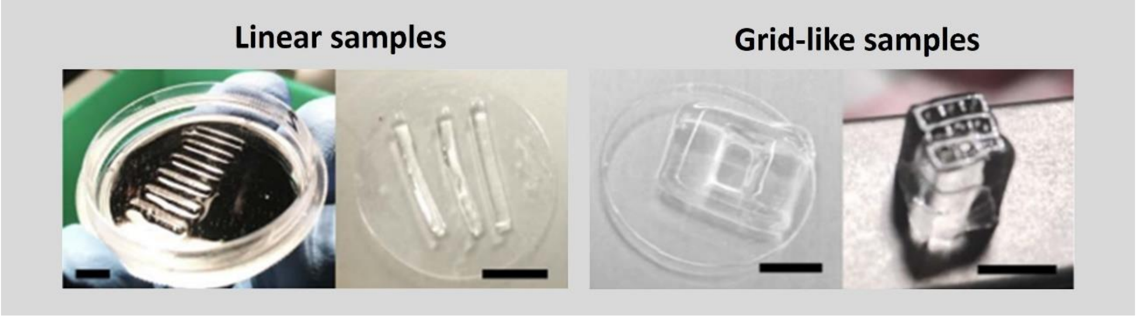

Figure 3.15 Printable geometries can be obtained with the Direct Laser Writing (DLW) system. Linear samples of 1 mm width, with a variable length and a thickness variable in a range between 100 µm and a few millimeters (left side). Grid-like samples (right side). Scale bars = 5 mm.

More complex geometries can also be printed adjusting the movements of both x and y motors at a time, as in the case of grid-like samples (Figure 3.15 - right panel). The preliminary tests conducted enhanced the necessity to decrease even more the initial pre-gel volume solution.

For this reason, a PDMS O-ring (as reported in Figure 3.16), with an inner diameter of 6 mm and 0.5 mm in thickness was created and used on top of the membrane/coverslip, allowing to decrease the bioink volume up to 15 µl.

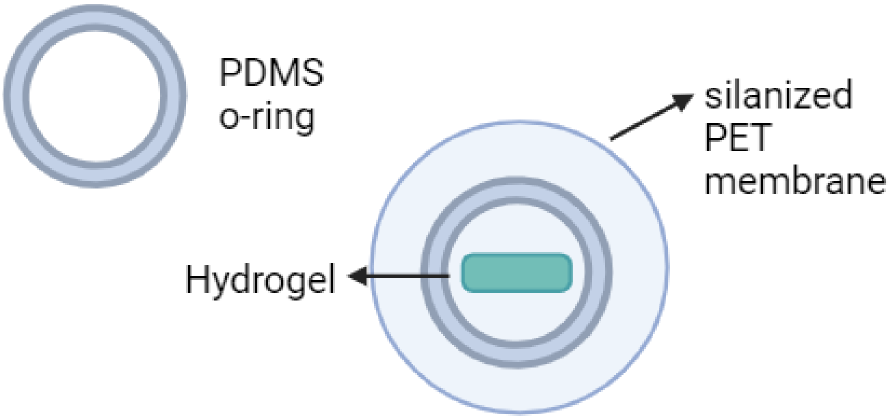

Figure 3.16. Schematic representation of a hydrogel fabricated using a PDMS O-ring to better minimize and confine the pre-gel solution.

To create our hydrogel scaffold, the bioink was prepared by dissolving the norbornene-pullulan /PEG link in the presence of LAP as a photoinitiator, in Milli Q water (N-PLN: PEG-Link: LAP, 5 mM:4 mM, 0.2 mM). Once ready, the solution is pipetted into the PDMS O-ring, which is placed on top of a silanized PET membrane (it4ip), (Ø:10 mm, thickness: 12 µm, pore size: 0.4 µm), inserted inside of a 6-well plate. The photopolymerization process takes place in dark conditions. After that, the hydrogel is rinsed with warm PBS and gently wiped with Kim Wipe tissue (KimTech Science). The samples can be kept inside a 24-well plate with PBS at 4ºC for later characterization.

3.3. Characterization

3.3.1. Volume swelling analysis

The swelling behavior was analyzed for different hydrogel formulations. The pre-gel solutions were irradiated at 405 nm wavelength to photopolymerize hydrogels on top of previously silanized PET membranes. Right after the photopolymerization, the samples were washed with PBS to remove non-photopolymerized residues and carefully wiped with a Kim Wipe tissue (Kim Tech Science).

Hydrogels were kept in PBS at 37 °C to induce swelling. Pictures of the hydrogels were taken at different time points with an optical microscope (MZ10 F, Leica), and the scaffolds' dimensions were checked and analyzed through ImageJ software. The volumetric swelling ratio was calculated as the ratio between the volume increase due to the swelling (difference between the swollen volume at a certain time "t" and initial volume at time 0) and the initial volume at time 0.

3.3.2. Atomic Force Microscopy (AFM) analysis

The mechanical performance of the samples was investigated using atomic force microscopy (AFM). AFM is a well-known technique for the local measurement of the mechanical properties of materials at the surface level. AFM indentations were performed on the surface of rectangular-shaped hydrogels fabricated with a DLA-SLA system (irradiation process) based on norbornene-dextran formulation.

The samples (RGD-Norbornene-Dextran: CD-Link: LAP – 0.5 mM: 3.5 mM: 3.5 mM: 0.5 Mm +/- 0.1 % Agarose) were crosslinked, by using distinct exposure times, on functionalized glass coverslips to avoid detachment. A JPK Nanowizard 4 machine (JPK Instruments) was used to perform the measurements with a V-shaped cantilever with a quadratic pyramidal tip of 35° (θ) face angle, and a nominal spring constant (k) of 0.08 N m−1 (PNP-TR-20, Nanoworld).

After calibration of the sensitivity, a series of local force–displacement (F–z) curves were measured at several points on the surface of the samples, indenting up to 5 μm. The values of the local surface stiffness were obtained by applying Hook's law and the Hertz model for a quadratic pyramidal tip to the force-displacement curves, assuming Poisson's coefficient of ~ 0.5.

3.3.3. Rheology analysis

The bulk properties of our hydrogels were explored through rheological measurements, in collaboration with Dr. Pòl Barcelona, at the University of Barcelona. The rheology analysis was conducted on hydrogels fabricated with different compositions (Formulation 2, 4, 5, 6), to compare their properties and to study the correlation between stiffness and hydrogel matrix composition.

Either formulation based on norbornene-pullulan and norbornene-dextran, in combination with three different linkers during the *in-situ* crosslinking, were investigated. A Discovery HR-2 rheometer equipped with an 8 mm parallel Peltier plate and a UV light source (Lightning cure ™ LC8 Hamamatsu) was employed for this purpose. Drop volumes of 13 μL of prepolymer solutions were crosslinked with 87.6 mW/cm^2 of fixed power density, measured at the crosslinking plane.

The Storage Modulus G’ data were obtained as a function of the oscillation strain, by applying a sweep of amplitude between 0.01% and 10^3 %, keeping constant the frequency to 1 Hz, with a fixed running temperature of 25°C. Assuming a Poisson’s coefficient value for the soft hydrogels of 0.5, as reported in the literature[311], Young’s Modulus (E) was calculated from the values of the Complex Modulus G*, which had been derived from the Storage G’ and the Loss G’’ modulus obtained as a function of the strain.

3.3.4. Degradation analysis

One of the most important aspects to consider among the hydrogels’ mechanical characteristics is the hydrogel integrity, to determine the scaffold suitability to sustain cell culture. The hydrogel performance was evaluated under cell culture conditions and a mass degradation study was performed using 3D-Life Dextranase solution (D10-1; > 4000 units/ml) provided by Cellendes, which cleaves the glycosidic bonds of dextran and induces the gel degradation. For this purpose, rectangular-shaped hydrogels were prepared, using the DLW system. Fresh bioink solutions: RGD: N-DEX:CD-Link: LAP (0.5 mM: 5 mM: 5 mM: 0.5 mM) and Agarose: RGD-N-DEX: CD- Link: LAP (0.1% w/v: 0.5 mM: 5 mM: 5 mM: 0.5) were prepared and irradiated with a 22 mW of power.

Right after the photopolymerization, the scaffolds were kept in submerged conditions with Dulbecco’s Modified Eagle Medium at 37 ºC for 72 hours into a 24-well plate, to induce swelling. Once the equilibrium was reached, by removing the excess of the medium, each sample was weighed separately.

After that, two different dilutions of 3D-Life Dextranase solution, (1:20) and (1:200) respectively, were added to each sample. The degradation process was monitored by weighing the samples, incubating at 37 ºC, every 4 minutes. Once the degradation was fully completed, the remaining mass (%) was calculated as the ratio between the mass after incubation with Dextranase (M_t) at time “t” and the mass at time 0 (M_0), multiplied by 100.

3.3.5. Production of stiffness-varying substrates

Our biomimetic methodology leverages the potential to develop comprehensive epidermal and dermal structures, encompassing a variety of cell types. Therefore, it is essential to produce scaffolds incorporating niches with specific microenvironments. Precise mechanical properties are required to fabricate gels capable of integrating the most representative skin tissue cells.

For this purpose, Interpenetrated Network (IPNs) hydrogels with reverse gelation properties were used. Once the polymerization conditions and the polymer molar ratio were optimized, the first attempt to produce stiffness-varying hydrogels using light sheet energy was conducted. Hydrogels were produced with a range of energy dosages spatially changing at the surface level, resulting in substrates with gradients of stiffness. Later, their micromechanical properties were analyzed by Atomic Force Microscopy (AFM), as described in section 3.3.2. Due to the sample size limitation, the SOLUS system was employed for these experiments. As described before, (section 3.2.1.2.) photocrosslinking occurs through a transparent window, by illuminating the bioink allocated rectangular-shaped PDMS pools from the bottom (Figure 3.17), while a movable dark acetate photomask, placed in between the glass window and PDMS pools containing the pre-gel solution was used to create the gradients (Figure 3.18-A-B).

To better control the movement of the photomask and apply different testing conditions, the photomask was coupled with a syringe pump using some clumps, which pulled it at a constant speed, gradually blocking the light path from the bottom. Its position is fixed by 3D-printed plastic support, guaranteeing accurate control of the energy dosage applied to each region of the sample (Figure 3.18). To facilitate the hydrogels' attachment to the testing surface, a previous silanization step was conducted to help indeed the consequent sample handling for the characterization. To apply a controlled energy dosage during the photopolymerization, along with the sample, the photomask speed needs to be calibrated first, defining some key parameters:

(i) the initial energy dosage (E_0) to be sure to get proper polymerization and hydrogel stability,
(ii) the desired final energy dosages (E_i) to establish different gradients,
(iii) the photomask speed v,
(iv) the sample length $\Delta x = x_i - x_0$.

Based on the photocrosslinking tests performed with Formulation 5, the initial energy dosage was fixed depending on the experiment, to $E_0 = 291.6$ mJ/cm^2, corresponding to 90 s (initial exposure time), or $E_0 = 583.2$ mJ/cm^2 corresponding to 180 s (initial exposure time) (Table 3.6).

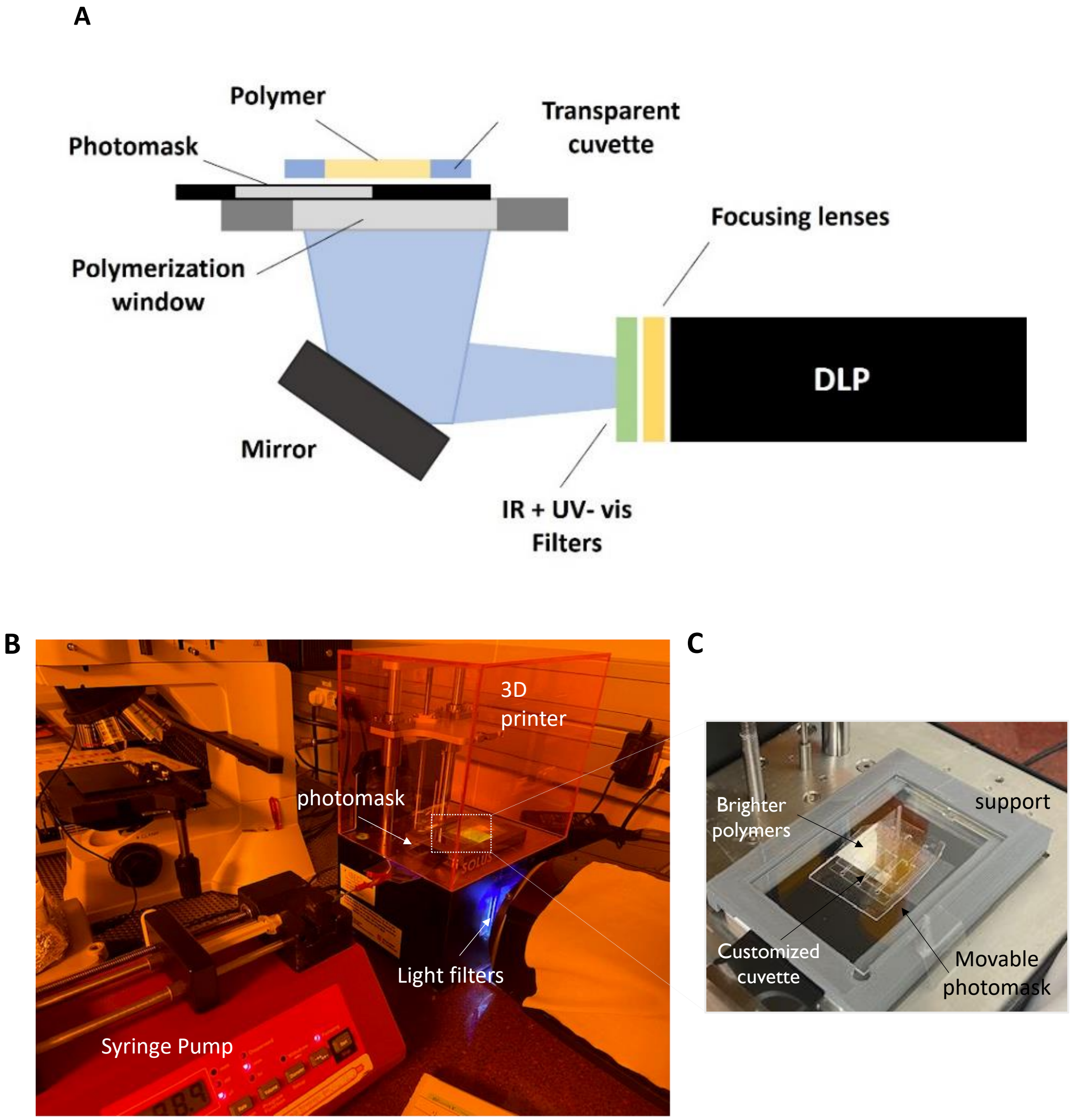

Figure 3.17. Representation of SOLUS system. (A) Schematic representation of the irradiation setup with the main components. **(B)** Setup to produce stiffness-varying substrates (IBEC facilities). **(C)** Detailed view of the photopolymerization area, including the polymer cuvettes and the dynamic photomask.

Softer but well-crosslinked scaffolds can be obtained. The sample sizes remained constant for all the sets of experiments: 10 mm in length, 4 mm in width, and 0.5 mm in thickness. To examine the influence of the pre-gel composition on the stiffness substrate formation, hydrogels with and without Low Melting Point (LMP) Agarose (0.1% w/v) were fabricated. First, a fresh pre-gel solution was prepared -RGD-Norbornene-Dextran: CD-Link: LAP- Formulation 5-(0.5 mM: 5 mM: 5 mM: 0.5 mM) and protected from the light.

Once the hydrogels were fabricated, according to the different characteristics (Table 3.6), they were kept at 4 ºC for a couple of days to reach the equilibrium swelling, before AFM measurements.

Table 3.6 Gradients created with the SOLUS setup and their corresponding characteristics.

Gradient ID	v (mm/min)	E_0 (mJ/cm^2)
Q_1	1.57	291.6
Q_2	1.18	291.6
Q_3	2.00	291.6
Q_4	2.50	583.2
Q_5	2.00	583.2
Q_6	3.33	583.2

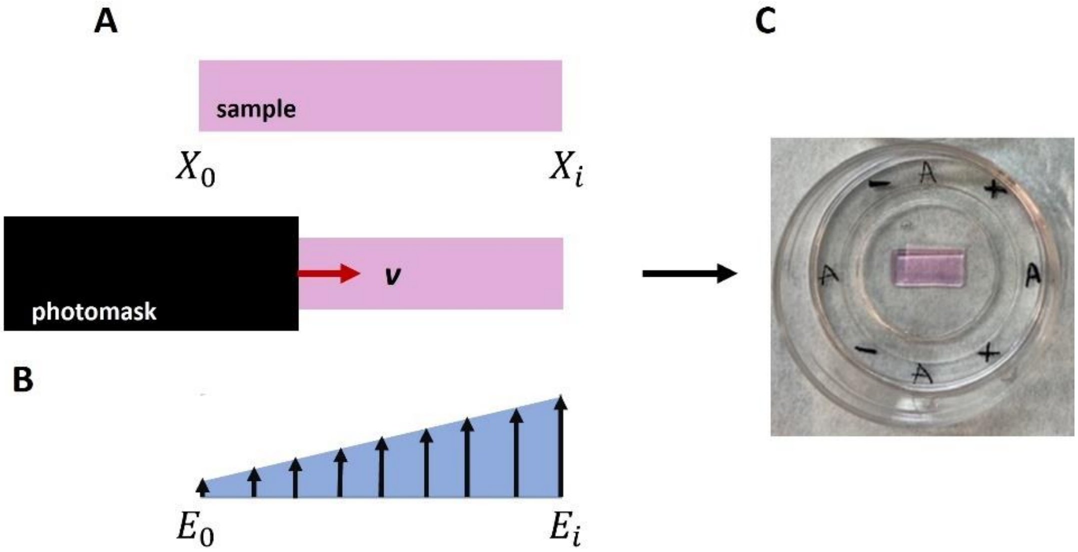

Figure 3.18 Stiffness gradient formation. Sketch of the photomask displacement at a constant speed v **(A)** for the formation of energy dosage gradients **(B).** Example of a stiffness-varying substrate obtained by using MatTek dish **(C).**

To provide a hard and more stable base for later characterization (AFM) or microscopy analysis, MatTek dishes (35 mm in diameter) were used as printing support, resulting in rectangular-shaped hydrogels of 10 x 4 x 0.5 mm^3 (Figure 3.18-C). After crosslinking, samples can be gently washed without effort and simply covered either with PBS or cell culture media and left in the specific conditions (4ºC or 37 ºC) to reach equilibrium swelling before their use.

3.4 Cell culture

3.4.1. NIH / 3T3 fibroblasts culture

NIH-3T3 mouse fibroblasts were employed at the beginning of the Ph.D. project to simulate the dermal compartment of our skin models. As a conventional cell line used for testing the cell viability within a new hydrogel composition, they were selected for the easy way to be cultured and their fast growth.

NIH-3T3 fibroblasts (ATCC® CRL-1658™) were cultured using NIH cell culture medium (DMEM - Gibco, Thermo Fischer Scientific) medium supplemented with 10% Fetal Bovine Serum (FBS) (Life Technologies) and 1% Penicillin-Streptomycin (Sigma-Aldrich)) at 37°C in a humidified incubator under a 5% CO^2 atmosphere. The stock of NIH-3T3 cells was maintained by periodically passing the cells every 3 days upon 80% confluency. Normally, cells were first rinsed with warm Phosphate Buffered Saline solution (PBS) (Life Technologies), then they were incubated with Trypsin-EDTA (Life Technologies) for 5 minutes at 37°C. Next, Trypsin-EDTA was neutralized by adding an equal volume of culture medium, and cells were centrifuged at 1200 rpm for 5 minutes. The supernatant was discarded, the pellet was resuspended in the culture medium, and the proportional volume was seeded in a new flask containing a warm culture medium.

3.4.2. Hs-27 human foreskin fibroblasts culture

Human foreskin Hs-27 fibroblasts (ATCC-CRL 1634) were used in this study to better mimic the dermal construct. Hs-27 were cultured and expanded in 25 cm^2 flasks in DMEM medium (Gibco, Thermo Fischer Scientific), supplemented with 10% v/v fetal bovine serum (FBS) (Gibco, Thermo Fischer Scientific) and 1% v/v Penicillin/Streptomycin (Sigma-Aldrich), with a cell density of 8×10^3 cells/cm^2. Hs-27 were kept in incubation at 37 °C and 5% CO_2, changing the medium every 2 days and passing them every 3 days, upon 70% confluency.

Cells were rinsed with warm phosphate-buffered saline solution (PBS) (Life Technologies), and then incubated at 37°C for 5 minutes with Trypsin-EDTA (Life Technologies). After that, Trypsin-EDTA was neutralized by adding an equal volume of culture medium, and cells were centrifuged at 130 g for 5 minutes. By discarding the supernatant, the pellet was resuspended in the culture medium, and the proportional volume was seeded in a new flask containing a warm culture medium.

3.4.3. HaCaT keratinocytes culture

HaCaT human immortalized keratinocytes were used, at the beginning of this study to recreate the epidermal construct of our skin scaffolds.

HaCaT cells (CLS 300493) were seeded on top of the cell-laden scaffolds, 3 days post-encapsulation. HaCaT cells were cultured in 25 cm^2 flasks, in DMEM (Gibco, Thermo Fischer Scientific), supplemented with 10% v/v fetal bovine serum (FBS) (Gibco, Thermo Fischer Scientific) and 1% v/v Penicillin/Streptomycin (Sigma-Aldrich), by using a cell density of 1 x 10^4 cells/cm^2. Cells were kept in incubation at 37 °C and 5% CO_2, changing the medium every 2 days and passing them twice a week, upon 80% confluency with a split ratio between 1:5 and 1:10. First, cells were rinsed with warm Phosphate Buffered Saline solution (PBS) (Life Technologies), and then incubated at 37°C for 10 minutes with Trypsin-EDTA (Life Technologies). After that, Trypsin-EDTA was neutralized by adding an equal volume of culture medium, and cells were centrifuged at 1200 rpm for 5 minutes. First, the supernatant was discarded, the pellet was resuspended in the culture medium, and the proportional volume was seeded in a new 25 cm^2 flask containing a warm culture medium.

3.4.4. Primary Epidermal keratinocytes (HEKn)

In the second stage of the project Primary Epidermal Keratinocytes: Normal, Human, Neonatal Foreskin (HEKn) were used in our biomimetic system to resemble a model closer to the native one.

The cells have been gently donated within the framework of the Brighter consortium from Technion Institute of Haifa, Israel. The cell batch (P.1) has been expanded using a maintenance medium (KMM): Epilife™ keratinocytes medium, supplemented with Human Keratinocytes growth factor (HKGS) and 0.06 mM $CaCl_2$, according to the protocol from Zoio et al.[312] Cells were kept in incubation at 37 °C and 5% CO_2, changing the medium every 2 days and passing them upon 70%- 80 % confluency (7-9 days). By removing the culture medium, cells were rinsed in pre-warmed Trypsin-EDTA for Primary cells solution (ATCC PCS-999-003) and then (1 ml for every 25 cm^2) of fresh Trypsin-EDTA was added. After cell detachment, the Trypsin Neutralizing Solution (ATCC PCS-999-004) was added to neutralize the Trypsin-EDTA solution. After centrifugation (180 g x 7 minutes), the supernatant aspired and the cell pellet was resuspended in a fresh medium. At this step, cells can be counted, and the proportional volume can be seeded in a new flask or on top of cell-laden scaffolds.

3.4.5. HUVEC endothelial cells

Human Umbilical Vein Endothelial cells- HUVECs- (C0035C-Invitrogen) were encapsulated together with Hs-27 human fibroblasts as the first attempt at system vascularization. HUVEC cells were cultivated in 25 cm^2 flasks in EndoGRO™ Medium complemented with a supplemented kit (Millipore), with a cell density of 2.5 x 10^3 cells/cm^2.

Cells were kept in incubation at 37 °C and 5% CO_2, changing the medium every 2 days and passing them twice a week, upon 80% confluency with a split ratio between 1:5 and 1:10. First, the culture medium was removed from the flask. Then, Trypsin-EDTA (Life Technologies) was added and immediately removed, followed by incubation at room temperature of 1-3 minutes, to ensure the cells dislodged from the flask. After that, Trypsin-EDTA was neutralized by adding an equal volume of Trypsin Neutralizer Solution, and cells were centrifuged at 180 g for 7 minutes. Finally, the supernatant was discarded, the pellet was resuspended in the culture medium, and the proportional volume was seeded in a new 25 cm^2 flask containing a warm culture medium.

3.5 Cells experiments

3.5.1. Cells encapsulation

3.5.1.1. Fabrication of Norbornene-pullulan-based hydrogels with NIH-3T3 cells

For the preliminary tests, Norbornene-Pullulan: PEG Link–based hydrogels (Formulation 2) were fabricated with the DLW system, as described in section 3.2.1.3, by using a power range between 13 mW and 30 mW, with NIH-3T3 mouse fibroblasts. Briefly, NIH-3T3 cells were prepared as mentioned in section 3.4.1, and after centrifugation, the pellet was resuspended into the pre-gel solution with a cell density of 7.5 x 10^6 cells/ml. After printing, cell-laden scaffolds were kept at 37 ºC under cell culture conditions, by changing the medium daily, for further characterization.

3.5.1.2. Fabrication of cell-laden scaffolds with Hs-27 human fibroblasts

To create a skin model closer to the native one, human dermal fibroblasts were encapsulated within different hydrogel-based compositions. Either in the case of the DLW bioprinting system or the DLP-SLA setup, the cell pellet was resuspended and mixed with a fresh pre-gel solution, right after the centrifugation. Different cell densities were evaluated and optimized over time, depending on the hydrogel composition, in a range between 1.5 x 10^6 cells/ml and 5 x 10^6 cells/ml.

3.5.2. Cell viability

For each pre-gel composition tested the cell viability of the cells embedded within the gels was evaluated by following the same protocol. Shortly, a calcein AM/ethidium homodimer-1 (EthD-1) LIVE/DEAD® viability/cytotoxicity assay (Invitrogen), was used.

Starting from day 1 post encapsulation, and proceeding at different time points, normally after 3 or 4, 7- and 10-days post encapsulation, cell-laden hydrogels were washed and incubated with EthD-1 at 4 μM EthD-1, Calcein AM at 2 μM and Hoechst 33342 (5 μg mL-1) (Invitrogen) for 20 minutes in the incubator. Samples were then well-washed, mounted in a PDMS pool placed on a cover glass slide, facing down, by using Fluoromount-G® (Southern Biotech) or PBS, and imaged immediately using a confocal laser scanning microscope (LSM800, Zeiss). A manual cell counter plugin in ImageJ software was employed for cell viability quantification.

3.5.3. Degradation analysis in the presence of the cells

Single network system-based formulations have been replaced by Interpenetrated network systems during the project, to take advantage of the single components' characteristics. The suitability of the IPN hydrogels, as the supportive extracellular matrix, has been evaluated thinking on the degradation of the gels due to the embedded cells and their further applications. Hence, some tests were performed to check the cell recovery ratio and the cellular viability after the full digestion of the hydrogels. To do so, the human skin fibroblast cell line, Hs-27, was used. Cells were mixed with the pre-gel solutions, as described before, at a density of 5 x 10^6 cells/ml and crosslinked using the proper printing conditions described for Formulation 5, by using the DLW system, either in the presence or in the absence of LMP-Agarose. Hydrogels with fibroblasts embedded were kept in standard cell culture conditions (37ºC and 5% CO_2), to reach the equilibrium swelling, exchanging cell culture medium every other day.

Then, 3D-Life Dextranase solution (dilution 1:20) was added to each sample and after complete digestion of the hydrogels (12 minutes), cells were collected, and resuspended in fresh cell culture media for counting. Finally, the cells were seeded on a culture Petri dish to evaluate their growth and proliferative capacity after recovery, 24 hours post-digestion.

3.5.4. Mounting within Transwell ® inserts

For creating skin barriers, commercial Transwell® inserts (Merck Life Science) were used, during our *in vitro* studies. First, the original membrane was removed.

Then, by using a double-sensitive pressure adhesive ring (PSA) (inner diameter: 6.5 mm and outer diameter:13 mm) the bioprinted scaffolds were manually positioned within the insert through tweezers and then fixed with another external PSA ring (Figure 3.19). Inserting the Transwell inside a 24-well plate (Merck Life Science), a gradient of diffusion was established, filling the apical and the basolateral compartments separately.

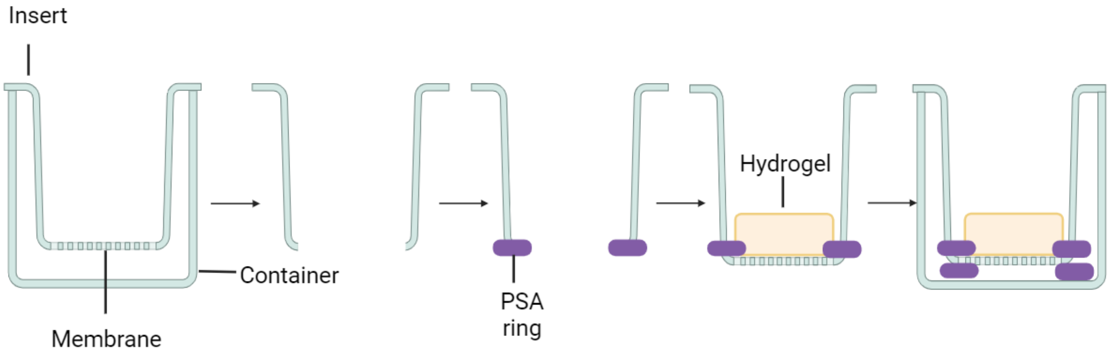

Figure 3.19 Schematic representation of the mounting procedure within the Transwell ® inserts (Biorender software).

3.5.5. Establishment of the epidermal compartment

Once the dermal compartment was established by cell encapsulation followed by the mounting of the scaffold within the Transwell® insert, submerged conditions were applied. Both the basolateral and the apical were filled with the culture medium of Hs-27 cells, to promote the fibroblast growth. Several tests were performed to prove the optimal time point to seed the keratinocytes on top of the cell-laden scaffold, showing a preference in 3 days post encapsulation, for most of the experiments.

In the first part of the work, Humans immortalized keratinocytes (HaCaT) were seeded on top of both the norbornene-pullulan-based hydrogels and norbornene-dextran-based scaffolds. Distinct cell densities were explored, depending on the composition of the gel, and the surface covering performances were evaluated. Briefly, HaCaT cells were prepared as described previously in section 3.4.3, and then the pellet was resuspended in a cell culture medium.

By removing the cell culture medium from the apical compartment, the cells were seeded on top of the hydrogel in a drop-like manner. The scaffolds were left 2 hours into incubation to allow the keratinocytes to attach to the gel's surface. After that, the apical compartment was filled with 200 µl of cell culture medium. The constructs were kept in submerged conditions for 7 days to allow cells to reach confluency and create a well-formed monolayer on top.

Then, to boost the keratinocytes' growth and their differentiation, Air-liquid-Interface (ALI) conditions were applied, at least for two weeks, by leaving the apical compartment exposed to the air and changing the medium for the basolateral part every two days. These samples were prepared for further characterization, such as immunofluorescence studies or Hematoxylin and Eosin staining.

3.5.6. Transepithelial electrical resistance measurements

The integrity of the cellular barrier created on top of the hydrogels was evaluated by a non-invasive, low cost and real-time *in vitro* assay[313,314]. The Transepithelial electrical resistance (TEER) is normally measured in Transwell; it is a quantitative parameter that allows for evaluating the electrical resistance generated by the cells, between the two Transwell® compartments, when they are growing and becoming confluent and mature.

To measure the resistance, a pair of electrodes are placed into the Transwell® inserts, one electrode on the apical side and another in the basolateral compartment. A 12.5 Hz square wave in low alternating current (AC) is applied through the electrodes, and the voltage across the cell barrier is measured through an EVOM3 epithelial Voltohmmeter (WPI world precision instruments). Equipped with an Endohm - 6G culture camber (World Precision Instruments). Values were monitored every two days throughout the culture period (21 days) and by applying Ohm's law, the resistance of the monolayer was extracted[313].

Before the measurements, the well plates containing the scaffolds inserted within the Transwell® were left at room temperature for 20 minutes, and in the meanwhile, the Endhom-6G chamber was filled with 1ml of warm culture medium. Once everything was set, the total electrical resistance was recorded for each sample (R_{total}).

The total electrical resistance registered every day was corrected with the blank value resistance (R_{blank}), which was the value measured before the keratinocytes seed on top of the cell-laden scaffold. The resistance of the monolayer over time was calculated by subtracting the blank value from the R_{total} for each time point. Then, this value was normalized for the surface area of our hydrogel, which corresponds to 0.05 cm^2 for the rectangular-shaped samples (DLW system) and 0.33 cm^2 for the disc-like samples (DLP-SLA system).

3.5.7. Epidermal compartment optimization

3.5.7.1. Surface coverage quantification

For the class of Interpenetrated Network system hydrogels, several optimization studies were conducted to promote a proper formation of the monolayer in a short time.

First, disc-like samples were fabricated with the DLP-SLA system, by using fresh pre-polymer solutions of RGD-N-Dex: CD Link: LAP +/- LMP-Agarose (0.5 mM: 3.5 mM: 3.5 mM: 0.5 mM +/- 0.1 % w/v), without cells embedded. The gels were mounted within the Transwell® inserts and kept in submerged conditions. HaCaT cells were seeded on top of the scaffolds, at different cell densities, respectively: 2.5 x 10^5 cells/sample, 3.75 x 10^5 cells/sample, and 5 x 10^5 cells/sample, and kept in submerged conditions for 21 days.

The cells' growth was monitored over time for all the cell densities by taking phase-contrast pictures of the surface coverage with a Thunder Microscope (Leica DMi8 Thunder Imager Live Cell). The surface coverage quantification was performed with Fiji Software, by measuring the area occupied by the cells and normalizing it for the substrate surface. After 21 days, for all the samples, Air-liquid-interface (ALI) conditions were applied to further characterize the gels with immunofluorescence and evaluate the cell density influence on the markers' expression of the monolayer.

3.5.7.2. Cell culture medium conditions

Besides the cell density optimization, the influence of the culture medium was also evaluated to promote keratinocyte differentiation. For this purpose, RGD-N-Dex: CD Link: LAP hydrogels were prepared with the SOLUS system, by encapsulating 2 x 10^6 Hs-27/ ml. The optimized protocol was followed by mounting the gels within the inserts, right after the encapsulation and keeping them in submerged conditions.

At this stage, half of the samples were cultured with DMEM medium supplemented with 10% FBS and 1% P/S, as we normally do; the remaining half was cultured by using Epilife™ medium, supplemented with S7 and 1% Anti-Anti. After 3 days post encapsulation, HaCaT cells were seeded on top of the cell-laden scaffold by using the optimized cell density obtained from the surface coverage study. For all the samples, independently from the culture medium used, submerged conditions were applied for 7 days, followed by 2 weeks of ALI conditions to boost the HaCaT differentiation. Then, the samples were monitored over time by brightfield inspections (Nikon Eclipse Ts2), and by immunofluorescence studies.

3.5.8 Towards a complex model: HEKn for resembling epidermis

Developing a complex skin model requires a full-thickness system that faithfully mimics the native one. To do this, primary human keratinocytes were used to resemble the epidermal compartment, on top of gels containing human dermal fibroblasts. To establish the skin barrier all the constructs were previously mounted within Transwell inserts before keratinocytes seeding. After 3 days, primary keratinocytes were seeded (16 x 10^4 – 18 x 10^4/sample) on top of the gels containing Hs-27.

The entire scaffolds were maintained in submerged conditions for 3 days: the basolateral compartment was filled with the fibroblasts culture medium; the apical compartment was filled with (HEKs) maintenance medium (KMM), supplemented with 1.5 mM $CaCl_2$ (Keratinocytes growth medium-KGM), to establish a complete monolayer on top.[312]

Then, to promote cell differentiation, Air-liquid Interface (ALI) conditions were applied. Hence, the apical part was left exposed to the air, leaving the surface as much as dry. The basolateral compartment was kept under ALI- conditions medium, by adding keratinocytes differentiation medium (KDM), which corresponds to the KGM medium (submerged conditions), supplemented with 50 µg/ml of L-ascorbic acid and 10 ng/ml of KGF up to 10 days. Samples were finally fixed with formalin, before further evaluation.

3.5.9. Hydrogels' vascularization

Our biomimetic approach consists of creating a skin model that counts not only on the inclusion of dermal fibroblasts and keratinocytes but can also include endothelial cells to promote the vascularization of the system. Hydrogels based on RGD-N-Dex: CD Hy Link: LAP +/- LMP-Agarose (0.5 mM: 3.5 mM: 3.5 mM: 0.5 mM +/- 0.1 % w/v) were prepared by encapsulating Hs-27 fibroblasts with HUVECs cells. Disc-like samples were fabricated with DLS-SLA 3D bioprinter.

As controls, disc-like samples based on both compositions were crosslinked by encapsulating only human fibroblasts or only HUVEC cells, to investigate how the co-culture can impact the rearrangement of the extracellular matrix. Samples were kept in culture for 7 days and then analyzed through immunofluorescence. For the hydrogels that only contain Hs-27, DMEM culture medium, supplemented with 10% FBS and 1% P/S was used. For the gels in co-culture conditions and with HUVECs only, EndoGRO™ Medium supplemented was employed.

Two distinct experiments were settled for this purpose:

1. Hs-27: HUVECs (ratio 2:1), controls: only Hs-27; only HUVECs.
2. Hs-27: HUVECs (ratio 1:3), controls: only Hs-27; only HUVECs.

For the gels based on only dextran composition a time exposure of 3-4 minutes was used, resulting in well-photopolymerized structures. In the presence of the Agarose, higher exposure times were employed (~ 4 minutes). For the gels where only HUVECs were encapsulated, the irradiation exposure was increased by up to 6 minutes.

3.5.10. Complete full-thickness skin model

Finally, a complete full-thickness skin model was also developed, including the dermis, epidermis, and vasculature system. Hence, HEKn cells were used to resemble the epidermal compartment, on top of gels containing human dermal fibroblasts alone and gels with a co-culture of fibroblasts and endothelial cells.

To establish the skin barrier all the constructs were previously mounted within Transwell® inserts before keratinocytes seeding. Both for the basolateral (Hs-27/HUVECs co-culture) and the apical compartment the EndoGRO™ Medium supplemented was employed. After 3 days, primary keratinocytes were seeded ($16 \times 10^4 – 18 \times 10^4$/sample) on top of the gels containing Hs-27 and Hs-27/HUVECs.

The entire scaffolds were maintained in submerged conditions for 3 days: the basolateral compartment was filled with endothelial medium; the apical compartment was filled with (HEKs) maintenance medium (KMM), supplemented with 1.5 mM $CaCl_2$ (Keratinocytes growth medium-KGM), to establish a complete monolayer on top. Then, to promote cell differentiation, Air-liquid Interface (ALI) conditions were applied. Hence, the apical part was left exposed to the air, leaving the surface as much as dry.

The basolateral compartment was kept under ALI- conditions medium, by adding keratinocytes differentiation medium (KDM), which corresponds to the KGM medium (submerged conditions), supplemented with 50 µg/ml of L- ascorbic acid and 10 ng/ml of KGF up to 10 days. Samples were finally fixed with formalin, before further evaluation.

3.5.11. Histological sections

Some hydrogel histological sections were also prepared to better visualize the cells spreading across the entire thickness of the scaffolds and the cells' growth on top. After the fixation with 10% neutral buffered formalin solution at RT for 30 min, samples were demounted from Transwell® inserts. Before performing the histological gels' cuts, a special embedding was necessary to preserve the feeble monolayer. The samples were immersed overnight at 4ºC with 10% $PEGDA_{575}$, (Sigma Aldrich) and 1 % Irgacure D-2959 in PBS.

A block of PEGDA solution was created around the gel using a mask aligner instrument (SUSS MicroTec MJB4) equipped with a mercury short arc lamp (OSR HBO 350 W/S). Briefly, a 2 mm thick PDMS stencil with a central round pool of 12 mm was attached to a plastic support and filled with the embedding solution. The construct was irradiated for 40 s at 25 mW/cm^2 of power density using UV light at 365 nm wavelength in a mask aligner. The resulting $PEGDA_{575}$ block was carefully removed, flipped, and placed back in the pool. The hydrogel to be embedded was then placed inside the pool, the embedding solution was added, and a coverslip was placed on top. After a second exposure of 200 s, the whole construct was flipped, more embedding solution was added, and a second coverslip was placed on top. After a third exposure of 200 s, the hydrogel resulted well embedded into a $PEGDA_{575}$ block.

Besides the PEGDA embedding, another cryopreservation solution was also tested. A more kindred solution based on Norbornene-pullulan: PEG-Link: LAP (5 mM: 4 mM: 0.2 mM) was tested for this purpose. The samples were first demounted from Transwell® inserts and fixed with a 10% neutral buffered formalin solution. Then, the solution (Norbornene-pullulan: PEG-Link: LAP) was prepared and the samples were kept submerged in this solution overnight. The day after, the blocking was performed by first pipetting the solution in a drop-like manner on top of the scaffold to completely cover it and then by irradiating the sample through DLP-SLA. The exposure time was increased up to 8 minutes, resulting in a sample completely embedded in a norbornene-based solution.

In both cases, samples were immersed overnight in 30% sucrose solution (Sigma Aldrich) at 4°C, then embedded in optimal cutting temperature (OCT) compound (Tissue-Tek® O.C.T. Compound, Sakura® Finetek) and stored at -80 ºC for at least 12 h. Finally, they were cut with a cryostat (Leica CM195), and histological cross-sections of 8 μm thickness were recovered, attached to glass coverslips, air dried, and stored at -20ºC until use. This last procedure was carried out by the Histopathology facility services from IRB at PCB.

3.5.12. Immunostaining and immunofluorescence analysis

The distribution of the cells within the hydrogels (Hs-27 human fibroblasts and HUVEC cells) and on top of the cell-laden surface (human immortalized keratinocytes -HaCaT- and the primary epidermal human, neonatal keratinocytes -HEKn-), together with the morphology, the proliferative capacity, and the possibility to secrete specific proteins, was evaluated through immunofluorescence analysis.

Briefly, after several days in culture, the scaffolds were first carefully removed from the Transwell® inserts or the 24-well plate and placed in a new one. After some washing steps with warm PBS, the samples were fixed, at different time points, depending on the experiment, with 10% neutralized formalin (Sigma-Aldrich) for 1 hour in shaking conditions. After 3 cycles of washing in shaking conditions, they were permeabilized with 0.5% Triton X-100 (Sigma-Aldrich) and incubated for 1 hour at 4 ºC. Consequently, samples were blocked with 1% BSA (Sigma-Aldrich), 3% donkey serum (S30-M, Sigma-Aldrich), and 0.2% Triton X-100 in PBS for 2 h at RT. Then, samples were incubated with primary antibodies (Table 3.7.) overnight at 4°C followed by several PBS washings. Lastly, samples were incubated for 1 h at RT, in shaking conditions, with 0.1% BSA, 0.3% donkey serum, and adequate secondary antibodies (Table 3.8.) plus DAPI. The gels were prepared for immunofluorescence analysis, by mounting them in PBS or Fluoromount G® mounting solution (Southern Biotech) on coverslips using PDMS spacers and flipping them on top of the glass coverslip.

Fluorescence images were acquired using a confocal laser scanning microscope (LSM 800, Zeiss) with 10x objective (NA = 0.3, WD = 2.0), 20x objective (NA = 0.8, WD = 0.55) or 40x objective (NA=1.4, WD=0.13). The laser excitation and emission light spectral collection were optimized for each fluorophore. The pinhole diameter was set to 1 Airy Unit (AU). A z-step between 1 µm - 5 µm was used, depending on the experiment. The acquired Z-stacks were processed through ImageJ software.

3.5.13. Hematoxylin and Eosin staining

The samples based on Formulation 4, with a co-culture of Hs-27/ HaCaT, Formulation 6 with a co-culture of Hs-27/ HaCaT or Hs-27/HEKn, and Formulation 6 with a co-culture of Hs-27/HUVECs and HaCaT were embedded in paraffin and stained for the Hematoxylin and Eosin. The scaffolds were embedded in an automatic tissue processor machine (Tissue Tek VIP, Sakura) resulting in paraffin-embedded sections of 8 µm thick.

The process was carried out by the Histopathology facility services from IRB at PCB. Before the staining, the samples were kept overnight at room temperature. The slides were incubated with Harris Hematoxylin (Sigma-Aldrich) for 2.5 minutes and then left under running cold water for 3 minutes. After that, the slides were incubated in an acid alcohol solution (0.3 % HCl in ethanol) for 1 minute, followed by another washing step of 3 minutes. After 1 minute of incubation in ammonia water (0.3 % ammonia in Milli Q water) and a subsequent washing step (3 minutes), the sections were incubated with Eosin for 1 minute. Finally, the slides were dehydrated following 3 distinct incubations in Ethanol (95%) for 1 minute, Ethanol (100%) for 30 s, Ethanol (100%) for 1 minute; and 2 incubations in xylene solution for 3 minutes. At the end of the protocol, the slides were ready to be mounted in a xylene-based mounting medium (Eukitt) and processed.

3.6. Antibodies

3.6.1. Primary antibodies

Table 3.7. List of primary antibodies used for immunostainings throughout the thesis.

NAME	TYPE	SOURCE	DILUTION
Anti-CD31	Rabbit polyclonal	Abcam ab28364	1:50
Anti-collagen type IV	Goat	Biorad134001	1: 250
Anti-E-cadherin	Mouse IgG2a K	BD Biosciences 610181	1: 1000
Anti- Endoglin	Rabbit polyclonal	Santa Cruz sc 20632	1:50
Anti-Fibronectin	Rabbit	Sigma F3648	1: 100
Anti-Fibronectin	Mouse	Santa Cruz sc-52331	1: 200
Anti-Filaggrin	Rabbit polyclonal	Abcam ab81468	1: 1000
Anti-Involucrin	Mouse monoclonal	Abcam ab68	1:500
Anti-Keratin 10	Rabbit polyclonal	Biolegend 905401	1:400
Anti- Keratin 10	Rabbit monoclonal	Abcam ab76318	1:400
Anti Keratin 14	Rabbit polyclonal	Biolegend 905301	1:400
Anti-Ki67	Rabbit IgG mAb	Abcam ab16667	1:100
Anti-Laminin	Rabbit polyclonal	Abcam ab11575	1:200
Anti-Loricrin	Rabbit monoclonal	Abcam ab198994	1:250
Anti-Vimentin	Mouse monoclonal	Santa Cruz sc- 6260	1:100
Anti-Vimentin	Rabbit IgG	Cell Signaling 5741	1:200
Anti-Vimentin	Rabbit monoclonal	Abcam ab92547	1:250
Anti- VE-cadherin	Rabbit polyclonal	Abcam ab33168	1:200

3.6.2. Secondary antibodies

Table 3.8. List of secondary antibodies used for immunostainings throughout the thesis.

TYPE	MADE IN	NAME	SOURCE	DILUTION
Anti-mouse	Donkey	Alexa Fluor™ 647 donkey anti-mouse IgG (H+L)	Invitrogen A-31571	1:500
	Donkey	Alexa Fluor™ 568 donkey anti-mouse IgG (H+L)	Invitrogen A-10037	1: 500
	Donkey	Alexa Fluor™ 488 donkey anti-mouse IgG (H+L)	Invitrogen A-21202	1: 500
Anti-rabbit	Donkey	Alexa Fluor™ 647 donkey anti-rabbit IgG (H+L)	Invitrogen A-3157	1: 500
	Donkey	Alexa Fluor™ 568 donkey anti-rabbit IgG (H+L)	Invitrogen A-10042	1: 500
	Donkey	Alexa Fluor™ 488 donkey anti-rabbit IgG (H+L)	Invitrogen A-21206	1:500
Anti-goat	Donkey	Alexa Fluor™ 488 donkey anti-rabbit IgG (H+L)	Invitrogen A-21447	1:500
	Donkey	Alexa Fluor™ 568 donkey anti-goat IgG (H+L)	Invitrogen A-11057	1:500
	Donkey	Alexa Fluor™ 488 donkey anti-goat IgG (H+L)	Invitrogen A-11055	1:500

DAPI (1:1000, Thermo Fisher Scientific); Rhodamine-phalloidin (1:140).

3.7. Statistics

For all the experiments, statistical analysis was performed, presenting the data as the mean ± standard deviation (SD) or as mean ± standard error of the mean (SEM), as defined in the corresponding figure caption. The graphs were plotted using GraphPad Prism 8.3.0 software (GraphPad). Distinct replicates were used in all the studies, and detailed information about the number of replicates (n), depending on the formulation and/or working conditions is indicated in each figure caption. Statistical significance was investigated by the t-student test, or two-way ANOVA, depending on the experiment. Differences were considered statistically significant if $p < 0.05$.

4. Results

4.1. Fabrication of scaffolds based on Norbornene-thiol-ene chemistry

Norbornene-thiol-ene chemistry is the fulcrum of this study. The aim of the work resides in the possibility of developing norbornene-based hydrogels as a valid alternative to collagen-based scaffolds for engineering skin models. These hydrogels are prepared using a light-based 3D bioprinting system, and thiol-ene click chemistry, to get, in a short time, biocompatible gels with a homogeneous network. Pre-gel solutions will be examined, starting from a single network, and ending up with interpenetrated network systems.

During the entire work, six polymer-based formulations will be studied and discussed. All the formulations are correlated to each other, and each formulation's change represents the natural and consequent update of the previous one, intending to improve and/or overcome all the drawbacks faced in terms of printability of the material, reproducibility, cell sustainability, and sample handling. Hence, based on the criteria of employing norbornene-thiol-ene click chemistry, different combinations of polymer/crosslinker were considered. In the first part, the printability of several norbornene-thiol-ene-based formulations will be discussed. Then, the results of the formulation selected as the most suitable one will be presented together with modifications made to improve the mechanical properties of the gels and their biocompatibility.

Later, an alternative formulation will be analyzed, to sustain cell spreading and the formation of the epidermis construct, resulting in the first epithelized-dermis model developed within the Ph.D. project. Subsequently, a new type of hydrogels, based on a combination of two distinct polymer systems, will be introduced, to develop an improved model that combines the peculiar functions and characteristics of the single components to raise the gels' performances with reliable dimensions and reduce materials costs. Within this section, a method to develop stiffness-varying substrates will be also discussed. Finally, the last experiments will be devoted to the last formulation studied, the most suitable for supporting cell growth and enhancing cell differentiation, which will be largely described together with the first trials of the system's vascularization.

4.1.1. Preliminary printability tests to fabricate scaffolds based on Norbornene-thiol-ene chemistry

First, polyvinyl alcohol (PVA) and pullulan (PLN) polymers were selected as the main components of the preliminary formulations, due to their characteristics. For instance, PVA, a synthetic polymer, is widely employed in tissue engineering since it allows tuning both the tensile strength and the flexibility of the scaffolds, improving their durability.[315] On the other side, pullulan is a natural polymer that possesses several advantages, such as high hydration capacity and biocompatibility,[316] resulting in largely used in wound healing because it promotes fibroblast proliferation and epithelization.[147] Both polymers were coupled with norbornene, which resulted in reactive double bonds. Thiol-modified polyethylene glycol (PEG) and hyaluronic acid (Hy) were used as crosslinkers. By employing a commercial 3D-bioprinting system (SOLUS), three different combinations of polymer/crosslinker were tested, always using LAP as a photoinitiator.

The first formulation considered (Table 3.1- Materials and Methods section) was combining norbornene-polyvinyl alcohol (N-PVA) with PEG- Link and LAP (5 mM: 5 mM: 5 mM) -Formulation 1. A fresh bioink solution (2 ml) was prepared, so once the pre-gel solution was allocated inside the vat, disc-like gels of 4 mm in diameter and with a thickness in the range of 0.5 mm – 1 mm, were printed by varying different working parameters. The CAD design (circular shape) was printed layer-by-layer from the bottom, on top of previously silanized PET membranes, used as printing support. By fixing the exposure energy to 61.5 mJ/cm^2, which corresponds to 5 s of exposure time per printed layer, and the number of the bottom layers (n = 2), as a general threshold to get photopolymerization, the impact of the layer thickness on the gels' morphology was evaluated.

Hence, by setting the exposure time of 5 s both for the bottom layers and for the upper ones, the layers' thickness was varied to 10 µm and 20 µm. As depicted in the pictures in Figure 4.1, there was some crosslinking, but no good scaffolds were obtained with this polymer formulation. Specifically, in the first trial (Figure 4.1-a) for a layer thickness of 10 µm, a weak structure was achieved, resulting from almost no photopolymerization. In Figure 4.1-b, although increasing the layer thickness up to 20 µm, the resulting structure was a fragile gel, which did not present a proper consistency.

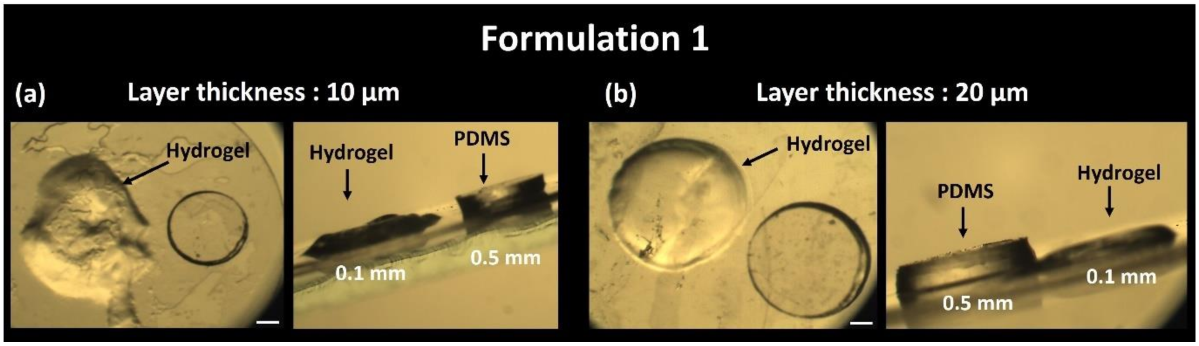

Figure 4.1. Bioprinting tests (Formulation 1). Top and lateral views of bioprinting tests of disc-like hydrogels based on Formulation 1 (N-PVA: PEG-Link: LAP ~ 5 mM: 5 mM: 5 mM); PDMS structures were used for the height comparison. Hydrogels with a single layer thickness of 10 µm (a), and 20 µm (b), respectively. Scale bars = 1 mm.

Before totally discarding Formulation 1, ulterior tests were conducted. Since the layer thickness did not impact the formation of the gels, another parameter was considered. The layer thickness was kept constant at 20 µm and the influence of energy dose per layer on the gels' structure was assessed.

First, the exposure time of the bottom layers was tuned (Figure 4.2 -left panel-), and the normal layers' exposure time was set to 10 s, to evaluate the influence of the energy dosage on the base of the gels' scaffolds. Despite the huge contrast between the two trials, (a) 5 s exposure - and (c) 30 s exposure-, the resulting gels did not present the intended shape, showing again the unsuitability of this composition to be photocrosslinked under these experimental conditions.

Lastly, two more fabrication trials were performed (Figure 4.2 -right panel-). By keeping constant the layers' thickness to 20 µm, the exposure of the normal layers was tuned between 2 s and 5 s, and the exposure time of the bottom layers was fixed to 2 s, to explore the impact of the energy dosage on the formation of the scaffolds' body. Top view pictures (Figure 4.2 b,d) showed polymerized gels for both conditions. Lateral views enhanced more defined structures compared to the ones previously depicted (where the energy dosage of the bottom layers was tuned), even though scaffolds had irregular borders. To enhance the printability of gel structures, facilitating the achievement of self-supporting and homogenous formations, a modification was deemed requisite.

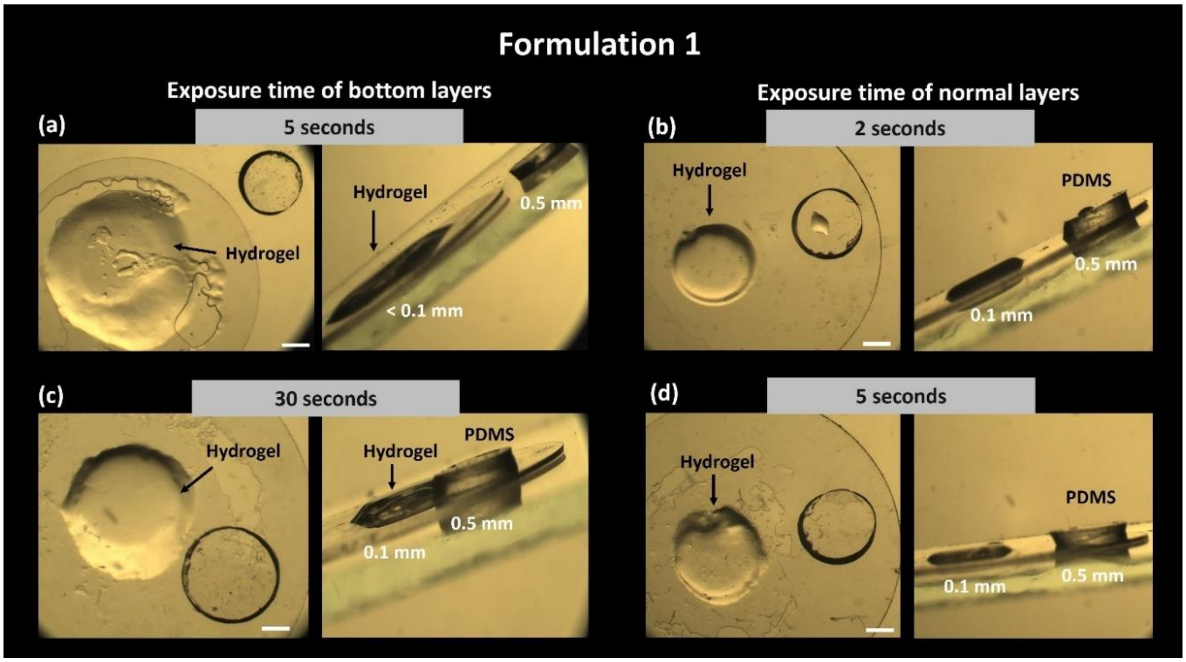

Figure 4.2. Bioprinting tests (Formulation 1). Top and lateral views of bioprinting tests of disc-like hydrogels based on Formulation 1 (N-PVA: PEG-Link: LAP ~ 5 mM: 5 mM: 5 mM); PDMS structures were used for the height comparison. **Left panel -**Hydrogels with different exposure times of bottom layers: 5 s (a) and 30 s (c). **Right panel-** Hydrogels with different exposure times of normal layers: 2 s (b), and 5 s (d) respectively. Scale bars = 1 mm.

Thus, a second formulation was evaluated, to determine the robustness of the norbornene crosslinking approach. For this purpose, gels based on norbornene-pullulan (N-PLN) with PEG-Link and LAP (5 mM: 5 mM: 0.2 mM)- Formulation 2- were fabricated. The layer thickness of, respectively 10 and 20 µm (Figure 4.3- a,c and b,d), were employed to print several scaffolds. Well-crosslinked structures were obtained in both cases, despite the differences in thickness. For lower layer thicknesses (10 µm), two different structures were photo-crosslinked, using CAD slicing of 50 and 100 slices, respectively, (Figure 4.3 a and c) resulting in well-formed structures, although the height's difference, as expected, due to the distinct slicing. A slight deformation in the borders was observed, especially visible in the lateral-view pictures (Figure 4.3. a, c- right). Then, the layer thickness was fixed to 20 µm, and two new gels were crosslinked by setting the exposure time of the bottom layer at 5 and 10 s. Again, well-defined scaffolds were observed. Although the difference in terms of exposure time (10 s for the first structure (Figure 4.3 b), versus 5 s for the second one (Figure 4.3 d), consistent and easy-to-handle gels were obtained, in both cases. Thus, these preliminary printability studies suggested the potential of norbornene-pullulan-based formulations to be photocrosslinked in the presence of visible light with a low content of LAP.

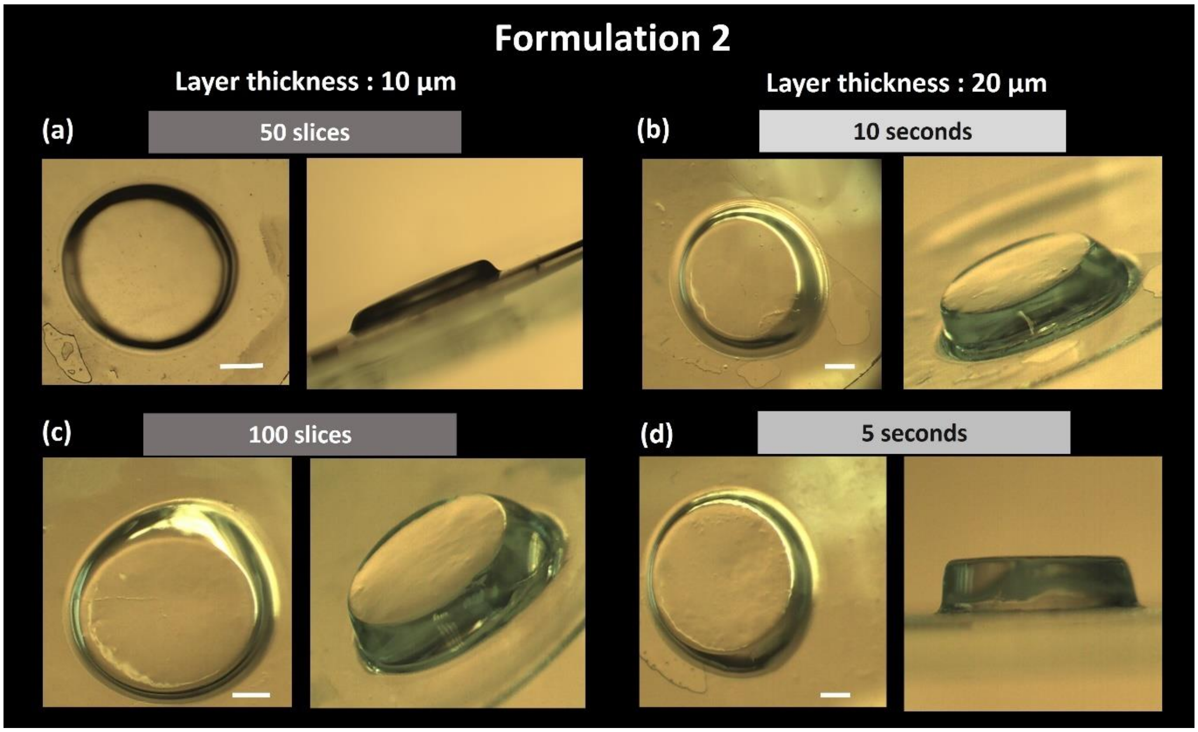

Figure 4.3. Bioprinting tests (Formulation 2). Top and lateral views of bioprinting tests of disc-like hydrogels based on Formulation 2 (N-PLN: PEG-Link: LAP ~ 5 mM: 5 mM: 0.2 mM). **Left panel-** Hydrogels with a single layer thickness of 10 µm, with respectively 50 slices (a) and 100 slices (c). **Right panel-**Hydrogels with a single layer thickness of 20 µm, with different exposure times of the bottom layer, respectively 10 s (b) and 5 s (d). Scale bars = 1 mm.

All the 3D structures examined present common characteristics, showing self-standing, without revealing relevant defects in terms of shape and definition or highlighting overexposure portions, normally localized in some scaffolds' regions[317]. Inevitably, the parameters considered affected the resulting scaffolds, as the modest variation in terms of structures' robustness. For example, by tuning the CAD slicing it's possible to control the gels' height. On the other side, layer thickness influenced the gels' consistency, as in the case of thicker layer thickness, where sturdy gels were recognized (Figure 4.3 b, d), compared to the softer constructs reported in Figure 4.3 a, c.

In the third combination, norbornene-pullulan (N-PLN) was employed together with a thiol-modified hyaluronic acid (Hy-Link) and LAP, Formulation 3, (4 mM: 4 mM: 0.2 mM) to evaluate the impact of the new crosslinker on the gel's printability. Hyaluronic acid can represent a valid alternative, as one of the major components of the extracellular matrix, especially considering further cell encapsulation. However, synthetic polymers such as polyethylene glycol offer more controllable mechanical properties, such as strength and viscoelasticity, implementing water adsorption capacity, and guaranteeing better control during the fabrication process.

For Formulation 3, the first parameter tuned was the layer thickness, while the exposure times of the bottom and normal layers were settled to 5 s. Photocrosslinking was achieved for all the printing parameters assayed. By changing the layer thickness between 10 µm and 20 µm (Figure 4.4 - a, c) no relevant differences were detected. Self-standing scaffolds were obtained, presenting regular circular shapes.

Then, the impact of the energy dosage was evaluated both on the bottom and on the normal layers. Fixing the layer thickness to 20 µm, the bottom layer exposure was set to 5 s, and the exposure time of normal layers was increased to 10 s first (Figure 4.4 b), resulting in thin but well-polymerized structures. Finally, the bottom layers' exposure was increased up to 10 s, together with the exposure of the normal layers to 15 s, (Figure 4.4 d). So, better prints with sharper edges were reached. Although the good results registered with this last combination, comparing scaffolds based on Formulation 3 with the ones we got with Formulation 2, a clear distinction was noticed.

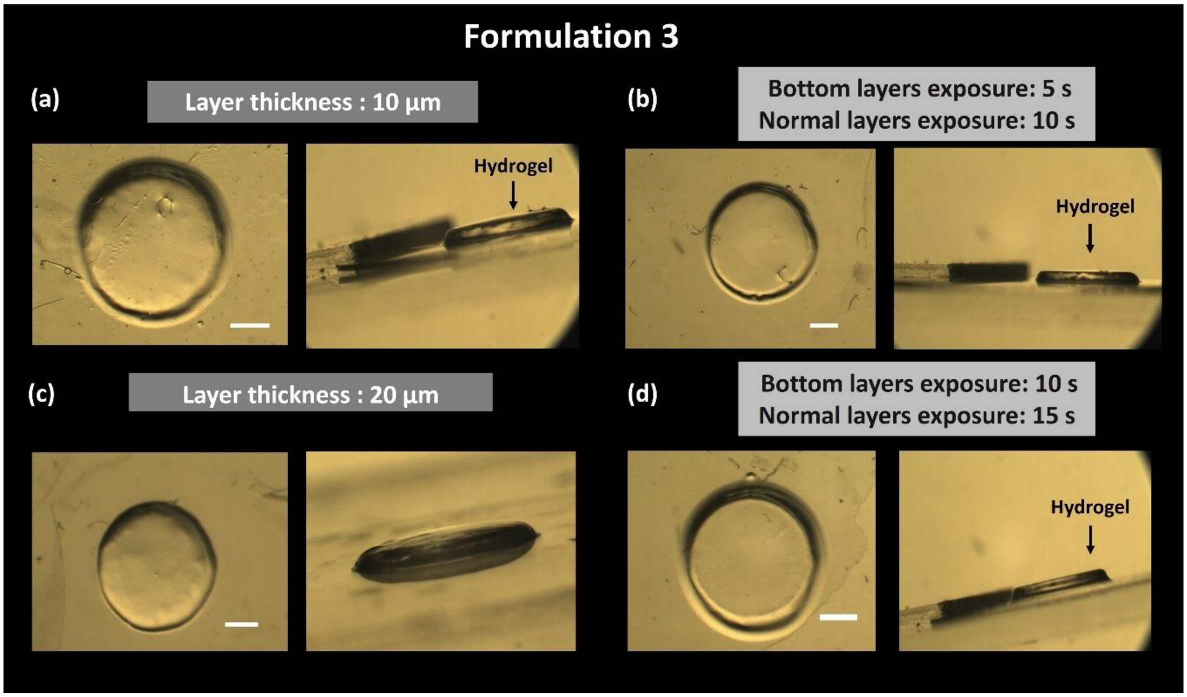

Figure 4.4. Bioprinting tests (Formulation 3). Top and lateral views of bioprinting tests of disc-like hydrogels based on Formulation 3 (N-PLN: Hy-Link: LAP ~ 4 mM: 4 mM: 0.2 mM); PDMS structures were used for the height comparison. **Left panel-** Hydrogels with constant exposure times of bottom and normal layers (5 s), and single layer thickness of 10 µm (a) and 20 µm –(c) respectively; **Right panel-** Hydrogels with a fixed layer thickness (20 µm), with - 5 s, and 10 s of bottom and normal layers exposure, respectively (b); 10 s and 15 s of bottom and normal layers exposure (d). Scale bars = 1 mm.

Gels obtained by using PEG-Link revealed (Formulation 2) higher robustness and thickness and they do not appear as soft as the ones based on Formulation 3 during the handling. In the presence of a Hy-linker, a weaker polymerization can be perceived, resulting in flabby structures.

Therefore, after these preliminary printability tests, the formulation based on norbornene-pullulan and PEG-Link was determined as the easiest to print and was selected for further experiments.

4.2. Printability tests by using a Direct Laser Writing (DLW) system

As described before, to perform photocrosslinking tests by using a DLP system (SOLUS 3D-bioprinter) an initial bioink volume of 2 ml was required. This imposed severe limitations to ensure enough supply of the non-commercial bioinks, which were produced on a small scale. To cope with this problem, we decided to employ an alternative homemade printing system based on Direct Laser Writing (DLW), a technique that uses only 15 µl of solution to print.

The apparatus (Section 3.2.1.3) was previously settled in our group for hydrogel fabrication and to test new blends of materials, both commercially and in-house modified. Hence, before translating the norbornene-pullulan composition to this new equipment, first, a well-known polymer, $PEGDA_{4000}$, largely used in biofabrication was employed to determine a preliminary interval of printing parameters. A solution of 10% of $PEGDA_{4000}$ and 0.2% of LAP in HBSS + 1% P/S was prepared (~ 0.5-0.3 ml). Modulating the z-distance of the 405 nm laser diode to the focus plane of the sample through a micromotor, respectively at 10 and 20 nº steps in the z-direction, and varying the light power, (13 mW-22 mW) stripped-like hydrogels were photo-crosslinked on top of silanized cover glass, allocated inside of a 24-well plate.

Several printability trials were performed, evaluating the impact of working parameters, such as the z-distance and the light power on the hydrogel's structures, on the shape, consistency, and robustness of the hydrogels obtained. Some examples are reported here. Thus, from these studies, it was concluded that the z-distance influences the dimensions of the gels along the y-axis (width). In fact, at shorter laser diode z-distance (nº steps =10) correspond wider structures, due to bigger areas of the pre-gel solution receiving the minimum dose for being polymerized. This led to collapsing scaffolds that could not stand by themselves and resulted in fragile gels, which are easy to be damaged once rinsed and gently wiped post-fabrication (Figure 4.5 a). On the other hand, although tiny scaffolds were obtained by increasing the nº steps, which means reducing the energy dose per superficial area available, the scaffold's consistency was improved, resulting in tough hydrogels, and not subject to breakage (Figure 4.5 b).

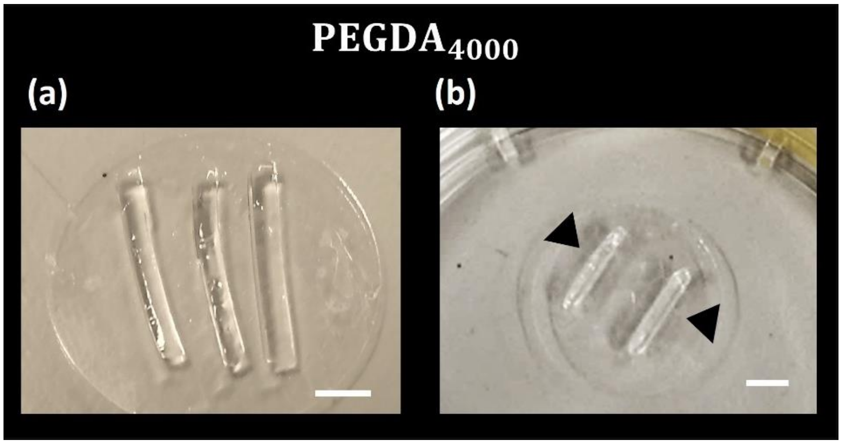

Figure 4.5. PEGDA$_{4000}$ based stripped-like hydrogels fabricated with Direct Laser Writing (DLW) system. (a) Hydrogels photocrosslinked with shorter z-distance (nº of steps = 10). **(b)** Hydrogels photocrosslinked with longer z-distance (nº of steps = 20). Scale bars = 1 mm.

From these printability tests, it was concluded that an appropriate z-distance was necessary to get consistent gels. Despite the larger structures can be obtained at shorter distances, higher ones are recommended to get easy-to-handle gels.

The optical power also influences the hydrogel structure. According to the literature studies, higher optical powers correspond to higher hydrogel widths, due to the higher accumulated optical energy per unit area.[310] The same behavior occurs when the stage velocity decreases.

4.3. Single network-based hydrogel system

4.3.1 Norbornene-based hydrogels: Formulation 2

Once settled the DLW system and verified the potentiality of this equipment to photocrosslink and produce proper scaffolds, norbornene-based polymers (N: PLN: PEG Link: LAP) -Formulation 2- were designed as the focus of the work.

Due to a shortage of polymer material, the volume required for the printing by the DLW system was reduced even more. For that, circular PDMS o-rings (Ø = 6 mm) of different heights were employed to confine the volume, by placing it on top of the cover glasses, which were allocated in a 24-well plate. The use of PDMS is convenient and possible with thiol-ene chemistry because this reaction is not inhibited by oxygen.[210] Then, fresh bioink solutions were prepared (5 mM: 4 mM: 0.2 mM) and printability tests were carried out in these conditions. All the trials were conducted with a power of 22 mW, a speed of 0.3 mm/s, and a z-distance of 20 nº of steps. First, thicker PDMS pools (height: 2 mm) were used, which allocate 50 µl. Starting from this pre-gel volume, polymerized gels have been obtained, as the one shown in (Figure 4.7-a), which exhibits a rectangular-shaped structure, tending to fall on its side.

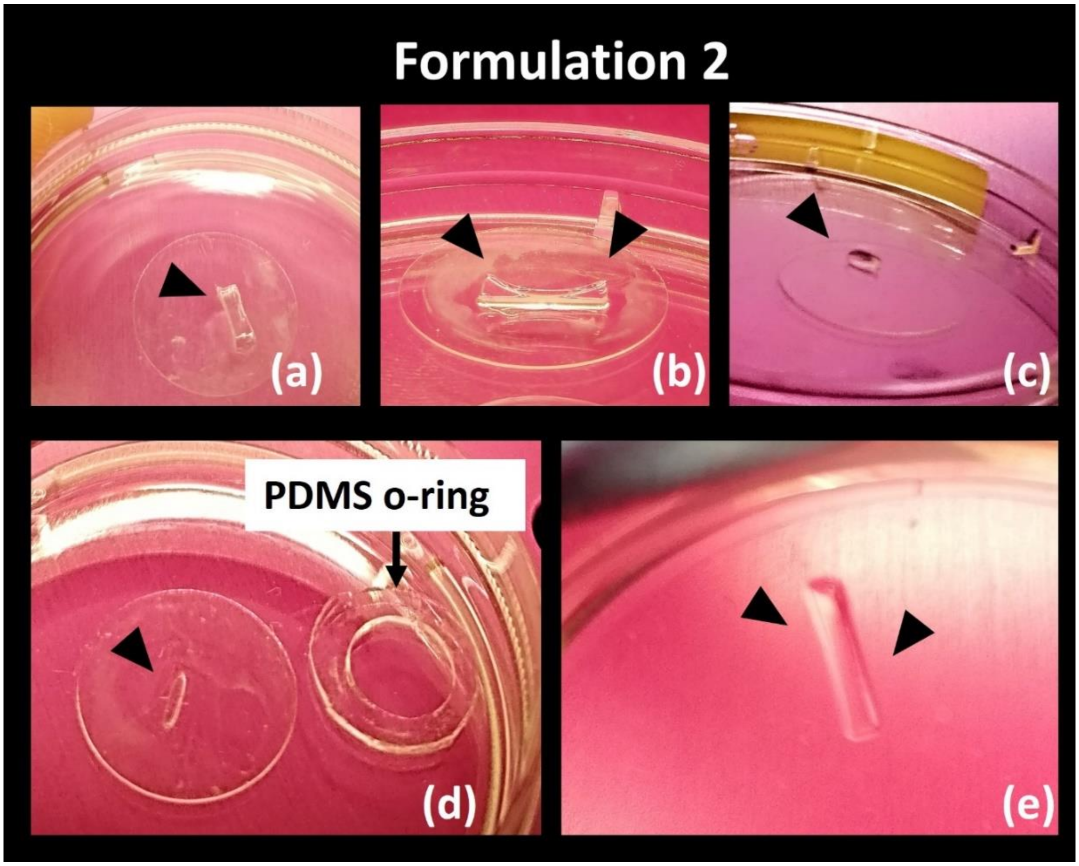

Figure 4.6. Examples of stripped-like hydrogels photo-crosslinked with the DLW system by using a PDMS circular ring (Ø = 6 mm). Hydrogels were realized with a PDMS o-ring with 2 mm in height, with a starting volume of 50 µl **(a)** and 35 µl **(b),** respectively. **(c)** Hydrogel was realized by using a PDMS o-ring with 1 mm in height and ~ 30 µl of initial volume. Hydrogels fabricated with a PDMS ring of 0.5 mm in height, and a starting volume of < 15 µl, with z-distance of 20 **(d)** and 25 **(e).**

By decreasing the volume allocated in the pool up to 35 µl, the strongest gel can be achieved (Figure 4.6-b), which can remain standing, even though doesn't present regular edges. The gels manifest sharp borders, enhancing a concave structure towards the inside, reflecting the pre-gel meniscus pre-polymerization, since this lower volume does not fill completely the pool.

To cope with this effect, the height of the PDMS-o-ring was further reduced to 1 mm. To fill the pool, the volume was decreased to less than 30 µl, resulting in good scaffolds but simultaneously tiny and shorter (Figure 4.6-c), probably due to the lower aspect ratio. After this evidence, again the PDMS ring's height was reduced even further, up to 0.5 mm, (Figure 4.6-d), causing a discrete reduction in terms of sample sizes. Thus, the last implementation counts on the change of the z-distance raised to 25 n° of steps, leading to a sample, that displays (i) a good ratio between the superficial area and the height, (ii) regular and squared borders, (iii) no residues of not crosslinked materials and (iv) properly lean on the cover-glass, easy to wash and wipe (Figure 4.6-e).

At this stage, it was demonstrated how to remarkably minimize the required volume for the photopolymerization, moving from DLP-SLA equipment to a DLW apparatus. By employing the ploy of the PDMS pool, the essential volume was set at 15 µl per sample. Moreover, the crosslinking reaction was very fast, and rectangular-like hydrogels of dimensions (5 mm x 1 mm x 0.5 mm) were constructed in a few seconds.

4.3.2 Swelling properties of norbornene-based hydrogels

Because of its relevance to the biocompatibility properties, the water uptake capacity of norbornene-based hydrogels under different photocrosslinking conditions was investigated. Thus, rectangular-like hydrogels were fabricated with a 405 nm laser diode, setting the z-distance at 25 nº of steps. Right after photopolymerization, the dimensions of the samples were monitored from time 0 up to 24 hours post-crosslinking, by taking pictures of the scaffolds.

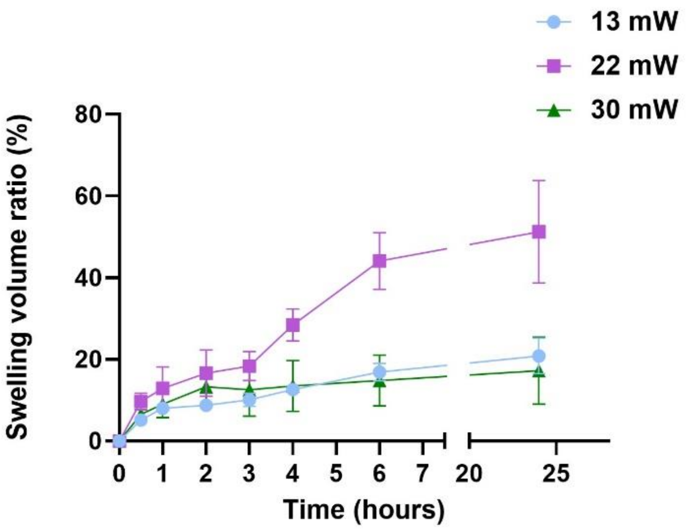

Figure. 4.7. Swelling behavior. Volume swelling ratio for N-PLN: PEG-Link gels (5 mM: 4 mM), fabricated applying different light powers: 13 mW (light blue); 22 mW (magenta); 30 mW (green). Values are shown as the mean ± SEM (2 < n < 3). N=2 independent experiments.

The behavior of gels' swelling was comparable among the different powers used during photocrosslinking, reaching the equilibrium 24 hours after fabrication. Generally, no correlation between power increase and the uptake capacity increase was noticed. However, all the gels reached the maximum peak after 24 h, as depicted in Figure 4.7, enhancing higher values for the hydrogels obtained with 22 mW of power. Either for lower power (13 mW) or for the highest one (30 mW), the swelling registered was > 10%, before reaching the equilibrium. For the intermediate ones, instead, the swelling reached 40% of the initial volume, enhancing an important increase already in the first 6 hours compared to the other conditions.

This study represents the first attempt at hydrogel characterization, to elegy the optimal working parameters and to get hydrogels that display the appropriate characteristics to support cells. Anyway, the results achieved are in line with the ones registered for other types of hydrogels, such as GelMa and PEGDA[317], largely used for gut 3D model applications and in tissue engineering. [311]

4.3.3. Analysis of the bulk's properties

Further analysis of the stiffness matrix of these hydrogels was run. As described in Section 3.3.3., the rheological characterization took place during *in situ* crosslinking.

A fresh pre-gel solution was prepared, and different crosslinking trials were performed in rows. For this purpose, the measurements were carried out on distinct samples (n=4) photocrosslinked at the moment. The dynamics of the crosslinking process were recorded while exposing the pre-gel solution to UV light (Figure 4.8-a), during the *in-situ* crosslinking. The crosslinking reaction initiates when the light is activated, reaching a polymerization plateau in under 3 seconds.

The data of Storage G' and Loss G'' modules obtained as a function of the strain were analyzed, and the resulting bulk Elastic Modulus (Young's Modulus~ kPa) was calculated assuming a Poisson's coefficient of 0.5. The results, as depicted in Figure 4.8-b, expressed an average value of 5 kPa, fitting in the range of other acellular scaffolds,[318] used for resembling skin models. The values' discrepancy between the different samples analyzed was caused by the experimental error since the pre-gel drop was manually deposited on the rheological plate, provoking some variations.

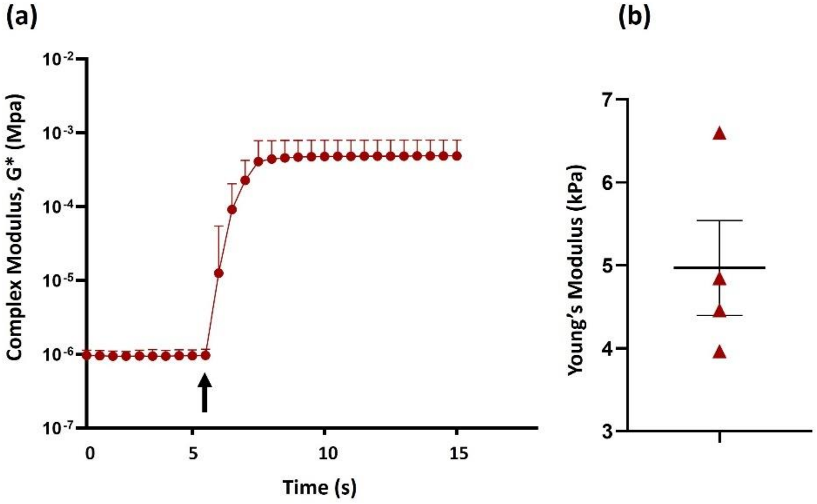

Figure 4.8. Rheology study. (a) Complex Modulus G* (MPa) curves registered during the real-time crosslinking process for Formulation 2 (red). The arrow indicates when the light stimuli was switched on. **(b)** Young's Modulus values are calculated from the complex Modulus, derived from the Storage and Loss Modules as a function of the strain. Values are shown as the mean ± SEM (n=4).

4.3.4. Cell compatibility studies

4.3.4.1. Encapsulation and cell viability studies of NIH-3T3 cells.

Once established that the hydrogels possessed mechanical stiffness acceptable to support cell encapsulation, even though the soft nature displayed, qualitative cell viability experiments were performed to demonstrate the biocompatibility and the non-toxicity of this material's composition. Hence, a cell suspension of 7.5 x 10^6 NIH-3T3/ml was mixed with a fresh pre-gel solution (N-PLN: PEG-Link ~ 5 mM: 4 mM) with LAP as photoinitiator at 0.2 mM. Distinct irradiation power/speed combinations were used for this purpose. Several gels were printed (3 mm in length, 1 mm in width, and 0.5 mm in height), and the cells' viability was evaluated at different time points by using Live/Dead ™ viability/cytotoxicity assay, as reported in Figure 4.9.

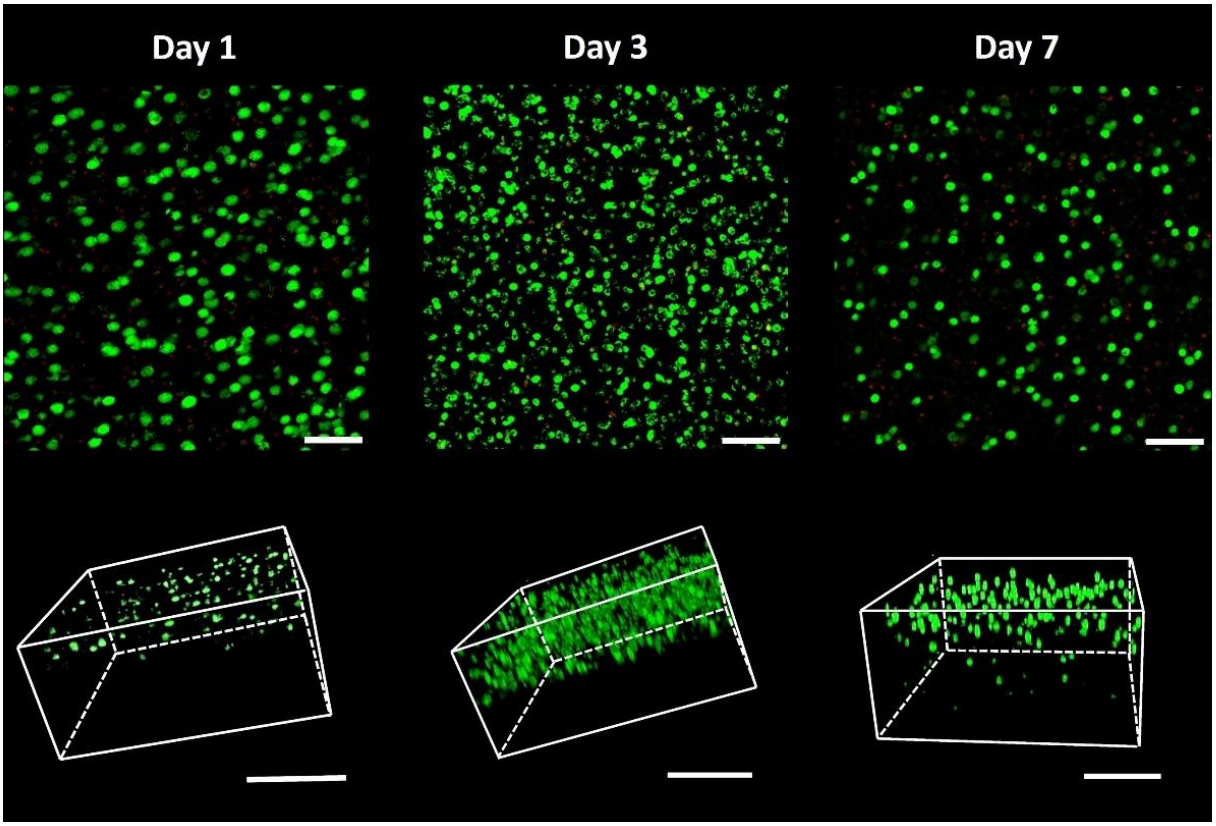

Figure 4.9. Live & dead assay. Cell viability of NIH-3T3 encapsulated within N-PLN: PEG-Link hydrogels (22 mW,0.3 mm/s) at days 1, 3, and 7. Maximum intensity projections (upper row), live cells stain in green, dead cells stain in red. Scale bar = 100 µm. 3D reconstruction (lower row) to show the spatial distribution of the cells within the entire gel's thickness. Scale bar = 200 µm.

As shown in Figure 4.9, from the maximum intensity projections view (upper row), most of the mouse fibroblasts were alive over time. On day 1, the cells were mainly distributed on the gel surface and in the upper layers, as visible from the 3D reconstruction (bottom row).

On day 3, a huge increase in the cell number was appreciable, demonstrating the capacity of the cells to grow within the gel composition. Moreover, NIH-3T3 fibroblasts appeared more uniformly distributed within the entire gel's volume. 7 days post encapsulation, an evident decrease in terms of alive cells was observable, indicating the inadequacy of the gels' composition to support cells for a longer time culture. In addition, mouse fibroblasts did not show any protrusion or spreading, remaining visible roundish. The same cell behavior was also observed for the other conditions tested. Hence, from this assay, we concluded that even though this composition certainly allowed keeping alive most of the cells, unfortunately, it cannot guarantee their spreading and elongation.

Although mouse fibroblasts are widely used in tissue engineering studies, because they are easy to culture, and represent the first approach to test the cytocompatibility of the materials, some limitations correlated to the cells' growth normally occurred.

4.3.4.2. Encapsulation and cell viability studies of human Hs-27 cells.

Based on the previous experiments, the decision to improve the scaffolds' performance to embed cells within was embraced by moving to a more reliable cell line. For this purpose, human foreskin fibroblasts (Hs-27) were chosen to better mimic the dermal compartment. A fresh cell suspension of 5 x 10^6 fibroblasts/ml was prepared and mixed with a pre-gel solution (N-PLN: PEG-Link ~ 5 mM: 4 mM). As in previous experiments, gels were fabricated with distinct power conditions, 13 mW, and 22 mW in that case, to investigate the influence of different working conditions on the cell viability within the gels. Again, the cell viability assay was performed at different time points, 1 day, 4 days, and 7 days post-fabrication. From the maximum projection pictures (Figure 4.10- left side), it was visible that the cells did not elongate nor protrude within the scaffolds, although, this time, they were more uniformly distributed along the entire gel's volume from the first day post-encapsulation, as enhanced from the 3D-reconstruction views. Quantifying the number of the cells alive along the time, for both crosslinking conditions, it was evident that higher powers promoted the viability. More than 83% of cells were alive on day 1 post encapsulation (22 mW), against less than 80% registered for lower power (13 mW). A decrease was noticed after 7 days, reaching a percentage of 75% for higher power and even lower for the other condition.

However, the cell spreading was not reached, suggesting that the hydrogel composition does not encourage proper growth and elongation of the human fibroblasts, even if it was biocompatible with the cells, guaranteeing a homogenous distribution of the cells within the substrate.

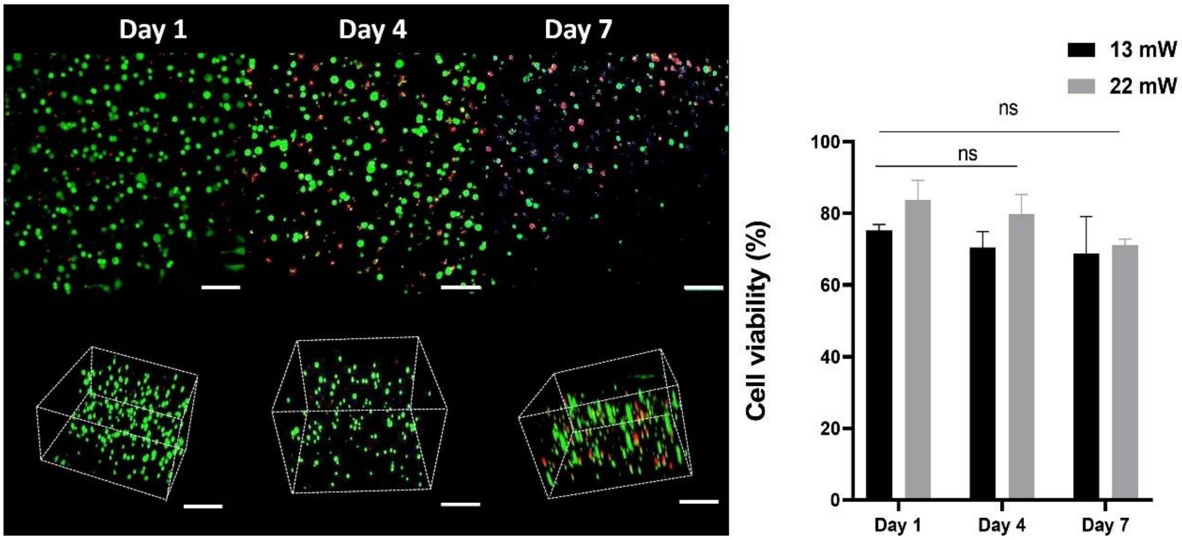

Figure 4.10. Live & dead assay. Cell viability of Hs-27 encapsulated within N-PLN: PEG-Link hydrogels (22 mW and 13 mW, 0.3 mm/s) at days 1, 4, and 7. **Left panel-** maximum intensity projections-upper row-, live cells stain in green, dead cells stain in red (22 mW). 3D reconstruction to show the spatial distribution of the cells within the entire gel's thickness-bottom row-. **Right panel-** Cell viability (%) quantification of human fibroblasts within hydrogels crosslinked with 13 mW (black bars) and 22 mW (grey bars), respectively. Values are shown as the mean ± SEM (n = 2 per condition). T-test performed. Scale bar = 100 µm.

4.3.5. Co-culture study.

Despite the issues encountered with the cell encapsulation, where no cells' elongation was noticed, a co-culture study was conducted. It is well-known that the coexistence of two different cell types in a co-culture system highly promotes the growth of the single-cell group, favoring their interconnections and resulting in the expression of their representative markers. [319]

The aim was to develop a gel construct able to contain first fibroblasts inside, and then keratinocytes on top, to resemble the full-thickness model. Because of that, human-immortalized keratinocytes (HaCaT) were selected as precursor prototypes of cells to echo the epidermal compartment. Considering this, new hydrogels (5 mm in length, 1 mm in width, and 0.5 mm in height) with human fibroblasts encapsulated (5 x 10^6 Hs-27/ml) were crosslinked (22 mW, 0.3 mm/s). Right after the embedding, the constructs were mounted within the Transwell® inserts and kept in submerged conditions. On day 3 post-encapsulation, a cell suspension of 3 x10^5 HaCaT/cm^2 was added and cultured on top of the hydrogels to resemble the epidermal layer (Figure 4.11).

The entire cell-laden scaffolds with keratinocytes on top were maintained in submerged conditions for 1 week, by changing the medium every 2 days. On day 7 post-HaCaT cell seeding, the hydrogels were fixed, and immunofluorescence analysis was performed to investigate the potentiality of the co-culture systems and the expression of their indicative markers.

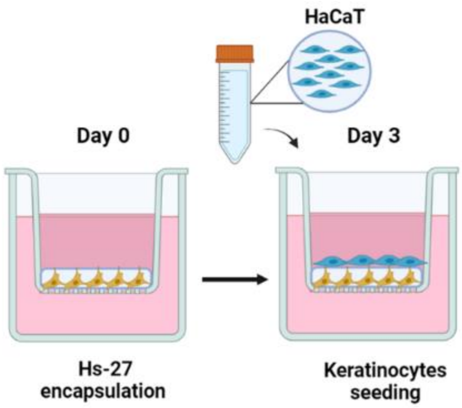

Figure 4.11. Schematic representation of the co-culture process (Biorender software). Cell-laden constructs are first crosslinked (day 0) and mounted within the Transwell®. After 3 days in submerged conditions, a cell suspension of immortalized keratinocytes (HaCaT) is seeded on top of the constructs.

The immunofluorescence study underlined how the cells were well-expressing F-actin (yellow), showing a good proliferative capacity, as enhanced by the Ki67 signal (magenta), after 7 days post-seeding. However, as observable in Figure 4.12**,** unfortunately, all the keratinocytes, which were seeded on top of the gels, fell on the membrane, where the hydrogel was printed.

Regardless of the co-culture conditions adopted, no implementations were reached, demonstrating that a change of strategy was necessary. Although Formulation 2 showed good mechanical properties, and a cell-friendly environment, it was unable to support cells' growth, thus, changes in terms of pre-gel compositions were also considered.

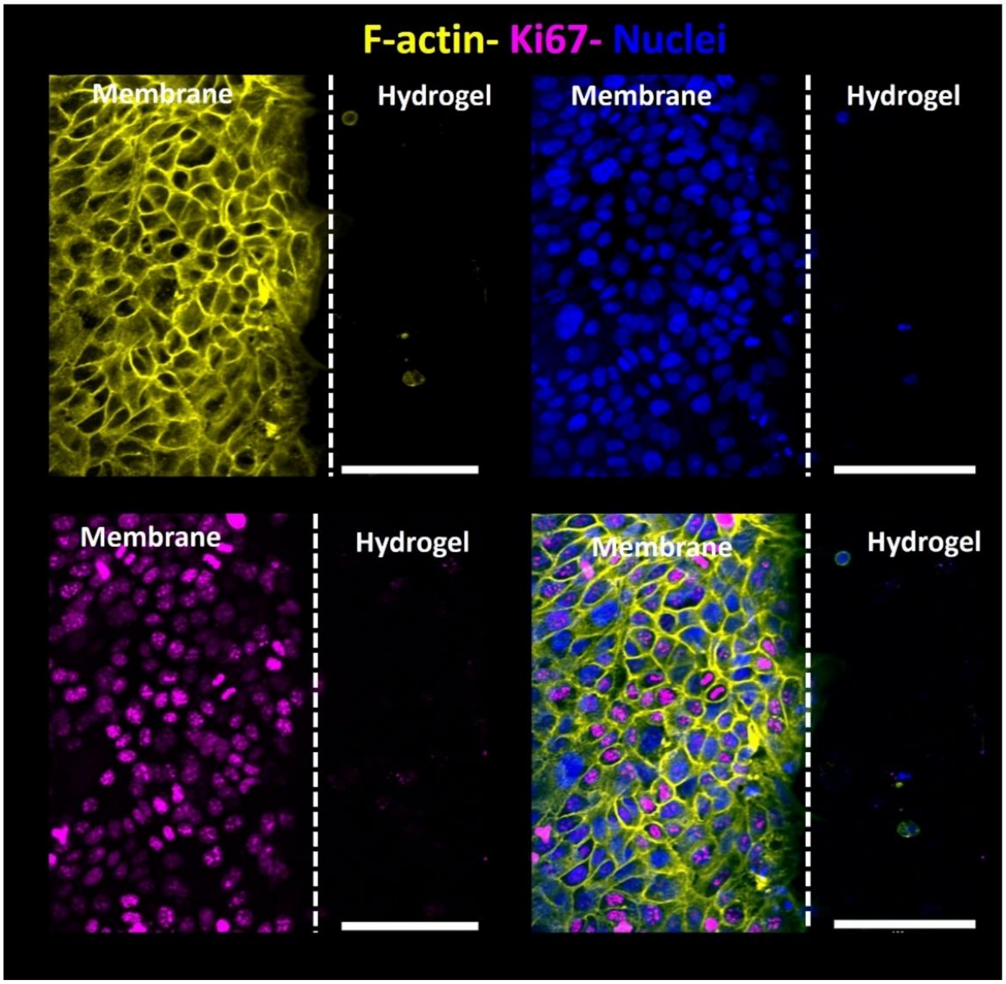

Figure 4.12 Immunofluorescence study. Top view projections at day 7 post-seeding of co-culture systems (Hs-27/HaCaT) within N-PLN: PEG-Link hydrogels, stained for F-actin (yellow), Ki67 (magenta). DAPI (blue) stained the nuclei. Merged channels on the right (bottom row). Scale bar = 100 µm.

4.3.6 Formulation 2- RGD functionalized.

Formulation 2 gels showed interesting characteristics to develop full-thickness skin models, despite their soft nature. However, multiple tests including cells, either inside the substrate or on top of them, underlined a route change demand. Cell viability assays exhibited the inadequacy of this composition to boost cell spreading within the extracellular matrix. At the same time, the first attempts to co-culture keratinocytes and fibroblasts to obtain full-thickness skin failed, proving the non-suitability of the formulation itself to be used as a cell culture scaffold. Therefore, within the framework of the BRIGHTER project, new reagents were developed by our partners (Cellendes, GmbH, Germany), to overcome these drawbacks. RGD-peptide motifs (Acetyl-Cys-Doa*-Doa-Gly-Arg-Gly-Asp-Ser-Pro-NH_2) were added to the norbornene-pullulan polymer to improve, at first, the fibroblasts' elongation across the substrates.

Hence, different contents of RGD portions (0.5 mM and 1 mM) were anchored to the polymer to explore their impact on cell support. Preliminary fabrication tests were again conducted by using fresh solutions (**RGD**-N-PLN: PEG-Link: LAP ~ **0.5 mM or 1 mM-** 4.08 mM: 4 mM: 0.25 mM) to ensure the correct photopolymerization of the new materials, by using a power range between 13 mW and 30 mW and demonstrating that power does not affect the gels' structure. Considering this, for the next experiments, the intermediate power -22 mW- was used to photocrosslink the hydrogels, taking into account the higher uptake capacity revealed during the swelling tests (with the same preparation without RGD- 22 mW-).

4.3.6.1 Encapsulation and cell viability studies of Hs-27 cells.

Cell viability assays were performed to evaluate the repercussions of the RGD peptide on the growth and elongation of Hs-27 within the scaffolds.

In Figure 4.13 the viability of Hs-27 was reported for 1 day and 7 days post-encapsulation for different RGD content. Although the distinct content of RGD peptide, no significant differences in cell viability were registered, as enhanced by the quantification graph.

An even distribution was noticed across the gels' matrix, for both the formulations tested. However, no protrusions were recognized. On day 1, for higher RGD concentration (1 mM), a slightly higher percentage of alive cells was appreciated (up to 90 % ± 2.2) in comparison to the other preparation (0.5 mM) (86% ± 2.1). After 7 days, the higher content of RGD did not favor the viability of the cells, causing a sudden decrease in both cases.

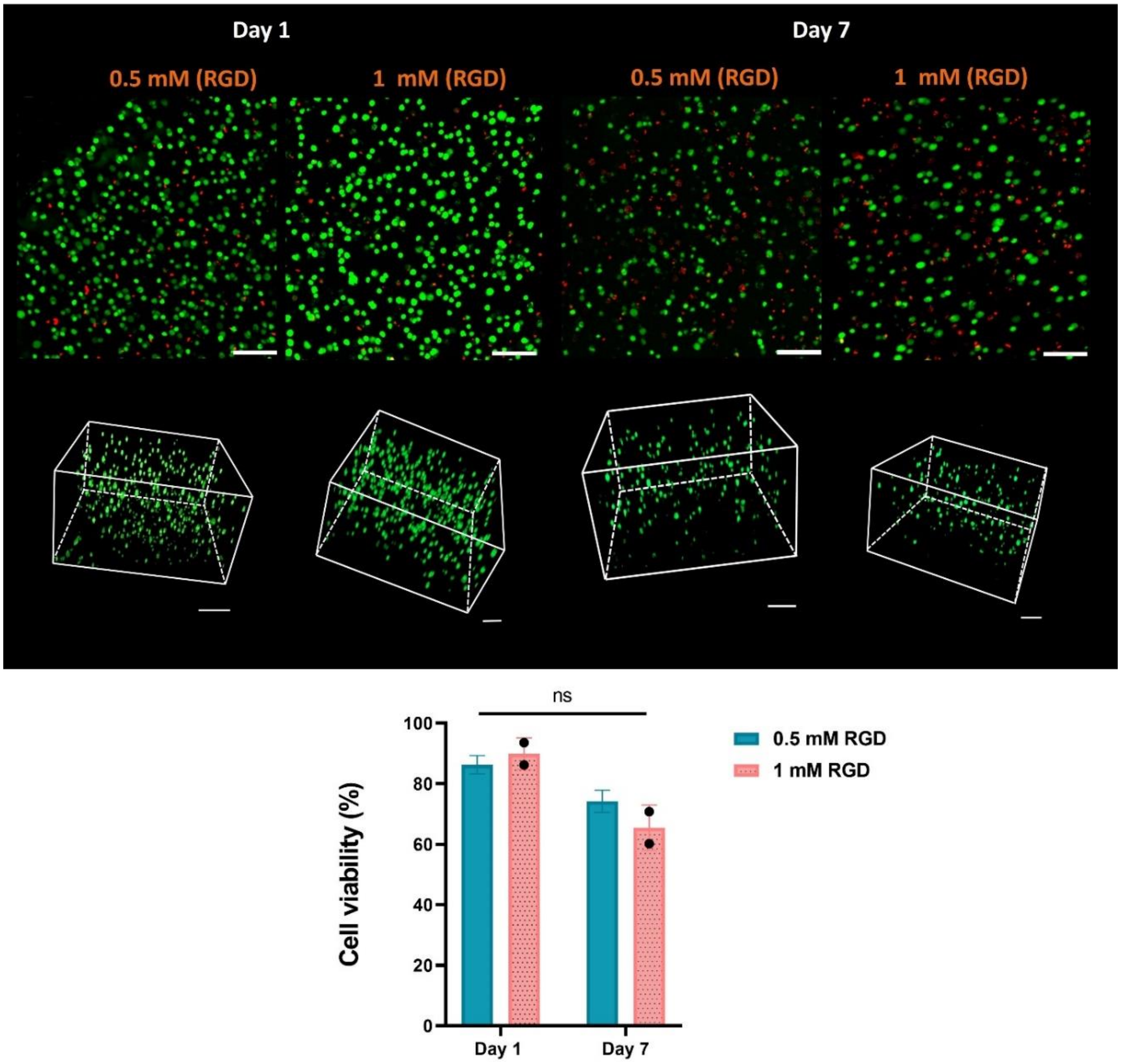

Figure 4.13. Live & dead assay. Cell viability assay of Hs-27 within scaffolds fabricated with different content of RGD peptide, 0.5 mM, and 1 mM. Maximum intensity projections in the first row, on day 1 and day 7, (live cells- green; dead cells – red). 3D view of the entire gels' volume in the second row. Scale bars = 100 µm. Cell viability quantification between the 2 different RGD contents (0.5 mM- light blue; 1 mM- pink). A t-test was performed for this experiment. Values are the mean ± SD (n = 3 per each condition).

4.3.6.2. Co-culture study

Co-culture studies were also performed to investigate if the RGD presence has an impact on keratinocyte attachment. Briefly, new gels were prepared, with and without human fibroblasts encapsulated (5 x 10^6 Hs-27/ml) containing respectively 0.5 mM and 1 mM of RGD content. This experiment aimed to compare cell-laden scaffolds and cell-free scaffolds and their influence on keratinocyte attachment on the surface, evaluating two distinct RGD contents.

Immortalized HaCaT cells (3 x 10^5 cells/cm^2) were seeded in a drop-like manner on the gels' surface 1-hour post fabrication (with and without fibroblasts encapsulated). The constructs were kept in incubation, in submerged conditions, and monitored over time by taking brightfield pictures on day 1, and day 5. As reported in Figure 4.14, the brightfield inspection revealed a huge difference between the scaffolds that contain fibroblasts inside and the ones without cells embedded.

In the upper panel, for cell-laden substrates, from the beginning (24 hours post-seeding), most of the cells were anchored to the surface, although some of them fell on the PET membrane. By following the evolution of cell attachment, most of the cells were still anchored to the gels' surface, establishing a monolayer over the constructs, 120 hours post-seeding. By focusing on the RGD content, it was noticed that it exhibited a strong effect on the gels' matrix. For higher concentrations of the RGD peptide (1 mM)- upper panel- second row- an unmistakable shrinkage over time was evident, resulting in an obvious contraction of the substrate, drastically expressed on day 5.

In contrast, looking at the cell-free scaffolds, the situation appeared different. Starting from 24 hours post-HaCaT seeding, in the absence of fibroblasts, just a few cells resulted attached on the gels 'surface, with a slightly higher percentage visible for the higher RGD content- bottom panel- second row-. This status did not change over time, as depicted after 120 hours -bottom panel-, independently from the amount of RGD-peptide. Thus, with these studies, it was demonstrated that the coexistence of the fibroblasts with the keratinocytes drastically impacts the adherence of cells hookup on top of the surface, also due to the paracrine cell signaling. Moreover, this analysis highlighted that RGD motifs' presence influences the shrinkage of the scaffolds, depending on the concentration content.

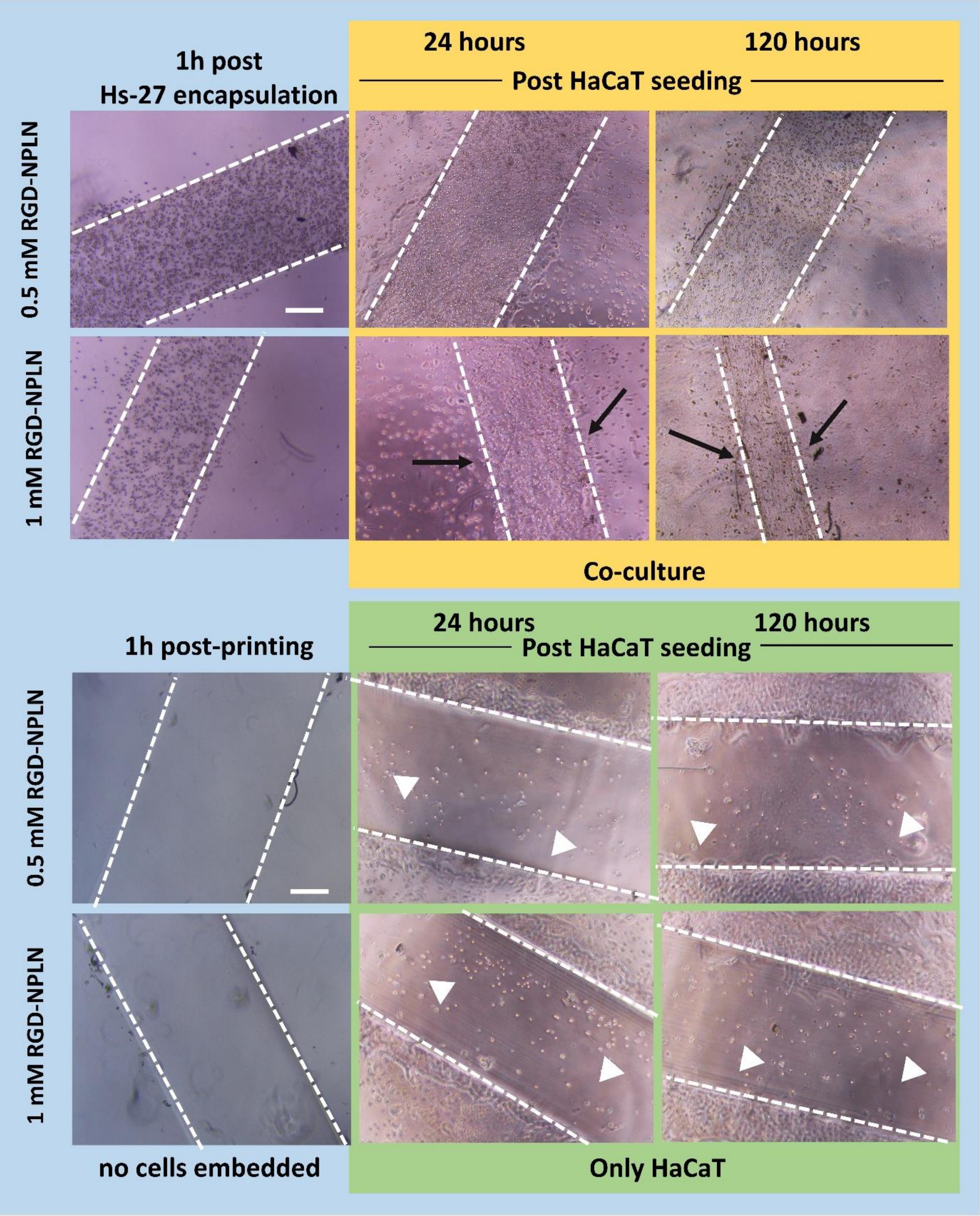

Figure 4.14. Brightfield inspection. Brightfield pictures of HaCaT cells, respectively seeded on top of the cell-laden scaffolds, containing human dermal fibroblasts (top panel) and on top of cell-free substrates (bottom panel), based on Formulation 2- RGD functionalized composition, respectively after 24, and 120-hours post-seeding. The first row shows the seeding on top of scaffolds with lower RGD content (0.5 mM); the second row refers to the seeding on top of scaffolds with higher RGD content (1 mM). Black arrows are pointing to the evident scaffolds' shrinkage (upper panel). White arrows are pointing the cells distributed on the hydrogels' surface (bottom panel). Dashed lines indicate the hydrogels' borders. Scale bars = 200 µm.

Simultaneously with these experiments, photocrosslinking tests were performed by Cellendes, GmbH. After careful observation, some photopolymerization defects were ascertained, as in the example reported in Figure 4.15-upper panel-. For these structures with Hs-27 encapsulated, a phase separation was noticed across the matrix (as indicated by the dashed line), showing non-uniform portions of the substrate (left and right parts of the gel). A deeper investigation was also conducted in our facilities, by crosslinking scaffolds with Hs-27 encapsulated. The power was changed in a range between 13 mW and 30 mW keeping both RGD contents.

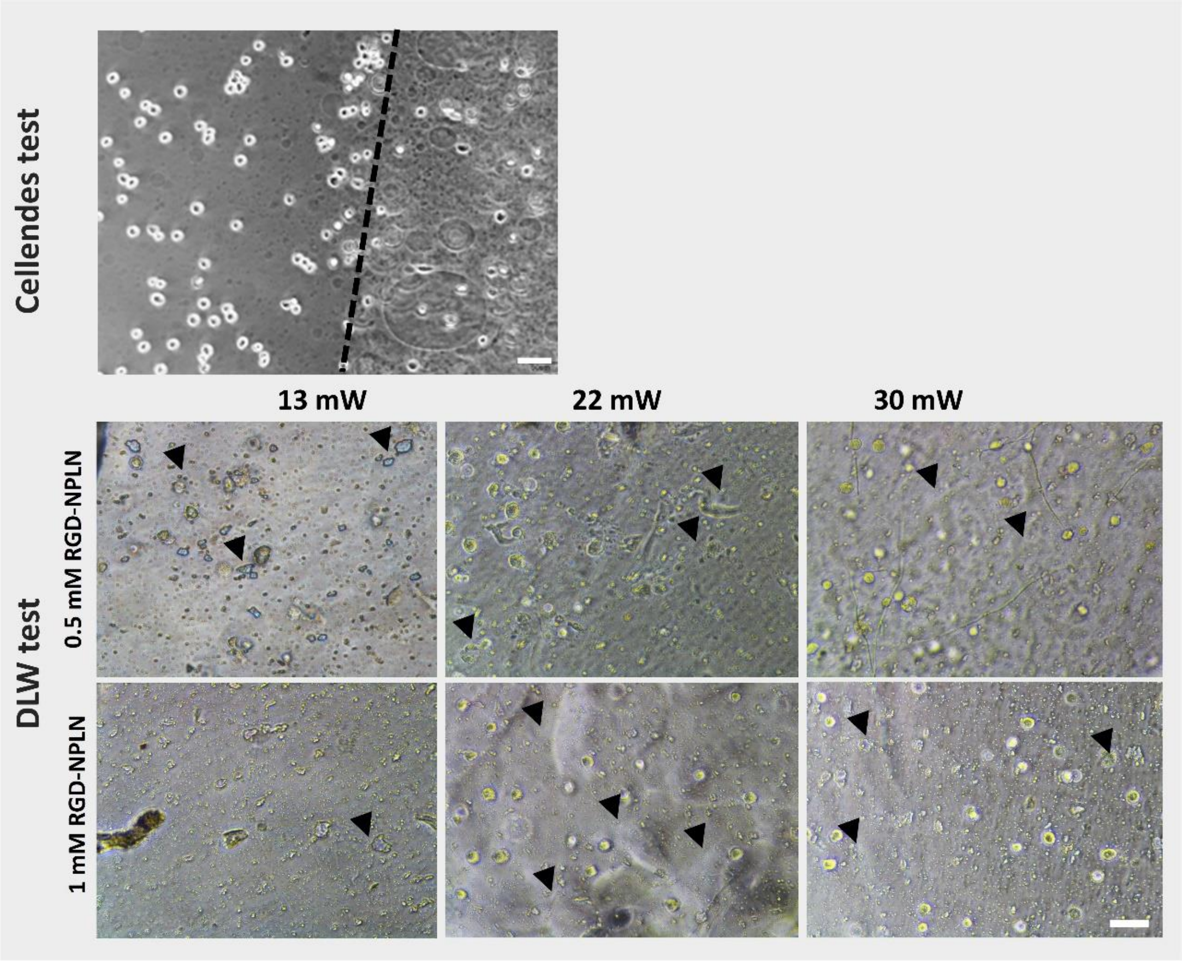

Figure 4.15. Brightfield inspections of gels' defects. Upper panel- Example of polymerization defects observed within hydrogels fabricated by using Formulation 2- RGD-functionalized- composition (4.08 mM: 4 mM: 0.25 mM, with an RGD content between 0.5 mM and 1 mM) with Hs-27 cells encapsulated. The dashed line indicates the phase separation. Scale bar = 50 µm. Picture provided by Cellendes, GmbH, Germany. **Lower panel-** Inhomogeneities observed within hydrogel scaffolds with Hs-27 cells embedded, photopolymerized by using Formulation 2- RGD-functionalized composition (4.08 mM: 4 mM: 0.25 mM, with an RGD content of 0.5 mM and 1 mM). Black triangles indicate the defects. Scale bar = 500 µm.

As shown in Figure 4.15 -lower panel- any real phase separation was revealed for our gels. However, intrinsic defects were noticed, indicating a heterogeneous gel matrix, independently from the distinct photocrosslinking conditions tested and the different RGD content.

Indeed, although the studies performed until now showed the potentiality of our 3D-bioprinting system, enhancing the possibility of getting crosslinked structures in which human fibroblasts can be embedded, the defects expressed after photopolymerization, together with the incapability of the cells to spread and elongate, were the main important factors that led to the consideration of a different strategy.

4.4. Formulation 4: RGD-N-PLN: CD-Hy Link: LAP

Previous studies highlighted how fundamental a change of route was. Despite the advantages shown by the Norbornene-Pullulan-based formulation, and the improvements introduced by the RGD-functionalization, some modifications in the formulation were mandatory, both to promote cell spreading within the gels or cells' attachment on their surface, simultaneously preserving the scaffolds from shrinkage.

Thus, a new crosslinker based on hyaluronic acid-carrying thiol groups, the 3D-Life CD-Hy Link (Cellendes GmbH), was adopted. The novelty of this crosslinker resides in the presence of a cell-degradable (CD) matrix metalloproteinase (MMP) -cleavable peptide sequence (Pro-Leu-Gly-Leu-Trp-Ala), that can be cleaved by a broad range of MMPs, such as MMP1, MMP3, MMP7, and MMP9[320]. Hence, this means that cells can locally degrade the polymer network if they produce the indicated MMPs.

Preliminary studies were conducted by our partners identifying the optimal molar ratio between polymer/crosslinker (1:1). Keeping constant this ratio, they defined a range between 2 mM and 3 mM, to get proper gel structures.

Based on these trials, some polymerization tests were first performed in our facilities to determine the optimal molar concentration according to our DLW system characteristic, resulting in well-defined structures with delineated edges by using 2.5 mM of molar content (Figure 4.16), which was considered for the following experiments. Additionally, the power values were also tuned in a range between 13 mW and 30 mW, showing the intermediate condition -22 mW- the optimal one.

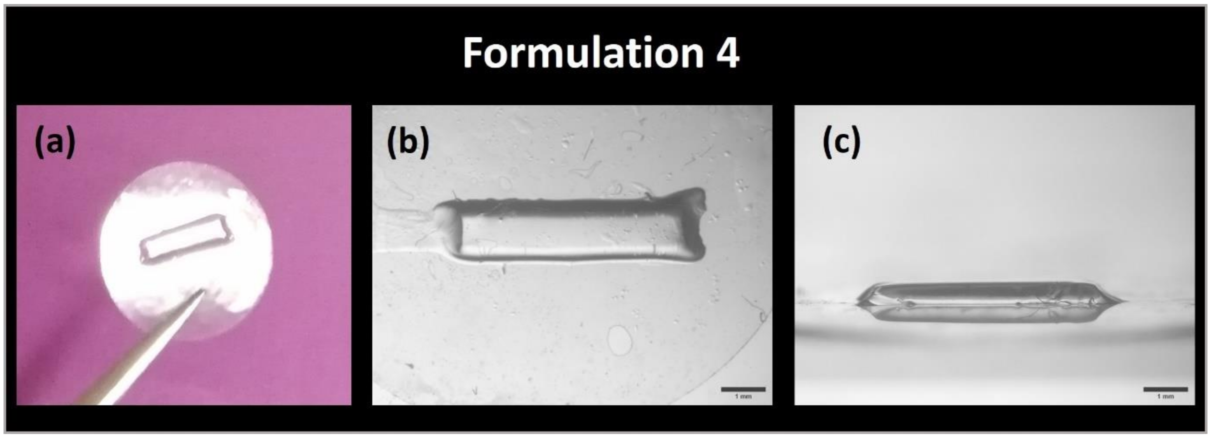

Figure 4.16. Printability tests. Examples of hydrogels fabricated by using Formulation 4, by using a molar content N-PLN: CD-Hy Link (1:1) of 2.5 mM. **(a)** Picture of a scaffold right after photopolymerization. **(b)** Top and **(c)** lateral views at t=0 taken by Stereo Microscope (Olympus, SZX2-ILLB). Scale bar = 1 mm.

4.4.1. Characterization of hydrogels based on Formulation 4

4.4.1.2 Swelling properties

First, hydrogels based on Formulation 4 were analyzed in terms of swelling behavior. Rectangular-shaped hydrogels, like the ones depicted in Figure 4.16, were fabricated using a power of 22 mW, the optimal power, as emerged from the printability tests, and kept in PBS while monitoring their change in dimensions.

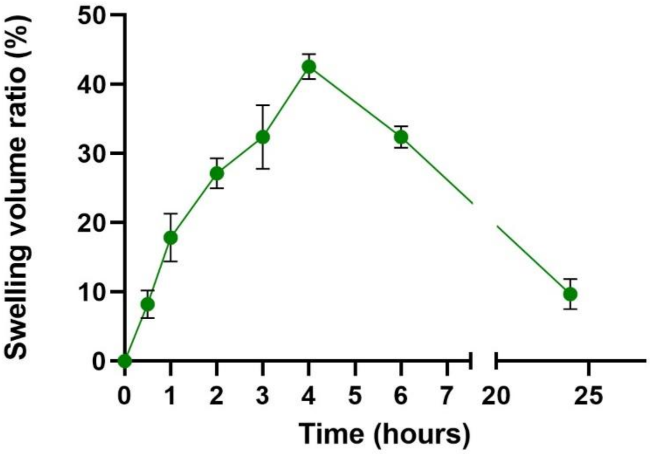

Figure 4.17. Swelling behavior. Volume swelling ratio for RGD-N-PLN: CD-Hy Link: LAP gels (0.92 mM: 2.5 mM: 2.5 mM: 0.5 mM), fabricated applying a light power of 22 mW. Values are shown as the mean ± SD (n= 6).

The water uptake capacity of the hydrogels based on Formulation 4 was evaluated over time and the equilibrium swelling was reached after 24 hours post-fabrication, as enhanced by Figure 4.17.

In the first 4 hours of post-photopolymerization, as the gel absorbed the water, the polymer network expanded and an increase in terms of swelling volume ratio was registered up to more than 40% of the initial volume. Then, over time, the elastic forces within the polymer network started to balance the osmotic forces. Changes in the crosslinking density also occurred affecting the gel's ability to retain water and causing a decrease in the swelling capacity, as shown by the profile's decrease after 24 hours.

4.4.1.3 Rheology characterization

The bulk mechanical properties of scaffolds based on Formulation 4 were also investigated by rheological measurements. This time, the dynamics of the crosslinking process were recorded and compared to the ones shown using Formulation 2.

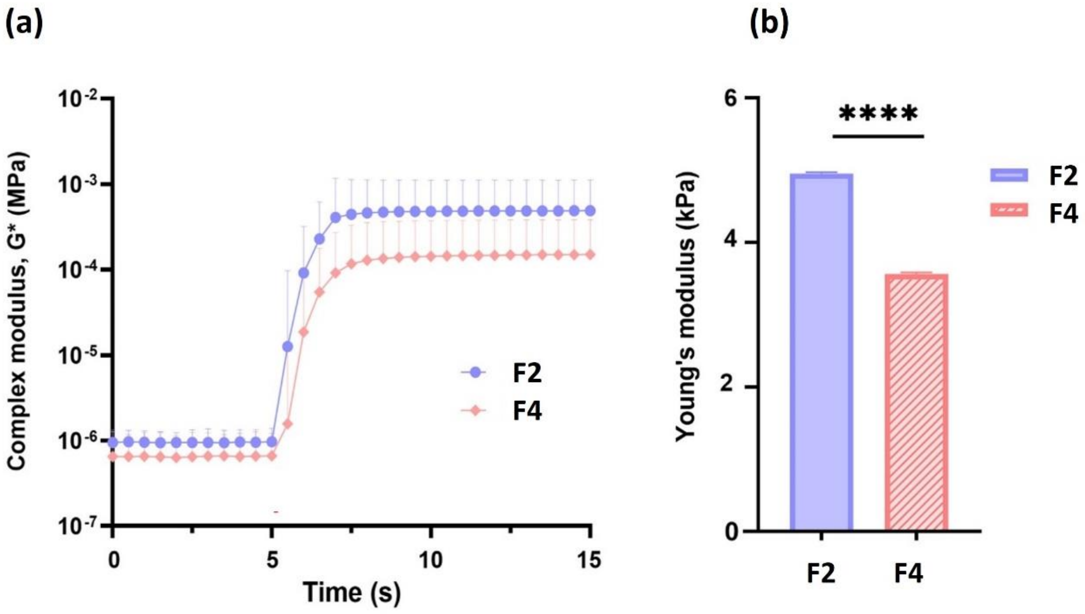

Figure 4.18. Rheology study. (a) Complex Modulus G* (MPa) curves registered during the real-time crosslinking process for Formulation 2 (violet) and Formulation 4 (pink). **(b)** Young Modulus values were obtained for in-situ polymerization tests (Formulation 2 (violet, n=4), Formulation 4 (pink, n=5)). In all graphs, values are presented as mean ± SD. T-test performed. $p < 0.05$. (p-value = 0.0001 (****)).

Under identical testing conditions, Formulation 2 enhanced a higher complex modulus G* compared to Formulation 4, which is translated to statistically significant higher Young's Modulus values, 4954 Pa ± 1015 and 3565 Pa ± 1596, respectively (Figure 4.18-b), probably due to the higher N-pullulan and PEG-Link concentrations.[321]

For both compositions, the Complex Modulus G* was calculated from the values of the Storage G' and Loss Modulus G'' derived as a function of the strain. Consequently, the Young Modulus E was obtained by assuming a Poisson's coefficient of 0.5.

Despite the differences in terms of formulations' composition, due to the different crosslinkers and the presence of the RGD peptide, the complex Modulus curves described for both polymers are very similar in shape, with resulting Young's Modulus values (4954 Pa ± 1015 and 3565 Pa ± 1596) comparable to other soft gels used in skin tissue engineering[322] (0.5 – 12 kPa for acellular collagen scaffolds).[318] Understanding the gels' mechanical properties is a pivotal point since it has an impact on cells contained within the matrix as well as the cells growing on top and thereupon on the skin repair process.

4.4.2. Encapsulation and cell viability studies of Hs-27 cells.

Once established the adequacy of Formulation 4- based gels to be photocrosslinked, presenting a well-defined structure and expressing mechanical properties comparable to other biocompatible materials normally used in skin regeneration, the feasibility of supporting cells embedded within the scaffolds was also evaluated.

Again, Hs-27 cells were considered for this purpose. The cell viability was evaluated over time, 1 day, 3-, and 7 days post encapsulation through live & dead assays. Hydrogels were crosslinked using both 22 mW and 30 mW, to elucidate the influence of the working power on the cell's behavior.

On day 1, 88% and 90 % of the cells were alive, respectively for 22 mW and 30 mW, demonstrating the no-cytotoxicity of the gel matrix. Moreover, as represented by the staining in Figure 4.19-a, fibroblasts were uniformly distributed along the gel's thickness. On day 3, evident cell protrusions were appreciated, proving that the presence of the cell-degradable peptide induced fibroblasts growth.

No significant differences in terms of cellular viability were registered, at this time point, independently of the working conditions used for encapsulation (22 mW and 30 mW) (Figure 4.19-c). The cellular behavior radically changed on day 7. Although the fibroblast elongation was easily observed, a decrease in the living cells percentage was detected, reaching 75% (22 mW) and 70 % (30 mW), respectively.

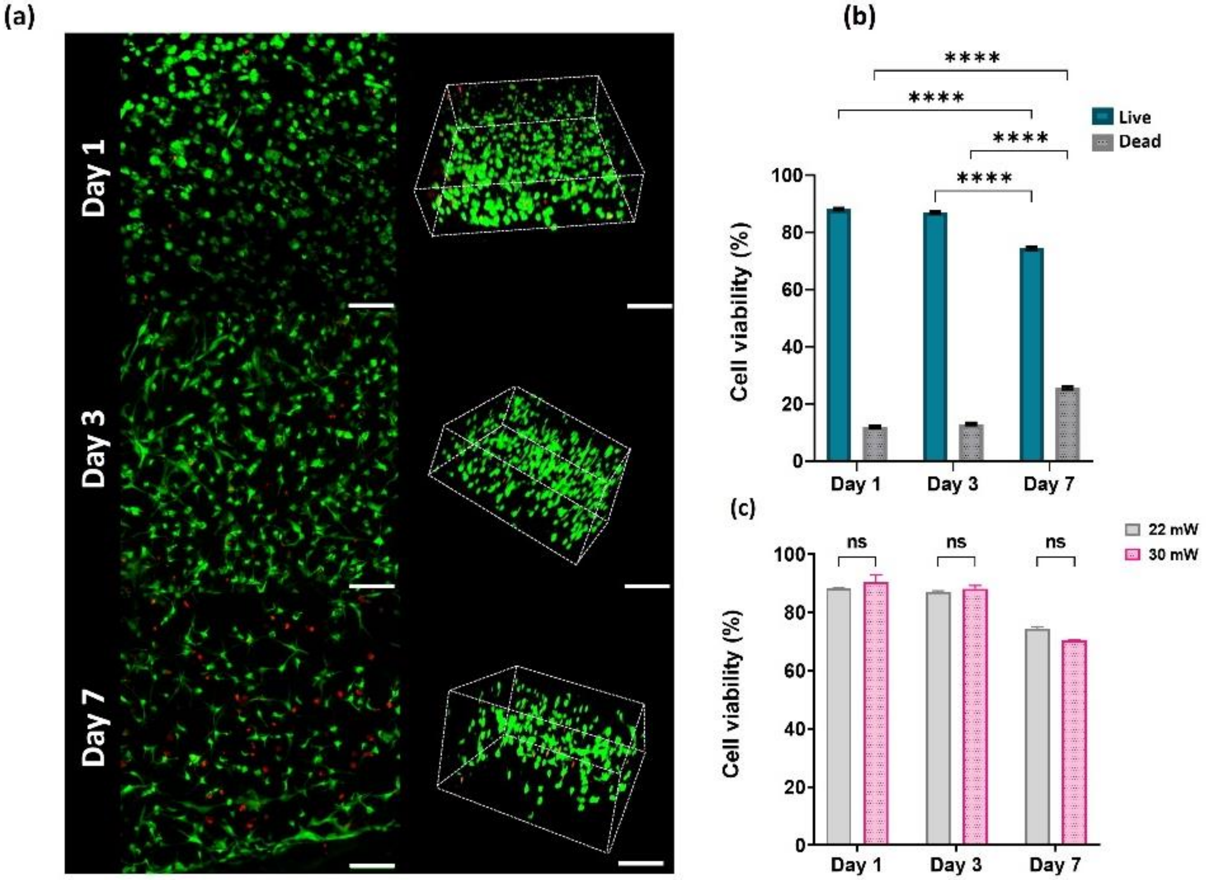

Figure 4.19. Live & dead assay. Hs-27 viability within RGD-N-PLN: CD-Hy Link hydrogels (Formulation 4). **(a)** Maximum projections of merged channels- left panels- and 3D reconstructions of representative samples fabricated with a power of 22 mW, respectively at days 1, 3, and 7 post encapsulations. Scale bars = 100 µm. Cell viability quantification within **(b)** hydrogels crosslinked with 22 mW of power (live cells-light blue; dead cells- grey). **(c)** Comparison of cell viability values obtained using 22 mW (grey bars) and 30 mW (pink bars). Values are shown as the mean ± SEM (n = 2 per each condition). A two-way ANOVA test was performed, $p < 0.05$. (p-value = 0.0001, (****)). N= 2 independent experiments.

The slight difference between the two fabrication conditions indicates that a lower power dosage corresponds to a higher number of alive cells upon time (7 days). Hence, based on these considerations, the lower power (22 mW) was selected for further experiments involving fibroblasts' encapsulation, guaranteeing higher cell viability.

The live and dead assay demonstrated the suitability of Formulation 4- based gels, not only to support fibroblast encapsulation but also to promote their elongation and spreading within the scaffold matrix, overcoming the issues faced up until this moment, with the previous polymer composition. Once established the appropriateness of this gel composition, additional studies were performed, to better investigate the Hs-27 growth.

4.4.3. Formulation 4- based hydrogels to sustain the dermal construct

The cell viability assay revealed the great potential of Formulation 4 to sustain the formation of a proper dermal construct, toward a full-thickness complex model. For the first time, starting from day 3 post-encapsulation, Hs-27 fibroblasts enhance their elongation within the scaffolds. Considering this evidence, an immunofluorescence study was required to investigate the cells' development through the expression of the most representative cell markers.

Different scaffolds fabricated with the same protocol described above (using 22 mW) were fixed and then stained at different time points. Vimentin was chosen as the cytoskeleton marker, and its signal, here reported in green (Figure 4.20), was largely exhibited on day 4, where the fibroblasts manifested a strong elongation along the cell-laden scaffolds and started to form a network within the matrix.

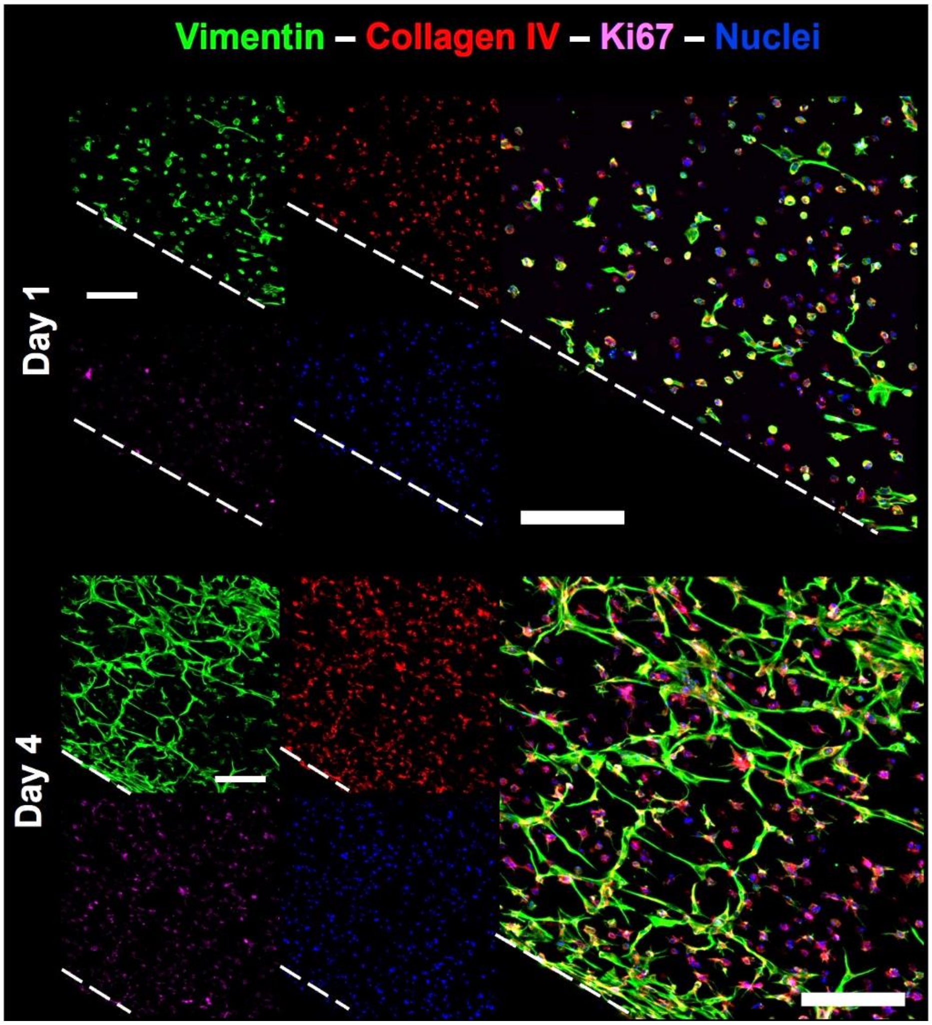

Figure 4.20. Immunofluorescence study on dermal compartment. Top view magnification of cell-laden hydrogels based on Formulation 4, on day 1 (upper panel) and day 4 (lower panel) post-encapsulation. Immunofluorescence study of specific markers, Vimentin (green), Ki67 (magenta), Collagen IV (red). Nuclei stained in blue. Dashed lines mark the edges of the hydrogels. Scale bar = 200 µm (top), scale bar = 100 µm (bottom).

A proliferative cell marker, Ki67 (magenta), was also shown at earlier time points (day 1) becoming more evident over time (day 4) proving the proliferative capacity of cells encapsulated within Formulation 4-based gels.

The presence of collagen, which makes up around 80% of our skin,[323] was also revealed in this study. Specifically, we used collagen IV, as it is secreted by fibroblasts, and is also present in the basal lamina.[21,22] Its expression, (red signal) was already observed from day 1, becoming more visible on day 4, especially in the cells' surroundings. Collagen plays an important role, since it has many benefits on the skin, keeping it firm, plump, and supple, contributing to mechanical properties, organization, and shape of tissues.[324]

These results not only confirm the appropriateness of the polymer composition, but they also validate the 3D-bioprinting system, and the working parameters used to develop this dermal model, building the foundations to evolve a full-thickness system.

4.4.4. Formulation 4- based gels recreate the epidermal compartment: moving towards a full-thickness skin model

The development of a dermal counterpart able to support the formation of an intricate human fibroblast network represents the starting point for establishing a robust epidermal construct on top. The cell-laden scaffolds were first mounted within Transwell® inserts, right after the photopolymerization, and kept in submerged conditions for 3 days to swell and permit the fibroblasts to spread within the matrix. Then, a cell suspension of HaCaT cells (6 x 10^6 cells/cm^2) was seeded on top of the gels in a drop-like manner and left for 2h to allow the proper cell attachment. Later, the apical cavity of the insert was filled with the corresponding culture medium. To get an even distribution of keratinocytes, the entire constructs must be maintained in submerged condition for 7 days. Posterior to this period, (ALI) conditions were applied as illustrated in Figure 4.21, to raise keratinocytes' growth and later their stratification. The method presented allowed the creation of the first attempt at a full-thickness skin model, in which a dermal layer, composed of human dermal fibroblasts embedded in a biocompatible extracellular matrix, and an epidermal compartment represented by human keratinocytes, were distinguishable. The cells' arrangement within and on top of the hydrogels was studied by immunofluorescence, at different time points, to monitor the cells' expansion, growth, and evolution over time. For this study, some samples were fixed 14 days post-HaCaT seeding, (1 week under submerged conditions + 1 week under ALI conditions), and later stained. To check the dermal compartment, vimentin, and collagen IV markers were again selected and compared with previous staining. In the case of the epidermal layer, keratin 10 and keratin 14 were employed.

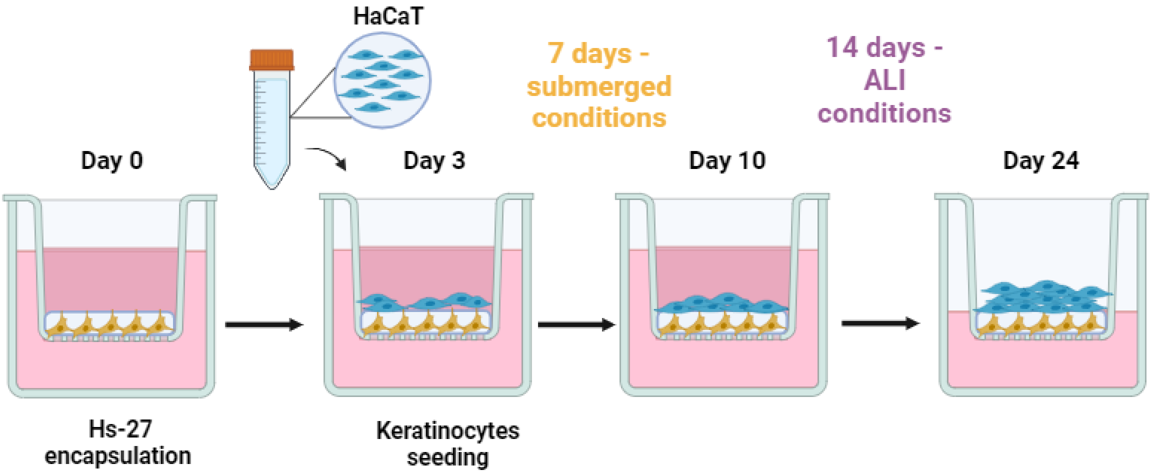

Figure 4.21. Schematic representation of the co-culture protocol (Biorender software). Hydrogels with human dermal fibroblasts-Hs-27- mounting within Transwell® insert (day 0). Human immortalized keratinocytes -HaCaT- seeding on top of cell-laden hydrogels (day 3). After 7 days of submerged culture, (day 10), Air-liquid-Interface (ALI) conditions were applied, for 14 days up to day 24.

The immunofluorescence study highlighted the beginning of the formation of a promising full-thickness model. As reported in Figure 4.22, the constructs revealed how a progress establishment of the epidermal layer was taking place. A homogeneous dermal construct was observable underneath the epidermis, which was marked by keratin 10 and keratin 14.

The vimentin signal (green) points out the spreading of human fibroblasts within the gel matrix. Collagen IV enhances the potentiality of the co-culture system to secrete this protein, demonstrating how the co-presence of fibroblasts and keratinocytes may increase the amount of protein secreted. Keratin 10 and keratin 14 signals were instead localized in the cytoplasm of epidermal keratinocytes, respectively in the suprabasal and basal layers. At this stage, both were well-expressed, indicating that HaCaT cells may potentially be suitable to reproduce the *in vivo* situation, by applying such specific culture conditions. Hence, it was proved that Formulation 4 was a good option to resemble not only the dermal structure but favoring the formation of the epidermis on top, showing a regular expression of particular markers for its basal layers.

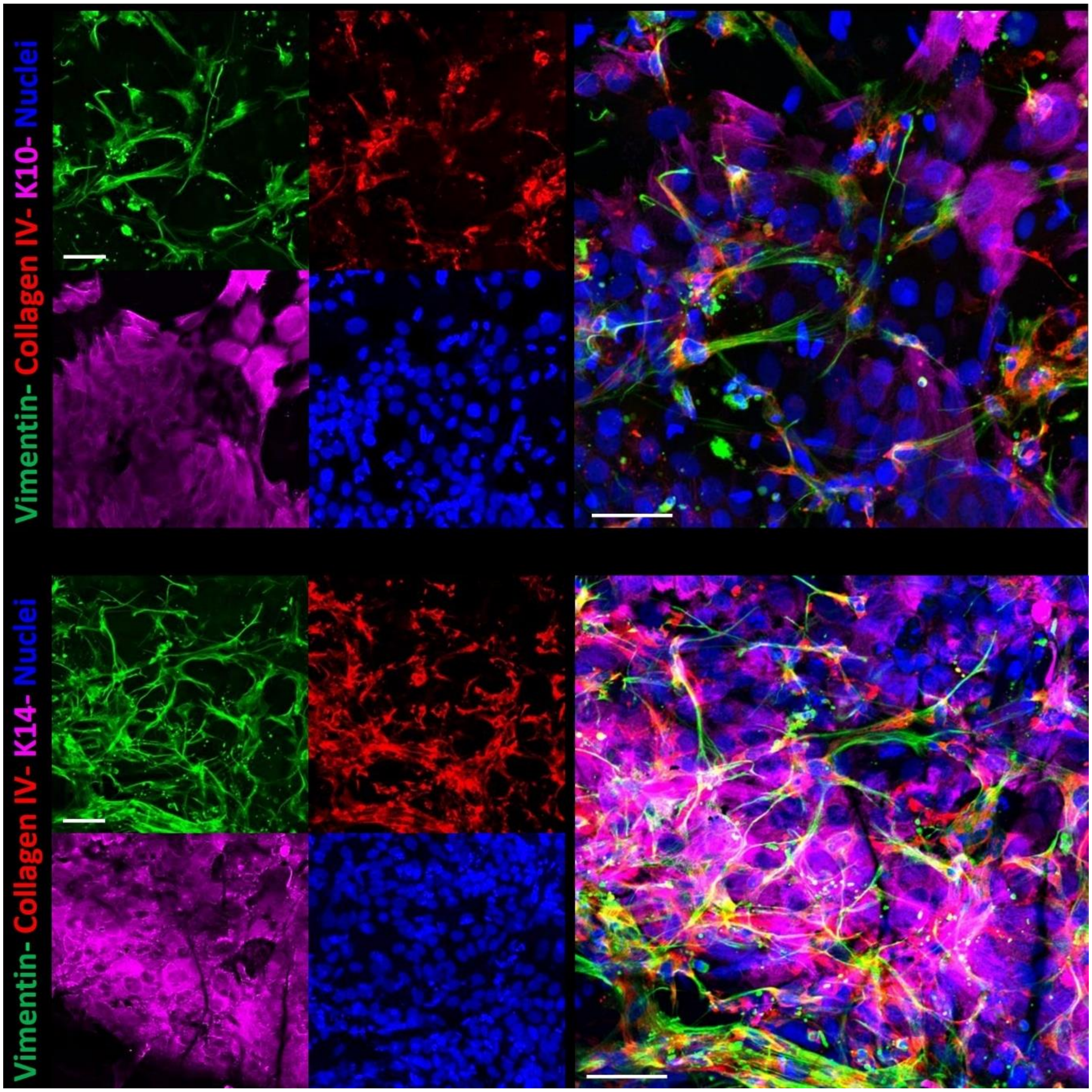

Figure 4.22. Effects of 1 week of ALI conditions on the co-culture (Hs-27/HaCaT) systems. Top view maximum projections of co-culture systems (Hs-27/ HaCaT) 14 days post-HaCaT seeding. Vimentin (green) and collagen IV (red) stained human fibroblasts; Keratin 10- K10 (magenta)- upper panel and Keratin 14- K14 (magenta)- lower panel-stained keratinocytes. DAPI (blue) stained nuclei. Scale bars = 50 µm

To better distinguish the interconnections between the epidermis and dermis, immunofluorescence tests were also performed on the gels' cross sections. For this purpose, part of the hydrogels was manually cut with a scalpel and flipped to take Z-stack pictures. As reported in Figure 4.23, cross-sections revealed the crosstalk between human fibroblasts and human keratinocytes. Vimentin signal showed how the protruded fibroblasts were in direct contact with keratinocytes growing on top. Collagen IV expression was also exhibited, showing both a dense signal in the top layers, due to its presence in the basal lamina, and being visible within the whole gel matrix.

Keratin 14 signal (magenta) also underlined a compact monolayer on top of the gel, identifying intricate connections between the summit of the scaffolds and the dermis underneath.

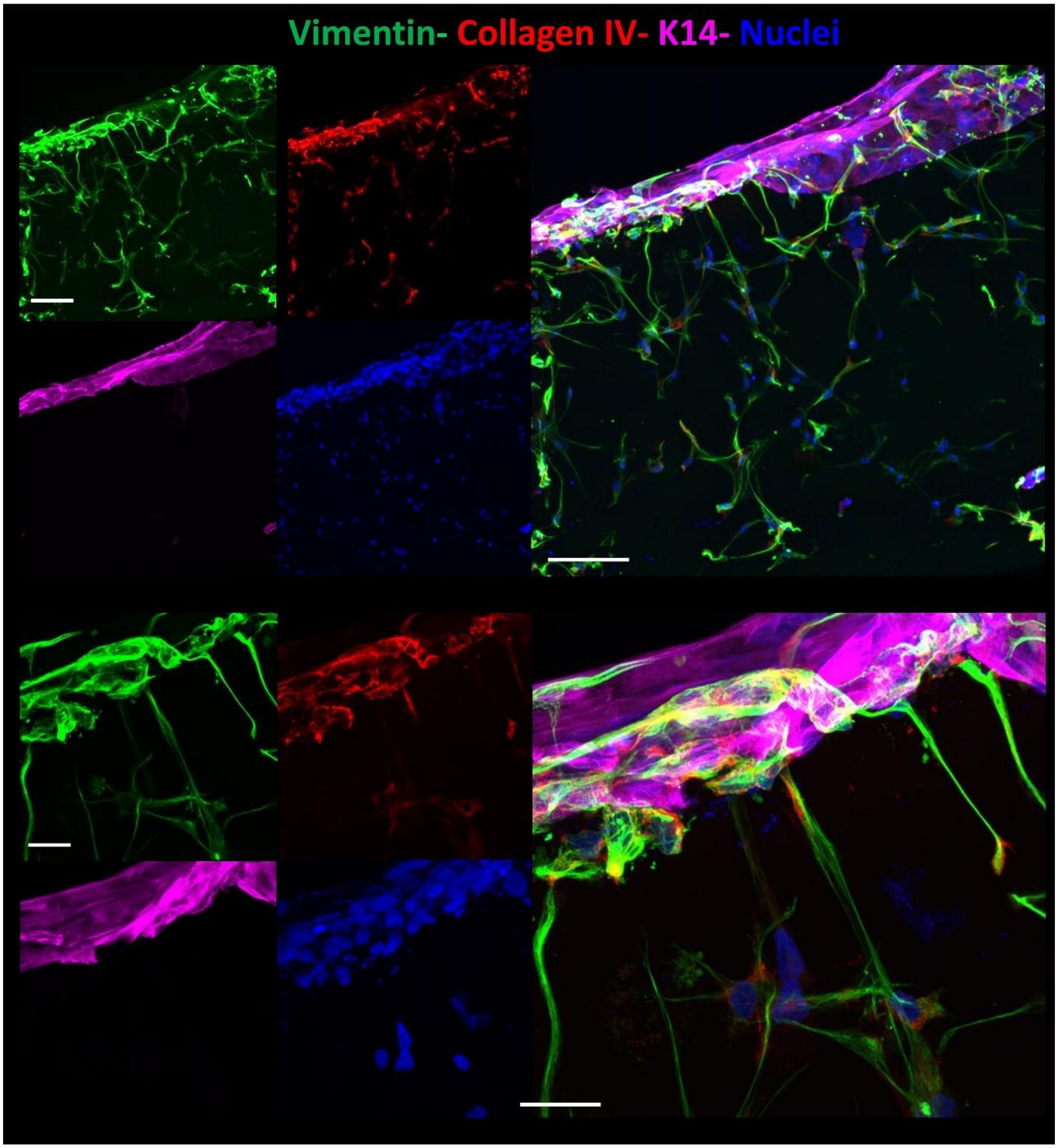

Figure 4.23. Effects of 1 week of ALI conditions on the co-culture (Hs-27/HaCaT) systems- cross-section views. Immunostaining of the cross-section views, respectively with lower (top panel) and higher (bottom panel) magnification, 14 days post-HaCaT seeding. Vimentin (green), collagen IV (red), keratin 14 (magenta), DAPI stained nuclei. Scale bar = 100 µm (top panel); Scale bar = 25 µm (bottom panel).

The construct development was investigated at a longer culture time, comparing how the different co-culture conditions were affecting the cells' behavior and their expansion. Distinct scaffolds were kept for 24 days in culture. For some of them, ALI conditions were applied on day 10, and kept until day 24 (14 days ALI); instead, other constructs were kept under submerged conditions for the entire period (Figure 4.24).

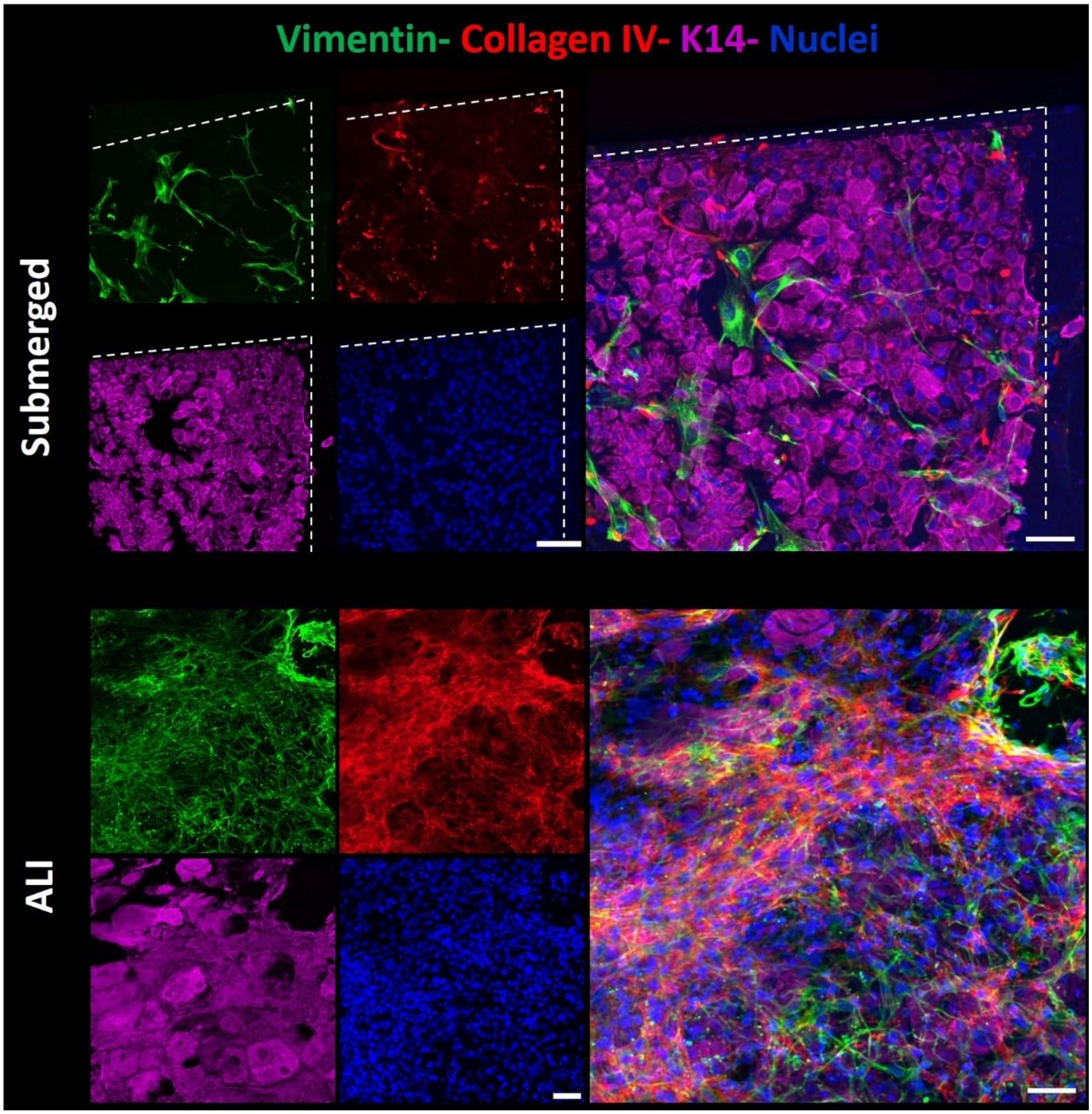

Figure 4.24. Effects of 2 weeks of submerged vs. 2 weeks of ALI conditions on the co-culture (Hs-27/HaCaT) systems. Top-view maximum projections of co-culture systems under distinct culture conditions after 24 days. **Top panel**- 21 days under submerged, **bottom panel**- 7 days under submerged conditions, and 2 weeks under ALI conditions. Vimentin (green), collagen IV (red), keratin 14 (magenta). DAPI (blue) stained nuclei. Single channels on the left, merged channels on the right of the respective panels. Dashed lines represent the edges of the hydrogels. Scale bars = 100 µm.

At long culture time points, the distinct working conditions were drastically impacting the scaffold's development. In Figure 4.24, the comparative study between the top-view maximum projections pointed in an obvious manner to the influence of the single conditions on the co-culture constructs.

For instance, considering both the vimentin and the collagen IV signals, respectively in green and red, a filamentous and fragmented expression was appreciated for the submerged conditions, highlighting a reduced number of cell connections within the matrix. Fibroblasts were elongated as they normally are within this gel composition and showed their capability to express and secrete collagen IV.

However, the situation seriously changed when ALI conditions were applied for two weeks. As expected from early culture time points analyzed, Hs-27 fibroblasts together with HaCaT cells created an intricate structure, as enhanced by the vimentin and keratin 14 expressions. The hydrogel extracellular matrix appeared compacted, with cells expanded and spread along the entire thickness. Also, there was an increase in the collagen IV expression, making an entangled structure inside the gels. Regarding the keratin 14 expression, a huge difference was observed.

Although in the upper panel-submerged conditions-, the protein signal was recognized (magenta), indicating the formation of a fleeting covering of the hydrogel's surface, single cells can be distinguished, since they were discontinuously attached, enhancing, sometimes, vacant spaces in between. On the other side, when ALI conditions were applied (bottom panel -Figure 4.24), a well-organized and more homogeneous HaCaT coverage was observed, also showing organized cell portions on top of the basal monolayer. Comparing the merged channels' views, the influence of ALI conditions was more evident. The well-established network was remarked, showing a close-packed skin model.

Rather, under submerged conditions, the merged channels picture did not reveal the dense structure, even manifesting a weak monolayer, from which the underneath dermis was penetrating. Besides these trials, further investigations were performed keeping both culture conditions, to better understand their impact on the formation of the skin construct. Moreover, the small dimensions of these gels make them difficult to handle, so several replicas were necessary, especially when cross-sections were analyzed.

Gels' cross-sections were investigated to get a wide overview of the close contacts between the dermal fibroblasts and the epidermis above. With this aim, new hydrogels were first half-cut and flipped to take pictures. As reported in Figure 4.25, all the markers appeared well expressed, either in submerged or under ALI conditions, proving the efficiency of the gels' composition to provide an adequate cell-friendly microenvironment.

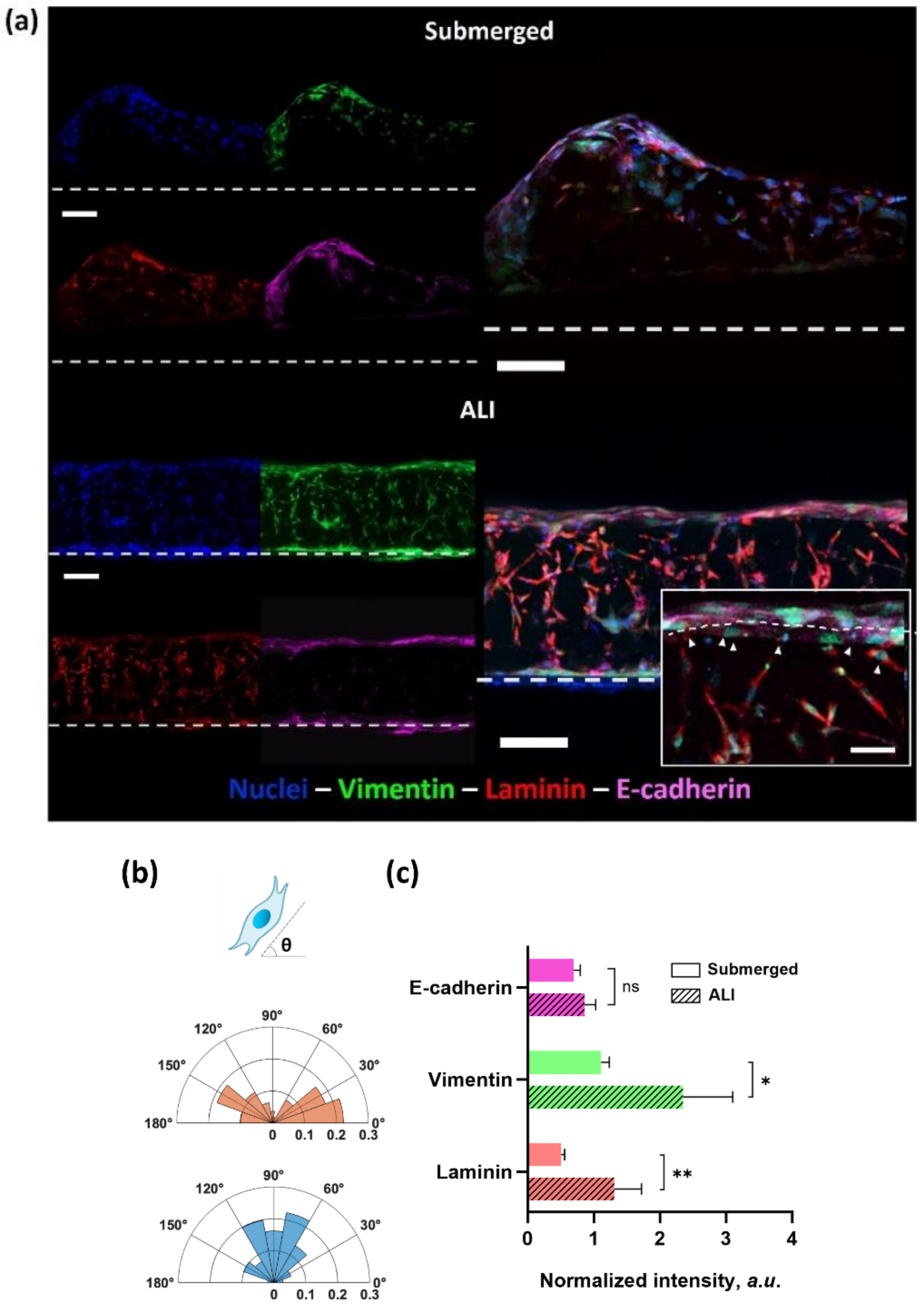

Figure 4.25. Effect of the co-culture conditions on full-thickness scaffolds. (a) Cross sections of immunofluorescence staining of constructs 24 days post-fibroblasts encapsulation. Nuclei (blue), vimentin (green), laminin (red), and e-cadherin (magenta), for submerged and ALI conditions (top and bottom, respectively). Dashed lines refer to the PET membranes (hydrogels' support). Inset shows a detailed view of the interaction of the fibroblasts with the keratinocytes on the basement layer. Scale bar = 25 µm. **(b)** Nuclei orientation between submerged (orange) and ALI (blue) conditions. **(c)** Quantitative analysis of the markers' expression for both submerged and ALI conditions. Values, normalized, are shown as mean +/- SD (n = 3). * p = 0.0283; ** p = 0.0495. Scale bars = 100 µm. Adapted from Cirulli et al.[325]

However, by analyzing the z-stack projections, it appeared quite evident that ALI conditions improve the cells' performance. The vimentin expression enhanced how under submerged conditions, the marker was mostly confined to the top layers, resulting in less expressed in the middle part of the constructs or underneath.

Furthermore, in the ALI-referred pictures, the cells' arrangement manifested a different disposition, underlining how cells distributed on the apical layers were strictly in contact with the cells located underneath in the dermis compartment, until the bottom of the gels. As reported in Figure 4.25-b, from the plots of nuclei orientation between submerged and ALI conditions, it was evident how under the ALI regime, a higher distribution of nuclei was oriented between $60^o < \Theta < 120^o$ with the surface.

It is well-known that epidermal-dermal communication through the basement membrane plays an important role in skin homeostasis. One of the key components of this membrane is surely the laminin, essential for epidermal attachment and fundamental to enhancing the recovery of damaged skin. It also provides a stable attachment, translatable into an intact basement membrane at the epidermal-dermal junctions[326]. With this scope, laminin was also investigated during these studies. Its expression was compared between the two situations, with a significantly higher expression when ALI conditions were applied, as well as for the vimentin expression, resulting in 2.1- and 2.6-fold higher, respectively (Figure 4.25-c). Moreover, a reticulate structure was well-recognized under ALI.

The epithelial cadherin (e-cadherin) was selected as an adherence junction protein. This protein is part of the cadherins superfamily, which are transmembrane or membrane-associated glycoproteins that mediate Ca^{2+}-dependent cell-cell adhesion and are well-recognized for their important role during the morphogenesis of many organs.[327,328] Even if for both circumstances the e-cadherin (magenta) was well exhibited, without significant differences (as emerged from the quantification analysis) (Figure 4.25-c), less compactness was visualized under submerged conditions, where a fragmented signal trend was noticed. Vice versa, under ALI a continuous cell tendency was appreciated on the apical side, proving the advantages of this condition to promote a monolayer establishment.

4.4.5. Skin compartmentalization

4.4.5.1 Dermis construct

Establishing a proper full-thickness skin model counts on the proper formation of dermal and epidermal counterparts. The current available full-thickness models, as reported in the literature, show several limitations, being suitable just for short-period studies including non-human extracellular matrix components or presenting a weak skin barrier function.[312]

In our work, we tried to overcome this limitation by designing a dermal construct in which Hs-27 fibroblasts were encapsulated within a biocompatible extracellular matrix based on Formulation 4 (RGD-N-PLN: CD-Hy Link) and applying different co-culture approaches. After 24 days post fibroblast encapsulation, our scaffolds showed peculiar markers' expressions, demonstrating the suitability of the polymer composition to sustain the extracellular matrix-containing cells for a long period, regardless of the co-culture environments.

Again, a comparative study of submerged versus ALI conditions was conducted to better understand the cells' behavior in relationship to the external conditions. As in the previous trials, vimentin and collagen IV markers were selected, together with a new protein: fibronectin. Besides being one of the fundamental components of the dermis, fibronectin is one of the major constituents in the provisional matrix assembled during the process of repairing skin wounds.[329] This protein is assembled in a cell-driven process into a complex and fibrillar network[330], and its fibrils are necessary to form scaffolds for other ECM proteins, for example, collagen and proteoglycans.[331,332] At the same time, fibronectin is a key substrate for keratinocytes to migrate and re-epithelialize the wound gap in the epidermis.[333] Due to its functionalities, it was a must to investigate its expression. Fibrillar structures (green signal) were identified both under the submerged conditions - top panel- and under ALI- bottom panel, (Figure 4.26-a-b). However, a more convoluted fibril grid was formed in the matrix where ALI was applied, supported by the higher expression, as depicted in Figure 4.26-b. Also, vimentin and collagen IV signals showed a more entangled mesh compared to submerged conditions, although their expressions were not significantly different (4.26-b). All the results proved the importance of endeavoring separate settings before electing the favorable one.

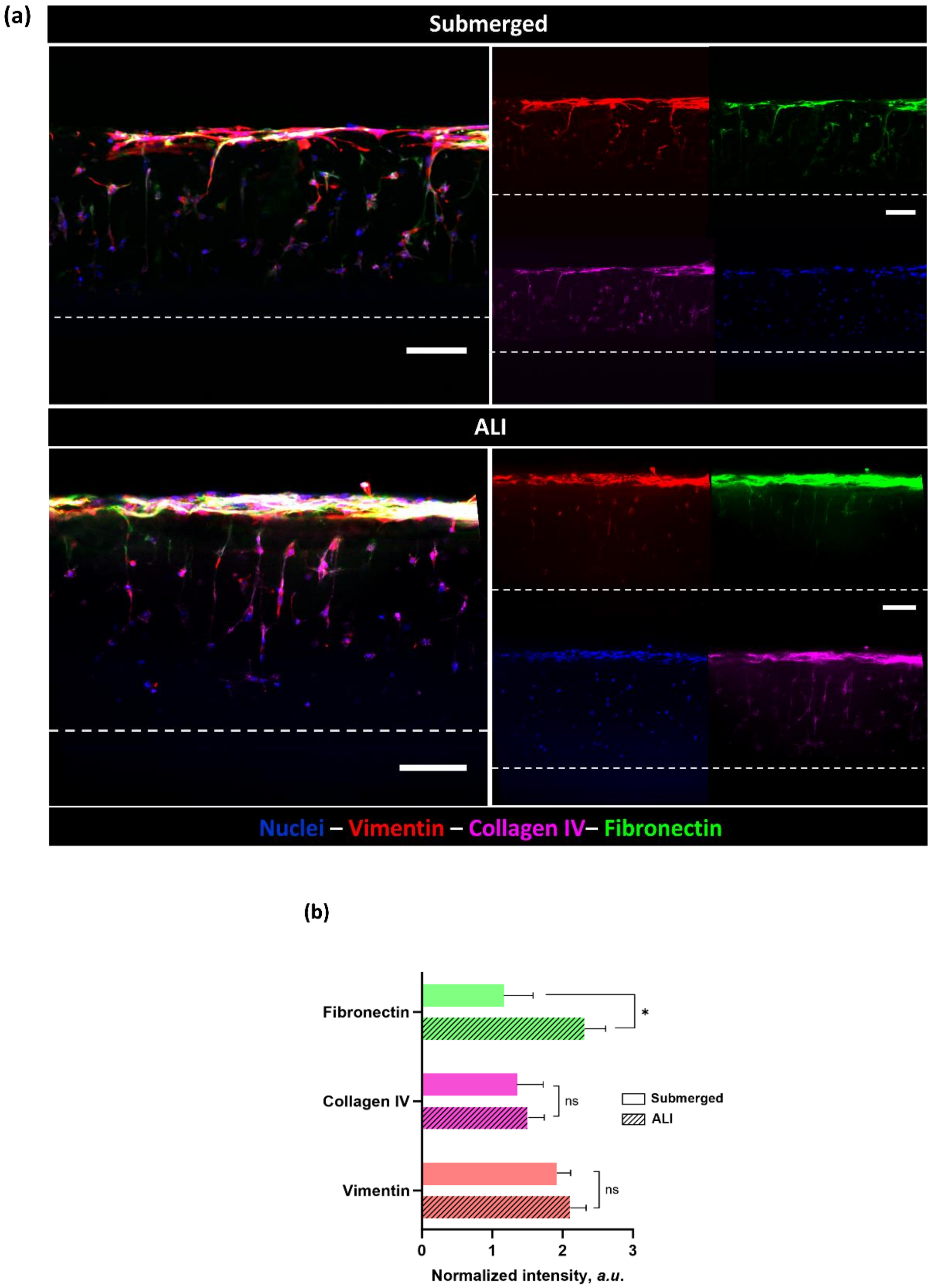

Figure 4.26. Effect of the co-culture conditions on the dermal compartment. Top panel- construct view under submerged conditions; Bottom panel -construct view under ALI conditions. Dermal fibroblast markers: Collagen IV (magenta), Fibronectin (green), Vimentin (red). DAPI stained nuclei. Single channels-left merged channels- right. Scale bars = 100 µm. **(b)** Quantification of the expression of the different markers for both submerged and ALI conditions. Values, normalized, are shown as mean +/- SD (n = 3). * p = 0.0311. Adapted from Cirulli et al.[325]

4.4.5.2. Epidermis construct

Once corroborated the dermis was formed under distinct environmental surroundings, validating the expression of the most significative cells' markers, the epidermal compartment was also evaluated through an exhaustive study. Together with the comparative immunofluorescence assay, meaningful especially to appreciate the impact of the air exposure on the monolayer stratification and differentiation, largely discussed in the literature, the integrity barrier was also examined.

First, an overview of the epidermis cross-sections, with Transepithelial electrical resistance measurements of the barrier created by keratinocytes on top of the hydrogels' matrix was furnished. From the dermis structure evaluation, it was demonstrated that the formation of the basement membrane occurred, as enhanced by laminin expression. So, the development of the basal layer of the epidermis was verified by two specific markers, keratin 14, and e-cadherin. Keratin 14 is an intermediate filament protein that provides structural support in the basal layer of the epidermis,[334] and is highly specific for basal proliferative keratinocytes together with keratin 5; in contrast, keratin 1, and keratin 10, are normally used to mark the keratinocytes in the early differentiation stage.[335]

Briefly, skin development is not only regulated at the keratinocyte level but also requires coordination among multiple cells. Hence, thanks to adhesion proteins, which include adherence junctions, tight junctions, and desmosomes, communications among the epithelial cells can be established, as well as cells and mesenchyme. [336,337] In particular, the adherence junctions are formed by transmembrane cadherin family proteins, and e-cadherin represents the one that makes up most adherence junctions, playing an important role in skin development regulation.[337]

Therefore, both markers' expression was explored, showing an evident and well-distributed signal, independently of the conditions applied (Figure 4.27-a). Keratin 14 expression enhanced the basal layer generation. Even though the quantification study (Figure 4.27-b) did not reveal significant variations under the two distinct conditions, a more compact and continuous keratinocyte structure was appreciated under ALI. E-cadherin denoted establishing the adherence junctions between the cells, appearing denser when applying ALI conditions. However, as it was visible from the f-actin signal, which stained both the epidermis cells and the fibroblasts underneath, tangible connections between the two cell lines were better appreciated under ALI. A well-resembled structure was defined in these conditions, guaranteeing a clean-cut crosstalk, as it was observable in the *in vivo* systems.

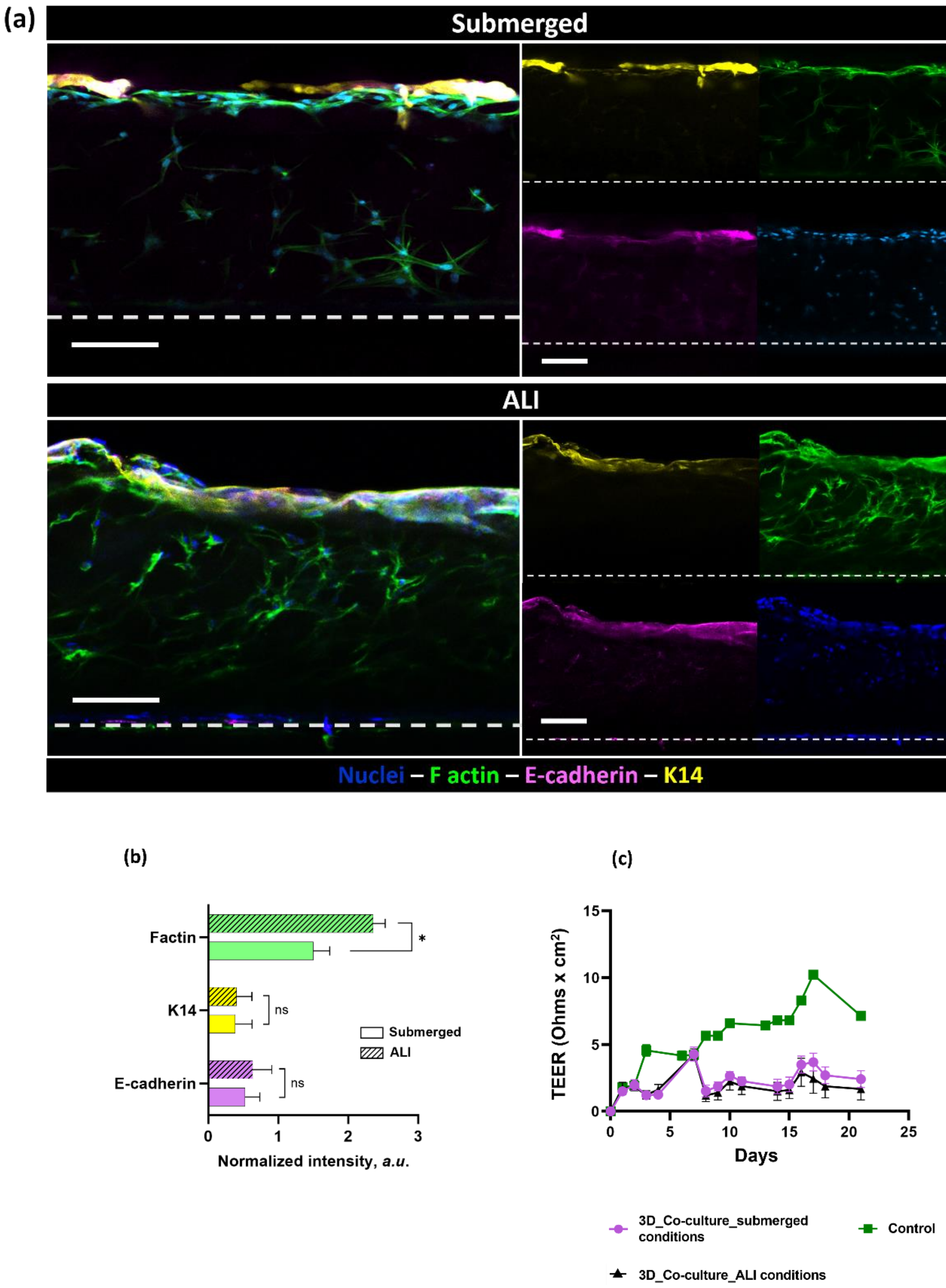

Figure 4.27. Effect of the co-culture conditions on the epidermal compartment. (a) Cross-sectional views of full-thickness skin models (Hs-27/HaCaT) after 24 days post-fabrication. Skin epidermis immunofluorescence study, under submerged- left panel- and under ALI conditions- right panel-. F-actin (green), e-cadherin (magenta), keratin 14 (yellow). Nuclei are stained blue. Scale bars = 100 µm. Dashed line marking the PET membranes (hydrogel's support). **(b)** Quantification of the expression of the different markers for both submerged and ALI conditions. Values, normalized, are shown as mean +/- SD (n = 3). * p = 0.0381. **(c)** Transepithelial electrical resistance (TEER) measurements of HaCaT barrier along 21 days post-seeding. Full-thickness constructs under submerged (dots, magenta) and ALI (triangle, black) conditions. HaCaT seeded on conventional Transwell ® inserts – control (squares, green). Values are reported as the mean +/- SEM (3 < n < 7). N=4 independent experiments. Adapted from Cirulli et al.[325]

Besides the adhesion junctions, tight junctions represent one of the focal aspects of interpreting the barrier integrity. Transepithelial electrical resistance (TEER) is the measurement of electrical resistance across a cellular monolayer; this reliable and non-invasive method allows us to confirm the integrity and permeability of the monolayer.[338]

TEER reflects the ionic conductance of the paracellular pathways in the epithelial monolayer, where the flux of non-electrolyte tracers, expressed by the coefficient of permeability, means both the paracellular water flow and the pore size of the tight junctions.[339] As reported in Figure 4.27-c, low values were registered throughout the entire experiment (21 days.) For the first 7 days under submerged conditions, all the constructs showed a lower tendency compared to the controls. After that, an imperceptible tendency of constructs under submerged conditions to rise was noticed. However, no significative differences were observed, between submerged and ALI conditions. Since the values varied in a range between 0- and 5- (Ω x cm^2), the first conclusion was that HaCaT cells present a scarce capacity to form strong tight junctions.[340] This evidence was also confirmed by the low values (up to 10 Ω x cm^2) recorded when the same cells were seeded on the conventional Transwell® inserts and not on top of our soft scaffolds, resulting in even lower values exhibited compared to other epithelial cells growing on a hard porous membrane.[341]

Indeed, with these studies, we proved the suitability of this polymer composition (Formulation 4) as the first eligible to develop an *in vitro* full-thickness skin model, in which dermal and epidermal compartments were distinguishable. Despite the soft nature of these gels, as displayed from the mechanical characterization conducted, good cell viability was proved, demonstrating the potentiality of the method used to photocrosslink the cell-laden scaffolds. The proper formation of a dermis structure was also guaranteed, in which human dermal fibroblasts were successfully supported and able to grow and spread, secreting collagen and fibronectin as they normally do in the *in vivo* systems. A proper basement membrane can also be recognized during the skin models resembling, as manifested by laminin expression. Although the limited capacity of the HaCaT cells to form tight junctions, a continuous monolayer on top of the hydrogels with embedded fibroblasts can be distinguished, even though different co-culture conditions were applied. An entangled mesh was also recognized from 14 days post-HaCaT seeding, enhancing an evident crosstalk between the intricate network formed in the extracellular matrix with the keratinocytes above. The epidermal substrate formation was defined by keratin 14, which appeared well-distributed, pointing out a proper establishment of the basal layer.

E-cadherin corroborated the presence of adherence junctions in between the monolayer; however, as aforementioned, tight junctions were not formed as proved also through the TEER measurements. The comparative study between the ALI and the submerged conditions underlined the greatness of the air-liquid interface circumstances which better promote the cells' interaction along the matrix's thickness and encourage the monolayer development. Overall, these results confirmed the potential of norbornene-pullulan-based bioinks as competitive models for *in vitro* studies, representing a valid alternative to collagen-based systems.

4.5. Interpenetrating network-based hydrogels system

4.5.1 Formulation 5: RGD-N-DEX: CD-Link: LAP +/- Agarose

In the previous section, the first approach on how to develop an epithelized-dermal *in vitro* model was largely discussed. Even though pullulan is a biocompatible material, well-known in tissue engineering, and widely used to resemble different tissues, the process of functionalizing norbornene-pullulan was not easy to handle, as described in the Materials and Methods section. Furthermore, the high purification cost of pullulan still represents an obstacle for large-scale experiments. On the other side, the model we developed in the previous section still has not reached the canons required for a full-thickness skin model. One of the main objectives of this thesis is to develop a hydrogel that faithfully mimics the native skin, presenting (i) reliable characteristics in terms of both mechanical properties and (ii) single-cellular-compartment maturation (either dermis or epidermis), (iii) reaching well-differentiated epidermis layer; requirements that can also be persecuted by increasing the samples' dimensions and area. Besides this consideration, in the evaluation of other potential options, the possibility of exploring a new class of polymer-based systems was raised. In particular, we focused on the Interpenetrating polymer network (IPN) systems, which gained visibility in recent years.

IPN systems are based on the combination of two polymers in network form, where at least one of them is synthesized and/or crosslinked in the presence of the other polymer.[342] One of the key points is that this combination of polymers must generate an advanced multi-component system with a new profile.[343] Currently, their use has drastically increased due to their non-toxicity, and biocompatibility.[344] In this framework, the choice of polymers for IPN formation was focused first on dextran, for its suitable characteristics. Dextran-based hydrogels have recently been used as cell culture scaffolds to promote neovascularization and skin regeneration in third-degree burn wounds.[345,346] Moreover, they seemed to accelerate the recruitment of the endothelial cells to the wound area, resulting in neovascularization just after a week of treatment.[346]

On the other side, IPN allows the development of hydrogels with reversible properties, by combining polymers with reverse properties. For instance, after photopolymerization, one of the components (not crosslinked) could be dissolved and removed, resulting in structures with more complex geometries.

As discussed in the introduction section, the selection was focused on low melting point (LMP) Agarose. The IPN systems here illustrated, consist of a removable Gel System 1 (based on Agarose) and a photocrosslinkable Gel System 2 (water-soluble polymers, such as dextran, with groups for orthogonal thiol-ene chemistry). Because dextran hydrogels lack cell-specific adhesion in nature, RGD-modified sequences were provided.[347] Gel System 2 was modified either by introducing RGD-peptide, allowing cells to adhere to the hydrogel matrix, or by including in the crosslinker the CD portion- which will permit cells to cleave the crosslinkers with matrix metalloproteases, promoting cellular spreading and motility, enhancing matrix remodeling.[320] The aim of exploring a new polymer formulation based on IPN was to gain more insights into the influence of these types of matrices on the mechanical properties of the resulting hydrogels and to explore more in detail the impact on the cellular growth and progression, compared to the single network system based on the same water-soluble polymer.

First, some preliminary tests were performed to evaluate the crosslinking and the optimal molar content of the different components. In this scenario, a pre-gel composition based on norbornene-dextran modified with RGD-motifs, together with a modified poly-ethylene glycol containing cell-degradable portions linker (CD-Link), was prepared as usual, to create -RGD-N-Dextran: CD-Link: LAP- (Formulation 5). First, different crosslinking molar contents between polymer/crosslinker (N-Dex/CD-Link), (Table 4.1) were explored. Hence, different powers were employed to photopolymerize the scaffolds and analyze the effects on the resulting structures.

Table 4.1 Combination tested for the preliminary fabrication tests, varying the crosslinking molar contents between polymer and crosslinker, exploring a power range of 13- 41 mW.

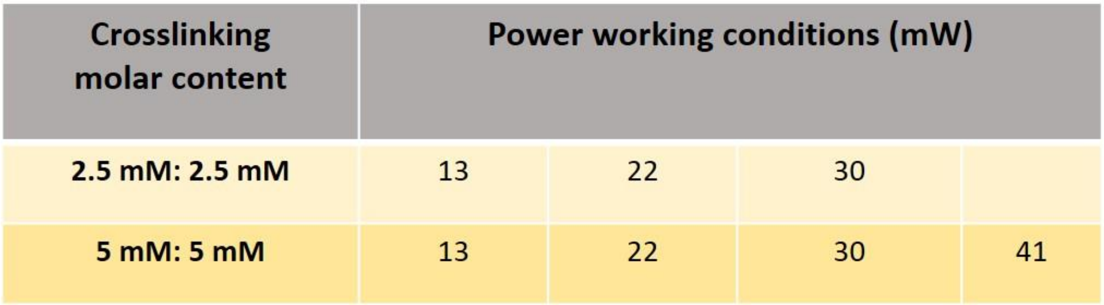

Crosslinking molar content	Power working conditions (mW)			
2.5 mM: 2.5 mM	13	22	30	
5 mM: 5 mM	13	22	30	41

As reported in Figure 4.28, the crosslinked structures produced with this new formulation were highly dependent on the molar content of the single components and the power used. At lower molar content (2.5 mM: 2.5 mM) no reproducibility in terms of gels' formation was observed, probably because we were in the crosslinking limit. In contrast, for higher molar content (5 mM: 5 mM), a strict dependence on the power was perceived, as deductible from Figure 4.28- lower panel-. The lower power conditions (13 mW and 22 mW) that we normally used to get hydrogel structures were insufficient this time to achieve a proper crosslinking of the gels. So, to be sure to obtain well-formed structures, it was necessary to increase the power to the allowed limit of our equipment, which corresponds to 41 mW.

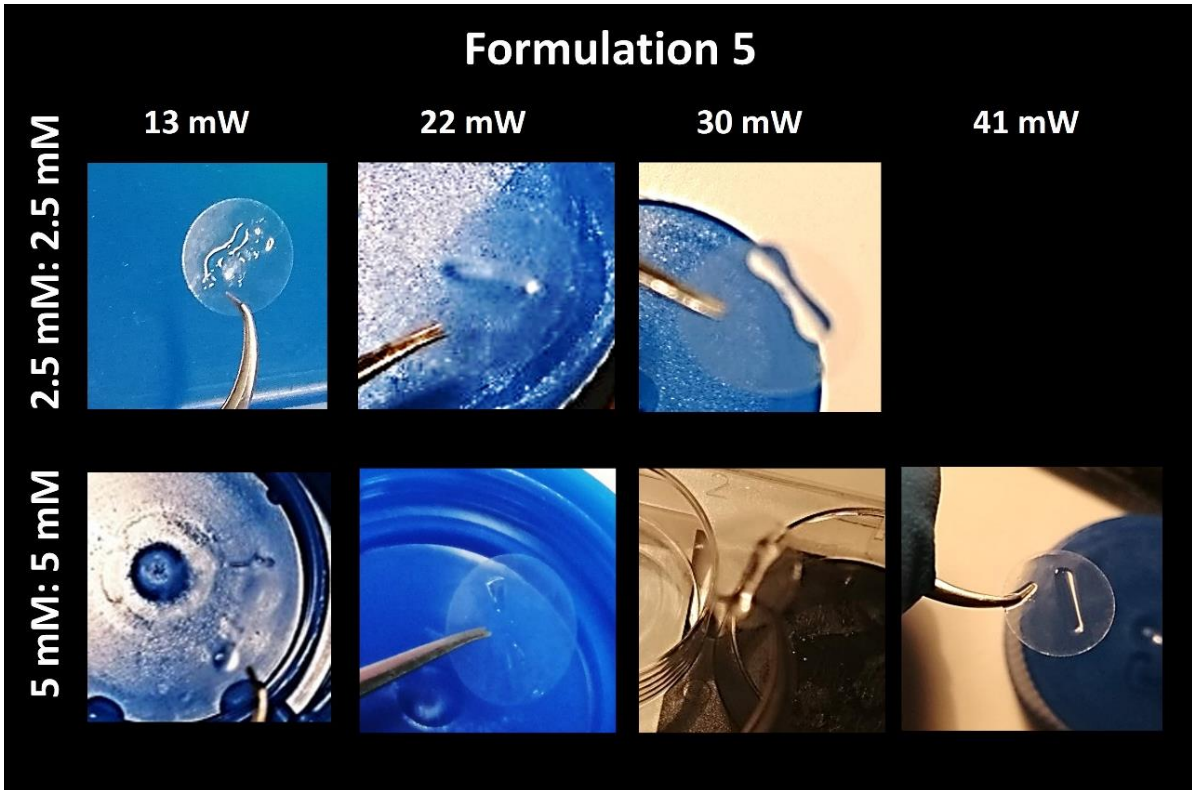

Figure 4.28. Printability tests. Examples of hydrogels based on RGD-N-Dex: CD- Link: LAP, with different molar contents between polymer and crosslinker (2.5 mM: 2.5 mM- upper-row- 5 mM: 5 mM – lower row-) and by varying the working power conditions in a range between 13 mW and 41 mW.

4.5.2. Swelling properties

As a first evaluation of the gels based on this new composition of interpenetrating network systems, the swelling behavior was evaluated, by printing scaffolds using the maximum power intensity (41 mW). Hydrogels only based on dextran (RGD-N-DEX: CD- Link: LAP – 0.5 mM: 5 mM: 5 mM: 0.5 mM) – Dextran formulation-, and hydrogels based on dextran + agarose (RGD-N-DEX: CD- Link: LAP + Agarose – 0.5 mM: 5 mM: 5 mM: 0.5 mM + 0.1 w/v %) -Agarose formulation-, were considered for this test.

In Figure 4.29 -a- it can be observed how the two compositions (+/- agarose) described a similar swelling profile over time. The volume increase peak was registered 24 hours post crosslinking, followed by a slight decrease, that reached the equilibrium after 48 hours, indicating that the presence of the agarose did not influence the gels' capacity to entrap water. Zooming into the first 5 hours (Figure 4.29-b) an overlap between the two compositions was noticed, up to 2 hours, followed by a modest decrease for the profile in the presence of the agarose.

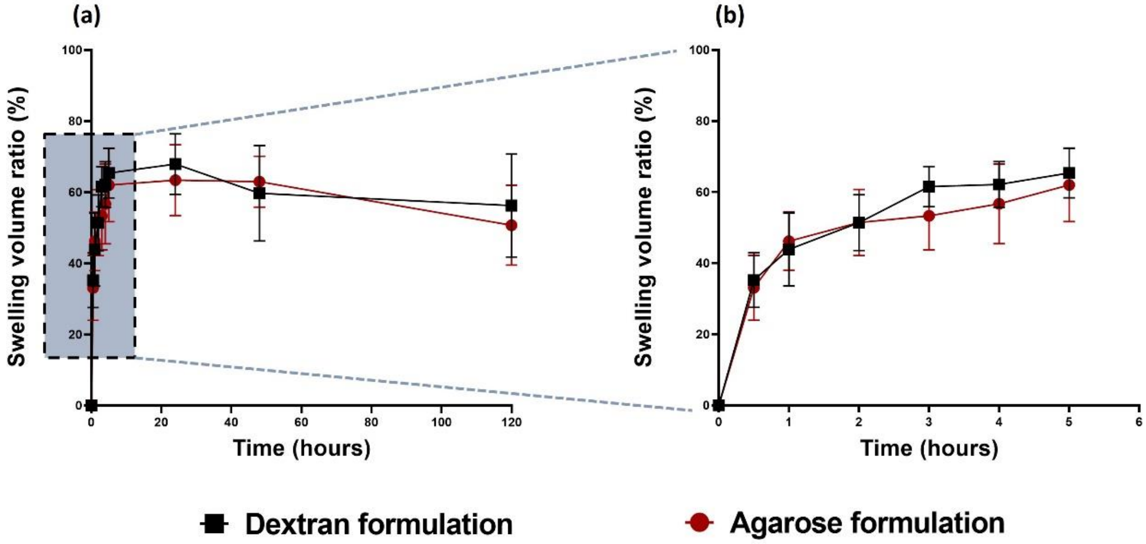

Figure 4.29. Swelling behavior. Volume swelling ratio for Dextran formulation (black squares) and Agarose formulation (red circles). **(a)** 120 hours post-fabrication. **(b)** Zooming of the swelling behavior in the first 5 hours post fabrication. Values are shown as the mean ± SEM (n = 4 per each condition).

4.5.3. Rheology characterization

The importance of examining the matrix elasticity resides in its influence on guide, for instance, stem cell differentiation, and extracellular matrix (ECM) deposition, which are necessary for tissue development and maintenance, influencing the wound healing process.[325]

In this contest, the bulk properties of the hydrogels based respectively on the single and interpenetrated network systems were evaluated through rheological measurements. As shown in Figure 4.30 slightly stiffer hydrogels (4 kPa - 5 kPa) were obtained, compared to the previous gels based on norbornene-pullulan polymer (and a different crosslinker) -Formulation 4 (3kPa- 4kPa), but still within the range of the soft gels used in bioengineering.

In particular, the presence of the agarose did not alter the elastic properties of the scaffold, resulting just in a slight reduction of the elastic modulus. Similar results were obtained by *Bachmann et al*[321], from rheological analysis conducted on PEG-link and dextran-based scaffolds (without norbornene) provided by the same supplier (Cellendes, GmbH, Germany) in which hydrogels stiffness was calibrated by varying the content polymer/crosslinker.

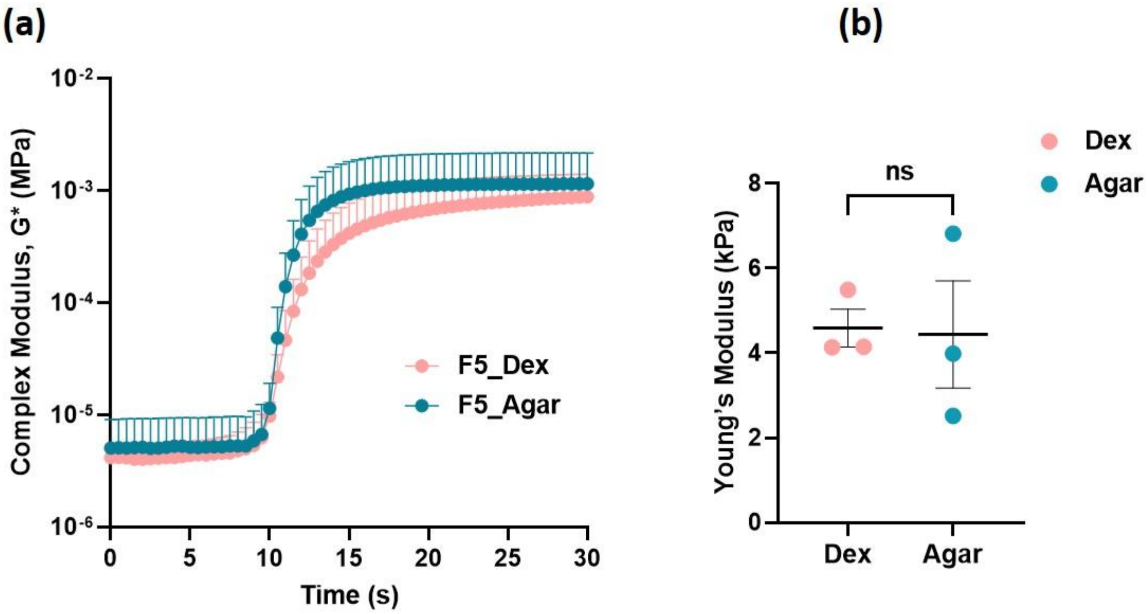

Figure 4.30. Rheology study. (a) Complex Modulus G* (MPa) curves registered during the real-time crosslinking process for Formulation 5- (Dextran only-pink) and (Dextran + Agarose- light blue). **(b)** Young's Modulus values of Dextran (-agarose) -based hydrogels (pink) and Agarose (Dextran + agarose) -based hydrogels (light blue) are calculated from the complex Modulus, derived from the Storage and Loss Modules as a function of the strain. Values are shown as the mean ± SD (a) and mean ± SEM (b) (n = 3 per each condition). T-test performed.

4.5.4. Analysis of the degradation of the scaffold mediated by the enzyme

The hydrogel integrity was also evaluated considering the enzymatic activity due to the presence of the cells that will be included in these systems. As a biocompatible polymer, dextran can be easily degraded by the action of dextranase which exists in human tissues.[348]Hence, mass degradation tests were run by using a 3D-Life Dextranase solution (D10-1; > 4000 units/ml, Cellendes, GmbH), at two different dilutions (1:20 and 1:200).

Figure 4.31 shows the degradation curves for both gels from Formulation 5. Despite the different conditions applied, the degradation rate of both gels' matrices occurred fast: for higher dextranase concentration (1:20) the entire process lasted 12 minutes, whereas, for lower enzymatic concentration (1:200), the total degradation of the gels occurred after 20 minutes. The presence of agarose did not have an impact on the process for both dilutions, showing an overlapping with the profile of dextran-only gels (single network) for higher enzyme concentrations (Figure 4.31-a). For lower concentrations of dextranase (Figure 4.31-b), a faster degradation was registered when agarose was included (interpenetrating network). This result was expected since the IPN system was designed to include agarose to create a more porous structure and facilitate cell arrangement within.

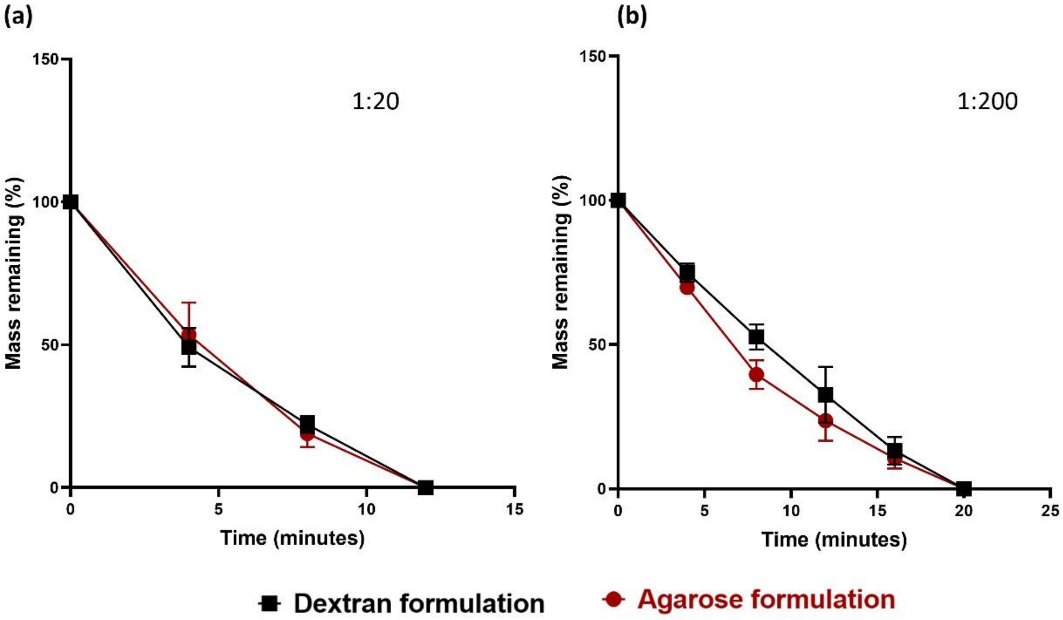

Figure 4.31. Analysis of hydrogels' degradation. Hydrogels' mass remaining (in percentage) after enzymatic degradation for RGD-N-Dex: CD-Link: LAP (0.5 mM: 5 mM: 5 mM: 0.5 mM)- (Dextran formulation-black profile) and RGD-N-Dex: CD-Link: LAP + Agarose (0.5 mM: 5 mM: 5 mM: 0.5 mM + 0.1% w/v)- (Agarose formulation-red profile). **(a)** (dilution 1:20) (n = 6 per each formulation) and **(b)** (dilution 1:200) (n = 3 per each formulation).

Once demonstrated that Formulation 5-based gels can be rapidly enzymatically degraded, the cell recovery post hydrogel degradation was also evaluated. Although DNA damage tests were not performed, thinking of further applications, such as potentially *in vivo* studies, a pilot study was conducted.

Cell-laden hydrogel scaffolds were printed as usual, by encapsulating Hs-27 human fibroblasts (5 x 10^6cells/ml), either in the presence or in the absence of LMP-agarose and kept in standard culture conditions. Then, by following the study described in section 4.5.4, a dextranase solution (dilution 1:20) was added to each sample. After complete digestion, cells were collected and resuspended in fresh cell culture media, resulting in a cell recovery ratio of 94.2 % and 93.4%, respectively with and without the agarose content. Then, the cells recovered were seeded on a culture Petri dish to better evaluate their proliferative capacity post-recovery. In Figure 4.32, Hs-27 replated post-recovery are presented respectively after 6- and 24-hours, collected from the composition based on single (-agarose) and interpenetrated network (+ agarose).

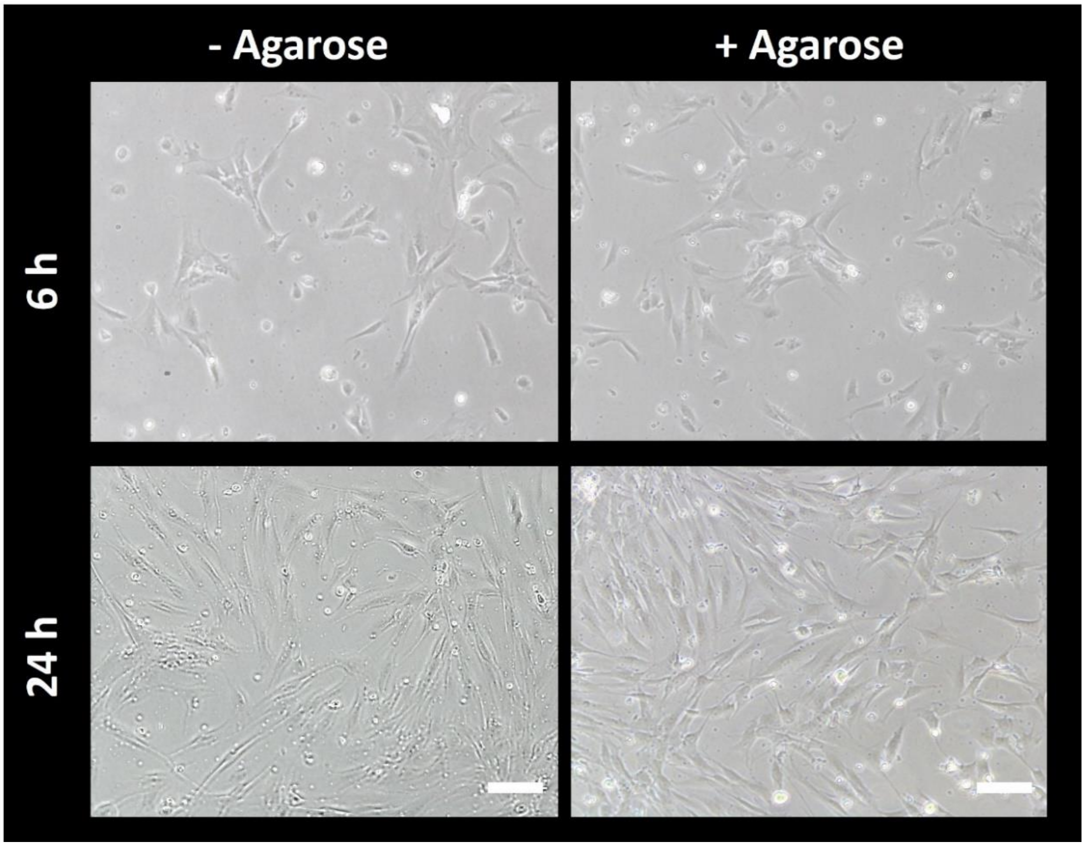

Figure 4.32. Brightfield inspection post-gel degradation. Brightfield pictures of cells growth post-recovery from single (left side) and from interpenetrated (right side) network, after 6 and 24 hours. Scale bars = 250 µm.

Together with the high percentage of cells recollected post-hydrogel degradation, the brightfield inspections clarify and enhance the great cells' status. Already after 6 hours post-re-seeding, the dermal fibroblasts showed their typical elongation, becoming more evident after 24 hours and manifesting cross-talking among themselves, independently from the agarose presence.

4.5.5. Analysis of the mechanical properties of stiffness-varying substrates

Developing full-thickness skin hydrogel models means resembling models not only containing the dermal and the epidermal compartments but also being adequate to include distinct types of cells. Specific mechanical properties must be reached to permit different cells to adhere and grow within the extracellular matrix. Hence, the optimal scaffold should present satisfactory requirements to support them, showing at the same time different stiffness to incorporate simultaneously a large cell spectrum.

Therefore, it was necessary to create a gradient of stiffness inside of the single model. For this purpose, new gels were printed using the SOLUS system. The initial energy dosage was set (E_0= 291.6 mJ/cm^2), corresponding to an exposure time of 90 s (section 3.3.5). Then, by defining 3 distinct photomask speeds (Table 3.6-Materials and Methods), gels based on Formulation 5 (+/- agarose) with gradients of stiffness were produced. Samples were kept at 4 ºC to reach the equilibrium swelling, right after the photopolymerization. Then, local stiffness measurements were performed through AFM analysis.

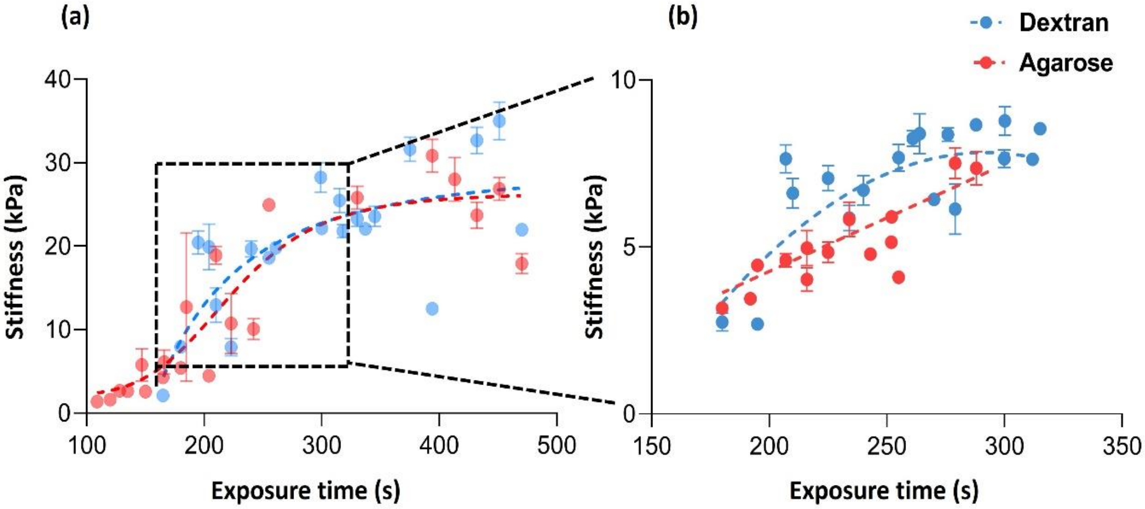

Figure 4.33. Atomic Force Microscopy study. Calibration curves of stiffness-varying substrates. **(a)** Calibration curves for dextran only (blue profile) and dextran + agarose-based gels (red profile) correspond to distinct stiffness by using gradients Q_1, Q_2, and Q_3. Values are shown as the mean ± SEM (10 < n < 12 per each condition). **(b)** Zooming of the calibration curves obtained for dextran only (blue profile) and dextran + agarose-based gels (red profile) by using gradients Q_4, Q_5, and Q_6, corresponding to a range of exposure time between 180 to 300 s. Values are shown as the mean ± SEM (n = 6 per each condition).

By fixing the initial energy dosage, three different gradients, Q_1, Q_2, and Q_3 were established. Hence, single structures that covered at once a wide stiffness window, between 1 and 35 kPa were obtained. The profiles described by the single compositions (with/without agarose) were similar, starting to overlap from 150 s of exposure time (Figure 4.33-a), indicating that the presence of the agarose did not affect the samples' stiffness. As enhanced by the chart, substantial variability was registered between 180 s and 300 s. So, a deeper study was conducted within this range, by defining three new gradients (Q_4, Q_5, Q_6), now narrowing the exposure time window from 180 s and up to 300 s (Table 3.6- Materials and methods).

In this narrow region considered (Figure 4.33- b), a quasi-linear trend was observed for both hydrogel compositions (+/- agarose). Despite the comparable Elastic Modulus values registered, in a range between 2 and 9 kPa, the dextran-based gels presented slightly higher values, meaning that at lower energy dosages, the presence of agarose could have an impact on the hydrogels' stiffness (Figure 4.33-b). Therefore, it was proved that hydrogel scaffolds with gradients of stiffness can be produced by the strategy presented. Indeed, by defining a threshold of energy dosage, corresponding to an initial exposure time to get proper polymerization, changeable stiffness can be reached simultaneously, in the same scaffolds by setting distinct final energy dosages (different photomask speeds) to create gradients. The wide range spectrum created was oscillating between 1 and 35 kPa, totally in line with hydrogels employed in skin tissue regeneration.[349,350] These tests represented a good starting point for further investigations, especially when more cell types must be included.

4.5.6. Cell viability studies

To investigate the impact of this new formulation on cellular viability for longer culture periods, Hs-27 encapsulation experiments were performed.

Therefore, cell-laden gels were photocrosslinked and examined starting from day 1 up to day 10 post-encapsulation. The maximum projections views (Figure 4.34-upper panel) demonstrated how this new formulation (dextran-based), containing matrix metalloproteinase-sensitive thiol-modified polyethylene glycol (CD-Linker), can favor the growth of the human dermal fibroblasts within the matrix.

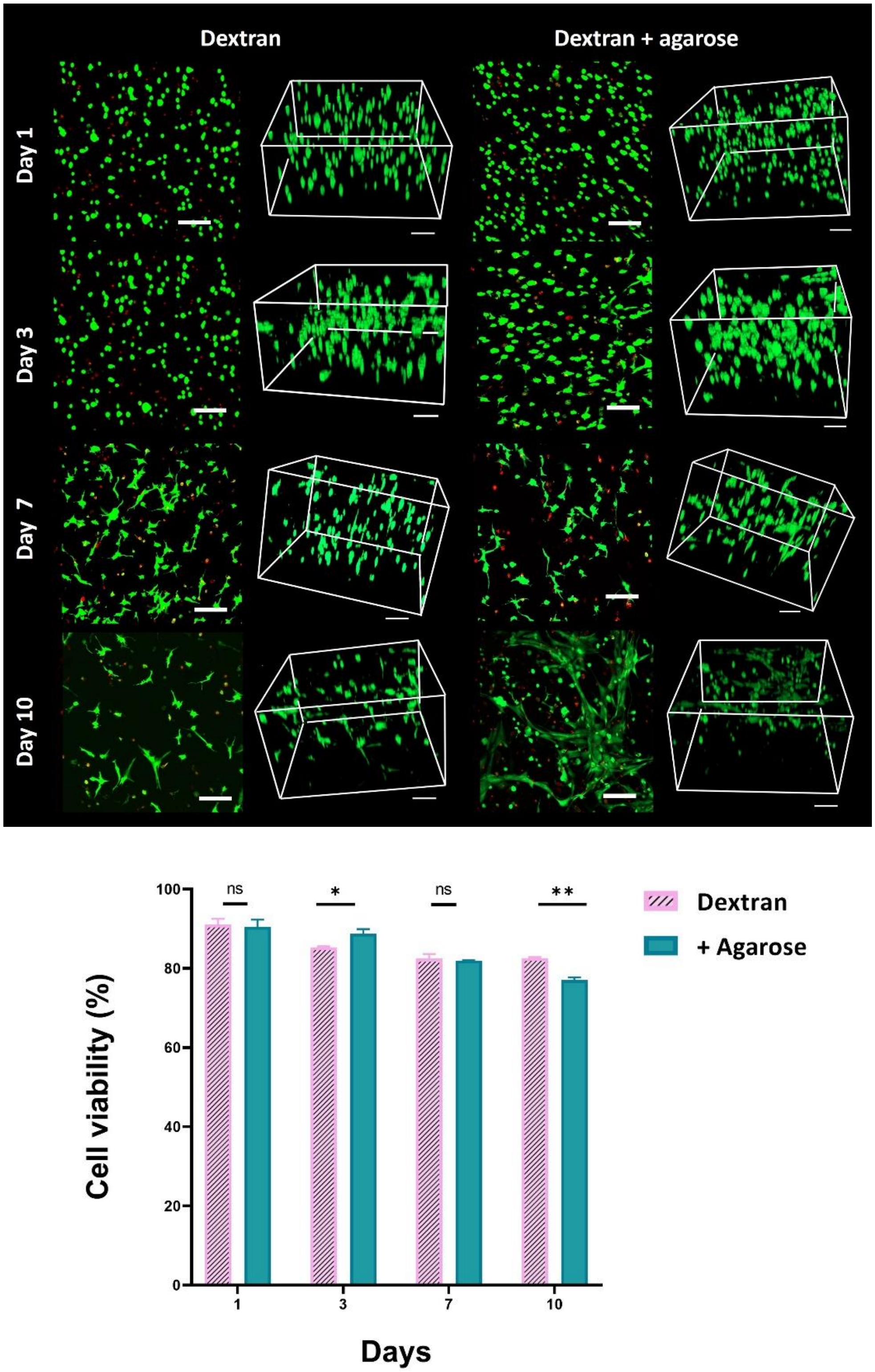

Figure 4.34. Live & dead assay. Hs-27 embedded within Formulation 5 – in the absence (left side) and in the presence of the agarose (right side), 1, 3, 7 -and 10 days post-encapsulation. **Upper panel-**Maximum projections of merged channels- live cells (green), dead cells (red), and 3D views. Scale bars = 100 µm. **Lower panel-** Cell quantification (dextran- pink bars) and (dextran + agarose- green bars). Values are shown as the mean ± SD ($n = 2$ per each time point and corresponding condition). A two-way ANOVA test was performed. $p < 0.05$ (p-value = 0. 001 (**).

Cells' protrusions were already distinguishable after 3 days post encapsulation, becoming more evident at day 7. Agarose presence drastically influenced the cells' behavior on day 10, where a very intricate network was appreciated (Figure 4.34). Instead, in the case of gels based only on norbornene-dextran, despite the fibroblast's elongations and uniform distribution all along the gel thickness, no entangled structure was recognized. Cellular viability quantification exhibited the advantages of this new formulation, Formulation 5, showing the highest viability rates registered until this moment. On day 1 post-encapsulation, (91% ± 1) of the cells were alive (Figure 4.34- bottom panel), either with agarose or without, representing promising data to support the importance of deeply exploring this new formulation. Despite the decrease noticed over time, good cell viability was kept until day 10 (82.6% ± 0.15), suggesting the suitability of this new gel's composition to sustain cell culture.

4.5.7. Cell density encapsulation optimization

Further improvements were also conducted to optimize the fibroblasts' encapsulation density. It is well-known in literature how the cell presence can influence the mechanical properties of the hydrogels. For instance, Rivero et al. observed a decrease in the Elastic modulus of PNIPAM-based scaffolds in the presence of cells and suggested that it was because of cell growth and the subsequent collagen production, which remodeled the matrix.[351] Thus, to minimize the impact on the mechanical characteristics of the gels due to the presence of fibroblasts embedded in the matrix, different cell encapsulation densities, 1.5 x 10^6 cells/ml, 2 x 10^6 cells/ml, and 2.5 x 10^6 cells/ml, were studied.

New rectangular-shaped hydrogels were printed, both in the presence and the absence of agarose, kept under culture in submerged conditions, for 7 days, and finally fixed. An immunostaining study using the specific markers for dermal fibroblasts was performed, to evaluate the impact of the cell density on (i) the cell distribution within the gels and (ii) the expression of the markers once they created a network. Besides the distinct amounts of cells encapsulated, all the scaffolds evaluated showed a perceptible expression of the single markers selected (Figure 4.35). Apart from the lowest cell density (1.5 x 10^6 cells/ml), where few cells were detected (+/- agarose), the intermediate and the higher cell densities manifested the adequate elongation of the dermal fibroblasts. The proper spreading of Hs-27 resulted in a great expression of the vimentin (green), pointing to the filamentous structures of the fibroblasts, accompanied by a conspicuous secretion of the collagen amount (red signals), Figure 4.35.

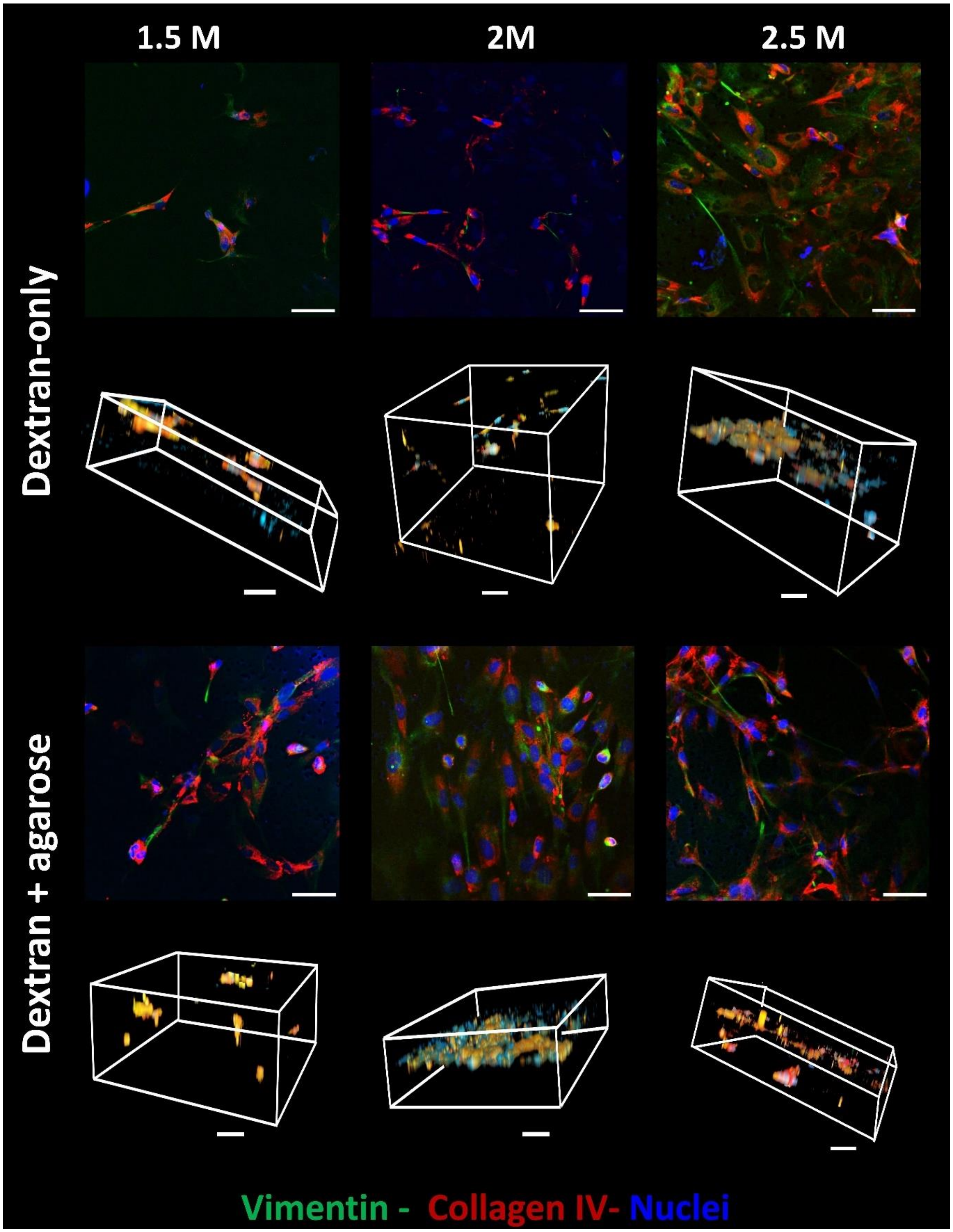

Figure 4.35. **Cell density optimization study.** Maximum projections and 3D views of different cell densities of Hs-27 encapsulated within gels based on Formulation 5 (dextran-only- upper panel), and (dextran + agarose- lower panel), respectively at 1.5 M, 2 M, and 2.5 M cells/ml, -7 days post-fabrication. Vimentin (green), collagen IV (red). DAPI stained nuclei (blue). Scale bars = 50 and 100 µm.

From these studies, no significant divergences were revealed between the two compositions, dextran-only (upper panel) and its dextran + agarose (lower panel). Normally, the agarose content had a strong impact on the cell distribution within the matrix and on the formation of a more fibroblast intricate network, as emerged from the viability assay, over a longer time culture. In this case, this evidence was mainly appreciated by looking at the intermediate and highest cell density, as reported in the 3D- views (Figure 4.35) in which a more branched arrangement was discerned when compared with the composition based only on dextran. Indeed, this evaluation resulted in the selection of 2 x 10^6 cells/ml as the optimal cell encapsulation, with a 60 % decrease compared to the previous one (5 x 10^6 cells/ml). The choice was made since it represented the threshold to get relevant cell spreading and markers' expression, 7 days post encapsulation, independently from the single or interpenetrated network system. Moreover, it was also considered that the cells encapsulated in the hydrogels can change profoundly their mechanical properties, so the increase in cell density often provoked a decrease in the strength of the scaffolds.[352] Therefore, by radically changing the cell density, it is possible to not alter the mechanical features, guaranteeing an adequate structure.

Once the reasonable threshold for the cell encapsulation was established, the following step was to recreate the epidermal layer on top of a deep-rooted scaffold. So, by considering the trials performed on Formulation 4, human immortalized keratinocytes (HaCaT) were seeded on top of cell-laden scaffolds, and placed within Transwell® inserts, 3 days post-encapsulation. For the first 7 days post-HaCaT seeding, submerged conditions were necessary to promote the homogenous cell distribution and the consequent monolayer formation. After that, to prompt the cell stratification and differentiation, Air-liquid-interface conditions were applied for the following days. Unfortunately, a visible scaffold degradation was noticed after 14 days post-HaCaT seeding, making them unable to support cell culture for a long time. This was probably correlated with the presence of matrix metalloproteinase cleavable (MMPs) recognition site which can be cleaved by the cells if they produce the corresponding MMPs. This aspect was important considering the advantages for the cells to spread when the hydrogel network locally loosens up. Thus, besides the promising results obtained in terms of cell viability and the suitability of the dextran-based matrix to keep up the cells, a new option was also evaluated. The change of strategy will be illustrated in the next section.

4.6. Interpenetrating network systems based on CD-Hy linker

4.6.1. Formulation 6: RGD-N-DEX: CD-Hy-Link: LAP +/- Agarose

Single and interpenetrated networks based on norbornene-dextran were characterized in the previous section, showing the potentiality of these polymers to guarantee consistent mechanical support and allow good cell viability within the matrix. However, the combination of RGD-norbornene-dextran, together with a modified polyethylene glycol crosslinker led to a rapid degradation of the scaffolds over time. Based on this evidence and considering some promising outcomes detected with Formulation 5, a new polymer configuration, Formulation 6, was set by combining the advantages of norbornene-dextran (in the presence/absence of LMP-agarose) with the CD-Hy link.

Starting again from the fabrication trials, first, the most convenient crosslinking molar content of the single components was established, always keeping the molar ratio polymer: crosslinker = 1:1. For the entire examination of this new formulation, the SOLUS equipment was employed to create samples with reliable dimensions, with a higher superficial area compared to the ones obtained when the DLW system was used. The preparation protocol for the pre-gel solution was the same as described in Formulation 5. So, by irradiating the pre-gel solution in a range between 3 and 4 minutes, circular-shaped hydrogels were produced with a molar content of (RGD-N-Dex: CD-Hy Link: LAP +/- LMP-Agarose, 0.5 mM: 3.5 mM: 3.5 mM: 0.5 mM +/- 0.1 % w/v).

4.6.2. Rheology characterization

The bulk properties of the new composition were evaluated through rheology measurements, during the *in-situ* crosslinking. At this stage, this analysis covered a significant role since it admits of primarily exploring the contribution of the agarose presence on the hydrogel's stiffness, and secondly comparing Formulation 5 and Formulation 6, detecting the major differences among the single/interpenetrated network systems studied until now, based on the same polymer (norbornene-dextran) but with different crosslinkers.

However, we should also keep in mind that the single compositions, Formulation 5 and Formulation 6-based hydrogels, were fabricated with the same molar ratio (polymer/crosslinker) (1:1), but a distinct molar macromer content, respectively (5 mM:5 mM- N-DEX: CD-Link) and (3.5 Mm: 3.5 mM- N-DEX: CD-Hy Link).

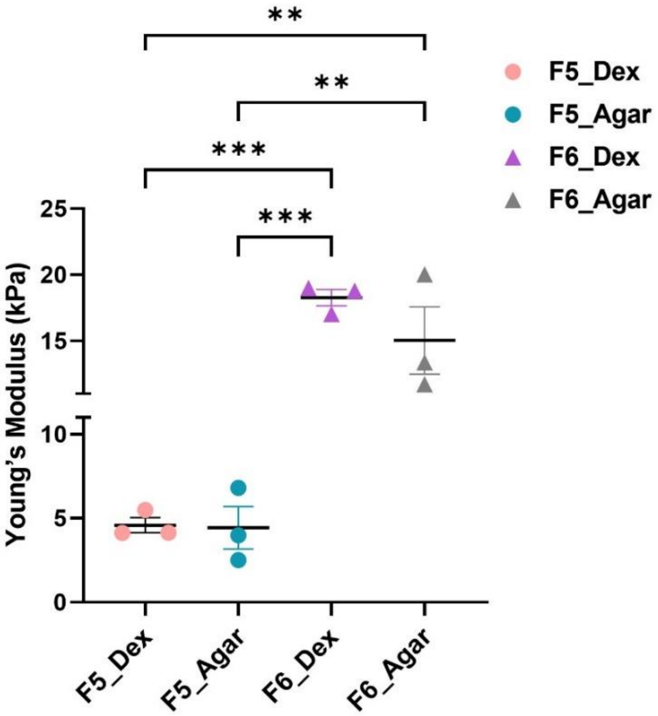

Figure 4.36. Rheology study. Young's Modulus values comparison between Formulation 5 and Formulation 6 calculated from the complex Modulus, derived from the Storage and Loss Modules as a function of the strain. Single networks (F5_Dex and F6_Dex – pink and violet), Interpenetrated networks (F5_Agar and F6_Agar- light blue and grey). n = 3 per each condition and formulation. One-way ANOVA was performed. $p < 0.05$. p-value = 0. 0003 (***)

The transition from the CD-link to the CD-Hy link marked a tangible difference in terms of elastic gels' characteristics. As enhanced by Figure 4.36, Formulation 6- based gels showed Young's Modulus values ranging between 15-18 kPa on average, resulting in 3 to 4-fold higher than the ones obtained for Formulation 5. However, all these results are still in the same order of magnitude and compliant with the one described in the literature[318] for acellular structures. Moreover, in the presence of agarose, again a slight decrease can be noticed. Conversely from norbornene-pullulan gels, for Formulation 6 (dextran-based), the crosslinker change drastically affected the resulting matrix's stiffness, pointing out the properties tunability of these gels.

From these mechanical results, it was expected that the new formulation had the potential to support cells, due to its stiff nature, although the degradation aspect must be investigated, especially at long culture periods.

4.6.3. Cell viability studies

From the biological point of view, the new formulation was first evaluated in terms of viability, to prove its appropriateness to endorse the fibroblasts' growth. The cell viability was evaluated over time, 2-, 5-, and 7 days post encapsulation.

As shown in Figure 4.37, from the 3D views, it was possible to appreciate that tendentially, the fibroblast distribution within dextran-based gels was observed starting from the upper layers. Instead, in the presence of the agarose, cells were mostly located in the central part of the gels, as emerged from the tests conducted on Formulation 5. This cell allocation was also recognized at later time points (day 5 and day 7), (Figure 4.37) where, in the presence of the agarose, a more homogenous cell distribution was detected. On day 2, for both the extracellular matrix compositions tested, with and without agarose, (91% ± 2.3 and 90.1% ± 7.3) of the cells were alive, strictly comparable at Formulation 5 results for the early time point (day 1) (Figure 4.37-lower panel). Slight lower values were reached when agarose was included over time, independently from the culture time point. Even after 5 days post-encapsulation, visible cell protrusions were observed for both compositions. A tiny decrease in viability was registered after 1-week post-encapsulation, as was normally observed for the other formulations studied. However, at day 7- the percentage of cells alive was still high (88.4 % ± 3.4 and 83.9% ± 7.3) (+/- agarose), if compared to Formulation 5 (81.9% ± 0.04 and 82.5 % ± 0.8), especially in agarose presence. Hence, we can conclude that the presence of a different crosslinker (CD-Hy Link) containing hyaluronic acid moieties affects cell viability rates at longer time points.

Therefore, this test underlined the efficacy of the new polymer combination -Formulation 6- with the optimized encapsulation condition to sustain the human dermal fibroblasts promoting their growth and guaranteeing elevated viability over time, which is one of the key points in tissue engineering, especially in the evaluation of the optimal biomaterials to resemble skin models. Due to these promising results, further evaluations were performed. Any signal of gels' degradation was observed up to 7 days post-embedding; however, deep studies were conducted to examine the gels' relevancy, either for a longer culture time (only dermal compartment) or in co-culture conditions (both dermal and epidermal compartments).

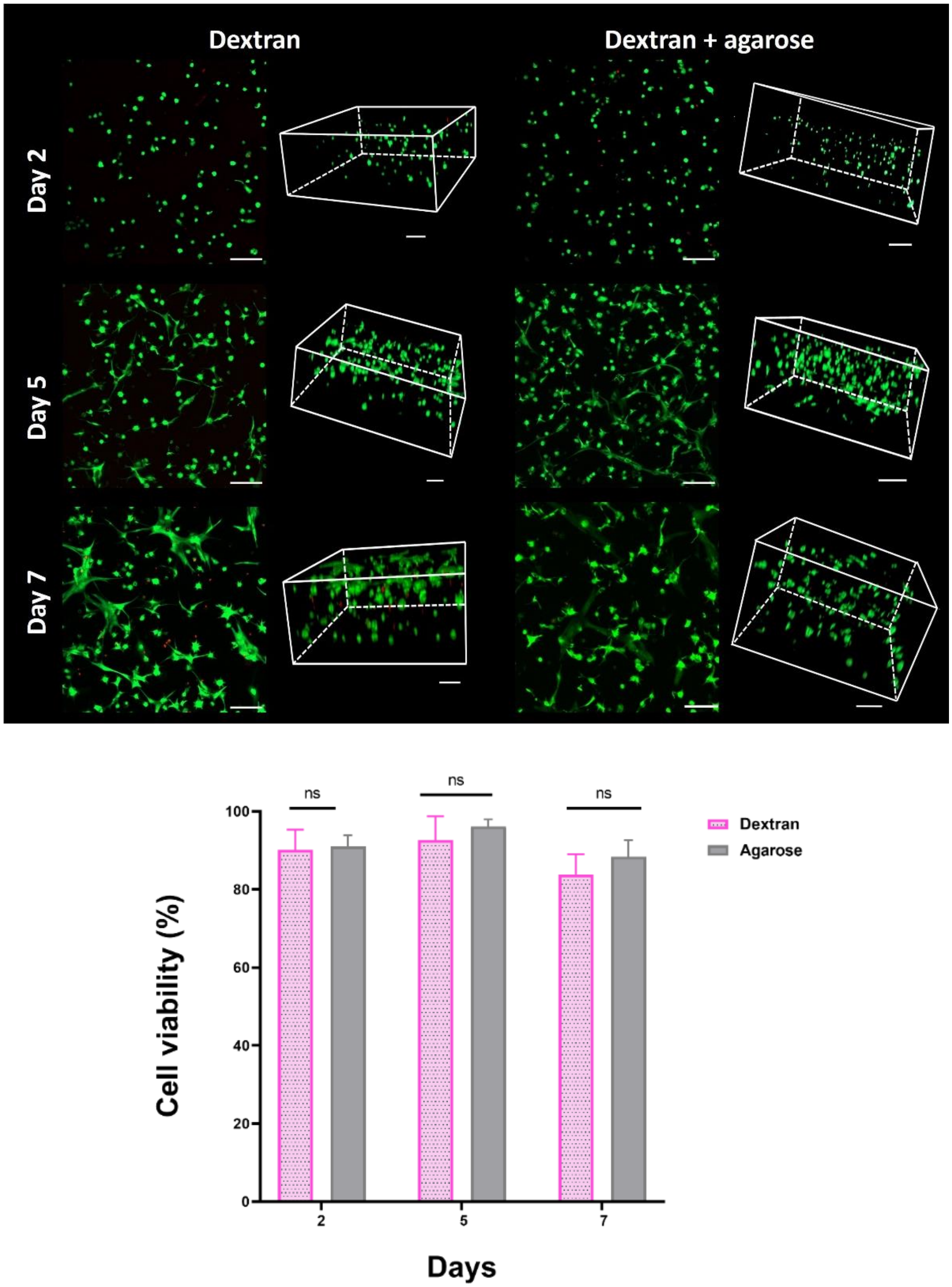

Figure 4.37. Live and dead assay. Hs-27 embedded within Formulation 6- in the absence (left panel) and in the presence of the agarose (right panel), 2-, 5-, and 7-days post encapsulation. **Upper panel-**Maximum projection of live cells (green) and dead cells (red), and 3D views. Scale bar = 100 µm**. Lower panel-** Cell quantification (dextran- only-pink columns), and (dextran + agarose -grey columns). Values are shown as the mean ± SEM (n = 3 per each condition and each time point). A two-way ANOVA test was performed.

4.6.4. Epidermal compartment formation

The mechanical tests performed, together with the viability assay, showed the potentiality of the Formulation 6-based gels as being a robust dermal construct to support an epidermal compartment. So, once the dermal structure was properly established, the following step was to obtain a strong epidermal layer on top and to evaluate its performance. The procedure followed was the same as described in Figure 4.38. New cell-laden gels were fabricated by irradiating for 4 minutes the pre-gel solution containing Hs-27 with the same encapsulation density suspension (2 x 10^6 cells/ml) verified during the live & dead assay and previously optimized in the study of Formulation 5. Right after fabrication, samples were mounted within the Transwell® inserts and kept under submerged conditions for 3 days. Then, HaCaT cells were seeded on top of the constructs in a drop-like manner (200 x 10^3 cells/sample) to cover the gels. Submerged culture conditions were maintained for 7 days at the end of which part of the samples was kept under the same conditions (submerged regime), and the rest were cultured in ALI up to day 24.

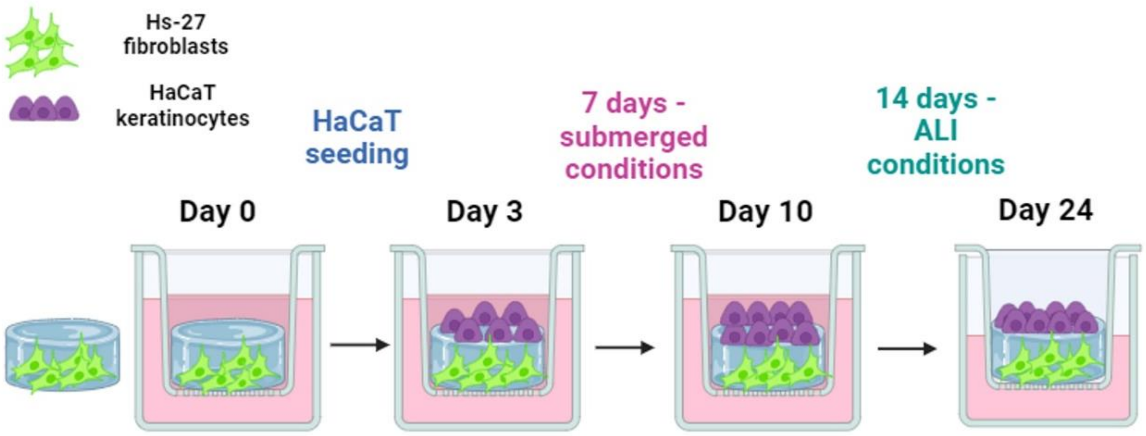

Figure 4.38. **Schematic representation of the co-culture protocol** (Biorender software). Hydrogels with human dermal fibroblasts-Hs-27- mounting within Transwell® insert (day 0). Human immortalized keratinocytes -HaCaT- seeding on top of cell-laden hydrogels (day 3). After 7 days of submerged culture, (day 10), Air-liquid-Interface (ALI) conditions were applied, for 14 days up to day 24.

Preliminary qualitative studies were conducted on all gel types (on Dextran only- and Dextran + agarose), at different time points, as described in Figure 4.39, to evaluate the influence of the extracellular matrix composition on the cells' behavior and to understand the cells' arrangement within and on top of the scaffolds. Specifically, histological cuts were used for this purpose, to visualize the single counterparts properly. Before doing that, a PEGDA immobilization was created to surround the gels and try to preserve their structure (section 3.5.11).

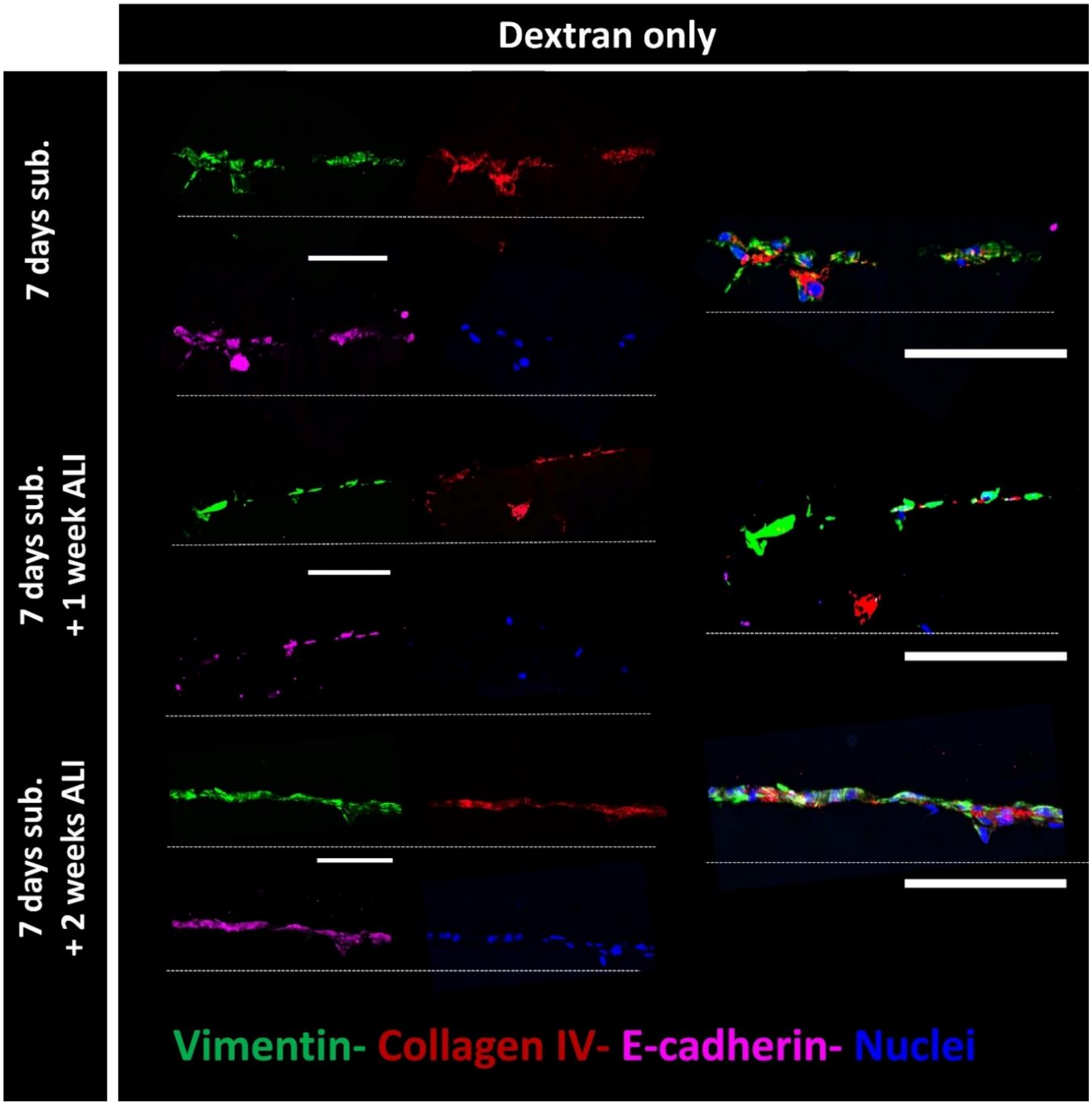

Figure 4.39. Evaluation of co-culture systems based on Formulation 6- Dextran only. Immunofluorescence of histological cuts respectively, 7 days in submerged conditions, 7 days submerged + 1 week ALI, and 7 days submerged + 2 weeks ALI. Single channels on the left, merged channels on the right. Vimentin (green), collagen IV (red), and e-cadherin (magenta). DAPI stained nuclei (blue). Dashed lines indicate the membranes. Scale bars = 100 µm.

All the markers were expressed for both compositions (Figures 4.39 and 4.40), -dextran-only and dextran + agarose compositions. While the dermal compartment marked by vimentin (green) and collagen IV (red) was distinguishable independently from the time points and the composition, the epidermis layer was not easy to identify. Especially at earlier time points (7 days submerged), the e-cadherin signal (magenta) pointed out how few HaCaT cells were able to adhere to the cell-laden scaffold, indicating a slow growth process.

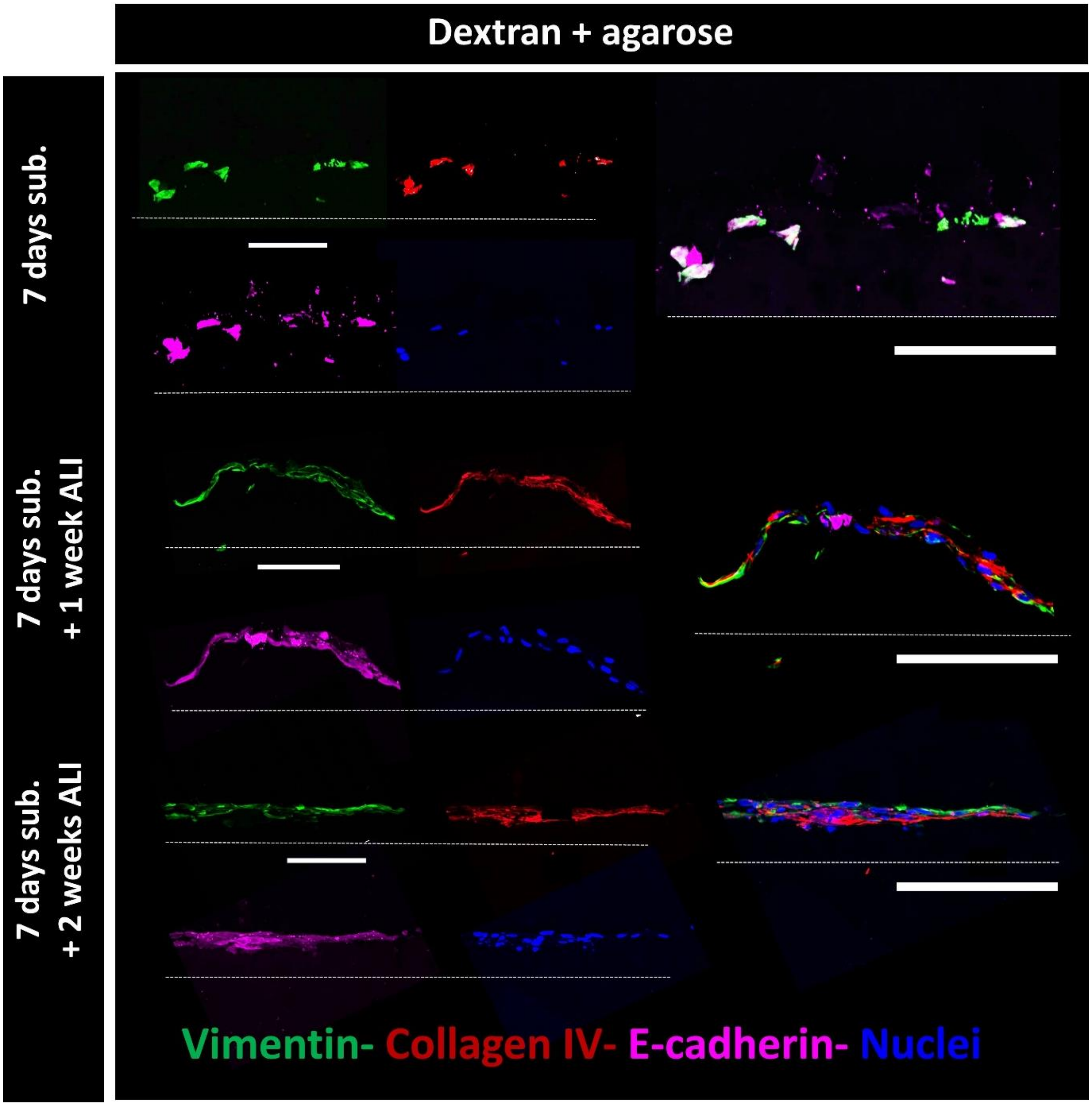

Figure 4.40. Evaluation of co-culture systems based on Formulation 6- Dextran + agarose. Immunofluorescence of histological cuts respectively, 7 days in submerged conditions, 7 days submerged + 1 week ALI, and 7 days submerged + 2 weeks ALI. Single channels on the left, merged channels on the right. Vimentin (green), collagen IV (red), and e-cadherin (magenta). DAPI stained nuclei (blue). Dashed lines indicate the membranes. Scale bars = 100 µm.

For the dextran-only composition (Figure 4.39), to detect a continuous epidermis above the dermal compartment, 7 days of submerged conditions + 2 weeks in ALI were necessary. At earlier time points, fragmented epidermis layers were noticed. Otherwise, in the presence of agarose (Figure 4.40) some improvements were already observed after 7 days of submerged conditions + 1 week of ALI, resulting in a regular epidermis layer along the histological cut, becoming a well-established compartment at longer time points (7 days submerged + 2 weeks ALI).

However, at this stage of the project, we were still far from a full-thickness skin model based on the current formulation- Formulation 6. Although through this formulation we improved the extracellular matrix stiffness, reaching satisfactory cell viability rates not only at early time points, the epidermis establishment still required many improvements. In particular, what we aimed to achieve was (i) the formation of a complete monolayer in a short time, (ii) its capability to be anchored on the dermal compartment, also at a long period, (iii) to promote stratification and differentiation. Hence, as a first attempt to generate a complete monolayer, a surface coverage analysis was conducted, by varying the HaCaT density seeded on top gels without fibroblasts embedded. So, the keratinocyte growth was monitored day by day, by taking brightfield pictures and quantifying the superficial coverage. As described in Figure 4.41, three different cell densities were adopted (250 x 10^3, 375 x 10^3, and 500 x 10^3 cells per sample) to select the optimal one, in terms of time request to colonize the entire surface.

It was observed that starting from day 1, cells were attached successfully for both compositions (Figure 4.41 -a and c-) independently from the cell density used, resulting in regions more or less colonized depending on the number of cells seeded. All the constructs were kept in a regime of submerged conditions until a uniform distribution was revealed and no detachment was observed (day 21). Simultaneously, the surface coverage quantification was conducted. For the higher cell density (500 x 10^3/ sample), the complete confluency was reached respectively at day 7 for dextran only (Figure 4.41-b) and at day 5 for dextran + agarose gels (Figure 4.41-d). For the intermediate density (350 x 10^3/sample), 9 days were needed to get a complete monolayer for both compositions (Figure 4.41 b, d). Finally, for the lowest density evaluated (250 x 10^3/ sample), a uniform distribution was reached at day 21 (dextran-only gels) and day 14 (dextran + agarose gels), (Figure 4.41 b, d), reflecting the results that emerged by the qualitative analysis conducted on the histological cuts, where a comparable HaCaT seeding density was used (200 x 10^3 cells/sample).

Once demonstrated that a complete monolayer was reached for all the conditions tested, the same samples were kept in culture for 2 additional weeks under ALI conditions to evaluate the epidermal markers' expression. Thus, combinations of different (i) scaffold matrix compositions (dextran-only and dextran + agarose gels) and (ii) cell densities were evaluated.

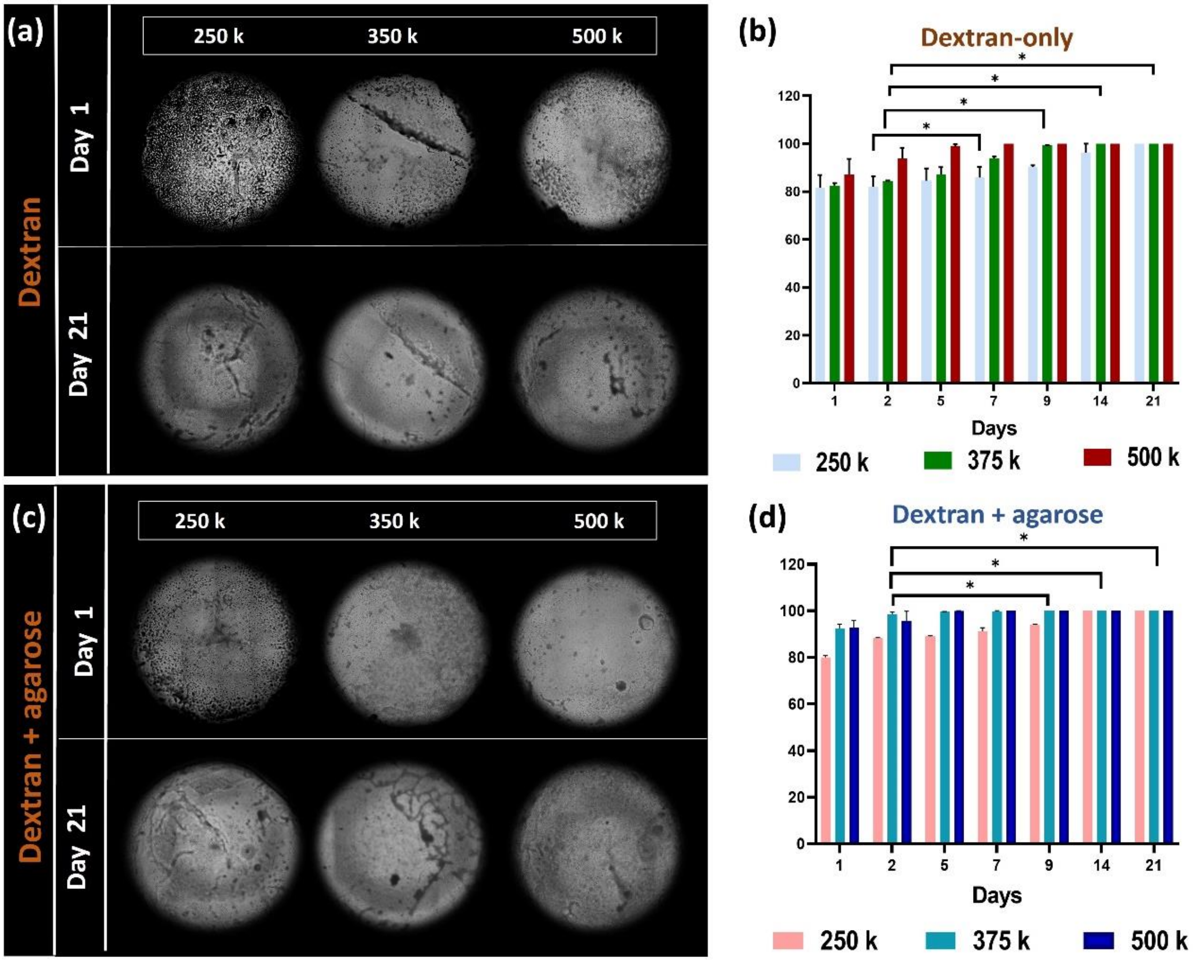

Figure 4.41. Surface coverage analysis at different cell densities. (a) Brightfield pictures and **(b)** coverage quantification up to day 21 of Dextran-only gels. **(c)** Brightfield pictures and **(d)** coverage quantification up to day 21 of Dextran + agarose gels. Seeding densities: 250k, 375k, and 500k cells per sample. Values are shown as the mean ± SEM (n = 2 per each condition). A two-way ANOVA test was performed. $p < 0.05$.

The expressions of both F-actin (yellow) and K14 (red) showed a good signal, regardless of the condition analyzed (Figure 4.42 -Dextran only- and Figure 4.43 -Dextran + agarose-). From a first observation, while at lower density cells appeared organized in clusters, showing interspaces among them, for the intermediate and highest densities, more homogenous monolayers can be appreciated for both compositions, as expected. However, apart from the different cells' arrangement, some uncovered regions were also detected for lower (250 k) and intermediate (375 k) cell densities (white arrows in Figure 4.42 and 4.43 -upper-panels-).

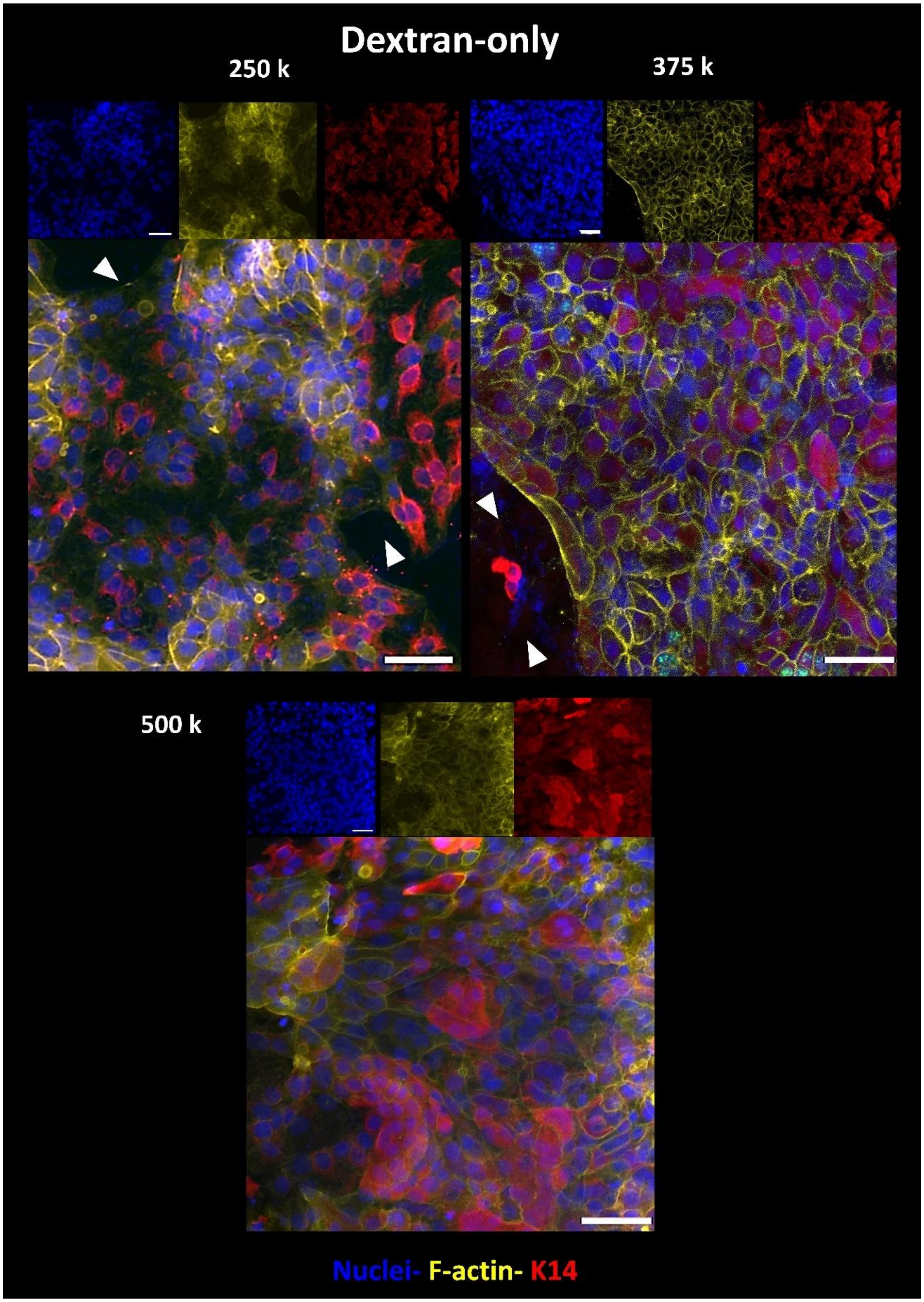

Figure 4.42. Evaluation of the markers' expression on dextran-only gels. Maximum projections of HaCaT immunofluorescence after 35 days in culture, study, using: (250 x 10^3/sample), (375 x 10^3/sample) and (500 x 10^3/sample). F-actin (yellow) and Keratin 14 (red). DAPI stain nuclei (blue). Scale bars = 50 µm.

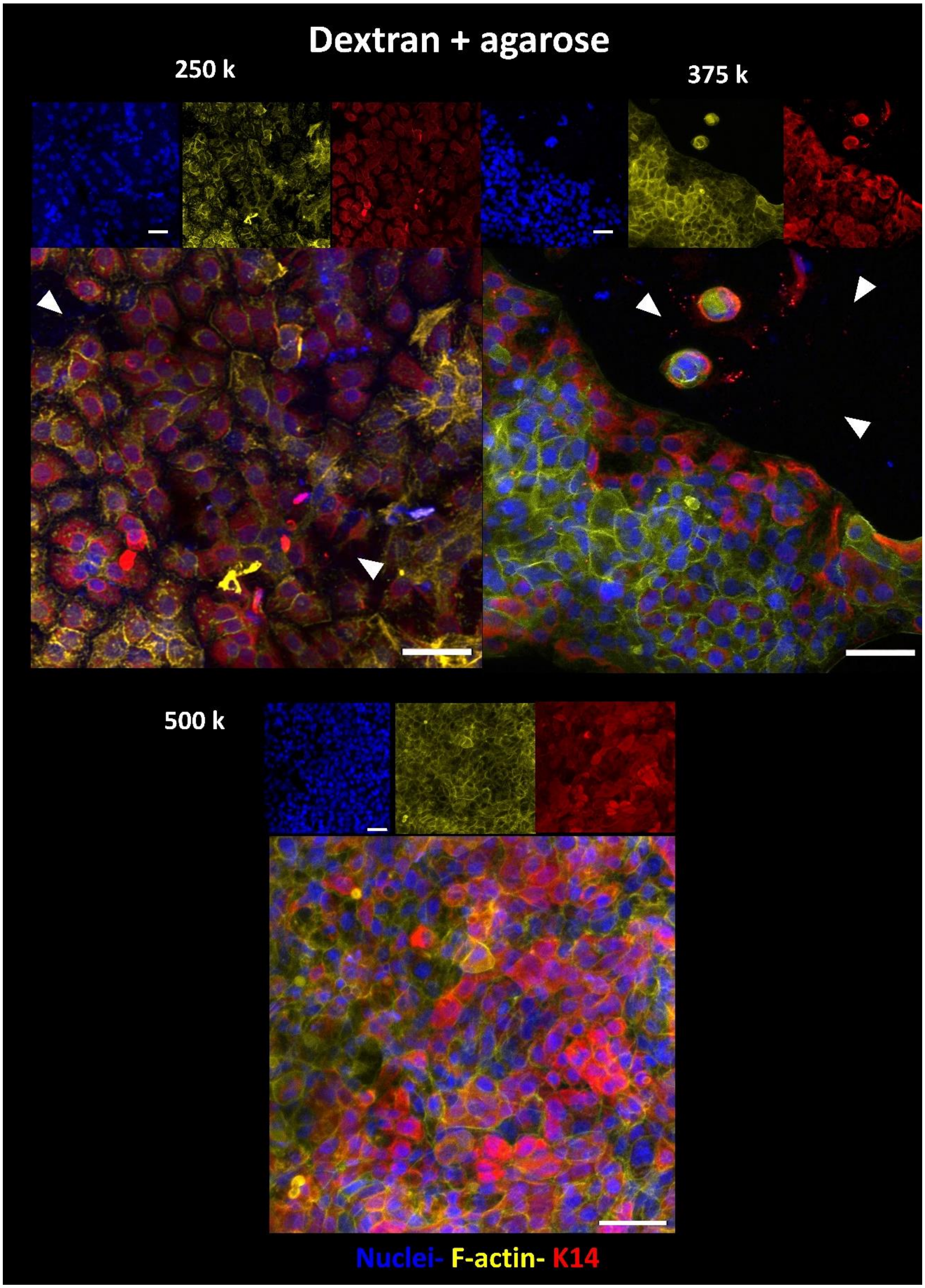

Figure 4.43. Evaluation of the markers' expression on dextran + agarose gels. Maximum projections of HaCaT immunofluorescence after 35 days in culture, study, using: (250 x 10^3/sample), (375 x 10^3/sample) and (500 x 10^3/sample). F-actin (yellow) and Keratin 14 (red). DAPI stain nuclei (blue). Scale bars = 50 µm.

Since the monolayer establishment was proven (Figure 4.41), the first hypothesis was that after a long time in culture (35 days), keratinocyte growth can also provoke matrix degradation, resulting in uncovered gel portions or even monolayer detachment. This detachment was probably correlated to the entire process in which the gels were processed for immunostaining, (fixation, washing steps, and antibody incubations) before the confocal analysis, considering the labile nature of the monolayer formed and the impossibility of HaCaT cells to create tight junctions. Based on the evidence, a further investigation was conducted. As emerged from the surface coverage analysis, to rapidly get a cells' confluence on top of the gels (7 days), the highest density (500 k) was considered as the optimal one. Additionally, compact structures without uncovered portions were detected only for this specific density. Hence, co-culture systems were created by encapsulating Hs-27 (2 x 10^6 cells/ml) and seeding HaCaT cells (500 x 10^3 cells/ sample) on top 3 days later. After 7 days in submerged conditions, 2 weeks of ALI conditions were applied. At this stage, samples were fixed, and a special embedding was realized to preserve their structures. This time, a norbornene-pullulan gel was used instead of PEGDA, to improve the affinity between the two gel types. Finally, some sample sections were obtained and investigated through Hematoxylin and Eosin staining. As depicted in Figure 4.44, a well-formed and continuous monolayer was visible along the entire section. The epidermis layer proved the adequacy of these interpenetrated scaffolds to support the monolayer formation, even though HaCaT cells do not form tight junctions. Elongated fibroblasts underneath the epidermis demonstrated the satisfactoriness of the extracellular matrix to promote their spreading within the gels. However, no stratification and differentiation of the keratinocyte monolayer were observed, although some studies reported in the literature proved that these cells could differentiate by applying proper culture conditions.[121]

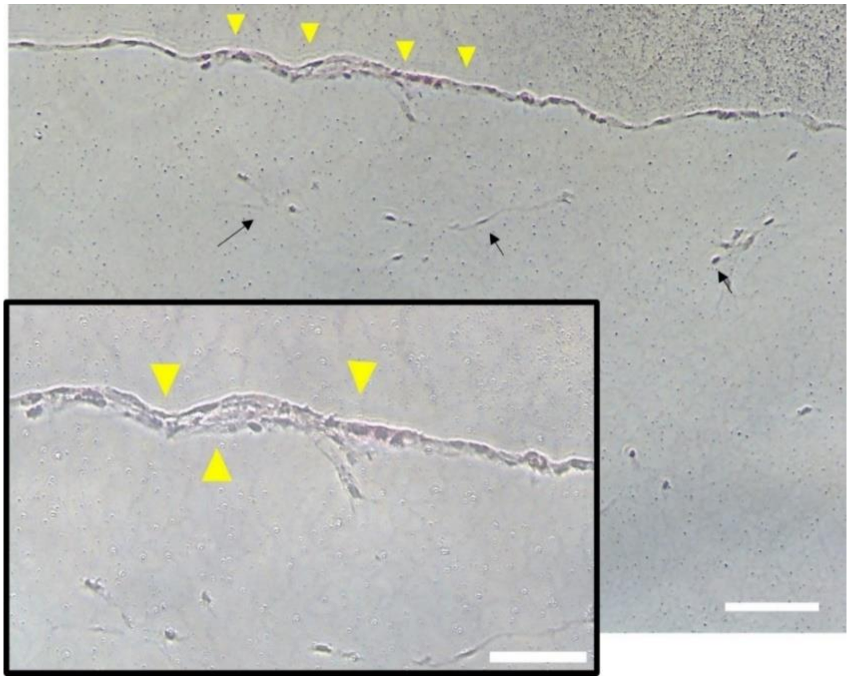

Figure 4.44. Hematoxylin and Eosin staining. Co-culture constructs based on Dextran + agarose gels. A cell monolayer (HaCaT cells) was identified on top of the gel (yellow triangles), covering the entire section analyzed (8 µm). Underneath the epidermis, and human dermal fibroblasts (Hs-27) - black arrows-. Scale bar = 50 µm. Zooming of the epidermis on the left side. Scale bar = 200 µm.

4.6.5. Epidermal compartment improvements

Epithelized-dermal scaffolds can be generated by using interpenetrated network systems. However, due to the drawbacks presented by the immortalized keratinocytes, further options were considered. Besides the cell density optimization, to promote keratinocyte growth and their stratification, a different culture medium (Epilife^{TM} medium -section 3.5.7.2-) was considered. For this purpose, co-culture systems were created, by seeding HaCaT cells (500 x 10^3 cells/sample) 3 days post-Hs-27 encapsulation (2 x 10^6 cells/ml), as we normally did. Then, half of the constructs were kept under submerged conditions (7 days) by using the cell culture medium used up to now (DMEM supplemented with 10% FBS, 1% P/S, in the presence of Normocin), followed by 2 weeks of ALI; the other half were kept in submerged regime, 7 days using the new medium (Epilife^{TM} medium, supplemented with specific S7 supplement and 1% of Anti-Anti). The constructs were explored by brightfield inspection over time, as reported in Figure 4.45. After the first 7 days in submerged conditions, some differences in the cells' disposition were already observed. In the case of the DMEM medium, it was more difficult to distinguish the arrangement of the cells on top of the scaffolds (Figure 4.45, top panel), while for the new culture medium used (Epilife^{TM} medium) a clear homogenous distribution was detected.

By following the development of the cell monolayer for longer periods, a more dense and defined distribution was reached with the constructs cultured with Epilife^{TM} medium (Figure 4.45, bottom panels), probably due to its composition richer in amino acids and vitamins, and with higher calcium content.

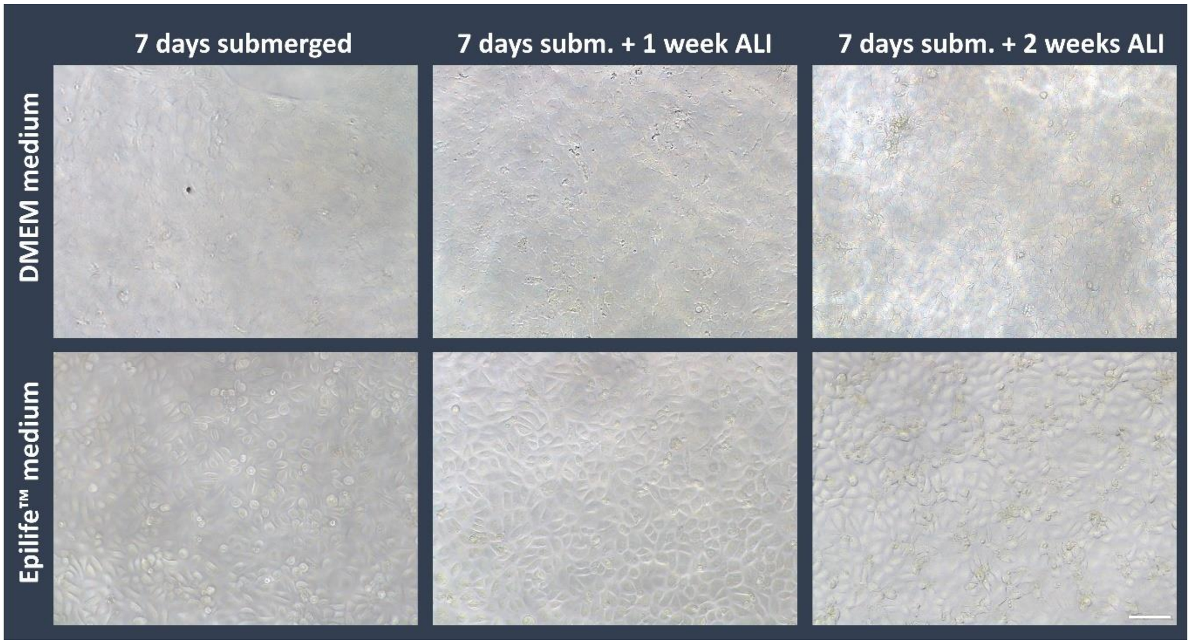

Figure 4.45. Brightfield pictures inspection of co-culture systems based on dextran gels. From left panels to right ones, respectively: 7 days under submerged conditions, 1 week- and 2 weeks of ALI, culturing the constructs with different cell culture medium- DMEM medium- apical row- and Epilife^{TM} medium – bottom row. Scale bar = 50 µm.

This first inspection was foreboding good HaCaT performance, starting from the early culture stage. So, preliminary immunofluorescence studies were conducted in parallel, to investigate the influence of the new medium on the markers' expression after 7 days of submerged conditions.

For the scaffolds cultured with Epilife^{TM} medium, depending on the sample examined, the immunofluorescence revealed a different cell arrangement on top of the scaffolds, as reported in Figure 4.46. The F-actin signal (yellow) was perfectly expressed for Sample A (Figure 4.46- upper panel), pointing to a homogeneous cell distribution. Laminin (green) was also expressed, indicating that the barrier between Hs-27 and HaCaT could be appreciated already after 7 days, and the e-cadherin signal (magenta) showed the adherence junctions on top of the scaffold. The situation changed for Sample B, where the F-actin appeared more fragmented, signaling the cluster organization of the cells. The same behavior was also recognized both for the laminin expression and for the e-cadherin.

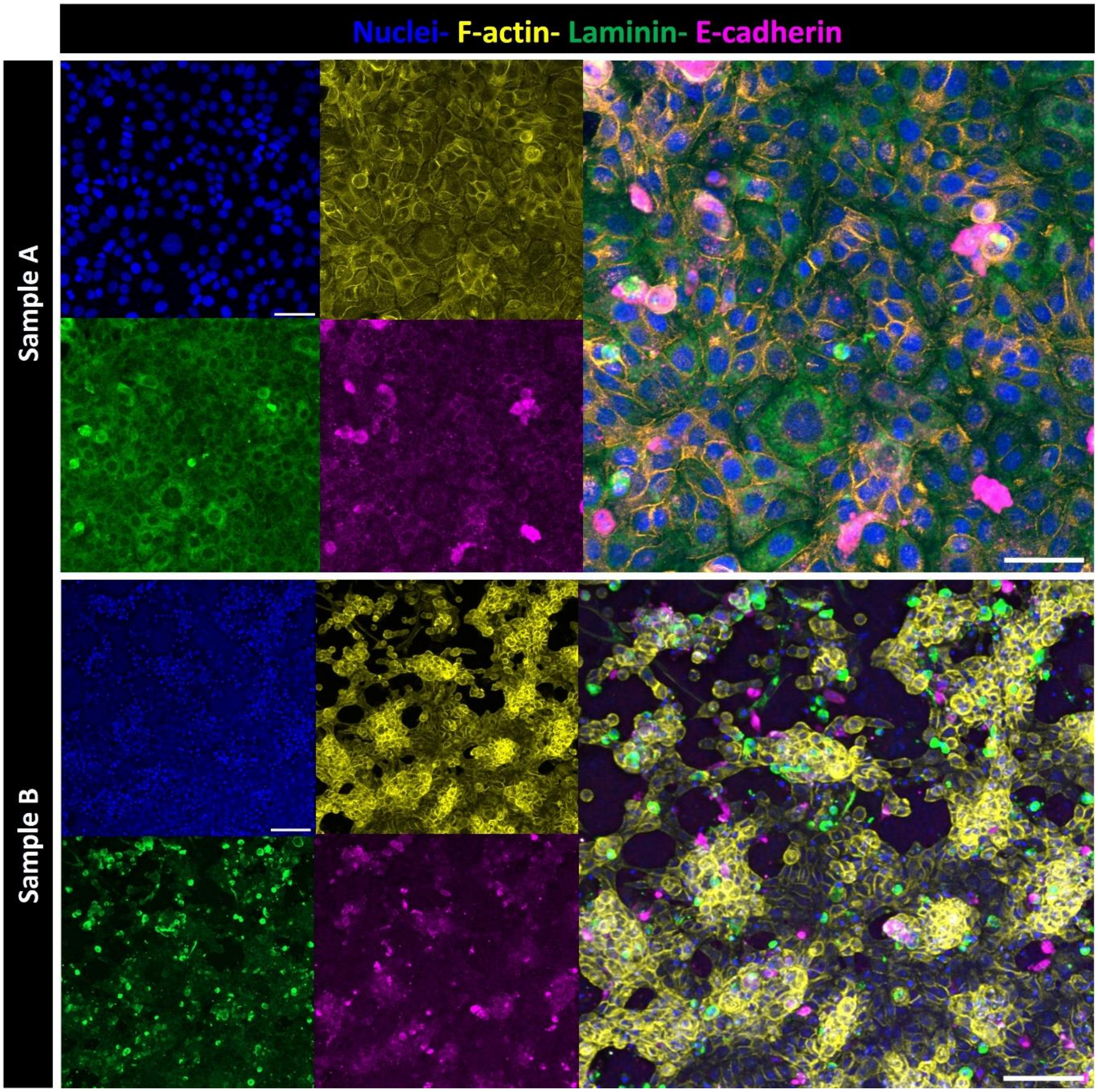

Figure 4.46. Evaluation of the markers' expression of a Hs-27/HaCaT system cultured with Epilife^{TM} medium. Maximum projections of HaCaT immunofluorescence after 7 days in submerged conditions for Sample A (upper panel) and Sample B (lower panel). F-actin (yellow), laminin (green), and e-cadherin (magenta). DAPI stain nuclei (blue). Example of a dextran+ agarose gel. Scale bars = 50 µm and 100 µm.

Also, in DMEM samples, the immunofluorescence revealed contrasting results. Depending on the sample inspected, a different HaCaT organization was recognized, revealing a monolayer more homogenously distributed in (Figure 4.47-Sample C) than (Figure 4.47-Sample D). On the other side, the old medium seemed to take part mostly in the fibroblast's expression underneath the monolayer (Figure 4.47). Both f-actin and laminin showed a different behavior this time, highlighting the elongated and spread characteristic fibroblasts' shapes. Comparable results were also obtained for gels based on dextran-only.

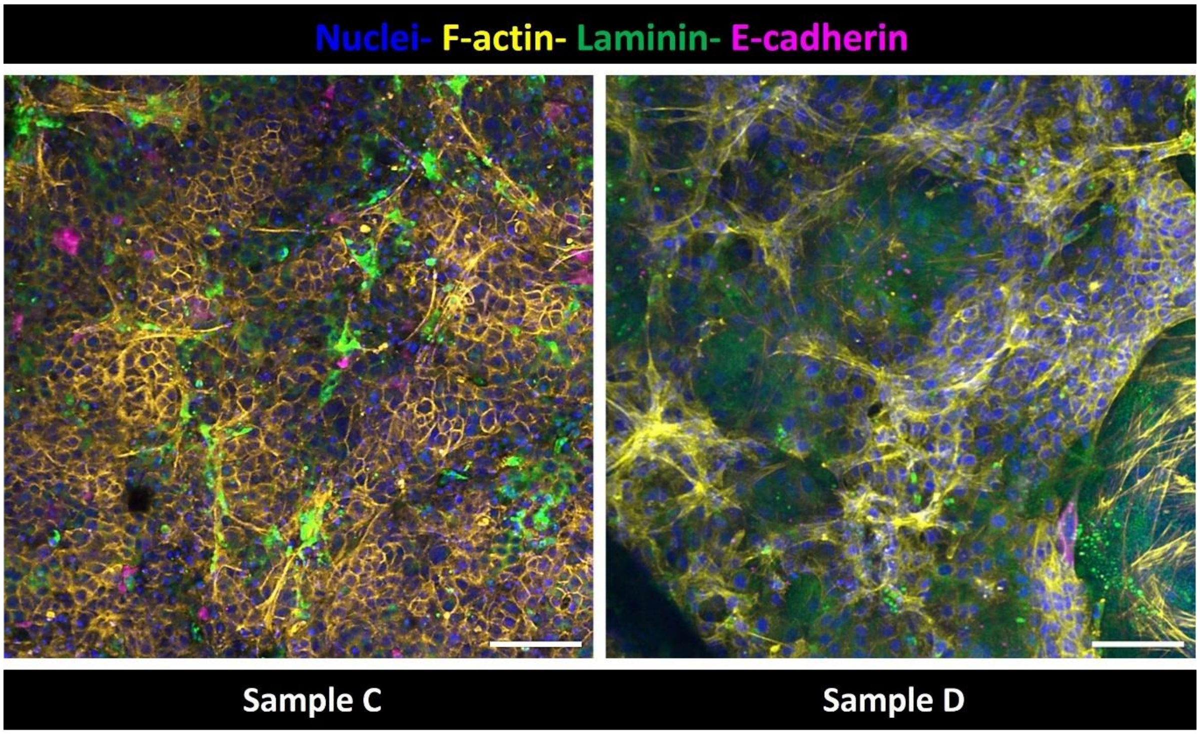

Figure 4.47. Evaluation of the markers' expression of a Hs-27/HaCaT system cultured with DMEM medium. Merged maximum projections of HaCaT immunofluorescence after 7 days in submerged conditions in Sample C (left panel) and Sample D (right panel). F-actin (yellow), laminin (green), and e-cadherin (magenta). DAPI stain nuclei (blue). Example of a dextran+ agarose gel. Scale bars = 100 µm.

Altogether these results shed light on the labile nature of the keratinocyte attachment on top of Formulation 6 gels, independently from the culture medium used. As observed for the immunofluorescence studies post-cell density optimization (longer culture periods), the monolayer persistency seems difficult to keep. Despite the new medium adopted (Epilife™), which undoubtedly had an impact on keratinocyte arrangement (Figure 4.45) and a less-stressful immunostaining protocol followed, we cannot reach a reliable model by combining Formulation 6 gels and HaCaT cells, ergo a change of strategy was required.

4.6.6. Towards a full-thickness skin model: HEKn

In addition to evaluating polymer composition for developing skin models, various studies have focused on identifying suitable cell types for resembling single scaffold compartments and optimizing culture conditions. HaCaT cells are commonly employed to recreate the epidermis in skin engineering since they can form a closer epithelial *in vivo* structure once transplanted onto mice or grown in organotypic cultures. However, they still have notable limitations.[353,354]

Even though these immortalized keratinocytes can show a significant degree of differentiation under specific conditions and after prolonged culture periods (up to six weeks), they cannot successfully achieve cornification.[121] Their stratification results are abnormal, with an atypical expression pattern of the cornified envelope-associated proteins, such as filaggrin and loricrin.[355] Hence, these models are still far from replicating native skin.

Our results indicate that by using HaCaT cells a thin epidermal layer can be established on top of a well-organized fibroblast network (Figure 4.44). However, this thin structure was not sufficient to promote differentiation. To enhance the performance of these cells, we first transitioned to a nutrient-rich medium, but this did not result in a significant improvement. To overcome these drawbacks, primary keratinocytes were considered. Human Neonatal foreskin primary epidermal keratinocytes (HEKn) were selected for establishing a differentiated epidermis on top of the fibroblast-laden gels. First, cells were expanded and kept in culture using a maintenance medium. In parallel, the dermal compartment was produced with SOLUS setup by encapsulating Hs-27 fibroblasts (2x 10^6 cells/ml) within circular-shaped constructs using Formulation 6 gels and placed in Transwell® inserts under submerged conditions. Three days post-encapsulation, primary keratinocytes (HEKn) were seeded on top of the cell-laden gels (in a range between 16 x 10^4 - 18 x 10^4 cells/scaffold) in a drop-like manner. This seeding cell density was selected based on the work of Zoio et al.[312] and preliminary tests conducted in our lab. The submerged conditions were maintained by culturing the basolateral compartment (corresponding to the dermis) with fibroblast medium, adding keratinocyte growth medium (KGM) in the apical compartment, to promote the keratinocyte monolayer formation on top. Once the surface of the scaffolds was completely covered (3 days post HEKn seeding), ALI culture conditions were applied for 10 extra days (Figure 4.48). During this period, the basolateral compartment was fed with the keratinocyte differentiation medium (KDM), which consists of KGM medium supplemented with a higher $CaCl_2$ concentration, ascorbic acid, and keratinocyte growth factor to boost the epidermis differentiation, while the apical compartment was fully exposed to air.

Given the short lifespan of primary keratinocytes compared to the HaCaT cells, the full-thickness constructs were fixed after 13 days post-primary keratinocyte seeding (corresponding to 16 days post-fabrication). It has been observed that after 12-14 days in culture, the skin organization is like the human skin, without revealing more differentiation.[356]

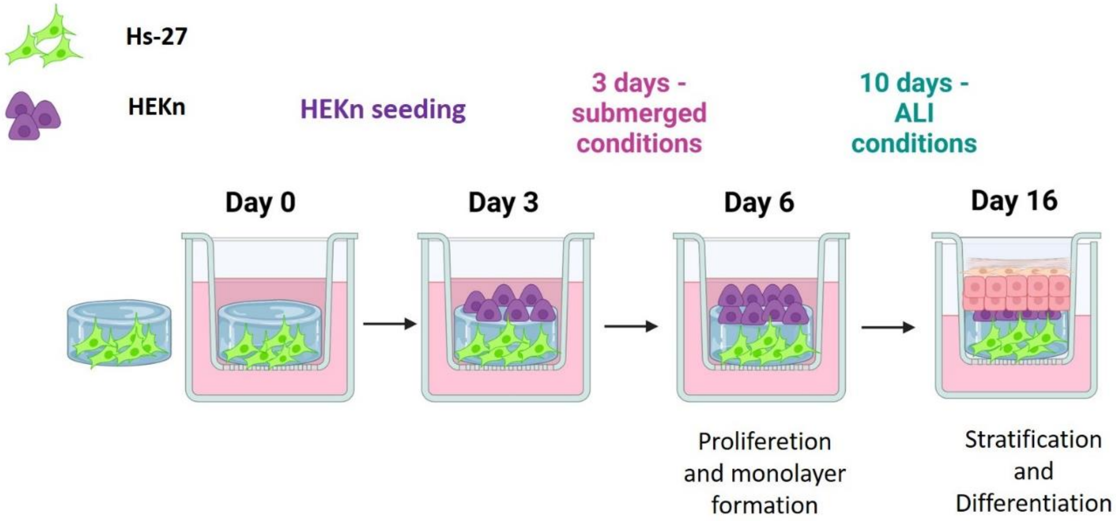

Figure 4.48. Schematic representation of the co-culture process. On day 0 hydrogels were fabricated encapsulating human dermal fibroblasts, followed by HEKn seeding on top of cell-laden scaffolds (day 3). On day 6, ALI conditions were applied up to day 16.

The hydrogels were cultured as illustrated in Figure 4.48, then fixed and stained. Initially, a general view of the hydrogel was investigated, identifying the bulk (the dermis) via the expression of vimentin and collagen IV, and the epidermis through the keratin 14 (k14) signal. As discussed in previous sections, the polymer composition of our hydrogels, Formulation 6, effectively sustains human fibroblasts within their bulk, ensuring their spreading (vimentin expression, green) and promoting collagen expression as indicated by collagen IV signal (red) (Figure 4.49). A well-established network of human dermal fibroblasts was formed within the scaffold, comparable to the previous results, even though the culture time was drastically reduced (13 days - vs 24 days). The epidermis above was first marked by keratin 14 (yellow) (Figure 4.49-top panel). K14 signal identifies an organized and quite compact monolayer, showing the adherence capacity of the primary keratinocytes in co-culture with fibroblasts on this hydrogels' formulation. A 3D view was also included to show the total cells 'arrangement within the entire matrix.

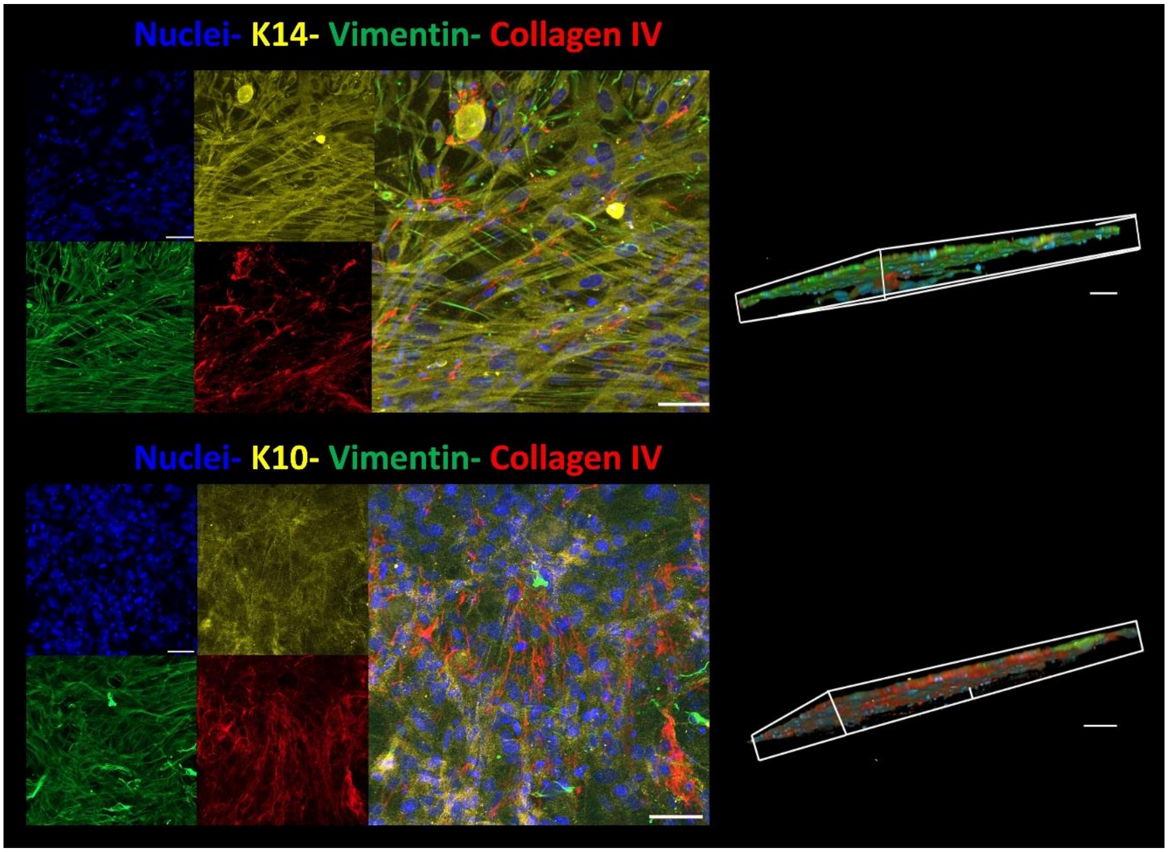

Figure 4.49. Immunofluorescence study of a full-thickness model (Hs-27/HEKn), 16 days post fibroblasts encapsulation. Single channels on the left, merged channel on the right: keratin 14-left and keratin 10-right (yellow), vimentin (green), and collagen IV (red). DAPI stained nuclei (blue). Examples from dextran + agarose gels. For each panel, maximum projections (left) and 3D views (right). Scale bars respectively 50 and 100 μm.

Besides the evaluation of keratin 14, which is confined in the basal layer of the epidermis colliding with the fibroblasts lying below, the keratin 10 signal, which normally appears on more differentiated supra-basal cells, was also evaluated (Figure 4.49- bottom panel). For the first time, a homogenous signal (yellow) could be distinguished on top of the dermal compartment, without showing detachment signals as observed before with HaCaT cells, proving the potential of the primary keratinocytes (HEKs) to mature and start to differentiate in our system.

To corroborate this hypothesis, further studies were performed. After fixation (day 16), part of the constructs was prepared for histology procedures, following the protocol described in the previous section. Then, samples were remitted to histology facilities, where 8 um sections were produced after OCT embedding. Finally, samples were stained following different strategies. First, Hematoxylin and Eosin staining were executed. As shown in Figure 4.50, a continuous epidermis layer can be appreciated along the entire histological cut (upper panel), demonstrating a better differentiation if compared with our previous HaCaT-based models.

From the zoom-in picture (lower panel), the HEKn stratification and differentiation can be clearly observed, resulting in distinct strata in the epidermis, which proved the ability of HEKn cells to adhere on top of Formulation 6-based gels, to grow, stratify, and differentiate in 13 days post-seeding.

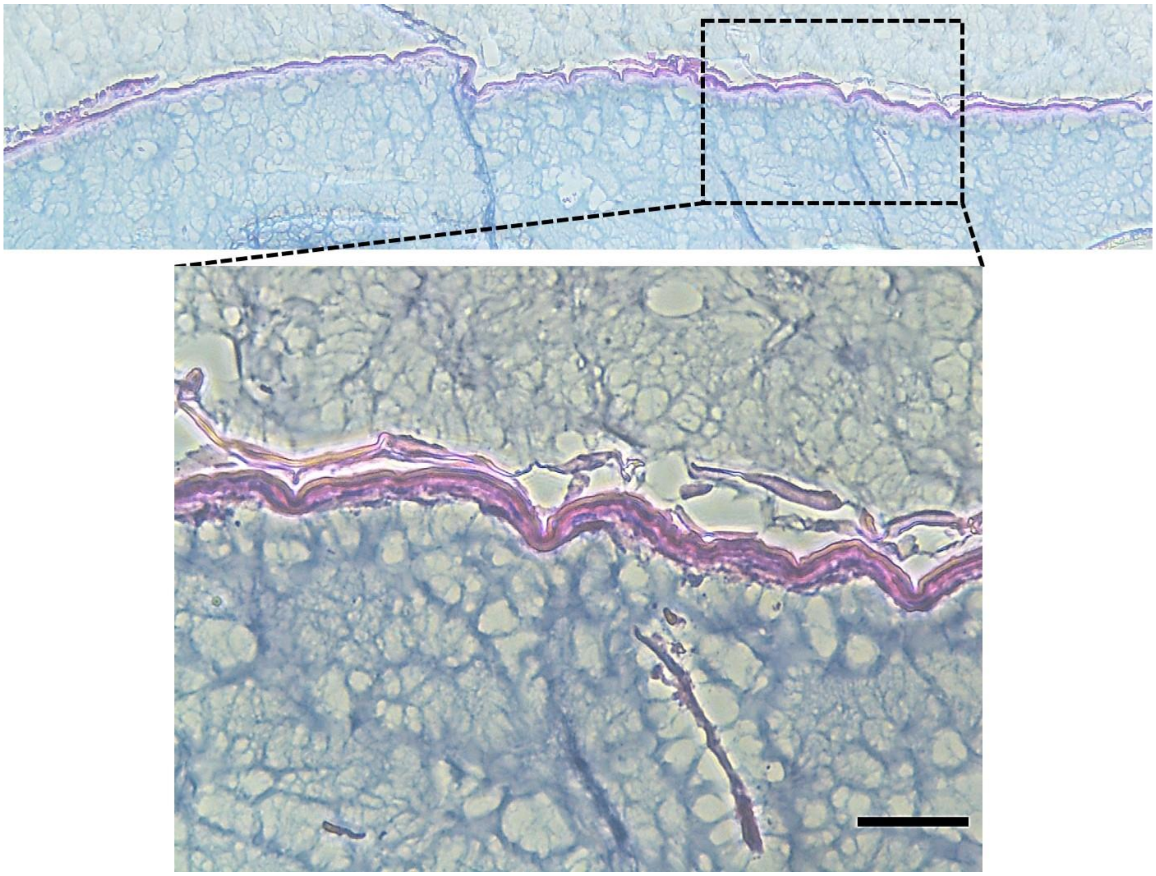

Figure 4.50. Hematoxylin and Eosin staining. The entire hydrogel section (8 µm in thickness)- upper panel- and a portion magnification – lower panel- containing HEKn differentiation and stromal compartment (Hs-27/HUVEC). Scale bar = 300 µm.

The human epidermis, which presents a thickness of more than 100 µm, is mainly composed of keratinocytes at different stages of differentiation.[357]In the scheme below (Figure 4.51) a general overview of the distinct single *strata* of the epidermis with the corresponding specific markers is illustrated. The outermost layer is called stratum corneum and it is formed of multiple layers of anucleate keratinocytes- the corneocytes-.[357] Moving from the outermost layer - the stratum corneum- to the deeper layer of the epidermis, there are stratum granulosum (SG), stratum spinosum (SS), and stratum basale (SB).

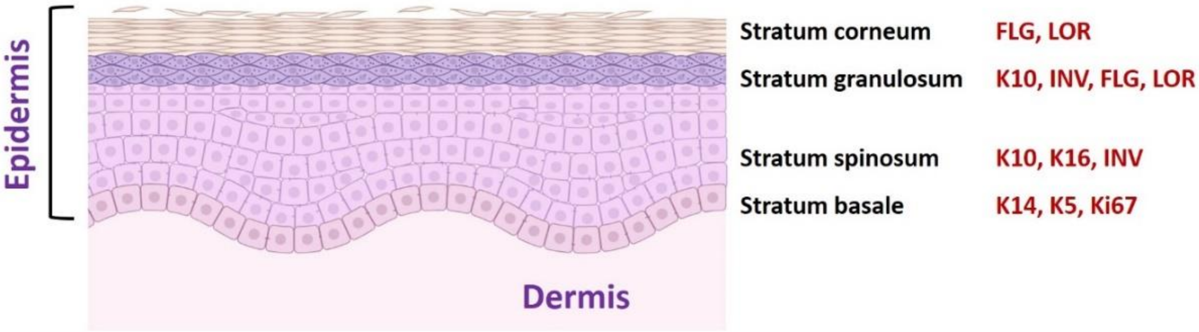

Figure 4.51. Specific markers for each stratum of the epidermis compartment. From the most differentiated layer (upper layer) – stratum corneum (filaggrin-FLG-, loricrin-LOR-), stratum granulosum (keratin 10-K10-, involucrin-INV-, filaggrin-FLG- loricrin-LOR-), stratum spinosum (keratin 10-K10-, keratin 16 -K16-, involucrin -INV-) to the basal layer (bottom layer) – stratum basale (keratin 14-K14-, keratin 5-K5-, Ki67).

Each layer, which is formed by keratinocytes, is distinct from the others depending on the differentiation state. So, the less differentiated cells are found in the stratum basale, while the terminally differentiated ones reside in the outermost layer. There is an additional layer just between the stratum corneum and the granulosum, known as stratum lucidum, which is found in the soles and palm, and represents the thickest parts of the skin (not represented in the scheme, Figure 4.51).[357] Hence, the potentials of primary keratinocytes (HEKn) were examined by investigating every single stratum of our reconstructed epidermis model corresponding to each state of the differentiation process (Figure 4.52). Each histological section was stained against specific epidermal markers to better spot the single differentiation state. Vimentin and collagen IV were included to better distinguish the dermal compartment underneath. The basal layer was identified by the expression of K14 (magenta) (Figure 4.52- lowest panel), revealing a complete monolayer on top of a well-organized dermal structure marked by vimentin (green) and collagen IV (red), as we previously observed in general top views of the scaffolds (Figure 4.49-left panel). In the basal layer, cells normally present a cubical shape. Undergoing the gradual differentiation process, they start changing their morphology, becoming increasingly flattened up to the stratum corneum where they are found as nucleus-free cells. However, at this stage of our qualitative studies, this evidence cannot be noticed.

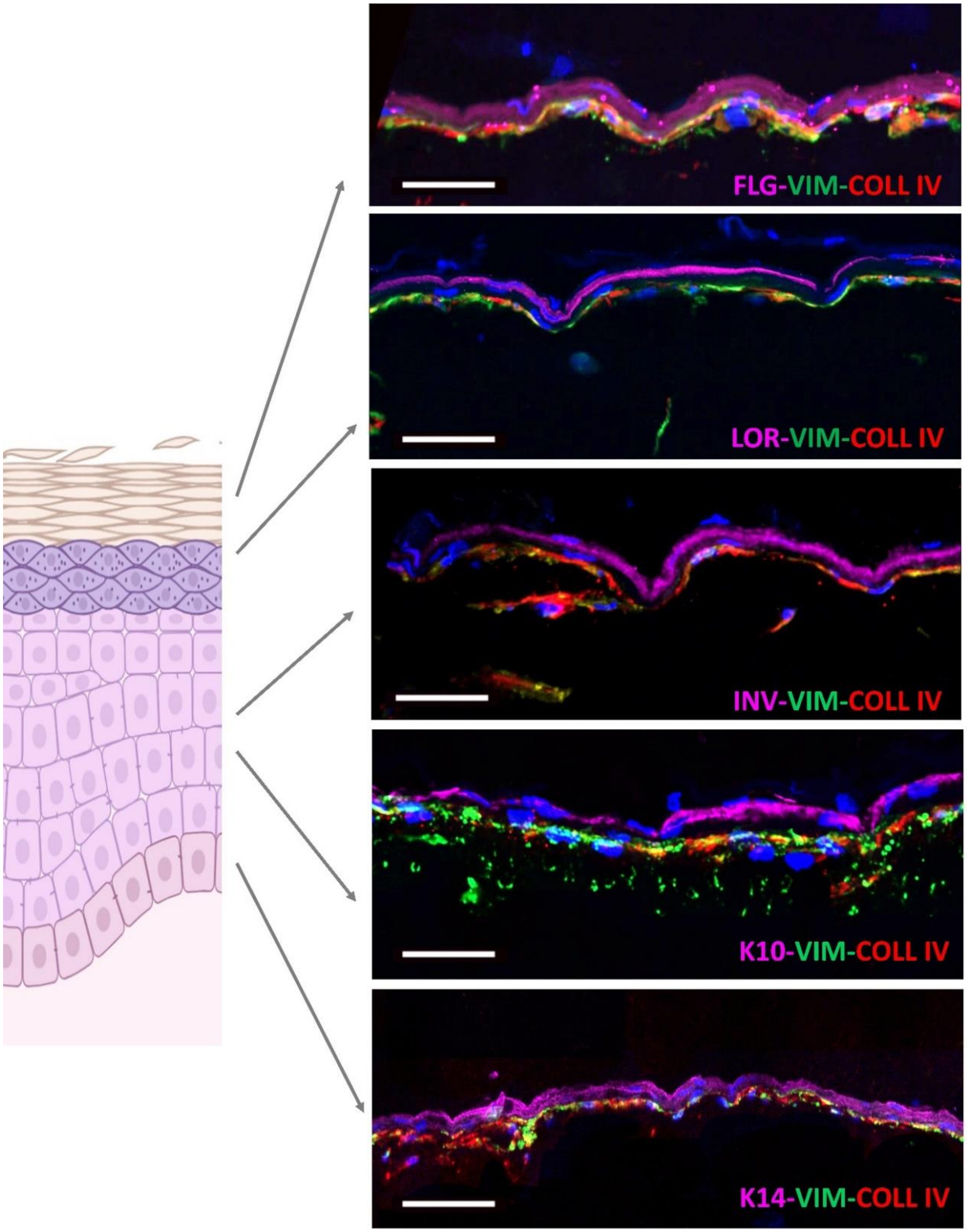

Figure 4.52. **Immunofluorescence studies of histological sections of Formulation 6-based hydrogels with a co-culture system (Hs-27/HEKn) 16 days post fibroblasts encapsulation.** Differentiation-specific markers of the later stage (Filaggrin, Loricrin, and Involucrin- magenta) and early stage (K10, K14- magenta) were used to stain HEKn. Vimentin (green) and collagen IV (red) were used to stain the dermis (Hs-27). DAPI stained nuclei (blue). Examples reported here are from norbornene-dextran (+ agarose) gels. Scale bars = 50 µm.

At different stages of the differentiation, keratinocytes expressed other specific keratins, such as K10 which can be appreciated both in the spinosum and the granulosum layers. In our samples, the K10 signal (magenta) was well-visible along the entire histological cut and distributed right upper of the basal layer (Figure 4.52 -second panel from the bottom). In the pathway of terminal differentiation, one of the most significative markers for the early stages is doubtless involucrin (INV), which is synthesized when keratinocytes have already left the basal layer and start to enlarge. Figure 4.52-third panel, shows INV expression (magenta), mainly distributed in the spinous layer, even though its signal could be also distinguished in the stratum granulosum. If the calcium level is increased to induce stratification, as in the case of the KDM medium employed during ALI culture conditions, INV$^+$ cells are directly expelled from the basal layer. This phenomenon means that the migration from the basal layer may be not a cause of terminal differentiation but its consequence.[358]

Together with INV, loricrin (LOR) is one of the major components of the cell envelope, facilitating terminal differentiation for the formation of the skin barrier.[359] Human LOR is an insoluble protein, and it is initially expressed in the granular layer during cornification. Its expression is strictly linked to the keratinocyte terminal differentiation *in vitro* and *in vivo*. As reported in Figure 4.52 (fourth panel, magenta) HEKn differentiated by developing a continuous granulosa layer-like structure, pointing to the beginning of the cornification. Moreover, it was demonstrated that LOR transcription can be upregulated when keratinocytes are induced to differentiate by calcium.[360]

Among the specific proteins of the cornified layer, there is filaggrin (FLG), which covers a crucial role in the structure and the function of stratum corneum (SC), the stratum that provides the physical barrier and acts as the first line of host defense against the external environment.[361] FLG expression was also revealed (Figure 4.52-upper panel-) in our model, pointing out at least, the beginning of keratinocytes' cornification. Since the FLG signal was also expressed in stratum granulosum, the complete formation of SC was difficult to demonstrate, as also revealed by hematoxylin and eosin staining (Figure 4.50). FLG relevance is also correlated to its ability to aggregate keratin intermediate filaments, although the mechanism is still not fully understood.[361,362] Comparative studies without including agarose in the polymer formulation were conducted in parallel, revealing no significant differences among the constructs.

These studies proved the development of a full-thickness skin model, where a well-formed dermal compartment and a differentiated epidermis construct have been established. Hence, this work provides a promising starting point to improve the model by the incorporation of different cell types.

4.6.7. Hydrogels' vascularization: towards a vascularized skin model

As reported in Section 3.5.9, our biomimetic approach counted on realizing a more complex skin model. Until this stage, the work focused on developing a strategy to obtain proper dermal and epidermal compartments. Once this objective was reached, endothelial cells were also included in the system, to echo the *in vivo* skin models. For this purpose, co-culture systems of human dermal fibroblasts (Hs-27) and endothelial cells (HUVEC) were prepared, based on Formulation 6 (with and without including agarose). First, Hs-27-laden and HUVEC-laden constructs were produced as controls, to check HUVEC's behavior when embedded in our gels. Then, some trials were performed to define the best co-culture ratio between Hs-27 and HUVEC cells. For all the above-mentioned tests, the constructs were kept under submerged conditions for 7 days, fixed, and then analyzed by immunofluorescence to inquire about the impact of the extracellular matrix composition (+/- agarose) on cells' behavior.

For the dextran-only based gels, HUVEC cells did not show an elongated shape, hence a proper CD-31 expression, which should make visible the adhesions between endothelial cells (Figure 4.53- left panel). Hs-27, instead, appeared elongated with well-visible connections, as expected (Figure 4.53- right panel).

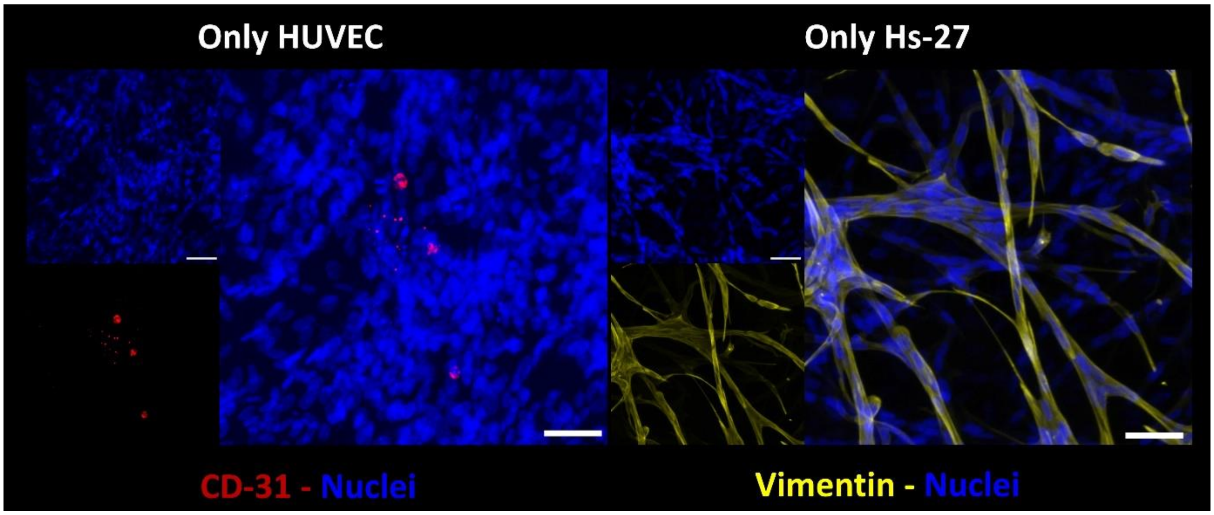

Figure 4.53. **Immunofluorescence of Dextran-only based gels, 7 days post-encapsulation**. HUVEC cells-left panel- and Hs-27- right panel (controls). CD-31 (red) stained HUVECs, and vimentin (yellow) stained Hs-27. DAPI was used to stain nuclei. Scale bars = 50 µm.

For the dextran + agarose gels, HUVEC cells enhanced a slightly higher CD-31 expression (Figure 4.54-left panel), even though no protrusion was observed. For Hs-27 alone, spread cells were noticed (Figure 4.54 -right panel) although they were not elongated as well as within dextran-only based gels.

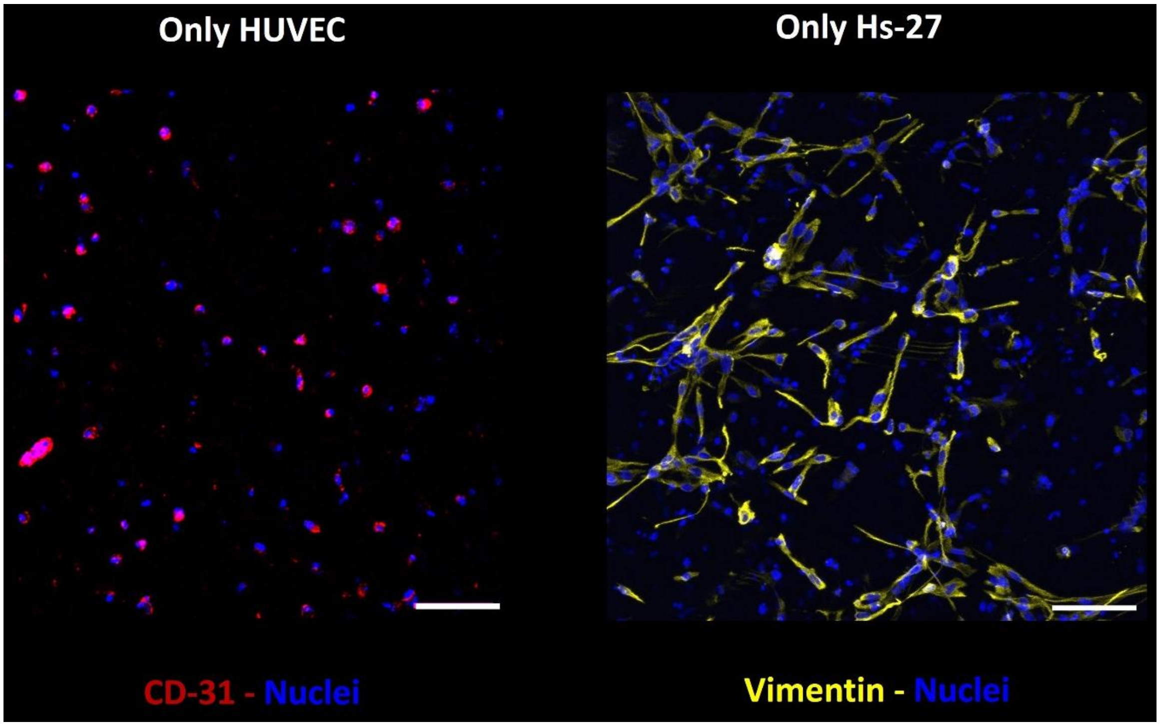

Figure 4.54. Immunofluorescence of Dextran +agarose-based gels, 7 days post-encapsulation. HUVEC cells-left panel- and Hs-27- right panel (controls). CD-31 (red) stained HUVECs, and vimentin (yellow) stained Hs-27. DAPI was used to stain nuclei. Scale bars = 50 µm.

For Hs-27 alone, the encapsulation density was kept as the one optimized (2 x 10^6 cells/ml), instead for HUVEC cells alone, preliminary tests were necessary. Since for a cell density of 2 x 10^6 cells/ml the CD-31 signal was almost undetectable, it was increased up to 3 x 10^6 cells/ml.

When the co-culture systems were prepared, different ratios of Hs-27: HUVECs were explored. First, a ratio Hs-27: HUVEC of 2:1, and a total density of 2 x 10 ^{6} cells/ml was considered. For dextran-only gels, noticeable differences were observed (Figure 4.55). Vimentin expression, marking both the cell types, was highly expressed, resulting in a dense cellular network. Moreover, CD-31 expression was also more visible, although the aspect was not the canonic one. Looking at the top maximum projection picture with merged channels (Figure 4.55 -bottom-left-) an intricate mesh was distinguishable, pointing out how the co-encapsulation leads to well-organized constructs. On the right side (Figure 4.55 -bottom-right-), a maximum projection view of the gels' bulk (inner of the gel) can be also appreciated, where cells resembled tubular-like structures (white arrows). Instead, for dextran + agarose-based gels, the CD-31 signal was not even detected, indicating that, with these conditions, just dextran-only gels could properly support Hs-27: HUVECs co-encapsulation. After several tests on distinct ratios of Hs-27/HUVEC, the optimal conditions were established, by using a total cells number of 2 x 10^6 cells/ml and a ratio of Hs-27/HUVEC of 1:3.

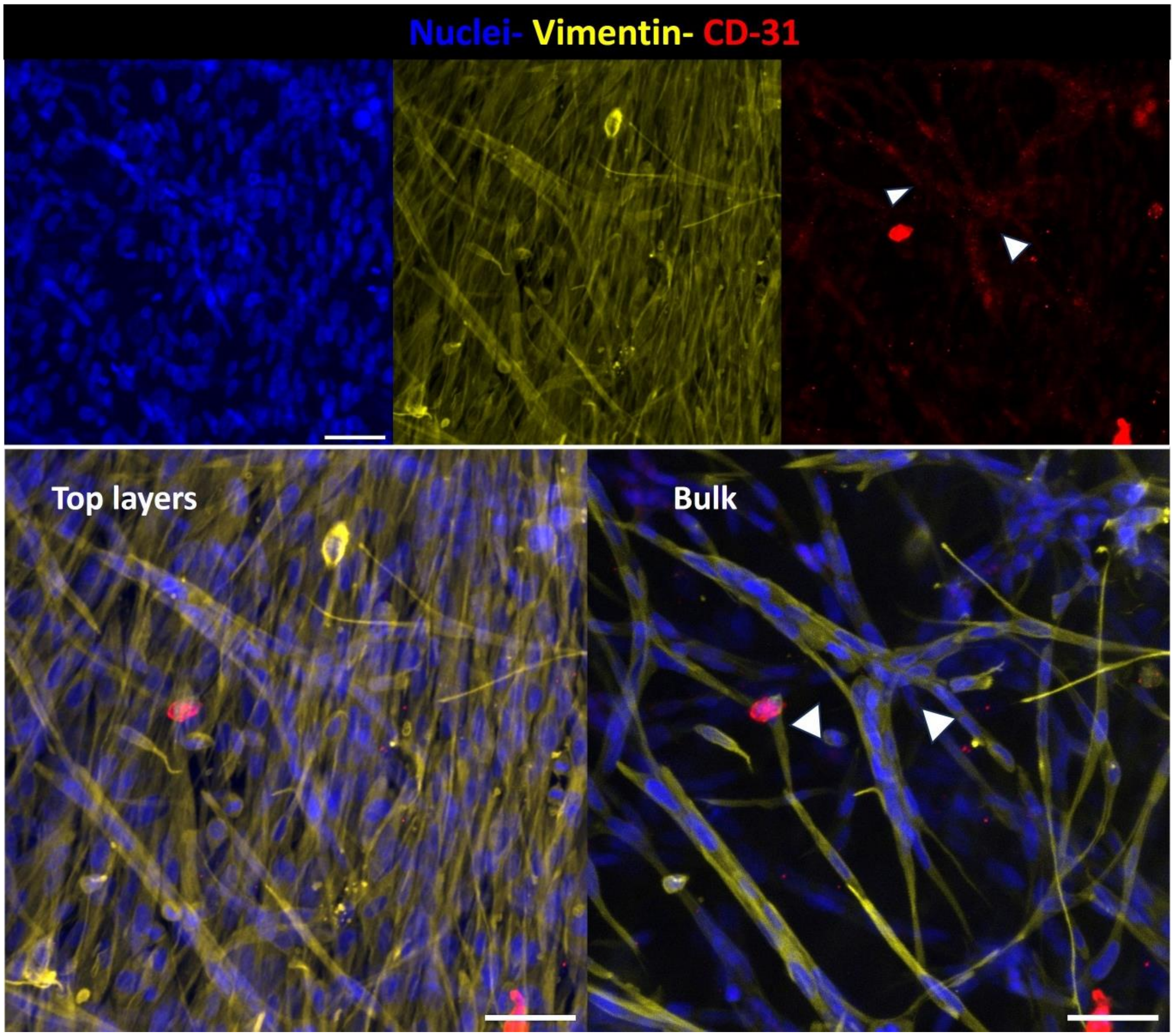

Figure 4.55. Immunofluorescence of co-culture systems (Hs-27: HUVEC - 2:1) within dextran-only based gels. Maximum projections 7 days post encapsulation. Vimentin (yellow) to stain both cell types, CD-31 (red) specific for HUVEC cells. DAPI was used to stain nuclei. Merged channel-top layers-bottom-left side; bulk view on the bottom-right side. Scale bars = 50 µm.

With the optimized conditions, for the dextran-only based gels (co-culture systems), the cells' behavior was not that dissimilar to the previous one. Vimentin was expressed, (Figure 4.56) even though the intricate network observed before this time was not so evident, probably due to the decrease of Hs-27, while the CD-31 signal showed again a spotted expression.

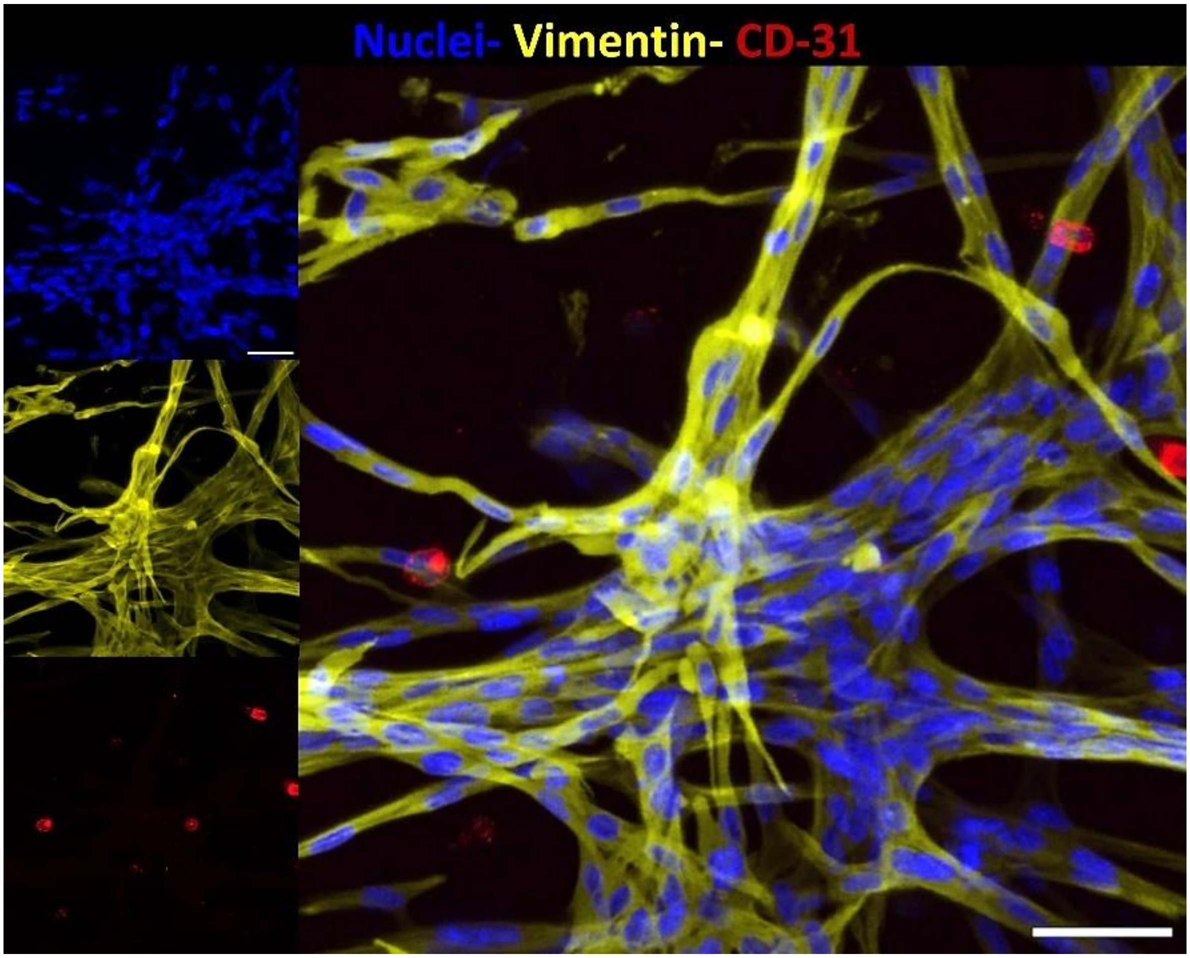

Figure 4.56. Immunofluorescence of co-culture systems (Hs-27: HUVEC - 1:3), within dextran-only based gel. Maximum projections 7 days post encapsulation. Vimentin (yellow) to stain both cell types, CD-31 (red) specific for HUVEC cells. DAPI was used to stain nuclei. Single channels -left side; merged channels – right side. Scale bars = 50 µm.

Surprisingly, for dextran-agarose gels, huge differences were observed. An entangled structure was noticed, where both cells created very dense connections among each other, leading to convolute and tubular systems (Figure 4.57). All the markers appeared expressed, showing a twisted and labyrinthine complex cell arrangement.

Together, these results indicated the potentiality of our models to be able to support a co-culture of dermal human fibroblasts with endothelial cells, to build a vascularized system. Although these tests represented the first attempt to combine our technology with different types of cells, promising steps were made, toward a complex skin model.

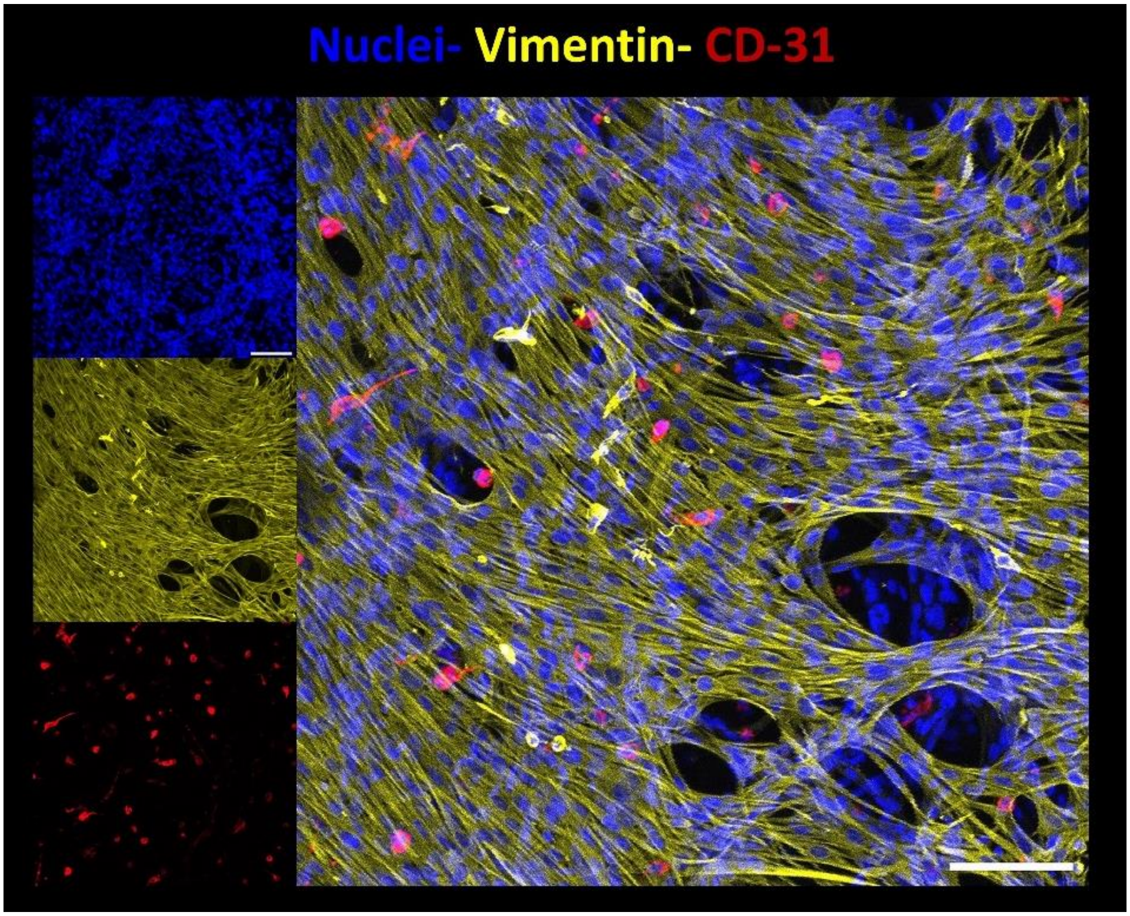

Figure 4.57. Immunofluorescence of co-culture systems (Hs-27: HUVEC - 1:3), within dextran + agarose-based gel. Maximum projections 7 days post encapsulation. Vimentin (yellow) to stain both cell types, CD-31 (red) specific for HUVEC cells. DAPI was used to stain nuclei. Single channels -left side; merged channels – right side. Scale bars = 100 µm.

4.6.8. Full-thickness vascularized skin model

Once the differentiation of the HEKn exhibited the potential of this hydrogel composition to establish a significant full-thickness skin model, further experiments were conducted to incorporate the vasculature system. As reported in section 4.6.7, preliminary studies on the co-encapsulation of Hs-27 and HUVEC cells corroborated the perspective of the scaffold developed to be functional also in the vasculature system inclusion. The possibility of creating a full-thickness model, in which keratinocytes successfully reach differentiation and endothelial cells can grow and forge a vasculature network together with dermal fibroblasts was the focus of this last experimental part.

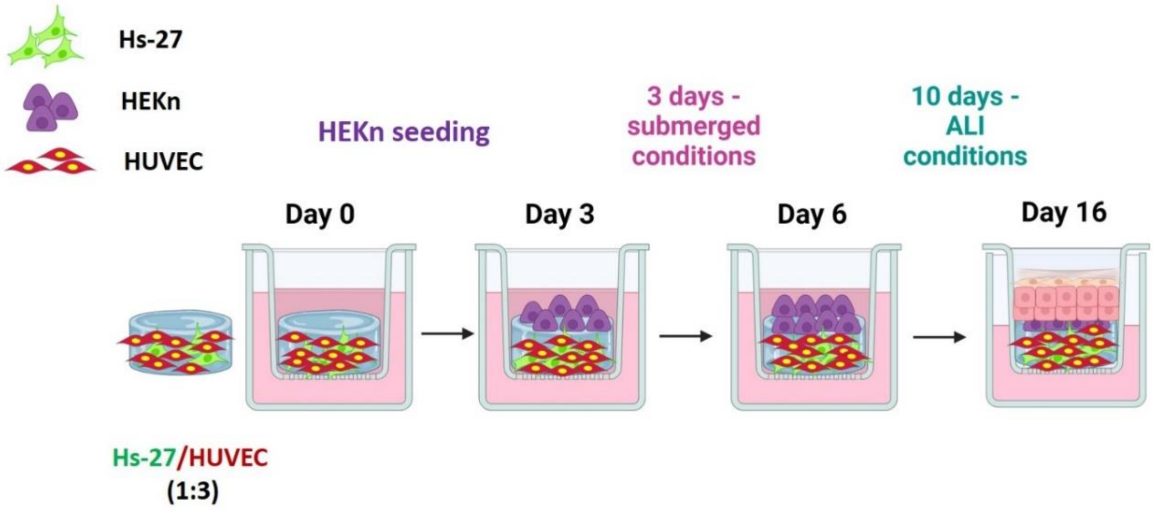

Figure 4.58. Schematic representation of the co-culture process. On day 0 hydrogels were fabricated encapsulating human dermal fibroblasts together with HUVECs (ratio 1:3), followed by seeding HEKn on top of cell-laden scaffolds (day 3). At day 6, Air-Liquid-Interface conditions were applied up to day 16.

According to previous experiments, a 1:3 ratio between Hs-27: HUVECs was selected as the optimal one. Besides the co-embedding in the stromal compartment of the gels, the protocol established to resemble the epidermis was kept invariant from the last experiments conducted, as illustrated in Figure 4.58. As a first approach, a general view of the entire constructs was explored, to understand if the co-presence of fibroblasts and endothelial cells was causing some alterations in the epidermal compartment. Hence, an immunofluorescence study was conducted: CD-31 (red) was selected to stain HUVECs cells while K14 (yellow) stained HEKn and collagen IV (green) to evaluate the collagen production.

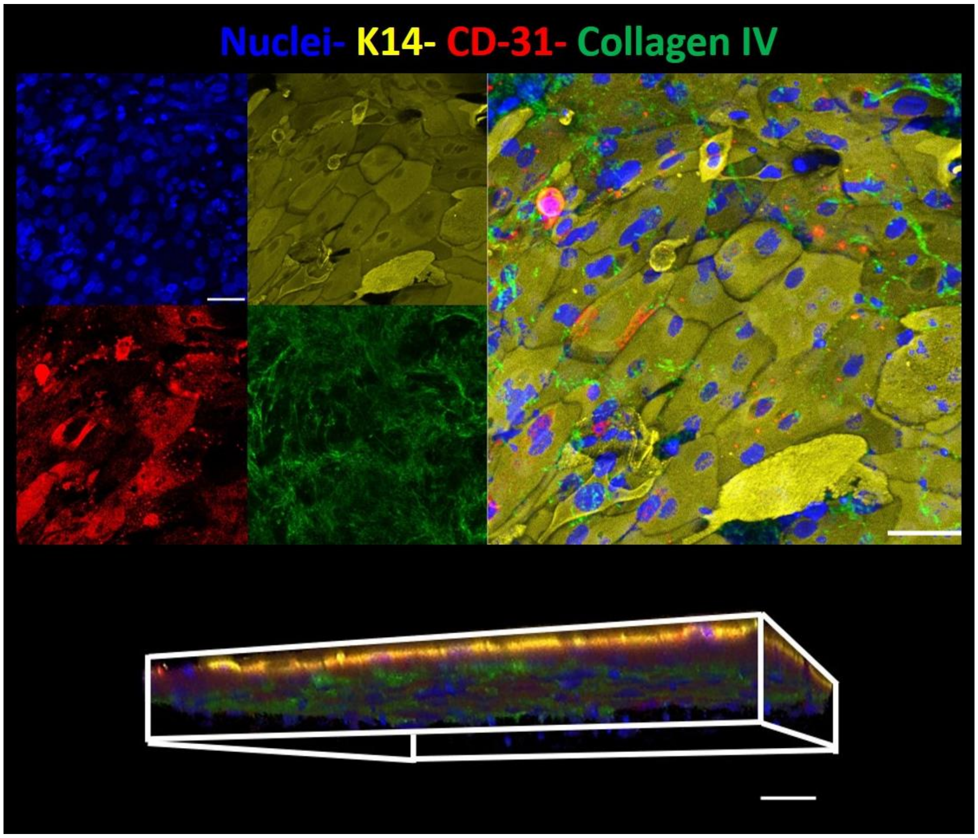

Figure 4.59. Immunofluorescence study of a vascularized full-thickness model (Hs-27/HUVEC/HEKn), 16 days post fibroblasts encapsulation. Maximum projection – upper panel – and 3D view – lower panel-. Single channels on the left, merged channel on the right: keratin 14 (K14) (yellow), CD-31 (red), and collagen IV (green). DAPI stained nuclei (blue). Scale bars respectively 50 µm and 100 µm.

As depicted in Figure 4.59, the K14 signal proves the epidermis monolayer establishment, showing a packed structure on top of the gels. Instead, the CD-31 signal (red), which previously appeared in a spotted way, is now well-expressed, indicating early and mature endothelial cells. Collagen IV was also highly expressed, showing a shape and distribution like HUVECs-free gels.

On the other hand, deeper studies were carried out to explore the epidermis' differentiation when endothelial cells were also included. Again, histological sections of the samples were prepared and stained. Hematoxylin and eosin staining were performed on the samples' sections to provide a more comprehensive view of the microanatomy of the tissues created (Figure 4.60). The study enhances a well-defined compartmentalization of the gels, showing distinctly the keratinocyte differentiation, organized in strata, and the dermal part with spread cells underneath, homogeneously distributed along the whole construct.

Spindle-like fibroblasts were discernible, despite the reduced sizes of the histological cut. As enhanced in Figure 4.60 (zoom-in), the different strata, respectively basale, spinosum, and granulosum were evident, together with elongated cells from the dermal compartment.

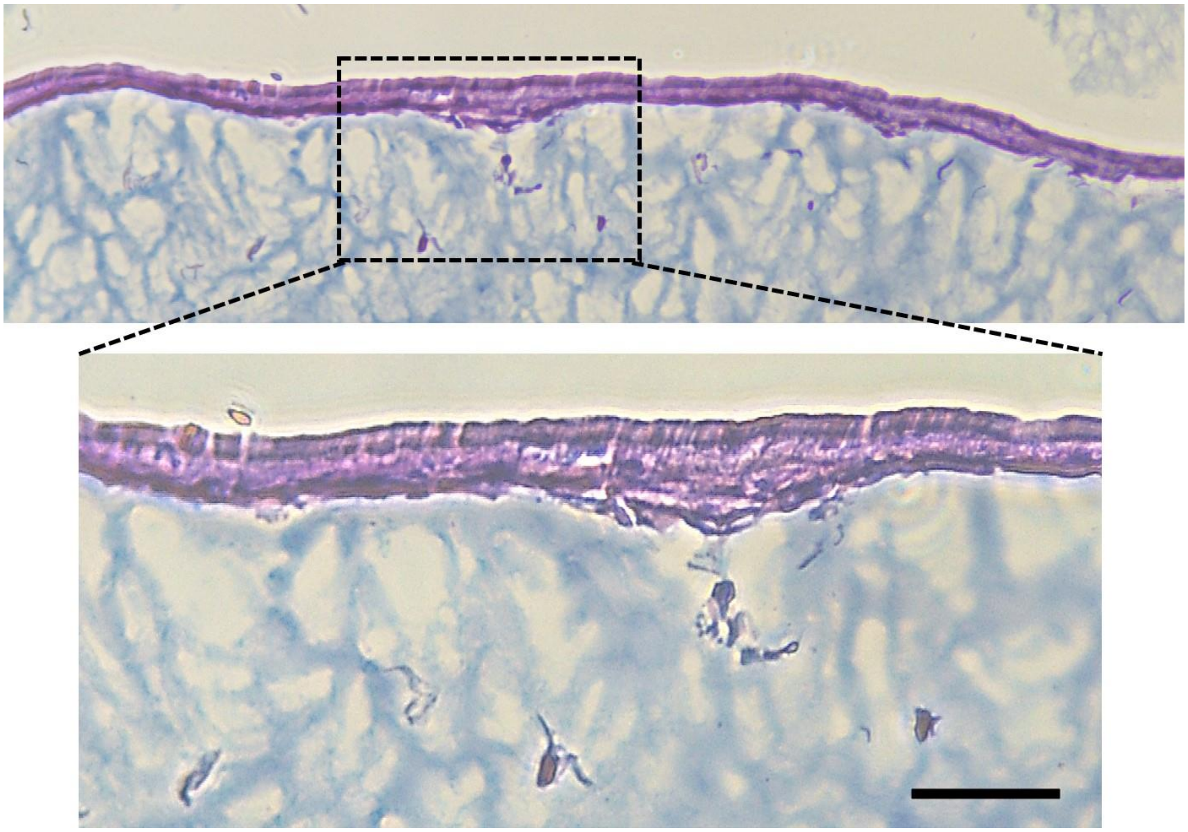

Figure 4.60. Hematoxylin and Eosin staining. The entire hydrogel section (8 μm in thickness)- upper panel- and a portion magnification – lower panel- containing HEKn differentiation and stromal compartment (Hs-27/HUVEC). Scale bar = 300 μm.

Later, the staining against the most representative differentiation markers was also performed. Starting from the inner epidermis and moving along the entire thickness, each marker was well-visible through the immunofluorescence study. As reported in Figure 4.61, for the stratum spinosum, both K10 and INV (both in magenta) appeared continuous and well-distributed along the entire section (bottom panels- Figure 4.61). Raising towards the later stage of the keratinocyte differentiation, LOR and FLG (both in magenta) were also expressed, pointing out the formation of stratum granulosum and, probably, the achievement of keratinocytes cornification (upper panels- Figure 4.61). As also observed from the previous staining (Figure 4.60), apart from the three distinct layers (basale, spinosum, and granulosum), we cannot affirm with certainty the formation of stratum corneum.

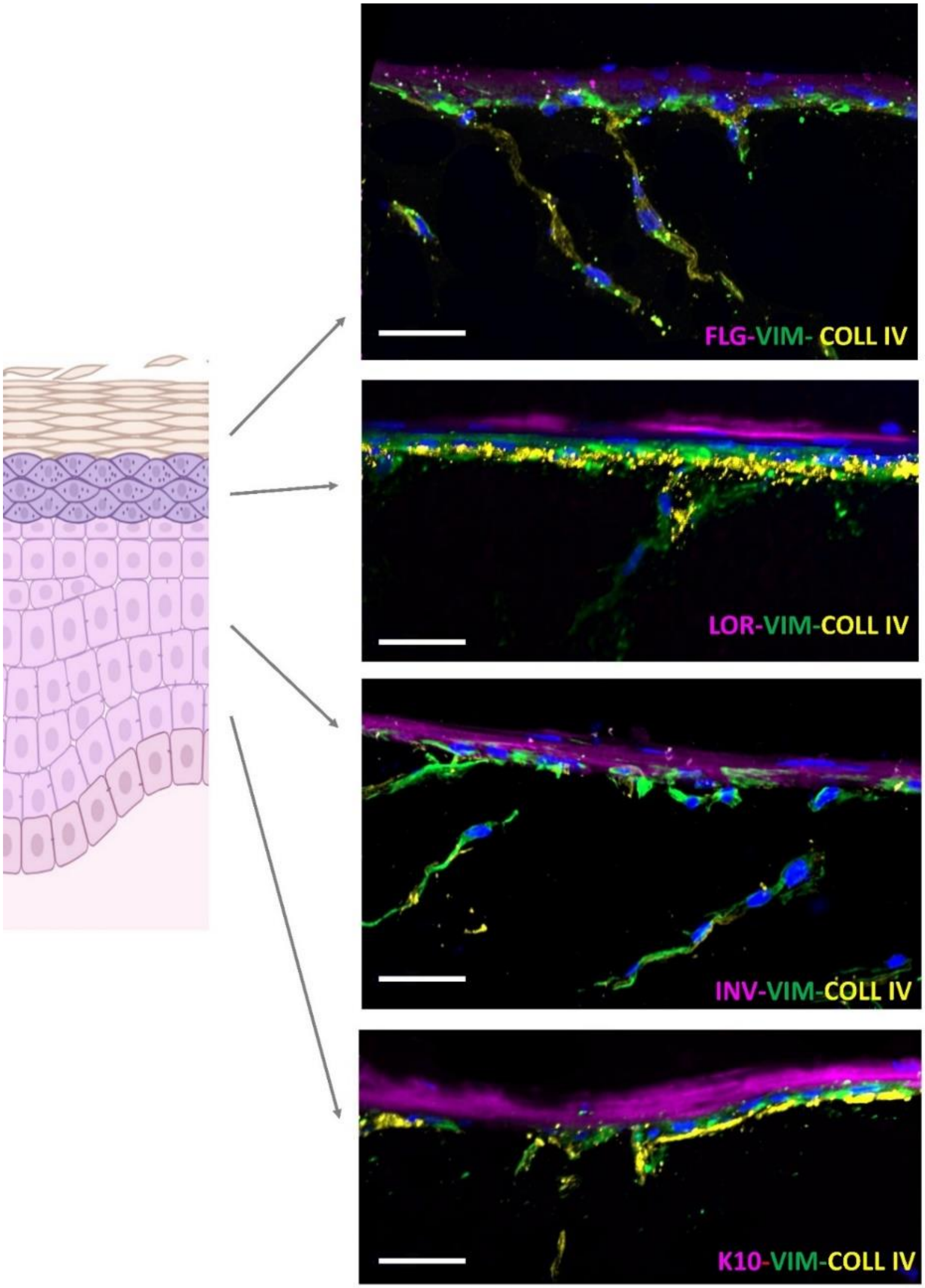

Figure 4.61. Immunofluorescence studies of histological sections of Formulation 6-based hydrogels with a co-culture system (Hs-27-HUVEC-HEKn) 16 days post-Hs-27/HUVEC encapsulation. Differentiation-specific markers of the later stage (FLG, LOR, and INV-magenta) and early stage (K10-magenta) were used to stain HEKn. Vimentin (green) and collagen IV (yellow) were used to stain the dermis (Hs-27/HUVEC). DAPI stained nuclei (blue). Examples reported here are from norbornene-dextran (- agarose) gels. Scale bars = 50 µm.

Although the epidermal compartment does not show significant variations compared to the gels without HUVECs (Figure 4.52), at least from this qualitative evaluation, the stromal compartment appeared quite different, with higher expressions of both vimentin (green), and collagen IV (yellow) just below the epidermis. Certainly, due to the co-encapsulation (HUVECs: Hs-27), cells seemed more elongated and spread compared to HUVECs-free gels (Figure 4.52). Hence, the incorporation of endothelial cells promotes the stromal arrangement, boosting the cells' elongation in an evident manner. Again, comparative studies between gels containing or not agarose were performed, without showing consistent differences. However, several independent experiments and quantitative analyses are necessary to establish the impact of agarose on the cells' behavior. Lastly, further inspections on the potential of the vasculature incorporation were preliminarily examined, by investigating endoglin expression. Endoglin is a glycoprotein primarily found on endothelial cells and its expression increases during inflammatory conditions and in skin lesions where there is endothelial cell proliferation. Endoglin can bind to transforming growth factor beta (TGF-beta), thereby decreasing its bioavailability. From this preliminary inquiry, as highlighted in the immunofluorescence study (Figure 4.62), the Endoglin signal (red) indicates activated endothelial cells, demonstrating their proliferative capacity. [363]

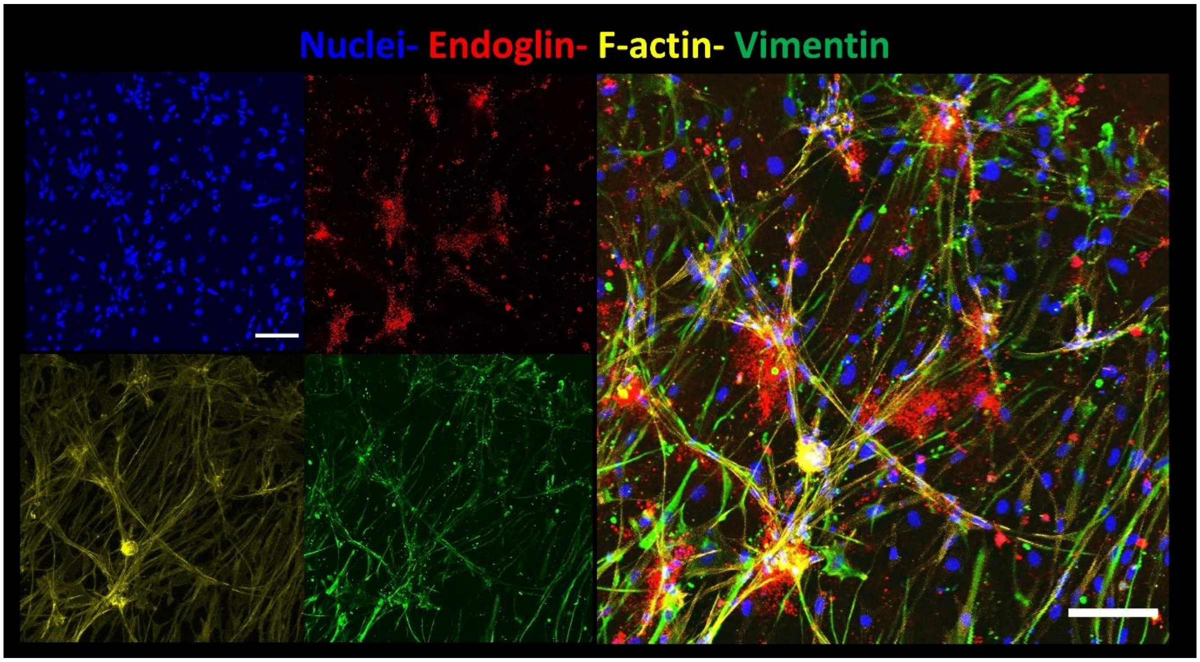

Figure 4.62. Immunofluorescence study of a vascularized full-thickness model (Hs-27- HUVEC-HEKn). Maximum projections 16 days post encapsulation. Single channels on the left, merged channel on the right: Endoglin (red), F-actin (yellow), and vimentin (green). DAPI stained nuclei (blue). Scale bars = 50 μm.

These last studies provide a significant step ahead in the panorama of skin tissue models resembling. Developing a gel structure able to recreate skin extracellular matrix, incorporating a vasculature system, and supporting a tangible epidermis differentiation above, represents a big achievement, proving the ability of our norbornene-dextran (+/- agarose) based hydrogels (Formulation 6) to robustly hold up a vascularized full-thickness skin model, closer to the *in vivo* one.

5. Discussion

Traditional two-dimensional (2D) cell studies fail to accurately represent the native architecture and functionality of human skin tissue. The human skin constitutes a dynamic environment, the complexity of which poses significant challenges for accurate recapitulation *in vitro*.[364] Currently, advanced *in vitro* models, including three-dimensional (3D) bioprinting and skin-on-a-chip platforms, present significant opportunities for enhancing our understanding of skin physiology and for the development of therapeutics and drugs. These models more accurately replicate the distinct layers of skin, facilitating the formation of an extracellular matrix (ECM) that supports multidirectional cell growth, and enables micronutrient distribution analogous to *in vivo* tissue. In addition to custom 3D skin models, numerous commercially available models based on prefabricated single or multilayer constructs, such as Episkin®, Epiderm®, and Apligraf®, are used for *in vitro* toxicity studies, permeation, efficacy testing, and grafting applications.[120] The general categorization of the *in vitro* skin models includes human reconstructed epidermis (RHE) and human skin equivalents (HSE). RHE models are primarily utilized for assessing phototoxicity and evaluating the effectiveness of commercial products in a standardized manner.[120] These models are generally based on isolated normal human keratinocytes that are expanded in a culture medium. To reliably reproduce the physiology and morphology of the human epidermis, the cells are seeded into Transwell® inserts and initially cultured under submerged conditions; then they are exposed to an air-liquid interface to promote differentiation, resulting in a complete process that typically takes between two and three weeks.[365] Conversely, HSE models incorporate a dermal layer, predominantly consisting of fibroblasts embedded within a three-dimensional matrix, in addition to a fully differentiated epidermis. The preparation of an HSE model begins with the cultivation of a fibroblast-loaded matrix for several days, followed by the seeding of keratinocytes on top of the cell-laden dermal scaffolds. This is performed using a protocol like that employed for RHE systems.

Several fabrication techniques have been applied for ECM regeneration, such as electrospinning, photocrosslinking, or 3D printing.[364] 3D bioprinting shows great potential for the fabrication of tissue-engineered skin, meeting either clinical or industrial requirements.[234] Throughout its flexibility, and reproducibility with high resolution, this method can be customized by mixing cells and suitable materials, previously selected, to be precisely distributed to achieve skin substitutes. In this context, hydrogels, made of natural or synthetic polymers, once blended with cells or organoids, provide an extracellular matrix resemblance, facilitating the diffusion of nutrients, growth factors, and cytokines through the constructs.[366]

Natural components often show deficient mechanical properties and decreased reproducibility, leading to the introduction of synthetic polymers, especially to fine-tune the characteristics of the gels.[367] Thereby, the peculiar properties of natural compounds, such as increased cell migration and proliferation, and the favorable characteristics of synthetic bioinks are mixed to regulate the printability, elasticity, and thermal stability of the resulting gel.[367] To establish a 3D-skin model, several criteria must be met, to provide both structural and rheological properties, essential for the bioprinting process while ensuring good cell interactions. The choice of biomaterial is a crucial factor for cell survival. It must be compatible with dermal end epidermal cells, stimulating their growth, and encouraging an appropriate host response after cell seeding, avoiding immunogenic reactions.[368,369]

Collagen is commonly considered the gold standard for skin regeneration due to its tissue-matching physiochemical properties. As one of the main structural proteins of the extracellular matrix, collagen provides excellent biocompatibility[367] and promotes cell adhesion, proliferation, and migration. However, it is not exempt from drawbacks, since collagen type I shows weak mechanical properties and tends to contract when fibroblasts are embedded within.[370] Gelatin, a denatured form of collagen, is also commonly used since it can be (i) physically crosslinked using thermal gelation, or (ii) photocrosslinked in the presence of a photoinitiator and UV light, when altered with photopolymerizable methacryloyl groups, as GelMa.[371] However, no single bioink presents ideal preconditions on its own, hence they are often combined. For instance, *Stratesteffen et al.*[372] combined collagen and GelMA enhancing cell spreading, and resulting in excellent cell viability, leading to the formation of capillary structures inside the gel.[372]

In this regard, the experiments presented in this thesis and the illustrated results aim to demonstrate how a new 3D *in vitro* skin model can be developed as an alternative to the existing ones. In the first part of the work, a 3D hydrogel scaffold was created based on thiol-ene click chemistry, satisfying specific parameters and resulting in an epithelized-dermal scaffold. Then, the physiological relevance of the developed skin model was increased to better replicate the native tissue, including a vasculature system.

Throughout the thesis project, different combinations of hydrogel compositions have been prepared by mixing natural polymers and synthetic/or natural compounds to investigate their characteristics and elect the more appropriate to resemble the skin model. As already discussed in the introduction part, the gelation process can occur through physical or chemical crosslinking. However, chemical crosslinking guarantees the formation of permanent and highly stable structures compared to physical crosslinking.[169]

The covalent hydrogels can be obtained via radical-mediated polymerization, step-growth polymerization (e.g. Diels-Alder reaction, thiol-based Michael-type conjugation), photopolymerization, or through bio-orthogonal click reactions. Radical-mediated polymerizations take place by applying an appropriate light source or through enzymatic activity. Although they occur quite fast and presenting sometimes the possibility of controlling kinetics reactions spatiotemporally, they usually contain high molecular weight and heterogeneous crosslinks. On the other hand, the step-growth polymerizations present no heterogenous crosslink, but they lack spatiotemporal control since the crosslinking starts after the reactive groups are mixed.[210] Photopolymerization initiated by light exposure, whether ultraviolet (UV) or visible light, permits easy control over the kinetics since the crosslinking initiation and termination can be modulated by light irradiation, however, the oxygen inhibition has effects on the polymerization profile.[373] Bio-orthogonal chemistry offers the advantage of not interfering with biological mechanisms, without being affected by the presence of salts and proteins, operating in aqueous solvents under different conditions.[374] Based on this, in 2009, *Anseth et al.*[209] developed a light- and radical-mediated step-growth polymerization scheme, based on the orthogonal reaction between thiol and norbornene, combining at the same time the positive aspects of radical-mediated polymerization and bio-orthogonal click reaction.

This thiol-norbornene click chemistry is the common thread among the numerous combinations tested in my PhD project. Numerable advantages, such as the depreciation of chemical toxicity and the subsequent reduction of the biological components' damage, make this chemistry particularly attractive in tissue engineering. The degree of network heterogeneity is minimized since no homopolymerization occurs between norbornene groups, unlike in the case of acrylate-based hydrogels. This results in an ideal hydrogel network structure composed of orthogonal crosslinks.[207] The reaction mechanism, extensively documented by *C.C. Lin et al*, is faster than acrylate-based chain growth polymerization,[212] not inhibited by oxygen, and requires low concentrations of photoinitiator and macromer.[210] Moreover, gels based on thiol-norbornene chemistry can be degraded by cell-secreted proteases when the protease-sensitive peptides are used in the crosslinker formulation (MMP-sensitive peptide linker).[218] This results in local microenvironment remodeling, which could be interesting also for *in vivo* applications.

Printability tests were conducted by employing a synthetic polymer -polyvinyl alcohol (PVA)- and a natural one -pullulan (PLN)-, coupled with norbornene, while thiol-modified polyethylene glycol (PEG) and hyaluronic acid (Hy) were used as crosslinkers. Specifically, three formulations were examined: N-PVA: PEG-link: LAP (Formulation 1), N-PLN: PEG-link: LAP (Formulation 2), and N-PLN: Hy-link: LAP (Formulation 3). Printability is one of the fundamental prerequisites to respect since the bioinks must be in contact with cells. As reported in section 4.1.1, among the combinations evaluated, the norbornene-pullulan-based preparation with PEG-link (Formulation 2) emerged as the easiest to be printable, resulting in robust and thick gels, easier to handle compared with the other preparations, which produced more flabby structures. Hence, based on these considerations, Formulation 2 resulted as the appropriate scaffold for further evaluation and cell inclusion.

This preparation utilizes pullulan, a natural polysaccharide widely used in tissue regeneration due to its thermal stability and structural flexibility. Furthermore, it has been demonstrated that pullulan-based scaffolds accelerated collagen synthesis as well as fibroblast proliferation and epithelization, a shortcoming in the wound healing process.[146] In 2022, *F. Zhaoxuan et al.*[375] described the potentiality of norbornene-pullulan bioinks for digital light processing 3D printing, highlighting their high shape fidelity as well as good printability. As mentioned in the section- Materials and Methods- 3.1.1, these norbornene-pullulan-based bioinks, developed in the framework of the European project (BRIGHTER), are prepared on a small scale and are not commercially available. Given the required volumes for the SOLUS system (2 ml of pre-gel solution per printed gel) an alternative strategy was considered. An in-house Direct Laser Writing (DLW) system, with a 405 nm wavelength laser diode, was adopted to minimize the pre-gel volume to 15 µl per printed gel, overcoming the limitations of the low materials' availability and enabling printing scaffolds within 10 s. The first challenge was to investigate the impact of the working parameters (e.g. z-distance, light power) on the hydrogels' morphology, and consistency. The printability tests shed light on the importance of evaluating the printing parameters for predicting gel geometry or understanding their influence on the behavior of encapsulated cells. For instance, a shorter z-distance of the laser diode resulted in wider gel structures. This could be related to bigger areas of the pre-gel solution receiving the minimum dose needed to crosslink, which could be due to either lower absorption or wider exposure area caused by the cone of light. The irradiation power range was accurately defined (13 mW- 30 mW) to permit gel printability, without damaging cells, and minimizing the irradiation exposure time (10s).

All these aspects were deeply investigated, together with the exploration of the optimal molar ratio between N-PLN and PEG-link (5:4), since it has been observed that gels cannot be obtained for other molar ratios polymer: crosslinker (e.g. 5:1, 5:2, and 5:3), likely due to the phase separation that occurs because PLN and PEG are not miscible in certain ratios.[376,377] The formulation selected is quite novel. Due to high cost and the weak mechanical properties,[378] pullulan composites are often developed with other biopolymers, resulting in optimal drug delivery systems as demonstrated by Duceac et al.[378] that developed chitosan-pullulan hydrogel beads.

Self-standing rectangular-shaped hydrogels (5 mm x 1 mm x 0.5 mm) based on Formulation 2 were successfully printed, with a molar content of (N-PLN: PEG- link: LAP- 5 mM: 4 mM: 0.2 mM) and then characterized. One of the key points to consider studying the hydrogels' bulk geometry, is doubtless the swelling since it is strictly dependent on the crosslinking degree and the porosity.[379] At a higher degree of crosslinking, the hydrogel flexibility or its capability to swell or shrink in response to stimuli decreases.[101] This is one of the reasons why collagen is generally modified because collagen-based gels do not swell.[380] Furthermore, as reported in the study by *Shih et al.,* [214] low swelling ratios correspond to higher values of Elastic Modulus, which is important for predicting the stiffness of the gels. For Formulation 2-based gels, created with increasing power radiation (13 mW, 22 mW, and 30 mW) the swelling behavior was analyzed, resulting in a swelling volume ratio higher than 10 % for lower and higher power, while 40% was reached for the intermediate one, enhancing an important increase in the first 6 hours. These results denoted a certain structure flexibility and a good degree of crosslinking, beyond that were in line with the ones expressed from other biocompatible materials used in 3D applications.[211]

An ideal bioink for skin regeneration needs to exhibit optimal viscosity or rheology, while simultaneously providing support for facilitating cellular proliferation and interaction.[367] As claimed by Kalra et al.,[381] skin is highly anisotropic and viscoelastic, with Young's Modulus values ranging between 5 kPa and 140 MPa, values that are strictly dependent on the technique used to be determined (indentation, tensile test, or torsion test). For example, Young's Moduli found by indentation are significantly lower than the ones found by tensile test since the indentation contact is very small. However, as reported by Crichton et al.[382] there is a great disparity in the data reported in the literature varying by a factor of over 3000.[382] Herein, defining an accurate range is still difficult, even though some guidelines can be considered, being in the same order of magnitude.

For instance, studies such as Elleuche et al. and Jachowcz et al.[350,383] reported skin elastic moduli ranging between 7-33 kPa, using probes of several millimeters scale, while Bader and Bowker reported moduli around 1 kPa, increasing scale.[382] In this context, the bulk analysis that we performed (Norbornene-pullulan: PEG link) denoted a matrix with an average value of the Elastic Modulus of 5 kPa, comparable to the data reported before and resulting higher than the ones shown by *Zhaoxuan et al.* [375](0.6 kPa- 1.2 kPa) for gels based on Norbornene-pullulan alone, photocured with UV light, probably due to the presence of the PEG link.

Once assessed the mechanical properties of the gels, we aimed to evaluate whether the simulated gel microenvironment could support and promote cell activities such as proliferation, elongation, adherence, and lately maturation, stratification, and differentiation.[384] In general, for other models, the cells mainly involved in resembling the complexity of skin tissue regeneration are fibroblasts, keratinocytes, including sometimes endothelial cells, or melanocytes. Due to the novelty of our formulation, the only cell study reported in the literature with a similar composition involved L929 cells (mouse fibroblasts), resulting in no cytotoxic models. However, reproducing a skin model that closely resembles the native tissue requires the use of human-derived cells. Hence, to establish our dermal compartment, human-dermal fibroblasts (Hs-27) were encapsulated within the gel matrix by mixing the cell suspension directly with the fresh pre-gel solution. High viability rates were displayed along the culture period, registering a higher percentage of live cells for higher power used (22 mW), both at day 1 and 7 post-encapsulation, (83% and 75 %, respectively), corroborating the no cytotoxicity of the composition. Unfortunately, no cell spreading was noticed, pointing out that probably Formulation 2 was not conducive to promoting cell activities.

As a first implementation, RGD peptides were coupled with norbornene pullulan since these peptide sequences are well-known for promoting fibroblast elongation within the extracellular matrix, enhancing their arrangement, and impacting cellular adhesion to the substrates.[385] Two contents of RGD were explored (0.5 mM and 1 mM), resulting in higher cell viability (86% ± 2.1 and 90% ± 2.2) at least on day 1, compared to the previous ones. The presence of RGD was also impacting the HaCaT adhesion, enhancing how keratinocyte attachment was favored only when fibroblasts were also embedded within the gels, due to the paracrine signal of the cells.[386] Anyway, the addition of the RGD sequence did not lead to the expected results. No fibroblast protrusions were observed, beyond that intrinsic polymeric defects were detected within the matrix (Figure 4.15). To overcome these drawbacks, a new crosslinker was introduced.

Specifically, the novelty of CD-Hy linker, based on hyaluronic acid (natural compound) and carrying thiol groups, was in the presence of cell degradable (CD) cleavable peptide, containing MMP sequences which allow cells to locally degrade the gel network if MMPs are produced.[320] Again, the printability of this new combination -Formulation 4- (RGD-N-PLN: CD-Hy link: LAP - 0.92 mM: 2.5 mM: 2.5 mM: 0.5 mM)- was assessed, fixing the ratio polymer: crosslinker (1:1) and using the same irradiation power window (13 mW to 30 mW).

Despite changing the crosslinker -CD-Hy link- the swelling profile reflected the same gel behavior described for Formulation 2 in the same power conditions (22 mW), with a 40% volume increase in the first 4 hours post-printing. Demonstrating that the new crosslinker did not affect the gels' uptake capacity, we wondered if the CD-Hy link had a repercussion on the bulk stiffness. As reported in Figure 4.18, the rheological analysis underlined a slight decrease in terms of Elastic modulus (3.5 kPa ± 1.5), suggesting that CD-Hy linker tended to produce softer matrices.

Besides the mechanical properties, we aimed to investigate the potential of these scaffolds to sustain cells and serve as viable alternatives for 3D-*in vitro* models, due to the intrinsic pullulan characteristics. The viability tests showed, for the first time, fibroblast elongation, indicating that cells liked the new extracellular matrix environment (possessing either RGD peptides and hyaluronic acid) and could easily protrude within it. Additionally, the viability percentage also raised on day 1 (88%) suggesting that Formulation 4 could potentially represent an effective dermal compartment for our skin model.

Establishing a robust dermal compartment capable of sustaining an epidermal layer requires meeting specific criteria. Although the soft nature of these scaffolds, cell viability rates, together with the fibroblast spreading, satisfied some of the fundamental requirements reported by Campbell et al.,[330] for resembling a suitable dermal model. Secreting collagen as in the native tissue, providing the formation of a basal membrane at the interface dermis/epidermis, and showing the typical fibrillar structures within the ECM network, fit also the important criteria to consider. Evaluating the expression of specific protein markers, which highlight dermis formation we confirmed the suitability of the gel scaffolds. To design the skin barriers that closely mimic the *in vivo* systems, our cell-laden gels (dermal compartment) were first mounted within Transwell® inserts and cultured in 24-well plates to establish a diffusion gradient by separately filling the apical and basolateral compartments. Then, the immunofluorescence studies described in sections 4.4.4, and 4.4.5 demonstrated the potential of these gels from the earliest culture periods (day 4, Figure 4.20) up to the longest ones (Figures 4.22, 4.23, and 4.24), in resembling a complex network akin to *in vivo* human fibroblasts. The visible entangled mesh and the distinguishable expression of cytoskeleton markers (vimentin and actin) were the proofs, indicating that our dermal compartment was a promising foundation for skin model development.

Additionally, collagen IV secretion and fibronectin expression, both essential factors in a well-organized dermis were observed, suggesting that the model was gradually approximating the native tissue structure. These findings laid the foundation for constructing a more complex structure that includes the epidermis layer. Hence, an epidermal compartment was created by seeding HaCaT cells on top of cell-laden gels, and this time, proper adhesion was achieved, resulting in a confluent monolayer over time. We believe that the presence of the basement membrane, as enhanced by laminin and collagen IV expressions, together with the presence of hyaluronic acid (CD-Hy link) drastically impacted the achievement of the epidermis.

Many studies reported in the literature displayed greater keratinocyte differentiation if cultured under ALI conditions compared to submerged conditions, together with the increasing extracellular matrix components' production.[121,387] Performing a comparative study between the conditions emerged that, for the dermal compartment, under ALI conditions, fibronectin levels raised, while the expressions of laminin and vimentin resulted even higher compared to submerged conditions, respectively 2.1 and 2.6-fold (Figure 4.25-c). Conversely, for the epidermis, as displayed in Figure 4.27-b, no significant differences in k14 and e-cadherin quantitative expressions were observed. Although keratinocyte localization on top of the gels appeared denser and more compact under ALI conditions (Figure 4.27-a), pointing out that ALI influenced the epidermis status, at this stage, with these systems (norbornene-pullulan and HaCaT cells), the air-exposure was not enough to promote keratinocyte differentiation, probably due to lack in tight junctions, as expressed by the low TEER values, and the soft nature of the gels.

However, with these studies, we demonstrated that photocrosslinked cell-laden gels based on Formulation 4 can be easily printed and kept in culture for up to 24 days post-encapsulation, without shrinkage signs, normally observed for collagen-based gels. Despite the soft nature of these scaffolds, albeit perfectly in line with acellular collagen-based and pullulan-only-based gels,[318,375] good cell viability was guaranteed. Considering that biological studies on norbornene-pullulan hydrogels are still scarce and the only ones presented in literature referred to compositions of pullulan blended with other polymers (e.g. chitosan-pullulan, pectin/carboxymethyl-pullulan), we were pioneers in producing epithelized dermis scaffolds based on norbornene-pullulan and CD Hy linker, validating either the composition and the 3D bioprinting system. A robust and intricate network (dermis) was defined by fibroblasts, perfectly spread within the gel, and a homogenous keratinocyte monolayer (epidermis) was built on top, beyond that a basal membrane was recognized at the interface. Altogether these achievements created an *in vitro* skin model ready to be used for permeability tests or pre-clinical studies in cosmetics. Although this first model marked a promising starting point, we were still far from what can be defined as a full-thickness model.

Collecting all the outcomes from the previous analysis, later in the thesis, we were compelled to develop a more sophisticated model. In the evaluation of valuable alternatives, we considered the high costs related to pullulan, which is three times more expensive than other polysaccharides.[148] Therefore, a new class of biopolymers that have recently gained popularity was pondered. It concerns IPN systems, based on the combinations of two polymers to generate a gel with the advantages of both components. Specifically, in our case, dextran and agarose were selected for their peculiar characteristics, such as promoting neovascularization during skin regeneration[346] and avoiding the cells sinking during the photopolymerization process. RGD sequences were also provided because dextran lacks cell-specific adhesion.[347] In this context, both CD-link and CD-Hy link were tested with this new blend of materials, generating respectively Formulation 5 and Formulation 6.

Starting from Formulation 5, as the first step, fabrication tests with the DLW system were designed to test the printability of these new materials. Surprisingly, even keeping the ratio polymer/crosslinker (1:1), this time, to get proper gels, the molar content of the single components was raised to 5 mM together with a higher power- 41 mW- corresponding to the limit of our in-house DLW system. Based on this evidence, we explored how these variations were impacting the mechanical properties first and then on the cell activities. A stronger water entrapping capacity (up to 60 % of the initial volume) was revealed compared to the previous formulation. Hence, for the inverse proportionality between swelling ratios and gels' stiffness,[214] we expected softer gels than before. Instead, from the bulk analysis, we got slightly higher Young Modulus values (4 kPa -5 kPa), that were completely reflecting the results reported in the literature for dextran/PEG-based gels,[321] without showing significant differences with/without agarose.

In the development of a reliable skin tissue model, besides the dermal/epidermal resembling, it is necessary to think about constructing an extracellular matrix that can potentially contain 50 different types of cells,[291] possessing simultaneously distinct stiffness to incorporate all the cells' variety. With some pilot experiments, we assessed a method to create stiffness-varying substrates. By initially irradiating the pre-gel solution and then gradually covering the light path with a photomask, gels with gradients of stiffness can be created (+/- agarose), resulting in scaffolds from the tunable properties within a range of (1-35 kPa). Being able to enhance the substrate stiffness resulted in fundamental for increasing both cell adhesion and proliferation.[388] Although additional investigations are needed, through these experiments we proved the possibility of establishing dextran-based-gels with a gradient of stiffness, paving the way for further evaluations in producing scaffolds with desired stiffness.

Besides that, cell activities were evaluated by exploring if the change of polymers (dextran +/- agarose) and mechanical stiffness provoked consequences. Switching from pullulan-based to dextran-based gels, the viability of cells incremented - (91%) on day 1- and (82.6%) on day 10, demonstrating the superiority of this composition -Formulation 5- in keeping a favorable environment for fibroblasts, independently from the agarose presence. Deeper studies enhanced also the capacity of cells to recover post-enzymatic gel degradation and being able to grow on top of hard substrates. As reported by Rivero et al.,[351] cells' presence inside the gels' matrix presented repercussions on the gels' stiffness which tended to decrease, due to the collagen production and the consequent ECM remodeling. So, to minimize the collateral effects of cell encapsulation, the number of Hs-27 embedded was drastically reduced from 5 x 10^6 cells/ml to 2 x 10^6 cells/ml, and co-culture systems were also investigated. Unluckily, the co-presence of Hs-27 and HaCaT led to a progressive hydrogel degradation, probably due to the cell-secreted proteases which locally degrade the gels, forcing us to abandon this polymer composition.

Formulation 6, based on the same polymer and counting on the CD-Hy link was the last composition examined during the PhD project. Disc-like shaped gels were successfully produced by irradiating the pre-gels solution from the bottom, in a short time (3-4 minutes), to avoid cell damage, using the SOLUS system, resulting in scaffolds with enlarged superficial areas for guaranteeing reliable models. The rheological characterization showed a drastic increase in the gels' stiffness (15-18 kPa) compared to Formulation 5, although still in the same order of magnitude, and better reflecting the stiffer nature of dextran polymer.[349] Also, the viability tests highlighted the superiority of Formulation 6 registering the highest values (-88.4% and 83.9%- +/-agarose) for a longer period. With these premises, co-culture studies were performed, using first submerged and later ALI conditions. While the dermis respected the required fees, largely expressing the distinct markers, such as vimentin and collagen IV, (Figures 4.39 and 4.40), conversely the monolayer on top was attained after several days post-culture, despite the conditions applied (ALI conditions).

To shorten the monolayer's confluency time, a surface coverage analysis allowed us to define the optimal seeding density. Co-culture studies and related analysis underlined the formation of a thin and labile monolayer on top of the dermal compartment (Figure 4.44), comparable to the one obtained by Zhao et al.[121] in collagen-based gels, 2 weeks post-ALI, and culturing HaCaT in the same conditions. However, we were still far from the well-differentiated models obtained in the same study[121] after 6 weeks in ALI, since even keeping our gels for longer times, no differences were shown and a local monolayer detachment was noticed, probably due to (i) the impossibility of cells creating tight junctions and (ii) prolonged culture times.

As a first improvement, we switched to a keratinocyte medium richer in nutrients, normally used with primary keratinocytes.[295] However, despite seeming to promote cell confluency (Figure 4.45) after 7 days, intensifying the compactness of the monolayer on top, similar detachment issues were faced again, constraining to change strategy. Several alternatives to HaCaT cells are presented in the literature, such as immortalized keratinocytes (h-TERT), which are becoming particularly attractive to study *in vitro* skin biology, due to their potential to re-epithelialize and secrete inflammatory wound-healing mediators[389]; or HEKn cells, largely used for their aptitude to differentiate and used in complex models where vascular systems are recapitulated.[283,295,312,390]

Taking profit of the Formulation 6 based-gels characteristics, new scaffolds were prepared and HEKn cells were seeded on top of them according to the protocol described in Figure 4.48. Immunofluorescence evaluation highlighted the complete formation of the epidermis, as indicated both by k14 and k10 expressions (Figure 4.49), and demonstrated the formation of the first differentiation layers (stratum basale and spinosum). Further analyses were conducted on histological sections to better investigate HEKn stratification and differentiation. Although the study by Tahri et al.[122] suggested the impossibility of achieving mature and differentiated HEKn cells on top of gelatin-based gels, 21 days post-incubation, our hematoxylin and eosin staining revealed the opposite. Furthermore, immunofluorescence studies corroborated this evidence as shown by the expression of specific markers corresponding to each differentiation state. As depicted in Figure 4.52, both stratum basale and stratum spinosum were clearly visible, with k14 and k10 fully expressed along the entire section. Additionally, the involucrin signal was uniformly distributed, suggesting the formation of the stratum granulosum. To prove this, later-stage markers,[361] -loricrin and filaggrin- were also examined. These markers start to be expressed in the granulosum layer, facilitating terminal differentiation up to the cornified epidermis. Due to their expressions co-localized either in the granulosum or the corneum layer, we cannot properly demonstrate the effective existence of the cornified stratum. However, our qualitative results are highly comparable with the ones reported for example for collagen-based gels[295,391] or full-thickness skin models reported by Zoio et al.[312] Anyhow, for the cornified layer further optimizations could be realized, such as finer controlling the dry gel' surface, during ALI conditions.

Because of the urgency to improve the conventional *in vitro* skin models and enhance their complexity, endothelial cells have been also included. Specifically, HUVEC cells have been employed, with a ratio (Hs-27: HUVECs- 1:3) determined based on literature and experimental studies.[390] The protocol followed was the same one used to develop our full-thickness skin model, with the inclusion of HUVEC cells contemporary to the Hs-27 encapsulation.

A successfully vascularized full-thickness skin model was achieved, as shown in Figure 4.61. Apart from the expression of the single differentiation state markers, by comparing this model with the no-vasculature-containing, a substantial difference was observed in the dermal compartment.

The co-existence of Hs-27 and HUVECs resulted in more elongated cells beneath the differentiated epidermis, demonstrating the ability of dextran-based gels to promote vascularization.[346] Furthermore, the complete skin model facilitated the expression of CD-31 (Figure 4.59), compared to the models without epidermis, as well as the Endoglin expression, which indicated activated endothelial cells,[363] and resulting in a clearly 3-layers distinction (basal, spinosum, and granulosum) as depicted in hematoxylin and eosin staining (Figure 4.60). Numerous improvements can be also implemented to get competitive models as the pre-vascularized scaffold-free 3D skin models designed for *in vivo* application by Miyazaky et al.[390] However, these studies pave the way for our dextran-based (+/-agarose) gels to be used as competitive 3D complex models in the panorama of *in vitro* models and tissue regeneration.

In conclusion, here we have demonstrated the development of a reliable vascularized-full-thickness skin model. Starting from both SN and IPN systems, based on Formulation 6, cell-laden gels can be fabricated by irradiating the pre-gel solution for a few minutes. Excellent cell viability can be achieved, due to the robust mechanical properties of the gels and the ECM composition. A vascularized-dermal compartment has been successfully generated by including both Hs-27 and HUVECs, enhancing cell spreading and the formation of tubular-like structures like those observed in the native tissue. Additionally, a differentiated epidermis was achieved, as elucidated by the presence of distinct differentiation strata and their corresponding markers. Hence, we designed a promising vascularized full-thickness 3D skin model for *in vitro* applications. Further efforts are surely required to build upon these results and make the models suitable for *in vivo* applications. For instance, stiffness-varying dextran-based gels can be produced by taking advantage of the method described, to easily incorporate other skin components, creating a highly competitive skin model. Thanks to the simplicity of our fabrication method, a more complex 3D skin model can be designed, including different cell types, such as melanocytes, stem cells, or dermal papillae cells for hair follicles resembling and making the model affordable for future perspectives.

6. Conclusions

The general goal of this thesis was to develop a 3D full-thickness skin model based on thiol-ene click chemistry, an alternative to the existent *in vitro* models, such as collagen-based gels which still represent the gold standard.

- A commercial (DLP-SLA) 3D bioprinting system -SOLUS system- based on layer-by-layer printing has been successfully used for selecting the optimal formulation (Norbornene-pullulan/ thiol-modified PEG-link) to establish an *in vitro* skin model, based on thiol-norbornene chemistry.
- By adopting an in-house Direct Laser Writing system (DLW), the pre-gel solution to create rectangular-shaped hydrogels was drastically reduced, permitting the creation of hydrogels in a few seconds. Norbornene-pullulan-based gels were successfully printed, with a low content of photoinitiator, in the presence of visible light, reducing cell damage during the photocrosslinking, and showing (i) a good water uptake capacity and (ii) soft extracellular matrices, perfectly in line with acellular soft materials used for skin regeneration. Optimizing the power exposure, gels resulted in no cytotoxic microenvironment for the cells and guaranteed good cell viability. With the introduction of RGD-peptides, and a natural-based crosslinker (CD-Hy linker), the human fibroblasts' elongation was promoted, establishing a robust dermal compartment, where fibronectin and collagen expression were appreciated.
- Epithelized-dermal skin scaffolds were easily realized by seeding human immortalized keratinocytes on top of the dermal constructs previously mounted within Transwell® inserts to recapitulate the native skin barrier. A comparative study between submerged and ALI culture conditions was conducted elucidating the potential of ALI conditions to promote the formation of an intricate network between fibroblasts and keratinocytes.
- Interpenetrated hydrogel network systems were also fabricated by irradiating the pre-gel solution, using the commercial SOLUS system specially modified. Dextran-based (+/- agarose) gels were largely studied, showing a stiffer matrix compared to norbornene-pullulan gels. Full-thickness skin models were developed after several optimizations (cell density, culture conditions, and introduction of primary keratinocytes) resulting in 3D scaffolds with distinguishable dermis and epidermis compartments. Specifically, keratinocytes manifested a similar stratification and differentiation observed *in vivo,* resembling the distinct strata: basale, spinosum, and granulosum.

- Vascularized- full-thickness skin models were also developed by including endothelial cells in the dermal compartment, proving the efficiency of the IPN-based gels to resemble a complex model.

- Finally, dextran (+/-agarose) gels with gradients of stiffness were also realized, demonstrating the possibility of creating hydrogels with tunable mechanical characteristics for including different cell types.

7. Bibliography

1. McKnight, G., Shah, J. & Hargest, R. Physiology of the skin. *Surgery (Oxford)* **40**, 8–12 (2022).
2. Venus, M., Waterman, J. & McNab, I. Basic physiology of the skin. *Surgery (Oxford)* **28**, 469–472 (2010).
3. Kanitakis J. Anatomy, histology and immunohistochemistry of normal human skin. Eur J Dermatol. 2002 Jul-Aug;12(4):390-9; quiz 400-1. PMID: 12095893.
4. Cirulli, A., Neves Borgheti-Cardoso, L., Torras, N., García-Díaz, M. & Martínez, E. Hydrogels as tissue barriers. *Hydrogels for Tissue Engineering and Regenerative Medicine* 433–466 (2024) doi:10.1016/B978-0-12-823948-3.00017-8.
5. Zhang, Z. & Michniak-Kohn, B. B. Tissue Engineered Human Skin Equivalents. *Pharmaceutics* **4**, 26–41 (2012).
6. Mitchell, B. & Sharma, R. The integumentary, skeletal and muscular systems. *Embryology* 19–25 (2009) doi:10.1016/B978-0-7020-3225-7.50007-5.
7. Takeo, M., Lee, W. & Ito, M. Wound Healing and Skin Regeneration. *Cold Spring Harb Perspect Med* **5**, a023267–a023267 (2015).
8. Kabashima, K., Honda, T., Ginhoux, F. & Egawa, G. The immunological anatomy of the skin. *Nat Rev Immunol* **19**, 19–30 (2019).
9. Menon, G. K., Cleary, G. W. & Lane, M. E. The structure and function of the stratum corneum. *Int J Pharm* **435**, 3–9 (2012).
10. Sandby-Møller, J., Poulsen, T. & Wulf, H. C. Epidermal Thickness at Different Body Sites: Relationship to Age, Gender, Pigmentation, Blood Content, Skin Type and Smoking Habits. *Acta Derm Venereol* **83**, 410–413 (2003).
11. Cursons, J. *et al.* Regulation of ERK-MAPK signaling in human epidermis. *BMC Syst Biol* **9**, 41 (2015).
12. Miller, C., Crampin, E. & Osborne, J. M. Multiscale modelling of desquamation in the interfollicular epidermis. *PLoS Comput Biol* **18**, e1010368 (2022).
13. Fuchs, E. Skin stem cells: rising to the surface. *J Cell Biol* **180**, 273–284 (2008).
14. Abdo, J. M., Sopko, N. A. & Milner, S. M. The applied anatomy of human skin: A model for regeneration. *Wound Medicine* **28**, 100179 (2020).
15. Mathes, S. H., Ruffner, H. & Graf-Hausner, U. The use of skin models in drug development. *Adv Drug Deliv Rev* **69–70**, 81–102 (2014).
16. Honari, G. & Maibach, H. Skin Structure and Function. in *Applied Dermatotoxicology* 1–10 (Elsevier, 2014). doi:10.1016/B978-0-12-420130-9.00001-3.

17. Ibrahim, A. A. E., Bagherani, N., Smoller, B. R., Bagherani, N. & Reyes-Baron, C. Anatomy and Organization of Human Skin. in *Atlas of Dermatology, Dermatopathology and Venereology* 1–24 (Springer International Publishing, Cham, 2021). doi:10.1007/978-3-319-45134-3_3-1.

18. Abraham, J. & Mathew, S. Merkel cells: A collective review of current concepts. *Int J Appl Basic Med Res* **9**, 9 (2019).

19. Rousselle, P., Braye, F. & Dayan, G. Re-epithelialization of adult skin wounds: Cellular mechanisms and therapeutic strategies. *Adv Drug Deliv Rev* **146**, 344–365 (2019).

20. Ishida-Yamamoto, A., Igawa, S. & Kishibe, M. Molecular basis of the skin barrier structures revealed by electron microscopy. *Exp Dermatol* **27**, 841–846 (2018).

21. Pozzi, A., Yurchenco, P. D. & Iozzo, R. V. The nature and biology of basement membranes. *Matrix Biology* **57–58**, 1–11 (2017).

22. Caley, M. P., Martins, V. L. C. & O'Toole, E. A. Metalloproteinases and Wound Healing. *Adv Wound Care (New Rochelle)* **4**, 225–234 (2015).

23. Shpichka, A. *et al.* Skin tissue regeneration for burn injury. *Stem Cell Res Ther* **10**, 94 (2019).

24. Madison, K. C. Barrier Function of the Skin: "La Raison d'Être" of the Epidermis. *Journal of Investigative Dermatology* **121**, 231–241 (2003).

25. Zhou, X. *et al.* Identification of Cell Markers and Their Expression Patterns in Skin Based on Single-Cell RNA-Sequencing Profiles. *Life* **12**, 550 (2022).

26. Wang, J. H.-C., Thampatty, B. P., Lin, J.-S. & Im, H.-J. Mechanoregulation of gene expression in fibroblasts. *Gene* **391**, 1–15 (2007).

27. Nejati, R., Kovacic, D. & Slominski, A. Neuro-immune-endocrine functions of the skin: an overview. *Expert Rev Dermatol* **8**, 581–583 (2013).

28. Arda, O., Göksügür, N. & Tüzün, Y. Basic histological structure and functions of facial skin. *Clin Dermatol* **32**, 3–13 (2014).

29. Niemann, C. & Horsley, V. Development and homeostasis of the sebaceous gland. *Semin Cell Dev Biol* **23**, 928–936 (2012).

30. Lu, C. & Fuchs, E. Sweat Gland Progenitors in Development, Homeostasis, and Wound Repair. *Cold Spring Harb Perspect Med* **4**, a015222–a015222 (2014).

31. Smith, K. R. & Thiboutot, D. M. Thematic review series: Skin Lipids. Sebaceous gland lipids: friend or foe? *J Lipid Res* **49**, 271–281 (2008).

32. Chu, G.-Y. *et al.* Stem cell therapy on skin: Mechanisms, recent advances and drug reviewing issues. *J Food Drug Anal* **26**, 14–20 (2018).

33. Brandner, J. M., Haftek, M. & Niessen, C. M. *Adherens Junctions, Desmosomes and Tight Junctions in Epidermal Barrier Function*. *The Open Dermatology Journal* vol. 4 (2010).

34. Niessen, C. M. Tight junctions/adherens junctions: Basic structure and function. *Journal of Investigative Dermatology* vol. 127 2525–2532 Preprint at https://doi.org/10.1038/sj.jid.5700865 (2007).

35. Bäsler, K. *et al.* The role of tight junctions in skin barrier function and dermal absorption. *Journal of Controlled Release* **242**, 105–118 (2016).

36. Balda, M. S. & Matter, K. Tight junctions and the regulation of gene expression. *Biochimica et Biophysica Acta (BBA) - Biomembranes* **1788**, 761–767 (2009).

37. Kirschner, N., Rosenthal, R., Günzel, D., Moll, I. & Brandner, J. M. Tight junctions and differentiation – a chicken or the egg question? *Exp Dermatol* **21**, 171–175 (2012).

38. Matter, K., Aijaz, S., Tsapara, A. & Balda, M. S. Mammalian tight junctions in the regulation of epithelial differentiation and proliferation. *Curr Opin Cell Biol* **17**, 453–458 (2005).

39. Takano, K., Kojima, T., Sawada, N. & Himi, T. Role of tight junctions in signal transduction: an update. *EXCLI J* **13**, 1145–62 (2014).

40. Perez-Moreno, M. & Fuchs, E. Catenins: Keeping Cells from Getting Their Signals Crossed. *Dev Cell* **11**, 601–612 (2006).

41. Evangelista, F., Dasher, D. A., Diaz, L. A., Prisayanh, P. S. & Li, N. E-cadherin Is an Additional Immunological Target for Pemphigus Autoantibodies. *Journal of Investigative Dermatology* **128**, 1710–1718 (2008).

42. Jefferson, J. J., Leung, C. L. & Liem, R. K. H. Plakins: Goliaths that link cell junctions and the cytoskeleton. *Nat Rev Mol Cell Biol* **5**, 542–553 (2004).

43. Kowalczyk, A. P., Bornslaeger, E. A., Norvell, S. M., Palka, H. L. & Green, K. J. Desmosomes: Intercellular Adhesive Junctions Specialized for Attachment of Intermediate Filaments. in 237–302 (1998). doi:10.1016/S0074-7696(08)60153-9.

44. Church, D., Elsayed, S., Reid, O., Winston, B. & Lindsay, R. Burn Wound Infections. *Clin Microbiol Rev* **19**, 403–434 (2006).

45. Atiyeh, B. S. & Costagliola, M. Cultured epithelial autograft (CEA) in burn treatment: Three decades later. *Burns* **33**, 405–413 (2007).

46. Wood, F. M., Kolybaba, M. L. & Allen, P. The use of cultured epithelial autograft in the treatment of major burn injuries: A critical review of the literature. *Burns* **32**, 395–401 (2006).

47. van den Broek, L. J., Bergers, L. I. J. C., Reijnders, C. M. A. & Gibbs, S. Progress and Future Prospectives in Skin-on-Chip Development with Emphasis on the use of Different Cell Types and Technical Challenges. *Stem Cell Rev Rep* **13**, 418–429 (2017).

48. Mathes, S. H., Ruffner, H. & Graf-Hausner, U. The use of skin models in drug development. *Adv Drug Deliv Rev* **69–70**, 81–102 (2014).

49. Stanton, D. N., Ganguli-Indra, G., Indra, A. K. & Karande, P. Bioengineered Efficacy Models of Skin Disease: Advances in the Last 10 Years. *Pharmaceutics* **14**, 319 (2022).

50. Jean, J., Lapointe, M., Soucy, J. & Pouliot, R. Development of an in vitro psoriatic skin model by tissue engineering. *J Dermatol Sci* **53**, 19–25 (2009).

51. Jean, J. & Pouliot, R. In Vivo and In Vitro Models of Psoriasis. in *Tissue Engineering* (InTech, 2010). doi:10.5772/8582.

52. Akasaka, E., Kleiser, S., Sengle, G., Bruckner-Tuderman, L. & Nyström, A. Diversity of Mechanisms Underlying Latent TGF-β Activation in Recessive Dystrophic Epidermolysis Bullosa. *Journal of Investigative Dermatology* **141**, 1450-1460.e9 (2021).

53. Itoh, M., Kiuru, M., Cairo, M. S. & Christiano, A. M. Generation of keratinocytes from normal and recessive dystrophic epidermolysis bullosa-induced pluripotent stem cells. *Proceedings of the National Academy of Sciences* **108**, 8797–8802 (2011).

54. Langley, R. G. B. Psoriasis: epidemiology, clinical features, and quality of life. *Ann Rheum Dis* **64**, ii18–ii23 (2005).

55. Bieber, T. Atopic Dermatitis. *New England Journal of Medicine* **358**, 1483–1494 (2008).

56. Clarysse, K. *et al.* JAK1/3 inhibition preserves epidermal morphology in full-thickness 3D skin models of atopic dermatitis and psoriasis. *Journal of the European Academy of Dermatology and Venereology* **33**, 367–375 (2019).

57. Shin, J. U. *et al.* Recapitulating T cell infiltration in 3D psoriatic skin models for patient-specific drug testing. *Sci Rep* **10**, 4123 (2020).

58. Bocheńska, K., Smolińska, E., Moskot, M., Jakóbkiewicz-Banecka, J. & Gabig-Cimińska, M. Models in the Research Process of Psoriasis. *Int J Mol Sci* **18**, 2514 (2017).

59. Liu, X., Michael, S., Bharti, K., Ferrer, M. & Song, M. J. A biofabricated vascularized skin model of atopic dermatitis for preclinical studies. *Biofabrication* **12**, 035002 (2020).

60. Lee, S. H. *et al.* Ameliorating effect of dipotassium glycyrrhizinate on an IL-4- and IL-13-induced atopic dermatitis-like skin-equivalent model. *Arch Dermatol Res* **311**, 131–140 (2019).

61. Portugal-Cohen, M., Cohen, D., Kohen, R. & Oron, M. Exploitation of alternative skin models from academia to industry: proposed functional categories to answer needs and regulation demands. *Front Physiol* **14**, (2023).

62. Götz, C. *et al.* Xenobiotic metabolism capacities of human skin in comparison with a 3D-epidermis model and keratinocyte-based cell culture as *in vitro* alternatives for chemical testing: phase II enzymes. *Exp Dermatol* **21**, 364–369 (2012).

63. Zappelli, C., Barbulova, A., Apone, F. & Colucci, G. Effective Active Ingredients Obtained through Biotechnology. *Cosmetics* **3**, 39 (2016).

64. Filaire, E. *et al.* Alternative in vitro models used in the main safety tests of cosmetic products and new challenges. *Int J Cosmet Sci* **44**, 604–613 (2022).

65. Cheng, S., Qu, X. & Qin, Y. Harmonisation of Animal Testing Alternatives in China. *Alternatives to Laboratory Animals* **45**, 333–338 (2017).

66. Fentem, J., Malcomber, I., Maxwell, G. & Westmoreland, C. Upholding the EU's Commitment to 'Animal Testing as a Last Resort'' Under REACH Requires a Paradigm Shift in How We Assess Chemical Safety to Close the Gap Between Regulatory Testing and Modern Safety Science'. *Alternatives to Laboratory Animals* **49**, 122–132 (2021).

67. Rodriguez, L. G., Wu, X. & Guan, J.-L. Wound-Healing Assay. in *Cell Migration* 023–030 (Humana Press, New Jersey). doi:10.1385/1-59259-860-9:023.

68. Grada, A., Otero-Vinas, M., Prieto-Castrillo, F., Obagi, Z. & Falanga, V. Research Techniques Made Simple: Analysis of Collective Cell Migration Using the Wound Healing Assay. *Journal of Investigative Dermatology* **137**, e11–e16 (2017).

69. Jonkman, J. E. N. *et al.* An introduction to the wound healing assay using live-cell microscopy. *Cell Adh Migr* **8**, 440–451 (2014).

70. Urciuolo, F., Passariello, R., Imparato, G., Casale, C. & Netti, P. A. Bioengineered Wound Healing Skin Models: The Role of Immune Response and Endogenous ECM to Fully Replicate the Dynamic of Scar Tissue Formation In Vitro. *Bioengineering* **9**, 233 (2022).

71. Chim, S. M. *et al.* EGFL6 Promotes Endothelial Cell Migration and Angiogenesis through the Activation of Extracellular Signal-regulated Kinase. *Journal of Biological Chemistry* **286**, 22035–22046 (2011).

72. Matsubayashi, Y., Razzell, W. & Martin, P. 'White wave' analysis of epithelial scratch wound healing reveals how cells mobilise back from the leading edge in a myosin-II-dependent fashion. *J Cell Sci* **124**, 1017–1021 (2011).

73. Bellas, E., Seiberg, M., Garlick, J. & Kaplan, D. L. In vitro 3D Full-Thickness Skin-Equivalent Tissue Model Using Silk and Collagen Biomaterials. *Macromol Biosci* **12**, 1627–1636 (2012).

74. Shen, Z. *et al.* Construction of tissue-engineered skin with rete ridges using co-network hydrogels of gelatin methacrylated and poly(ethylene glycol) diacrylate. *Materials Science and Engineering: C* **129**, 112360 (2021).

75. Chaudhari, A. *et al.* Future Prospects for Scaffolding Methods and Biomaterials in Skin Tissue Engineering: A Review. *Int J Mol Sci* **17**, 1974 (2016).

76. Bacakova, M. *et al.* <p>A two-layer skin construct consisting of a collagen hydrogel reinforced by a fibrin-coated polylactide nanofibrous membrane [Corrigendum]</p>. *Int J Nanomedicine* **Volume 14**, 7215–7216 (2019).

77. Casale, C., Imparato, G., Urciuolo, F. & Netti, P. A. Endogenous human skin equivalent promotes in vitro morphogenesis of follicle-like structures. *Biomaterials* **101**, 86–95 (2016).

78. PONEC, M. *In vitro* cultured human skin cells as alternatives to animals for skin irritancy screening. *Int J Cosmet Sci* **14**, 245–264 (1992).

79. Randall, M. J., Jüngel, A., Rimann, M. & Wuertz-Kozak, K. Advances in the Biofabrication of 3D Skin in vitro: Healthy and Pathological Models. *Front Bioeng Biotechnol* **6**, (2018).

80. Eberlin, S. *et al.* The *Ex Vivo* Skin Model as an Alternative Tool for the Efficacy and Safety Evaluation of Topical Products. *Alternatives to Laboratory Animals* **48**, 10–22 (2020).

81. Risueño, I., Valencia, L., Jorcano, J. L. & Velasco, D. Publisher's Note: "Skin-on-a-chip models: General overview and future perspectives" [APL Bioengineering **5** , 030901 (2021)]. *APL Bioeng* **5**, (2021).

82. dos Santos, C. E. M., Miranda, R. G., de Oliveira, D. P. & Dorta, D. J. Challenges and Opportunities for Integrating In Silico Models and Adverse Outcomes Pathways to Set and Relate New Biomarkers. *Water (Basel)* **12**, 3549 (2020).

83. Cascone, S. & Lamberti, G. Hydrogel-based commercial products for biomedical applications: A review. *Int J Pharm* (2020) doi:10.1016/j.ijpharm.2019.118803.

84. Aswathy, S. H., Narendrakumar, U. & Manjubala, I. Commercial hydrogels for biomedical applications. *Heliyon* Preprint at https://doi.org/10.1016/j.heliyon.2020.e03719 (2020).

85. Flaten, G. E. *et al.* In vitro skin models as a tool in optimization of drug formulation. *European Journal of Pharmaceutical Sciences* **75**, 10–24 (2015).

86. Yun, Y. E., Jung, Y. J., Choi, Y. J., Choi, J. S. & Cho, Y. W. Artificial skin models for animal-free testing. *J Pharm Investig* **48**, 215–223 (2018).

87. Mao, J. *et al.* Study of novel chitosan-gelatin artificial skin *in vitro*. *J Biomed Mater Res A* **64A**, 301–308 (2003).

88. Whang, K.-K., Kim, M.-J., Song, W.-K. & Cho, S. Comparative Treatment of Giant Congenital Melanocytic Nevi with Curettage or Er:YAG Laser Ablation Alone versus with Cultured Epithelial Autografts. *Dermatologic Surgery* **31**, 1660–1667 (2005).

89. You, H., Han, S., Lee, J. & Chang, H. Treatment of diabetic foot ulcers using cultured allogeneic keratinocytes—A pilot study. *Wound Repair and Regeneration* **20**, 491–499 (2012).

90. Abd, E. *et al.* Skin models for the testing of transdermal drugs. *Clinical Pharmacology: Advances and Applications* vol. 8 163–176 Preprint at https://doi.org/10.2147/CPAA.S64788 (2016).

91. Oliveira, I. M., Fernandes, D. C., Cengiz, I. F., Reis, R. L. & Oliveira, J. M. Hydrogels in the treatment of rheumatoid arthritis: drug delivery systems and artificial matrices for dynamic in vitro models. *J Mater Sci Mater Med* **32**, 74 (2021).

92. Seo, B.-B. *et al.* Injectable polymeric nanoparticle hydrogel system for long-term anti-inflammatory effect to treat osteoarthritis. *Bioact Mater* **7**, 14–25 (2022).

93. Carvalho, M. R., Maia, F. R., Vieira, S., Reis, R. L. & Oliveira, J. M. Tuning Enzymatically Crosslinked Silk Fibroin Hydrogel Properties for the Development of a Colorectal Cancer Extravasation 3D Model on a Chip. *Global Challenges* **2**, (2018).

94. Goy, C. B., Chaile, R. E. & Madrid, R. E. Microfluidics and hydrogel: A powerful combination. *React Funct Polym* **145**, 104314 (2019).

95. Vera, D. *et al.* Engineering Tissue Barrier Models on Hydrogel Microfluidic Platforms. *ACS Appl Mater Interfaces* **13**, 13920–13933 (2021).

96. Askari, M. *et al.* Recent progress in extrusion 3D bioprinting of hydrogel biomaterials for tissue regeneration: a comprehensive review with focus on advanced fabrication techniques. *Biomater Sci* **9**, 535–573 (2021).

97. Dutta, S. D., Hexiu, J., Patel, D. K., Ganguly, K. & Lim, K.-T. 3D-printed bioactive and biodegradable hydrogel scaffolds of alginate/gelatin/cellulose nanocrystals for tissue engineering. *Int J Biol Macromol* **167**, 644–658 (2021).

98. Liang, Y., He, J. & Guo, B. Functional Hydrogels as Wound Dressing to Enhance Wound Healing. *ACS Nano* **15**, 12687–12722 (2021).

99. Maleki, A. *et al.* Multifunctional Photoactive Hydrogels for Wound Healing Acceleration. *ACS Nano* **15**, 18895–18930 (2021).

100. Yang, Y., Liang, Y., Chen, J., Duan, X. & Guo, B. Mussel-inspired adhesive antioxidant antibacterial hemostatic composite hydrogel wound dressing via photo-polymerization for infected skin wound healing. *Bioact Mater* **8**, 341–354 (2022).

101. Peppas, N. A., Bures, P., Leobandung, W. & Ichikawa, H. Hydrogels in pharmaceutical formulations. *European Journal of Pharmaceutics and Biopharmaceutics* **50**, 27–46 (2000).

102. Drury, J. L. & Mooney, D. J. Hydrogels for tissue engineering: scaffold design variables and applications. *Biomaterials* **24**, 4337–4351 (2003).

103. Bahram, M., Mohseni, N. & Moghtader, M. An Introduction to Hydrogels and Some Recent Applications. in *Emerging Concepts in Analysis and Applications of Hydrogels* (InTech, 2016). doi:10.5772/64301.

104. Majcher, M. J. & Hoare, T. Applications of Hydrogels. in 453–490 (2019). doi:10.1007/978-3-319-95990-0_17.

105. Nitti, P., Demitri, C., Sannino, A. & Ambrosio, L. Fundamentals of hydrogels II—architecture and biodegradability. in *Hydrogels for Tissue Engineering and Regenerative Medicine* 13–28 (Elsevier, 2024). doi:10.1016/B978-0-12-823948-3.00001-4.

106. Ullah, F., Othman, M. B. H., Javed, F., Ahmad, Z. & Akil, H. Md. Classification, processing and application of hydrogels: A review. *Materials Science and Engineering: C* **57**, 414–433 (2015).

107. El-Sherbiny, I. M. & Yacoub, M. H. Hydrogel scaffolds for tissue engineering: Progress and challenges. *Glob Cardiol Sci Pract* **2013**, 38 (2013).

108. Singh, M. R., Patel, S. & Singh, D. Natural polymer-based hydrogels as scaffolds for tissue engineering. in *Nanobiomaterials in Soft Tissue Engineering* 231–260 (Elsevier, 2016). doi:10.1016/B978-0-323-42865-1.00009-X.

109. Manon-Jensen, T., Kjeld, N. G. & Karsdal, M. A. Collagen-mediated hemostasis. *Journal of Thrombosis and Haemostasis* **14**, 438–448 (2016).

110. Sorushanova, A. *et al.* The Collagen Suprafamily: From Biosynthesis to Advanced Biomaterial Development. *Advanced Materials* **31**, 1801651 (2019).

111. Eming, S. A., Martin, P. & Tomic-Canic, M. Wound repair and regeneration: Mechanisms, signaling, and translation. *Science Translational Medicine* vol. 6 Preprint at https://doi.org/10.1126/scitranslmed.3009337 (2014).

112. Silvipriya, K. S. *et al.* Collagen: Animal sources and biomedical application. *J Appl Pharm Sci* **5**, 123–127 (2015).

113. Achilli, M. & Mantovani, D. Tailoring mechanical properties of collagen-based scaffolds for vascular tissue engineering: The effects of pH, temperature and ionic strength on gelation. *Polymers (Basel)* **2**, 664–680 (2010).

114. Lopez-Garcia, M. d. C., Beebe, D. J. & Crone, W. C. Mechanical Interactions of Mouse Mammary Gland Cells with Collagen in a Three-Dimensional Construct. *Ann Biomed Eng* **38**, 2485–2498 (2010).

115. Ackermann, K., Lombardi Borgia, S., Korting, H. C., Mewes, K. R. & Schäfer-Korting, M. The phenion® full-thickness skin model for percutaneous absorption testing. *Skin Pharmacol Physiol* **23**, 105–112 (2010).

116. Braziulis, E. *et al.* Modified Plastic Compression of Collagen Hydrogels Provides an Ideal Matrix for Clinically Applicable Skin Substitutes. *Tissue Eng Part C Methods* **18**, 464–474 (2012).

117. Lotz, C. *et al.* Cross-linked Collagen Hydrogel Matrix Resisting Contraction To Facilitate Full-Thickness Skin Equivalents. *ACS Appl Mater Interfaces* **9**, 20417–20425 (2017).

118. Yeh, M. *et al.* A novel cell support membrane for skin tissue engineering: Gelatin film cross-linked with 2-chloro-1-methylpyridinium iodide. *Polymer (Guildf)* **52**, 996–1003 (2011).

119. Nicodemus, G. D. & Bryant, S. J. Cell Encapsulation in Biodegradable Hydrogels for Tissue Engineering Applications. *Tissue Eng Part B Rev* **14**, 149–165 (2008).

120. Hoffman, A. S. Hydrogels for biomedical applications. *Adv Drug Deliv Rev* **64**, 18–23 (2012).

121. Zhao, X. *et al.* Photocrosslinkable Gelatin Hydrogel for Epidermal Tissue Engineering. *Adv Healthc Mater* **5**, 108–118 (2016).

122. Tahri, S. *et al.* Human epidermal keratinocytes and human dermal fibroblasts interactions seeded on gelatin hydrogel for future application in skin in vitro 3-dimensional model. *Front Bioeng Biotechnol* **11**, (2023).

123. Kwak, B. S. *et al.* In vitro 3D skin model using gelatin methacrylate hydrogel. *Journal of Industrial and Engineering Chemistry* **66**, 254–261 (2018).

124. Hasnain, M. S. *et al.* Use of alginates for drug delivery in dentistry. in *Alginates in Drug Delivery* 387–404 (Elsevier, 2020). doi:10.1016/B978-0-12-817640-5.00015-7.

125. Lee, K. Y. & Mooney, D. J. Alginate: Properties and biomedical applications. *Prog Polym Sci* **37**, 106–126 (2012).

126. Aderibigbe, B. & Buyana, B. Alginate in Wound Dressings. *Pharmaceutics* **10**, 42 (2018).

127. Liberski, A., Latif, N., Raynaud, C., Bollensdorff, C. & Yacoub, M. Alginate for cardiac regeneration: From seaweed to clinical trials. *Glob Cardiol Sci Pract* **2016**, (2016).

128. Smith, A. M. & Senior, J. J. Alginate Hydrogels with Tuneable Properties. in 37–61 (2021). doi:10.1007/10_2020_161.

129. Neves, M. I., Moroni, L. & Barrias, C. C. Modulating Alginate Hydrogels for Improved Biological Performance as Cellular 3D Microenvironments. *Front Bioeng Biotechnol* **8**, (2020).

130. Kuo, C. K. & Ma, P. X. Ionically crosslinked alginate hydrogels as scaffolds for tissue engineering: Part 1. Structure, gelation rate and mechanical properties. *Biomaterials* **22**, 511–521 (2001).

131. Sun, J. & Tan, H. Alginate-Based Biomaterials for Regenerative Medicine Applications. *Materials* **6**, 1285–1309 (2013).

132. Afjoul, H., Shamloo, A. & Kamali, A. Freeze-gelled alginate/gelatin scaffolds for wound healing applications: An in vitro, in vivo study. *Materials Science and Engineering: C* **113**, 110957 (2020).

133. Hu, T. & Lo, A. C. Y. Collagen–Alginate Composite Hydrogel: Application in Tissue Engineering and Biomedical Sciences. *Polymers (Basel)* **13**, 1852 (2021).

134. Abasalizadeh, F. *et al.* Alginate-based hydrogels as drug delivery vehicles in cancer treatment and their applications in wound dressing and 3D bioprinting. *J Biol Eng* **14**, 8 (2020).

135. Heiligenstein, S. *et al. In Vitro* and *In Vivo* Characterization of Nonbiomedical- and Biomedical-Grade Alginates for Articular Chondrocyte Transplantation. *Tissue Eng Part C Methods* **17**, 829–842 (2011).

136. Xu, X., Jha, A. K., Harrington, D. A., Farach-Carson, M. C. & Jia, X. Hyaluronic acid-based hydrogels: from a natural polysaccharide to complex networks. *Soft Matter* **8**, 3280 (2012).

137. Hemshekhar, M. *et al.* Emerging roles of hyaluronic acid bioscaffolds in tissue engineering and regenerative medicine. *Int J Biol Macromol* **86**, 917–928 (2016).

138. Segura, T. *et al.* Crosslinked hyaluronic acid hydrogels: a strategy to functionalize and pattern. *Biomaterials* **26**, 359–371 (2005).

139. Tripodo, G. *et al.* Hyaluronic acid and its derivatives in drug delivery and imaging: Recent advances and challenges. *European Journal of Pharmaceutics and Biopharmaceutics* **97**, 400–416 (2015).

140. Caló, E. *et al.* Antimicrobial hydrogels based on autoclaved poly(vinyl alcohol) and poly(methyl vinyl ether-alt-maleic anhydride) mixtures for wound care applications. *RSC Adv* **6**, 55211–55219 (2016).

141. Bercea, M. *et al.* Self-healing hydrogels of oxidized pullulan and poly(vinyl alcohol). *Carbohydr Polym* **206**, 210–219 (2019).

142. Mishra, B. *et al.* A critical review on valorization of food processing wastes and by-products for pullulan production. *J Food Sci Technol* **60**, 2121–2131 (2023).

143. Van den Eynde, K., Boon, V., Gaspar, R. C. & Fardim, P. Biofabrication of Functional Pullulan by Aureobasidium pullulans under the Effect of Varying Mineral Salts and Sugar Stress Conditions. *Molecules* **28**, 2478 (2023).

144. Ganie, S. A., Rather, L. J. & Li, Q. A review on anticancer applications of pullulan and pullulan derivative nanoparticles. *Carbohydrate Polymer Technologies and Applications* **2**, 100115 (2021).

145. Li, X. *et al.* HLC/pullulan and pullulan hydrogels: their microstructure, engineering process and biocompatibility. *Materials Science and Engineering: C* **58**, 1046–1057 (2016).

146. Singh, R. S., Kaur, N., Hassan, M. & Kennedy, J. F. Pullulan in biomedical research and development - A review. *Int J Biol Macromol* **166**, 694–706 (2021).

147. Priya, V. S., Iyappan, K., Gayathri, V. S., William, S. & Suguna, L. Influence of pullulan hydrogel on sutureless wound healing in rats. *Wound Medicine* **14**, 1–5 (2016).

148. K.R., S. & V., P. Review on production, downstream processing and characterization of microbial pullulan. *Carbohydr Polym* **173**, 573–591 (2017).

149. Van Tomme, S. R. & Hennink, W. E. Biodegradable dextran hydrogels for protein delivery applications. *Expert Rev Med Devices* **4**, 147–164 (2007).

150. Sun, G., Shen, Y., Ho, C. C., Kusuma, S. & Gerecht, S. Functional groups affect physical and biological properties of dextran-based hydrogels. *J Biomed Mater Res A* **93A**, 1080–1090 (2010).

151. Sun, G. *et al.* Dextran hydrogel scaffolds enhance angiogenic responses and promote complete skin regeneration during burn wound healing. *Proceedings of the National Academy of Sciences* **108**, 20976–20981 (2011).

152. Zarrintaj, P. *et al.* Agarose-based biomaterials for tissue engineering. *Carbohydr Polym* **187**, 66–84 (2018).

153. Gaspar, V. M., Sousa, F., Queiroz, J. A. & Correia, I. J. Formulation of chitosan–TPP–pDNA nanocapsules for gene therapy applications. *Nanotechnology* **22**, 015101 (2011).

154. Ribeiro, M. P. *et al.* Development of a new chitosan hydrogel for wound dressing. *Wound Repair and Regeneration* **17**, 817–824 (2009).

155. Bao, P. *et al.* The Role of Vascular Endothelial Growth Factor in Wound Healing. *Journal of Surgical Research* **153**, 347–358 (2009).

156. Ribeiro, M. P., Morgado, P. I., Miguel, S. P., Coutinho, P. & Correia, I. J. Dextran-based hydrogel containing chitosan microparticles loaded with growth factors to be used in wound healing. *Materials Science and Engineering: C* **33**, 2958–2966 (2013).

157. Ko, H.-F., Sfeir, C. & Kumta, P. N. Novel synthesis strategies for natural polymer and composite biomaterials as potential scaffolds for tissue engineering. *Philosophical Transactions of the Royal Society A: Mathematical, Physical and Engineering Sciences* **368**, 1981–1997 (2010).

158. Lu, D. R., Xiao, C. M. & Xu, S. J. Starch-based completely biodegradable polymer materials. *Express Polym Lett* **3**, 366–375 (2009).

159. Liu, X., Holzwarth, J. M. & Ma, P. X. Functionalized Synthetic Biodegradable Polymer Scaffolds for Tissue Engineering. *Macromol Biosci* **12**, 911–919 (2012).

160. Sadr, N. *et al.* Enhancing the biological performance of synthetic polymeric materials by decoration with engineered, decellularized extracellular matrix. *Biomaterials* **33**, 5085–5093 (2012).

161. Baican, M., Stoleru, E. & Vasile, C. Cellular response to synthetic polymers. in *Handbook of Biomaterials Biocompatibility* 269–319 (Elsevier, 2020). doi:10.1016/B978-0-08-102967-1.00014-1.

162. Sachlos, E. & Czernuszka, J. Making Tissue Engineering Scaffolds Work. Review: The application of solid freeform fabrication technology to the production of tissue engineering scaffolds. *Eur Cell Mater* **5**, 29–40 (2003).

163. Berger, J., Reist, M., Mayer, J. M., Felt, O. & Gurny, R. Structure and interactions in chitosan hydrogels formed by complexation or aggregation for biomedical applications. *European Journal of Pharmaceutics and Biopharmaceutics* **57**, 35–52 (2004).

164. Boucard, N., Viton, C. & Domard, A. New Aspects of the Formation of Physical Hydrogels of Chitosan in a Hydroalcoholic Medium. *Biomacromolecules* **6**, 3227–3237 (2005).

165. Hoffman, A. S. Hydrogels for biomedical applications. *Adv Drug Deliv Rev* **64**, 18–23 (2012).

166. Hoare, T. R. & Kohane, D. S. Hydrogels in drug delivery: Progress and challenges. *Polymer (Guildf)* **49**, 1993–2007 (2008).

167. parhi, R. Cross-Linked Hydrogel for Pharmaceutical Applications: A Review. *Adv Pharm Bull* **7**, 515–530 (2017).

168. Berger, J. *et al.* Structure and interactions in covalently and ionically crosslinked chitosan hydrogels for biomedical applications. *European Journal of Pharmaceutics and Biopharmaceutics* **57**, 19–34 (2004).

169. Chang, B., Ahuja, N., Ma, C. & Liu, X. Injectable scaffolds: Preparation and application in dental and craniofacial regeneration. *Materials Science and Engineering: R: Reports* **111**, 1–26 (2017).

170. Łukaszczyk, J. *et al.* Evaluation of Oligo(ethylene glycol) Dimethacrylates Effects on the Properties of New Biodegradable Bone Cement Compositions. *Macromol Biosci* **5**, 64–69 (2005).

171. Yung, C. W., Bentley, W. E. & Barbari, T. A. Diffusion of interleukin-2 from cells overlaid with cytocompatible enzyme-crosslinked gelatin hydrogels. *J Biomed Mater Res A* **95A**, 25–32 (2010).

172. Davis, N. E., Ding, S., Forster, R. E., Pinkas, D. M. & Barron, A. E. Modular enzymatically crosslinked protein polymer hydrogels for in situ gelation. *Biomaterials* **31**, 7288–7297 (2010).

173. Kim, K. S. *et al.* Injectable hyaluronic acid–tyramine hydrogels for the treatment of rheumatoid arthritis. *Acta Biomater* **7**, 666–674 (2011).

174. Jin, R. *et al.* Injectable chitosan-based hydrogels for cartilage tissue engineering. *Biomaterials* **30**, 2544–2551 (2009).

175. Chen, T., Embree, H. D., Brown, E. M., Taylor, M. M. & Payne, G. F. Enzyme-catalyzed gel formation of gelatin and chitosan: potential for in situ applications. *Biomaterials* **24**, 2831–2841 (2003).

176. Yung, C. W. *et al.* Transglutaminase crosslinked gelatin as a tissue engineering scaffold. *J Biomed Mater Res A* **83A**, 1039–1046 (2007).

177. Bustamante-Torres, M. *et al.* Hydrogels Classification According to the Physical or Chemical Interactions and as Stimuli-Sensitive Materials. *Gels* **7**, 182 (2021).

178. Mahmood, A. *et al.* Polymeric Hydrogels and Nanogels: Classification, Development, and Pharmaceutical Applications. in *Hydrogels and Nanogels - Applications in Medicine [Working Title]* (IntechOpen, 2023). doi:10.5772/intechopen.1002194.

179. Lohani, A., Singh, G., Bhattacharya, S. S. & Verma, A. Interpenetrating Polymer Networks as Innovative Drug Delivery Systems. *J Drug Deliv* **2014**, 1–11 (2014).

180. Rokhade, A. P., Patil, S. A. & Aminabhavi, T. M. Synthesis and characterization of semi-interpenetrating polymer network microspheres of acrylamide grafted dextran and chitosan for controlled release of acyclovir. *Carbohydr Polym* **67**, 605–613 (2007).

181. Alemán, J. V. *et al.* Definitions of terms relating to the structure and processing of sols, gels, networks, and inorganic-organic hybrid materials (IUPAC Recommendations 2007). *Pure and Applied Chemistry* **79**, 1801–1829 (2007).

182. Toledo, P. V. O., Limeira, D. P. C., Siqueira, N. C. & Petri, D. F. S. Carboxymethyl cellulose/poly(acrylic acid) interpenetrating polymer network hydrogels as multifunctional adsorbents. *Cellulose* **26**, 597–615 (2019).

183. Myung, D. *et al.* Progress in the development of interpenetrating polymer network hydrogels. *Polym Adv Technol* **19**, 647–657 (2008).

184. Zheng, S. Y., Du, C. & Wu, Z. L. Interpenetrating polymer networks hydrogels. in *Hydrogels for Tissue Engineering and Regenerative Medicine* 331–346 (Elsevier, 2024). doi:10.1016/B978-0-12-823948-3.00021-X.

185. Sperling, L. H. & Mishra, V. The Current Status of Interpenetrating Polymer Networks. *Polym Adv Technol* **7**, 197–208 (1996).

186. Dragan, E. S. Design and applications of interpenetrating polymer network hydrogels. A review. *Chemical Engineering Journal* **243**, 572–590 (2014).

187. Dhand, A. P., Galarraga, J. H. & Burdick, J. A. Enhancing Biopolymer Hydrogel Functionality through Interpenetrating Networks. *Trends Biotechnol* **39**, 519–538 (2021).

188. Okay, O. General Properties of Hydrogels. in 1–14 (2009). doi:10.1007/978-3-540-75645-3_1.

189. Palacio, D. A., Urbano, B. F., Palencia, M. & Rivas, B. L. Preparation of alkylated chitosan-based polyelectrolyte hydrogels: The effect of monomer charge on polymerization. *Eur Polym J* **118**, 551–560 (2019).

190. Qiu, Y. & Park, K. Environment-sensitive hydrogels for drug delivery. *Adv Drug Deliv Rev* **53**, 321–339 (2001).

191. Lee, W.-F. & Chiu, R.-J. Investigation of charge effects on drug release behavior for ionic thermosensitive hydrogels. *Materials Science and Engineering: C* **20**, 161–166 (2002).

192. Ahmad, Z. *et al.* Versatility of Hydrogels: From Synthetic Strategies, Classification, and Properties to Biomedical Applications. *Gels* **8**, 167 (2022).

193. Singhal, R. & Gupta, K. A Review: Tailor-made Hydrogel Structures (Classifications and Synthesis Parameters). *Polym Plast Technol Eng* **55**, 54–70 (2016).

194. Williams, D. F. On the mechanisms of biocompatibility. *Biomaterials* **29**, 2941–2953 (2008).

195. Petrak, K. Polymers for use in drug delivery—property and structure requirements. *British Polymer Journal* **22**, 213–219 (1990).

196. Hu, W., Wang, Z., Xiao, Y., Zhang, S. & Wang, J. Advances in crosslinking strategies of biomedical hydrogels. *Biomater Sci* **7**, 843–855 (2019).

197. He, S. *et al.* Synthesis of biodegradable poly(propylene fumarate) networks with poly(propylene fumarate)–diacrylate macromers as crosslinking agents and characterization of their degradation products. *Polymer (Guildf)* **42**, 1251–1260 (2001).

198. Cho, E. *et al.* A novel synthetic route for the preparation of hydrolytically degradable synthetic hydrogels. *J Biomed Mater Res A* **90A**, 1073–1082 (2009).

199. Elbert, D. L., Pratt, A. B., Lutolf, M. P., Halstenberg, S. & Hubbell, J. A. Protein delivery from materials formed by self-selective conjugate addition reactions. *Journal of Controlled Release* **76**, 11–25 (2001).

200. Polizzotti, B. D., Fairbanks, B. D. & Anseth, K. S. Three-Dimensional Biochemical Patterning of Click-Based Composite Hydrogels via Thiolene Photopolymerization. *Biomacromolecules* **9**, 1084–1087 (2008).

201. RYDHOLM, A., ANSETH, K. & BOWMAN, C. Effects of neighboring sulfides and pH on ester hydrolysis in thiol–acrylate photopolymers. *Acta Biomater* **3**, 449–455 (2007).

202. Rydholm, A. E., Reddy, S. K., Anseth, K. S. & Bowman, C. N. Development and characterization of degradable thiol-allyl ether photopolymers. *Polymer (Guildf)* **48**, 4589–4600 (2007).

203. Zustiak, S. P. & Leach, J. B. Characterization of protein release from hydrolytically degradable poly(ethylene glycol) hydrogels. *Biotechnol Bioeng* **108**, 197–206 (2011).

204. Hoyle, C. E. & Bowman, C. N. Thiol–Ene Click Chemistry. *Angewandte Chemie International Edition* **49**, 1540–1573 (2010).

205. Alge, D. L., Azagarsamy, M. A., Donohue, D. F. & Anseth, K. S. Synthetically Tractable Click Hydrogels for Three-Dimensional Cell Culture Formed Using Tetrazine–Norbornene Chemistry. *Biomacromolecules* **14**, 949–953 (2013).

206. Koehler, K. C., Alge, D. L., Anseth, K. S. & Bowman, C. N. A Diels–Alder modulated approach to control and sustain the release of dexamethasone and induce osteogenic differentiation of human mesenchymal stem cells. *Biomaterials* **34**, 4150–4158 (2013).

207. Fairbanks, B. D. *et al.* A versatile synthetic extracellular matrix mimic via thiol-norbornene photopolymerization. *Advanced Materials* (2009) doi:10.1002/adma.200901808.

208. Lin, C.-C. & Metters, A. T. Hydrogels in controlled release formulations: Network design and mathematical modeling. *Adv Drug Deliv Rev* **58**, 1379–1408 (2006).

209. Fairbanks, B. D., Schwartz, M. P., Bowman, C. N. & Anseth, K. S. Photoinitiated polymerization of PEG-diacrylate with lithium phenyl-2,4,6-trimethylbenzoylphosphinate: polymerization rate and cytocompatibility. *Biomaterials* **30**, 6702–6707 (2009).

210. Lin, C. C., Ki, C. S. & Shih, H. Thiol-norbornene photoclick hydrogels for tissue engineering applications. *J Appl Polym Sci* **132**, 1–11 (2015).

211. Anseth, K. S., Bowman, C. N. & Brannon-Peppas, L. Mechanical properties of hydrogels and their experimental determination. *Biomaterials* **17**, 1647–1657 (1996).

212. Kloxin, A. M., Benton, J. A. & Anseth, K. S. In situ elasticity modulation with dynamic substrates to direct cell phenotype. *Biomaterials* **31**, 1–8 (2010).

213. DeForest, C. A. & Anseth, K. S. Cytocompatible click-based hydrogels with dynamically tunable properties through orthogonal photoconjugation and photocleavage reactions. *Nat Chem* **3**, 925–931 (2011).

214. Shih, H. & Lin, C.-C. Cross-Linking and Degradation of Step-Growth Hydrogels Formed by Thiol–Ene Photoclick Chemistry. *Biomacromolecules* **13**, 2003–2012 (2012).

215. Metters, A. & Hubbell, J. Network Formation and Degradation Behavior of Hydrogels Formed by Michael-Type Addition Reactions. *Biomacromolecules* **6**, 290–301 (2005).

216. Lutolf, M. P. *et al.* Synthetic matrix metalloproteinase-sensitive hydrogels for the conduction of tissue regeneration: Engineering cell-invasion characteristics. *Proceedings of the National Academy of Sciences* **100**, 5413–5418 (2003).

217. Anderson, S. B., Lin, C.-C., Kuntzler, D. V. & Anseth, K. S. The performance of human mesenchymal stem cells encapsulated in cell-degradable polymer-peptide hydrogels. *Biomaterials* **32**, 3564–3574 (2011).

218. Benton, J. A., Fairbanks, B. D. & Anseth, K. S. Characterization of valvular interstitial cell function in three dimensional matrix metalloproteinase degradable PEG hydrogels. *Biomaterials* **30**, 6593–6603 (2009).

219. Ki, C. S., Lin, T.-Y., Korc, M. & Lin, C.-C. Thiol-ene hydrogels as desmoplasia-mimetic matrices for modeling pancreatic cancer cell growth, invasion, and drug resistance. *Biomaterials* **35**, 9668–9677 (2014).

220. Aimetti, A. A., Machen, A. J. & Anseth, K. S. Poly(ethylene glycol) hydrogels formed by thiol-ene photopolymerization for enzyme-responsive protein delivery. *Biomaterials* **30**, 6048–6054 (2009).

221. ZONG, X. *et al.* Electrospun fine-textured scaffolds for heart tissue constructs. *Biomaterials* **26**, 5330–5338 (2005).

222. Moroni, L., de Wijn, J. R. & van Blitterswijk, C. A. 3D fiber-deposited scaffolds for tissue engineering: Influence of pores geometry and architecture on dynamic mechanical properties. *Biomaterials* **27**, 974–985 (2006).

223. Bacakova, M. *et al.* The potential applications of fibrin-coated electrospun polylactide nanofibers in skin tissue engineering. *Int J Nanomedicine* 771 (2016) doi:10.2147/IJN.S99317.

224. Vig, K. *et al.* Advances in Skin Regeneration Using Tissue Engineering. *Int J Mol Sci* **18**, 789 (2017).

225. Dong, R.-H. *et al.* In situ deposition of a personalized nanofibrous dressing via a handy electrospinning device for skin wound care. *Nanoscale* **8**, 3482–3488 (2016).

226. Liu, G.-S. *et al.* In Situ Electrospinning Iodine-Based Fibrous Meshes for Antibacterial Wound Dressing. *Nanoscale Res Lett* **13**, 309 (2018).

227. Duan, G. *et al.* Ultralight, Soft Polymer Sponges by Self-Assembly of Short Electrospun Fibers in Colloidal Dispersions. *Adv Funct Mater* **25**, 2850–2856 (2015).

228. Khalil, S. & Sun, W. Bioprinting Endothelial Cells With Alginate for 3D Tissue Constructs. *J Biomech Eng* **131**, (2009).

229. Ozbolat, I. T. & Yin Yu. Bioprinting Toward Organ Fabrication: Challenges and Future Trends. *IEEE Trans Biomed Eng* **60**, 691–699 (2013).

230. Seol, Y.-J., Kang, H.-W., Lee, S. J., Atala, A. & Yoo, J. J. Bioprinting technology and its applications. *European Journal of Cardio-Thoracic Surgery* **46**, 342–348 (2014).

231. Zhu, W. *et al.* 3D printing of functional biomaterials for tissue engineering. *Curr Opin Biotechnol* **40**, 103–112 (2016).

232. Knowlton, S., Anand, S., Shah, T. & Tasoglu, S. Bioprinting for Neural Tissue Engineering. *Trends Neurosci* **41**, 31–46 (2018).

233. Huang, Y., Zhang, X., Gao, G., Yonezawa, T. & Cui, X. 3D bioprinting and the current applications in tissue engineering. *Biotechnol J* **12**, (2017).

234. Weng, T. *et al.* 3D bioprinting for skin tissue engineering: Current status and perspectives. *J Tissue Eng* **12**, 204173142110285 (2021).

235. Gu, B. K., Choi, D. J., Park, S. J., Kim, Y.-J. & Kim, C.-H. 3D Bioprinting Technologies for Tissue Engineering Applications. in 15–28 (2018). doi:10.1007/978-981-13-0950-2_2.

236. Arslan-Yildiz, A. *et al.* Towards artificial tissue models: past, present, and future of 3D bioprinting. *Biofabrication* **8**, 014103 (2016).

237. Gudapati, H., Dey, M. & Ozbolat, I. A comprehensive review on droplet-based bioprinting: Past, present and future. *Biomaterials* **102**, 20–42 (2016).

238. Chahal, D., Ahmadi, A. & Cheung, K. C. Improving piezoelectric cell printing accuracy and reliability through neutral buoyancy of suspensions. *Biotechnol Bioeng* **109**, 2932–2940 (2012).

239. Mohamed, O. A., Masood, S. H. & Bhowmik, J. L. Optimization of fused deposition modeling process parameters: a review of current research and future prospects. *Adv Manuf* **3**, 42–53 (2015).

240. Kim, J. D., Choi, J. S., Kim, B. S., Chan Choi, Y. & Cho, Y. W. Piezoelectric inkjet printing of polymers: Stem cell patterning on polymer substrates. *Polymer (Guildf)* **51**, 2147–2154 (2010).

241. Gong, Y. *et al.* Study on linear bio-structure print process based on alginate bio-ink in 3D bio-fabrication. *Biodes Manuf* **3**, 109–121 (2020).

242. Wijshoff, H. The dynamics of the piezo inkjet printhead operation☆. *Phys Rep* **491**, 77–177 (2010).

243. Sears, N. A., Seshadri, D. R., Dhavalikar, P. S. & Cosgriff-Hernandez, E. A Review of Three-Dimensional Printing in Tissue Engineering. *Tissue Eng Part B Rev* **22**, 298–310 (2016).

244. Gurkan, U. A. *et al.* Engineering Anisotropic Biomimetic Fibrocartilage Microenvironment by Bioprinting Mesenchymal Stem Cells in Nanoliter Gel Droplets. *Mol Pharm* **11**, 2151–2159 (2014).

245. Onses, M. S., Sutanto, E., Ferreira, P. M., Alleyne, A. G. & Rogers, J. A. Mechanisms, Capabilities, and Applications of High-Resolution Electrohydrodynamic Jet Printing. *Small* **11**, 4237–4266 (2015).

246. Jayasinghe, S. N. & Townsend-Nicholson, A. Stable electric-field driven cone-jetting of concentrated biosuspensions. *Lab Chip* **6**, 1086 (2006).

247. Kim, H.-S. *et al.* OPTIMIZATION OF ELECTROHYDRODYNAMIC WRITING TECHNIQUE TO PRINT COLLAGEN. *Exp Tech* **31**, 15–19 (2007).

248. Workman, V. L., Tezera, L. B., Elkington, P. T. & Jayasinghe, S. N. Controlled Generation of Microspheres Incorporating Extracellular Matrix Fibrils for Three-Dimensional Cell Culture. *Adv Funct Mater* **24**, 2648–2657 (2014).

249. Jayasinghe, S. N., Qureshi, A. N. & Eagles, P. A. M. Electrohydrodynamic Jet Processing: An Advanced Electric-Field-Driven Jetting Phenomenon for Processing Living Cells. *Small* **2**, 216–219 (2006).

250. Dinca, V. *et al.* Directed Three-Dimensional Patterning of Self-Assembled Peptide Fibrils. *Nano Lett* **8**, 538–543 (2008).

251. Chrisey, D. B. The Power of Direct Writing. *Science (1979)* **289**, 879–881 (2000).

252. Barron, J. A., Wu, P., Ladouceur, H. D. & Ringeisen, B. R. Biological Laser Printing: A Novel Technique for Creating Heterogeneous 3-dimensional Cell Patterns. *Biomed Microdevices* **6**, 139–147 (2004).

253. Arnold, C. B., Serra, P. & Piqué, A. Laser Direct-Write Techniques for Printing of Complex Materials. *MRS Bull* **32**, 23–31 (2007).

254. Guillemot, F., Souquet, A., Catros, S. & Guillotin, B. Laser-assisted cell printing: principle, physical parameters versus cell fate and perspectives in tissue engineering. *Nanomedicine* **5**, 507–515 (2010).

255. Ringeisen, B. R., Othon, C. M., Barron, J. A., Young, D. & Spargo, B. J. Jet-based methods to print living cells. *Biotechnol J* **1**, 930–948 (2006).

256. Devillard, R. *et al.* Cell Patterning by Laser-Assisted Bioprinting. in 159–174 (2014). doi:10.1016/B978-0-12-416742-1.00009-3.

257. Michael, S. *et al.* Tissue Engineered Skin Substitutes Created by Laser-Assisted Bioprinting Form Skin-Like Structures in the Dorsal Skin Fold Chamber in Mice. *PLoS One* **8**, e57741 (2013).

258. Koch, L. *et al.* Laser Printing of Skin Cells and Human Stem Cells. *Tissue Eng Part C Methods* **16**, 847–854 (2010).

259. Serra, P., Duocastella, M., Fernández-Pradas, J. M. & Morenza, J. L. Liquids microprinting through laser-induced forward transfer. *Appl Surf Sci* **255**, 5342–5345 (2009).

260. Patrascioiu, A., Fernández-Pradas, J. M., Palla-Papavlu, A., Morenza, J. L. & Serra, P. Laser-generated liquid microjets: correlation between bubble dynamics and liquid ejection. *Microfluid Nanofluidics* **16**, 55–63 (2014).

261. Ali, M., Pages, E., Ducom, A., Fontaine, A. & Guillemot, F. Controlling laser-induced jet formation for bioprinting mesenchymal stem cells with high viability and high resolution. *Biofabrication* **6**, 045001 (2014).

262. Vanaei, S., Parizi, M. S., Vanaei, S., Salemizadehparizi, F. & Vanaei, H. R. An Overview on Materials and Techniques in 3D Bioprinting Toward Biomedical Application. *Engineered Regeneration* **2**, 1–18 (2021).

263. Mironov, V., Boland, T., Trusk, T., Forgacs, G. & Markwald, R. R. Organ printing: computer-aided jet-based 3D tissue engineering. *Trends Biotechnol* **21**, 157–161 (2003).

264. Shafiee, A. & Atala, A. Printing Technologies for Medical Applications. *Trends Mol Med* **22**, 254–265 (2016).

265. Fielding, G. A., Bandyopadhyay, A. & Bose, S. Effects of silica and zinc oxide doping on mechanical and biological properties of 3D printed tricalcium phosphate tissue engineering scaffolds. *Dental Materials* **28**, 113–122 (2012).

266. Munaz, A. *et al.* Three-dimensional printing of biological matters. *Journal of Science: Advanced Materials and Devices* **1**, 1–17 (2016).

267. Matai, I., Kaur, G., Seyedsalehi, A., McClinton, A. & Laurencin, C. T. Progress in 3D bioprinting technology for tissue/organ regenerative engineering. *Biomaterials* **226**, 119536 (2020).

268. Liu, W. *et al.* Rapid Continuous Multimaterial Extrusion Bioprinting. *Advanced Materials* **29**, (2017).

269. Dhariwala, B., Hunt, E. & Boland, T. Rapid Prototyping of Tissue-Engineering Constructs, Using Photopolymerizable Hydrogels and Stereolithography. *Tissue Eng* **10**, 1316–1322 (2004).

270. de Gruijl, F. R., van Kranen, H. J. & Mullenders, L. H. F. UV-induced DNA damage, repair, mutations and oncogenic pathways in skin cancer. *J Photochem Photobiol B* **63**, 19–27 (2001).

271. Melchels, F. P. W., Feijen, J. & Grijpma, D. W. A review on stereolithography and its applications in biomedical engineering. *Biomaterials* **31**, 6121–6130 (2010).

272. Heinrich, M. A. *et al.* 3D Bioprinting: from Benches to Translational Applications. *Small* **15**, (2019).

273. Li, H. *et al.* Digital light processing (DLP)-based (bio)printing strategies for tissue modeling and regeneration. *Aggregate* **4**, (2023).

274. Caprioli, M. *et al.* 3D-printed self-healing hydrogels via Digital Light Processing. *Nat Commun* **12**, 2462 (2021).

275. Hong, H. *et al.* Digital light processing 3D printed silk fibroin hydrogel for cartilage tissue engineering. *Biomaterials* **232**, 119679 (2020).

276. Lee, V. *et al.* Design and Fabrication of Human Skin by Three-Dimensional Bioprinting. *Tissue Eng Part C Methods* **20**, 473–484 (2014).

277. Cubo, N., Garcia, M., del Cañizo, J. F., Velasco, D. & Jorcano, J. L. 3D bioprinting of functional human skin: production and *in vivo* analysis. *Biofabrication* **9**, 015006 (2016).

278. Wang, S. *et al.* Three Dimensional Printing Bilayer Membrane Scaffold Promotes Wound Healing. *Front Bioeng Biotechnol* **7**, (2019).

279. Ozbolat, I. T. Bioprinting scale-up tissue and organ constructs for transplantation. *Trends Biotechnol* **33**, 395–400 (2015).

280. Albanna, M. *et al.* In Situ Bioprinting of Autologous Skin Cells Accelerates Wound Healing of Extensive Excisional Full-Thickness Wounds. *Sci Rep* **9**, 1856 (2019).

281. Vijayavenkataraman, S., Lu, W. F. & Fuh, J. Y. H. 3D bioprinting of skin: a state-of-the-art review on modelling, materials, and processes. *Biofabrication* **8**, 032001 (2016).

282. Yanez, M. *et al. In Vivo* Assessment of Printed Microvasculature in a Bilayer Skin Graft to Treat Full-Thickness Wounds. *Tissue Eng Part A* **21**, 224–233 (2015).

283. Abaci, H. E. *et al.* Human Skin Constructs with Spatially Controlled Vasculature Using Primary and iPSC-Derived Endothelial Cells. *Adv Healthc Mater* **5**, 1800–1807 (2016).

284. Kérourédan, O. *et al.* Micropatterning of endothelial cells to create a capillary-like network with defined architecture by laser-assisted bioprinting. *J Mater Sci Mater Med* **30**, 28 (2019).

285. Chouhan, D., Dey, N., Bhardwaj, N. & Mandal, B. B. Emerging and innovative approaches for wound healing and skin regeneration: Current status and advances. *Biomaterials* **216**, 119267 (2019).

286. Mori, N., Morimoto, Y. & Takeuchi, S. Skin integrated with perfusable vascular channels on a chip. *Biomaterials* **116**, 48–56 (2017).

287. Kolesky, D. B. *et al.* 3D Bioprinting of Vascularized, Heterogeneous Cell-Laden Tissue Constructs. *Advanced Materials* **26**, 3124–3130 (2014).

288. Min, D. *et al.* Bioprinting of biomimetic skin containing melanocytes. *Exp Dermatol* **27**, 453–459 (2018).

289. Ng, W. L., Qi, J. T. Z., Yeong, W. Y. & Naing, M. W. Proof-of-concept: 3D bioprinting of pigmented human skin constructs. *Biofabrication* **10**, 025005 (2018).

290. Wu, J.-J. *et al.* Hair follicle reformation induced by dermal papilla cells from human scalp skin. *Arch Dermatol Res* **298**, 183–190 (2006).

291. Abaci, H. E. *et al.* Tissue engineering of human hair follicles using a biomimetic developmental approach. *Nat Commun* **9**, (2018).

292. Miao, Y., Sun, Y. Bin, Liu, B. C., Jiang, J. D. & Hu, Z. Q. Controllable Production of Transplantable Adult Human High-Passage Dermal Papilla Spheroids Using 3D Matrigel Culture. *Tissue Eng Part A* **20**, 2329–2338 (2014).

293. Zhang, K. *et al.* Cellular Nanofiber Structure with Secretory Activity-Promoting Characteristics for Multicellular Spheroid Formation and Hair Follicle Regeneration. *ACS Appl Mater Interfaces* **12**, 7931–7941 (2020).

294. Jorgensen, A. M. *et al.* Multicellular bioprinted skin facilitates human-like skin architecture in vivo. *Sci Transl Med* **15**, (2023).

295. Pappalardo, A. *et al.* Engineering edgeless human skin with enhanced biomechanical properties. *Sci Adv* **9**, (2023).

296. Rossi, A., Appelt-Menzel, A., Kurdyn, S., Walles, H. & Groeber, F. Generation of a three-dimensional full thickness skin equivalent and automated wounding. *Journal of Visualized Experiments* (2015) doi:10.3791/52576.

297. El Ghalbzouri, A., Siamari, R., Willemze, R. & Ponec, M. Leiden reconstructed human epidermal model as a tool for the evaluation of the skin corrosion and irritation potential according to the ECVAM guidelines. *Toxicology in Vitro* **22**, 1311–1320 (2008).

298. Qin, X. H., Ovsianikov, A., Stampfl, J. & Liska, R. Additive manufacturing of photosensitive Hydrogels for tissue engineering applications. *BioNanoMaterials* vol. 15 49–70 Preprint at https://doi.org/10.1515/bnm-2014-0008 (2014).

299. Rafat, M., Rotenstein, L. S., You, J. O. & Auguste, D. T. Dual functionalized PVA hydrogels that adhere endothelial cells synergistically. *Biomaterials* **33**, 3880–3886 (2012).

300. Autissier, A., Letourneur, D. & Le Visage, C. Pullulan-based hydrogel for smooth muscle cell culture. *J Biomed Mater Res A* **82A**, 336–342 (2007).

301. Kumar, R., Chaudhary, P., Nimesh, S. & Chandra, R. Polyethylene glycol as a non-ionic liquid solvent for Michael addition reaction of amines to conjugated alkenes. *Green Chemistry* **8**, 356 (2006).

302. Garantziotis, S. & Savani, R. C. Hyaluronan biology: A complex balancing act of structure, function, location and context. *Matrix Biology* **78–79**, 1–10 (2019).

303. Pan, J. *et al.* Investigating the repair of alveolar bone defects by gelatin methacrylate hydrogels-encapsulated human periodontal ligament stem cells. *J Mater Sci Mater Med* **31**, 3 (2020).

304. Maiz-Fernández, S., Pérez-Álvarez, L., Silván, U., Vilas-Vilela, J. L. & Lanceros-Mendez, S. Photocrosslinkable and self-healable hydrogels of chitosan and hyaluronic acid. *Int J Biol Macromol* **216**, 291–302 (2022).

305. Hynes, R. O. & Zhao, Q. The Evolution of Cell Adhesion. *J Cell Biol* **150**, F89–F96 (2000).

306. Lowell, C. A. & Mayadas, T. N. Overview: Studying Integrins In Vivo. in 369–397 (2011). doi:10.1007/978-1-61779-166-6_22.

307. Jukes, J. M. *et al. A Newly Developed Chemically Crosslinked Dextran-Poly(Ethylene Glycol) Hydrogel for Cartilage Tissue Engineering*. www.liebertonline.com=ten.

308. Torras, N. *et al.* A simple DLP-bioprinting strategy produces cell-laden crypt-villous structures for an advanced 3D gut model. doi:10.1101/2022.02.09.479715.

309. Selimis, A., Mironov, V. & Farsari, M. Direct laser writing: Principles and materials for scaffold 3D printing. *Microelectron Eng* **132**, 83–89 (2015).

310. Wang, Z. *et al.* A Novel, Well-Resolved Direct Laser Bioprinting System for Rapid Cell Encapsulation and Microwell Fabrication. *Adv Healthc Mater* **7**, 1701249 (2018).

311. Anseth, K. S., Bowman, C. N. & Brannon-Peppas, L. Mechanical properties of hydrogels and their experimental determination. *Biomaterials* **17**, 1647–1657 (1996).

312. Zoio, P., Ventura, S., Leite, M. & Oliva, A. Pigmented Full-Thickness Human Skin Model Based on a Fibroblast-Derived Matrix for Long-Term Studies. *Tissue Eng Part C Methods* **27**, 433–443 (2021).

313. Srinivasan, B. *et al.* TEER Measurement Techniques for In Vitro Barrier Model Systems. *Journal of Laboratory Automation* vol. 20 107–126 Preprint at https://doi.org/10.1177/2211068214561025 (2015).

314. Arlk, Y. B. *et al.* Barriers-on-chips: Measurement of barrier function of tissues in organs-on-chips. *Biomicrofluidics* **12**, (2018).

315. Zulkiflee, I. & Fauzi, M. B. Gelatin-polyvinyl alcohol film for tissue engineering: A concise review. *Biomedicines* vol. 9 Preprint at https://doi.org/10.3390/biomedicines9080979 (2021).

316. Ramesan, R. & Sharma, C. P. *Pullulan as a Promising Biomaterial for Biomedical Applications: A Perspective Quantum Clusters for Cell Imaging View Project Advanced Biomaterials View Project*. http://www.sbaoi.org.

317. Torras, N. *et al.* A bioprinted 3D gut model with crypt-villus structures to mimic the intestinal epithelial-stromal microenvironment. *Biomaterials Advances* **153**, (2023).

318. Raub, C. B., Putnam, A. J., Tromberg, B. J. & George, S. C. Predicting bulk mechanical properties of cellularized collagen gels using multiphoton microscopy. *Acta Biomater* **6**, 4657–4665 (2010).

319. Lin, S., He, X. & He, Y. Co-culture of ASCs/EPCs and dermal extracellular matrix hydrogel enhances the repair of full-thickness skin wound by promoting angiogenesis. *Stem Cell Res Ther* **12**, (2021).

320. Knight, C. G., Willenbrock, F. & Murphy, G. A novel coumarin-labelled peptide for sensitive continuous assays of the matrix metalloproteinases. *FEBS Lett* **296**, 263–266 (1992).

321. Bachmann, B. *et al.* Stiffness Matters: Fine-Tuned Hydrogel Elasticity Alters Chondrogenic Redifferentiation. *Front Bioeng Biotechnol* **8**, (2020).

322. Achterberg, V. F. *et al.* The nano-scale mechanical properties of the extracellular matrix regulate dermal fibroblast function. *Journal of Investigative Dermatology* **134**, 1862–1872 (2014).

323. Oikarinen, A. Aging of the skin connective tissue: how to measure the biochemical and mechanical properties of aging dermis. *Photodermatol Photoimmunol Photomed* **10**, 47–52 (1994).

324. Ricard-Blum, S. The Collagen Family. *Cold Spring Harb Perspect Biol* **3**, a004978–a004978 (2011).

325. Cirulli, A., Borgheti-Cardoso, L. N., Torras, N. & Martínez, E. Mimicking human skin constructs using norbornene-pullulan-based hydrogels. *Int J Bioprint* **0**, 3395 (2024).

326. Nishiyama, T. *et al.* The importance of laminin 5 in the dermal–epidermal basement membrane. *J Dermatol Sci* **24**, S51–S59 (2000).

327. Van Den Bossche, J., Malissen, B., Mantovani, A., De Baetselier, P. & Van Ginderachter, J. A. Regulation and function of the E-cadherin/catenin complex in cells of the monocyte-macrophage lineage and DCs. (2012) doi:10.1182/blood-2011-10.

328. Halbleib, J. M. & Nelson, W. J. Cadherins in development: Cell adhesion, sorting, and tissue morphogenesis. *Genes and Development* vol. 20 3199–3214 Preprint at https://doi.org/10.1101/gad.1486806 (2006).

329. Gimeno-LLuch, I., Benito-Jardón, M., Guerrero-Barberà, G., Burday, N. & Costell, M. The Role of the Fibronectin Synergy Site for Skin Wound Healing. *Cells* **11**, 2100 (2022).

330. Campbell, I. D. & Humphries, M. J. Integrin Structure, Activation, and Interactions. *Cold Spring Harb Perspect Biol* **3**, a004994–a004994 (2011).

331. Sottile, J. *et al.* Fibronectin-dependent collagen I deposition modulates the cell response to fibronectin. *American Journal of Physiology-Cell Physiology* **293**, C1934–C1946 (2007).

332. Sabatier, L. *et al.* Fibrillin Assembly Requires Fibronectin. *Mol Biol Cell* **20**, 846–858 (2009).

333. Barker, T. H. & Engler, A. J. The provisional matrix: setting the stage for tissue repair outcomes. *Matrix Biology* **60–61**, 1–4 (2017).

334. Guo, Y. *et al.* Keratin 14-dependent disulfides regulate epidermal homeostasis and barrier function via 14-3-3σ and YAP1. *Elife* **9**, (2020).

335. Zhang, L. Keratins in Skin Epidermal Development and Diseases. in *Keratin* (IntechOpen, 2018). doi:10.5772/intechopen.79050.

336. Lee, J., Lee, P. & Wu, X. Molecular and cytoskeletal regulations in epidermal development. *Semin Cell Dev Biol* **69**, 18–25 (2017).

337. Tinkle, C. L., Lechler, T., Pasolli, H. A. & Fuchs, E. Conditional targeting of E-cadherin in skin: Insights into hyperproliferative and degenerative responses. *Proceedings of the National Academy of Sciences* **101**, 552–557 (2004).

338. Srinivasan, B. *et al.* TEER Measurement Techniques for In Vitro Barrier Model Systems. *SLAS Technol* **20**, 107–126 (2015).

339. Zucco, F. *et al.* An Inter-laboratory Study to Evaluate the Effects of Medium Composition on the Differentiation and Barrier Function of Caco-2 Cell Lines. *Alternatives to Laboratory Animals* **33**, 603–618 (2005).

340. Toole, B. P. Hyaluronan: From extracellular glue to pericellular cue. *Nature Reviews Cancer* vol. 4 528–539 Preprint at https://doi.org/10.1038/nrc1391 (2004).

341. Le Ferrec, E. *et al.* In vitro models of the intestinal barrier: The report and recommendations of ECVAM workshop 461,2. *ATLA Alternatives to Laboratory Animals* **29**, 649–668 (2001).

342. Sperling, L. H. & Hu, R. Interpenetrating Polymer Networks. in *Polymer Blends Handbook* 677–724 (Springer Netherlands, Dordrecht, 2014). doi:10.1007/978-94-007-6064-6_8.

343. Kim, S. J., Yoon, S. G. & Kim, S. I. Synthesis and characteristics of interpenetrating polymer network hydrogels composed of alginate and poly(diallydimethylammonium chloride). *J Appl Polym Sci* **91**, 3705–3709 (2004).

344. Lohani, A., Singh, G., Bhattacharya, S. S. & Verma, A. Interpenetrating Polymer Networks as Innovative Drug Delivery Systems. *J Drug Deliv* **2014**, 1–11 (2014).

345. Sun, G. *et al.* Dextran hydrogel scaffolds enhance angiogenic responses and promote complete skin regeneration during burn wound healing. *Proceedings of the National Academy of Sciences* **108**, 20976–20981 (2011).

346. João Maia. Dextran-based materials for biomedical applications. *Carbohydrates Applications in Medicine, 2014: 31-53 ISBN: 978-81-308-0523-8 Editor: M. H. Gil*.

347. Matsushige, C., Xu, X., Miyagi, M., Zuo, Y. Y. & Yamazaki, Y. RGD-modified dextran hydrogel promotes follicle growth in three-dimensional ovarian tissue culture in mice. *Theriogenology* **183**, 120–131 (2022).

348. Franssen, O., Vos, O. P. & Hennink, W. E. Delayed release of a model protein from enzymatically-degrading dextran hydrogels. *Journal of Controlled Release* **44**, 237–245 (1997).

349. Alves, P. *et al.* Dextran-Based Injectable Hydrogel Composites for Bone Regeneration. *Polymers (Basel)* **15**, 4501 (2023).

350. Jachowicz, J., McMullen, R. & Prettypaul, D. Indentometric analysis of *in vivo* skin and comparison with artificial skin models. *Skin Research and Technology* **13**, 299–309 (2007).

351. Rivero, R. E. *et al.* Mechanical and physicochemical behavior of a 3D hydrogel scaffold during cell growth and proliferation. *RSC Adv* **10**, 5827–5837 (2020).

352. Tian, X. Y. & Chen, X. B. Effects of Cell Density on Mechanical Properties of Alginate Hydrogel Tissue Scaffolds. *J Biomim Biomater Tissue Eng* **19**, 77–85 (2014).

353. Breitkreutz, D. *et al.* Integrin and basement membrane normalization in mouse grafts of human keratinocytes – Implications for epidermal homeostasis. *Differentiation* **61**, 195–209 (1997).

354. Schoop, V. M., Fusenig, N. E. & Mirancea, N. Epidermal Organization and Differentiation of HaCaT Keratinocytes in Organotypic Coculture with Human Dermal Fibroblasts. *Journal of Investigative Dermatology* **112**, 343–353 (1999).

355. Smits, J. P. H. *et al.* Immortalized N/TERT keratinocytes as an alternative cell source in 3D human epidermal models. *Sci Rep* **7**, (2017).

356. Roger, M. *et al.* Bioengineering the microanatomy of human skin. *J Anat* **234**, 438–455 (2019).

357. Zingkou, E., Pampalakis, G. & Sotiropoulou, G. Keratinocyte differentiation and proteolytic pathways in skin (patho) physiology. *International Journal of Developmental Biology* **66**, 269–275 (2021).

358. Watt, F. M. Involucrin and Other Markers of Keratinocyte Terminal Differentiation. *Journal of Investigative Dermatology* **81**, S100–S103 (1983).

359. Kim, B. E., Leung, D. Y. M., Boguniewicz, M. & Howell, M. D. Loricrin and involucrin expression is down-regulated by Th2 cytokines through STAT-6. *Clinical Immunology* **126**, 332–337 (2008).

360. Jang, S.-I. & Steinert, P. M. Loricrin Expression in Cultured Human Keratinocytes Is Controlled by a Complex Interplay between Transcription Factors of the Sp1, CREB, AP1, and AP2 Families. *Journal of Biological Chemistry* **277**, 42268–42279 (2002).

361. Drislane, C. & Irvine, A. D. The role of filaggrin in atopic dermatitis and allergic disease. *Annals of Allergy, Asthma & Immunology* **124**, 36–43 (2020).

362. Armengot-Carbo, M., Hernández-Martín, Á. & Torrelo, A. The Role of Filaggrin in the Skin Barrier and Disease Development. *Actas Dermo-Sifiliográficas (English Edition)* **106**, 86–95 (2015).

363. Kopczyńska, E. & Makarewicz, R. Endoglin - A marker of vascular endothelial cell proliferation in cancer. *Wspolczesna Onkologia* vol. 16 68–71 Preprint at https://doi.org/10.5114/wo.2012.27340 (2012).

364. Sutterby, E., Thurgood, P., Baratchi, S., Khoshmanesh, K. & Pirogova, E. Evaluation of in vitro human skin models for studying effects of external stressors and stimuli and developing treatment modalities. *VIEW* vol. 3 Preprint at https://doi.org/10.1002/VIW.20210012 (2022).

365. ROSDY, M., PISANI, A. & ORTONNE, J.-P. Production of basement membrane components by a reconstructed epidermis cultured in the absence of serum and dermal factors. *British Journal of Dermatology* **129**, 227–234 (1993).

366. Jensen, C. & Teng, Y. Is It Time to Start Transitioning From 2D to 3D Cell Culture? *Front Mol Biosci* **7**, (2020).

367. Sörgel, C. A., Cai, A., Schmid, R. & Horch, R. E. Perspectives on the Current State of Bioprinted Skin Substitutes for Wound Healing. *Biomedicines* **11**, 2678 (2023).

368. Manita, P. G., Garcia-Orue, I., Santos-Vizcaino, E., Hernandez, R. M. & Igartua, M. 3D Bioprinting of Functional Skin Substitutes: From Current Achievements to Future Goals. *Pharmaceuticals* **14**, 362 (2021).

369. Williams, D., Thayer, P., Martinez, H., Gatenholm, E. & Khademhosseini, A. A perspective on the physical, mechanical and biological specifications of bioinks and the development of functional tissues in 3D bioprinting. *Bioprinting* **9**, 19–36 (2018).

370. Sarrigiannidis, S. O. *et al.* A tough act to follow: collagen hydrogel modifications to improve mechanical and growth factor loading capabilities. *Mater Today Bio* **10**, 100098 (2021).

371. Gungor-Ozkerim, P. S., Inci, I., Zhang, Y. S., Khademhosseini, A. & Dokmeci, M. R. Bioinks for 3D bioprinting: an overview. *Biomater Sci* **6**, 915–946 (2018).

372. Stratesteffen, H. *et al.* GelMA-collagen blends enable drop-on-demand 3D printablility and promote angiogenesis. *Biofabrication* **9**, 045002 (2017).

373. Tehfe, M., Louradour, F., Lalevée, J. & Fouassier, J.-P. Photopolymerization Reactions: On the Way to a Green and Sustainable Chemistry. *Applied Sciences* **3**, 490–514 (2013).

374. Lepori, I. *et al.* Bioorthogonal "Click" Cycloadditions: A Toolkit for Modulating Polymers and Nanostructures in Living Systems. *Reactions* **5**, 231–245 (2024).

375. Feng, Z. *et al.* A novel photocurable pullulan-based bioink for digital light processing 3D printing. *Int J Bioprint* **9**, 104–117 (2022).

376. Springer-Verlag, ©, Nguyen, A.-L., Grothe, S. & Luong, J. H. T. *Applied Microbiology Biotechnology Applications of Pullulan in Aqueous Two-Phase Systems for Enzyme Production, Purification and Utilization*. *Appl Microbiol Biotechnol* vol. 27 (1988).

377. Singh, R. S., Kaur, N., Singh, D. & Kennedy, J. F. Investigating aqueous phase separation of pullulan from Aureobasidium pullulans and its characterization. *Carbohydr Polym* **223**, (2019).

378. Elangwe, C. N. *et al.* Pullulan-Based Hydrogels in Wound Healing and Skin Tissue Engineering Applications: A Review. *Int J Mol Sci* **24**, 4962 (2023).

379. Holback, H., Yeo, Y. & Park, K. Hydrogel swelling behavior and its biomedical applications. in *Biomedical Hydrogels* 3–24 (Elsevier, 2011). doi:10.1533/9780857091383.1.3.

380. Lai, V. K. *et al.* Swelling of Collagen-Hyaluronic Acid Co-Gels: An In Vitro Residual Stress Model. *Ann Biomed Eng* **44**, 2984–2993 (2016).

381. A, K. & A, L. Mechanical Behaviour of Skin: A Review. *Journal of Material Science & Engineering* **5**, (2016).

382. Crichton, M. L., Chen, X., Huang, H. & Kendall, M. A. F. Elastic modulus and viscoelastic properties of full thickness skin characterised at micro scales. *Biomaterials* **34**, 2087–2097 (2013).

383. Elleuch, K., Elleuch, R. & Zahouani, H. Comparison of elastic and tactile behavior of human skin and elastomeric materials through tribological tests. *Polym Eng Sci* **46**, 1715–1720 (2006).

384. Weng, T. *et al.* 3D bioprinting for skin tissue engineering: Current status and perspectives. *Journal of Tissue Engineering* vol. 12 Preprint at https://doi.org/10.1177/20417314211028574 (2021).

385. Trappmann, B. *et al.* Extracellular-matrix tethering regulates stem-cell fate. *Nat Mater* **11**, 642–649 (2012).

386. Zhang, T. *et al.* Investigating Fibroblast-Induced Collagen Gel Contraction Using a Dynamic Microscale Platform. *Front Bioeng Biotechnol* **7**, (2019).

387. Nilforoushzadeh, M. A. *et al.* Role of Cultured Skin Fibroblasts in Regenerative Dermatology. *Aesthetic Plast Surg* **46**, 1463–1471 (2022).

388. Mason, B. N., Califano, J. P. & Reinhart-King, C. A. Matrix Stiffness: A Regulator of Cellular Behavior and Tissue Formation. in *Engineering Biomaterials for Regenerative Medicine* 19–37 (Springer New York, New York, NY, 2012). doi:10.1007/978-1-4614-1080-5_2.

389. Reijnders, C. M. A. *et al.* Development of a Full-Thickness Human Skin Equivalent in Vitro Model Derived from TERT-Immortalized Keratinocytes and Fibroblasts. *Tissue Eng Part A* **21**, 2448–2459 (2015).

390. Miyazaki, H. *et al.* A novel strategy to engineer pre-vascularized 3-dimensional skin substitutes to achieve efficient, functional engraftment. *Sci Rep* **9**, 7797 (2019).

391. Schmidt, F. F., Nowakowski, S. & Kluger, P. J. Improvement of a Three-Layered in vitro Skin Model for Topical Application of Irritating Substances. *Front Bioeng Biotechnol* **8**, (2020).

8. Appendix

8.1. LumenX setup

During my PhD project, I had the opportunity to join the Laboratory of Dr. Hasan Erbil Abaci, at Columbia Irving Medical Center, for three months. Dr. Abaci is a pioneer in the 3D-skin models' development, with his well-known studies on tissue regeneration including human hair follicles. Based on his recent advances in the ability to regenerate an entire hair follicle (HF) from cultured human cells, my internship was focused on the development of a new biomimetic approach to generate hair follicles without the use of an external mold. For this purpose, a new DLP-layer-by-layer system was employed (Figure I).

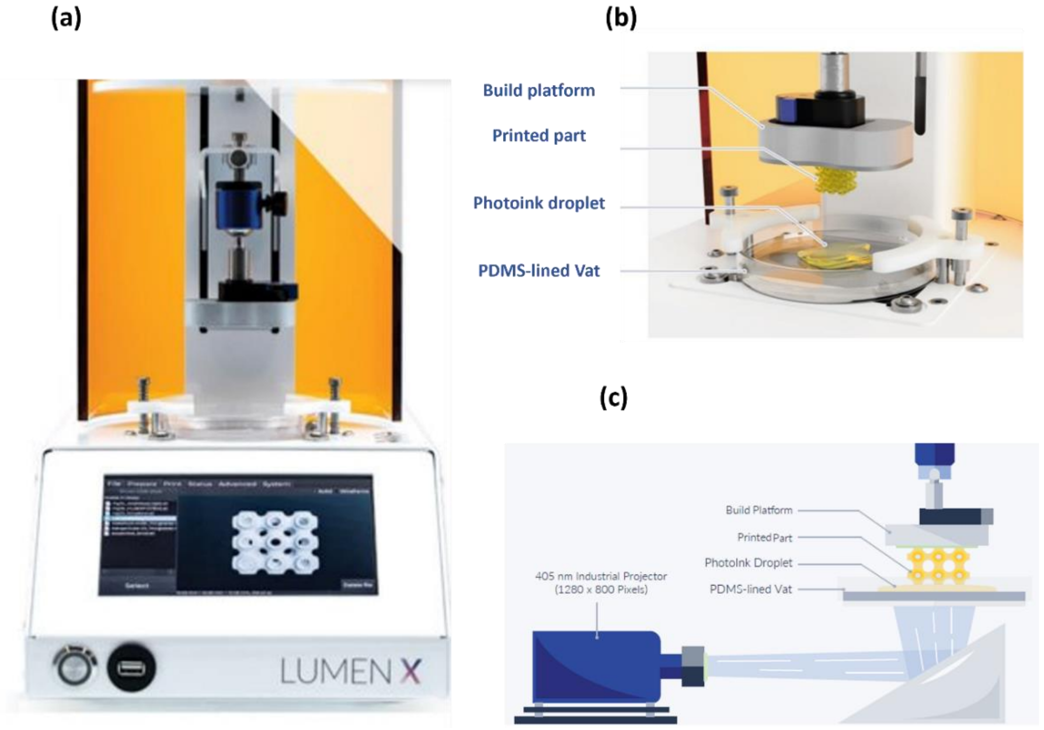

Figure I. LumenX setup. (a) General view and **(b)** its components. **(c)** Schematic representation of the LumenX mechanism.

The LumenX setup allows the building of solid hydrogels starting from a droplet of light-sensitive photo-ink allocated into a PDMS vat (Figure I -b). Through a blue-light projector (405 nm) coming from the bottom, which exposes a series of images according to the designs selected into the vat, like a slideshow, the droplet's areas exposed to the light are crosslinked and solidified creating a single layer (Figure I-c). The build platform moves up to allow each layer to stack and build the part.

The metal build platform holds prints for the entire printing duration. Thanks to its small size, it minimizes the photo-ink amount required. By swapping the build platform it is possible to recover the final scaffold using a spatula.

Table 1. Technical specifications of LumenX bioprinter system.

Dimensions (L x W x H)	43 x 24 x 41 cm
Power supply	AC 100-120V, 50/60 Hz, 10A or AC 200-240V, 50/60Hz, 5A
Projected image	1280 x 800 pixels
Pixel resolution (XY)	50 µm
Z- precision (motor-driven)	5 µm
Max build volume	65 x 40 x 50 mm
Projected light wavelength	405 nm
Intensity range	10-30 mW/cm^2
Electrical power input	100-265 VAC, 50-60 Hz, 100 W

This bioprinting system allows the fabrication of complex structures that can be previously designed and just uploaded into the system as STL files, including hollow structures and specific geometries. Thus, a 3D scaffold as depicted in Figure II-a (8.05 mm x 10.05 mm x 2.70 mm), was developed containing holes (Ø = 250 µm; 1 mm depth) in the central part for the later allocation of Dermal papillae cells. The first bioprinting trials were conducted with a pre-gel solution of PEGDA/GelMA from Cellink company (Composition I).

Volumetric's LumenX-PEGDA200 photoink is an advanced biocompatible and nonbiodegradable bioink specifically designed for the LumenX. The resulting hydrogel will be optically transparent with a stiffness between the lung and the skin. On the other side, Volumetric's LumenX-GelMA photo-ink is an optimized gelatin-based biodegradable bioink designed specifically for LumenX. Since there is no impact on cell viability, the GelMA photoink can be mixed with cell pellets. Hence, a pre-gel solution based on PEGDA200 (30%) and GelMA (70%) was freshly prepared to realize the constructs by tuning different parameters. Several trials were conducted before to get the optimal ones, by varying the printing bed temperature between 37ºC-70ºC and keeping constant the exposure layer time at 5.5 seconds, the burn-in at 3x, and the resolution at 50% corresponding to 20 mW/cm^2, which are the working parameters suggested by the company with these materials. By following the specific parameters reported, and setting the printing bed temperature at 50 ºC, well-formed structures were obtained as the one depicted in Figure II-b-c, respectively right after the photopolymerization and after swelling (5 hours).

Therefore, the next step involved cell encapsulation, by embedding neonatal human dermal fibroblasts (10^6 cells/ml). Before crosslinking the gel, the entire equipment was kept under UV exposure for 90 minutes, to guarantee sterile conditions.

By mixing the cell pellet with the pre-gel solution, and keeping the previous printing parameters, no well-defined structures were obtained, indicating that a route change was required.

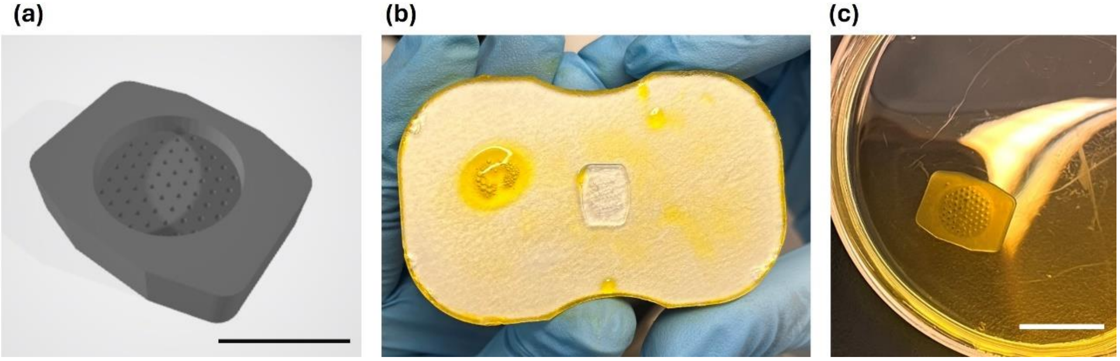

Figure II. (a) 3D-scaffold design. Hydrogel scaffold based on Composition I **(b)** right after the polymerization and **(c)** post-swelling (5 hours). Scale bars respectively 5 mm and 10 mm.

The time exposure of the single layers was increased up to 9 seconds, to get a proper polymerization. Unfortunately, immunofluorescence studies 14 days post-encapsulation revealed no cell spreading, although cells were positive for specific markers (Vimentin and Collagen IV). At this stage, Cellink materials -Composition I- resulted optimal for the fabrication of the constructs but not suitable to promote cells' growth and spreading.

As an alternative, a new composition based on commercial GelMA and PEGDA (Sigma Aldrich) largely employed in tissue engineering was adopted. For this set of experiments, a fresh solution based on PEGDA (1.25 %) GelMA (5%), LAP (0.4%), and tartrazine (0.05%) in Hank's Balanced Salt Solution (HBSS + 1 % P/S) -Composition II- was adopted, and several printing tests were conducted. Even though different exposure times (5.5 s – 30 s) were explored, changing the burn-in from time to time from 3x to 4x, up to 5x, and keeping constant the power to 20 mW/cm^2, no polymerization was reached. By maximizing the power value at 30 mW/cm^2 and setting the other parameters to the limit, not-well-polymerized structures were obtained.

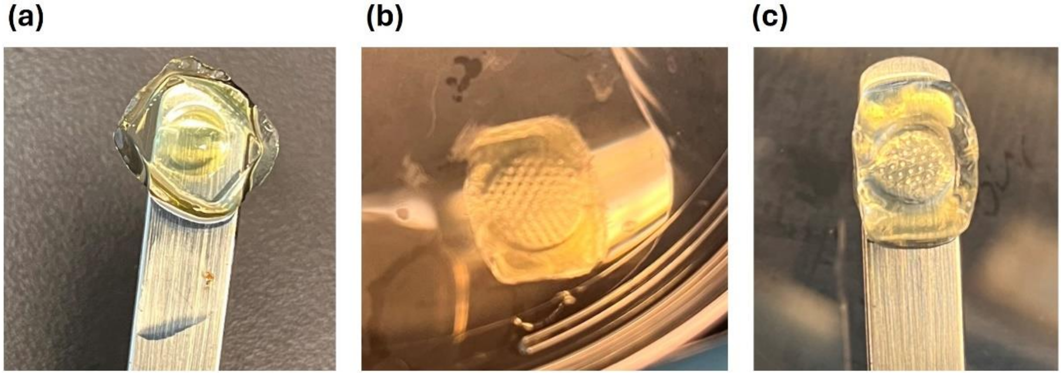

Figure III. Constructs based on PEGDA (3%) and GelMA (5%) -Composition II- using a power of **(a)** 25 mW/cm^2 and a power of 30 mW/cm^2, with an exposure time of 25 s and **(b)** a burn-in of 4x and **(c)** 3x.

Before totally abandoning this pre-gel formulation, the PEGDA content was doubled (3%) to confer resistance. Again, the first trials were performed with a lower power (20 mW/cm^2), without getting gels. Then, by increasing the power to 25- and 30 mW/cm^2, structures more or less faithful to the original design were obtained as in the picture (Figure III).

Although a good polymerization was reached by doubling the PEGDA content, showing structures closer to the one designed, again in the attempt to encapsulate cells, no reliable gels were obtained. The first explanation was traceable to the long time employed to get the gels since the working parameters were set to the limit (burn-in 4x and 25 s of time exposure). Hence, due to this evidence, a new design was considered, keeping the same dimensions as the previous one, with the only exception that the holes were planned for the entire depth of the scaffolds (Figure IV-a).

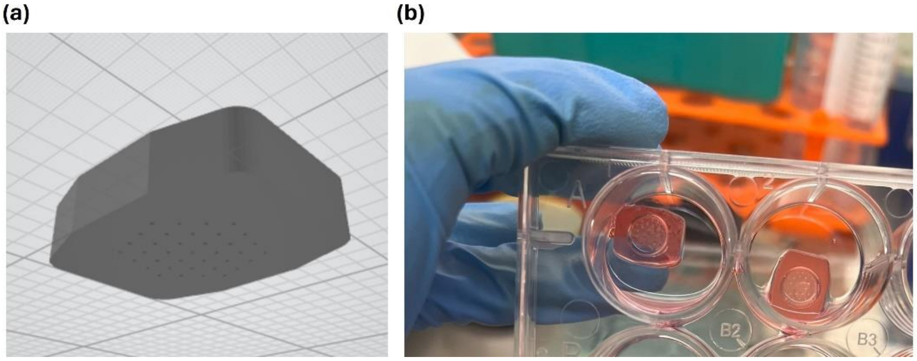

Figure IV. (a) New design adopted for Composition I and Composition II. **(b)** Examples of Composition I-based gels post-fabrication, obtained with the new design.

Composition I was first considered for this proposal. By adopting this new design, the photocrosslinking time was reduced by up to 14 minutes, becoming attractive, especially considering the cell encapsulation. With the power of 20 mW/cm^2, 9 seconds of exposure time, and a burn-in of 3x, gels well-polymerized were obtained (Figure IV-b).

An attempt at human dermal fibroblast encapsulation was conducted, which revealed the inadequacy of these scaffolds, based on Composition I, to promote cell elongation.

The same design was created by considering the Composition II solution, disclosing that it was necessary to raise both the power (30 mW/cm^2) and the exposure time (30 s), with a burn-in of 4x to crosslink structures with visible holes, even though they were not completely open as the ones showed for the Composition I-based materials (Figure V-a). Once these reliable structures were obtained, nHFBs were also encapsulated (1 x 10^6 cells/ml).

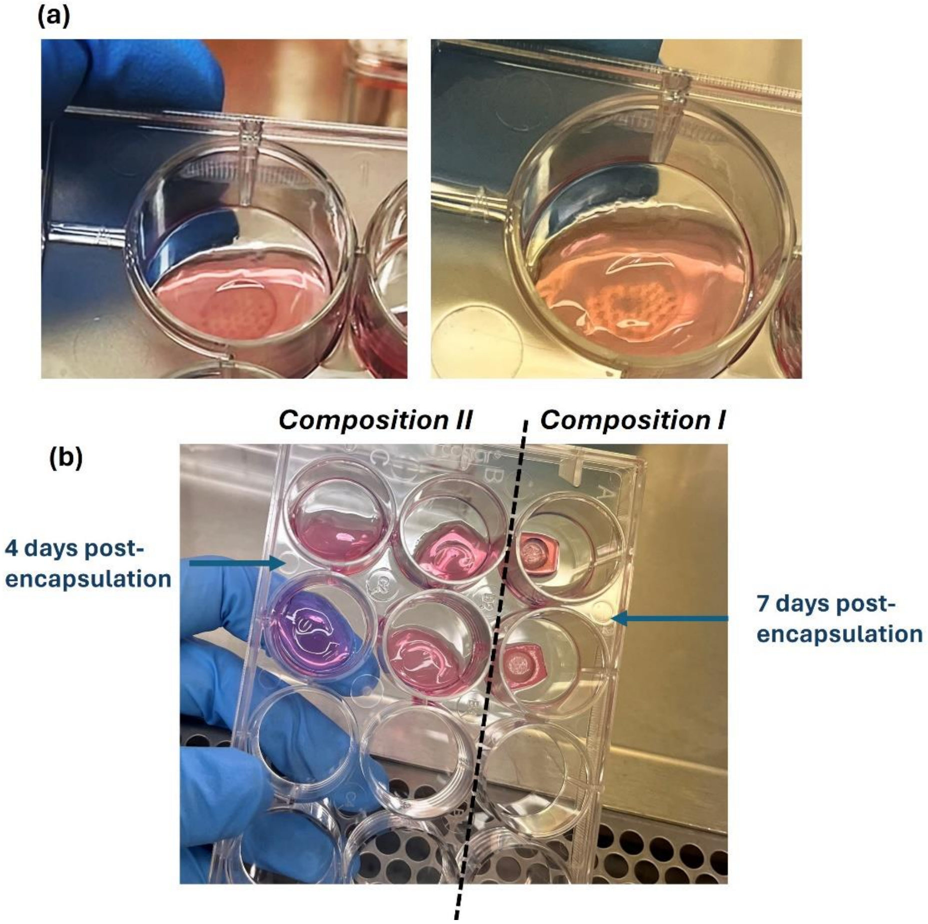

Figure IV. (a) Examples of Composition II- based gels post-fabrication, obtained with the new design. **(b)** Comparison between cell-laden scaffolds, based on: (left) Composition II– 4 days post-encapsulation- and (right) Composition I– 7 days post-encapsulation.

By monitoring the cell-laden scaffolds over time, a suspicious swelling was observed, making the gels difficult to handle. As enhanced in Figure V-b, cell-laden scaffolds based on Composition II, showed a swollen structure, even after 4 days post encapsulation (left), resulting in a not-defined shape. This evidence was more distinguishable when compared to cell-laden gels based on Composition I (right) which kept their shape after 7 days post fibroblast embedding. The comparative study enhances the limitations of Composition II, in terms of fabrication, although the improvements implemented, both in terms of composition and of setting parameters. On the other side, the commercial reagents developed for this equipment revealed that by tuning the working parameters well-defined structures can be realized.

Notwithstanding the potential for the construction of intricate gel architectures tailored to accommodate dermal papillae cells with precision, Composition I evinced limitations upon the incorporation of cells. This preliminary study represents a starting point in the panorama of building 3D complex structures through commercial bioprinting systems, without the use of an external mold. The importance of realizing complex *in vitro* approaches is becoming particularly attractive, considering the possibility of avoiding the use of external scaffolds, to design the final construct, that must be removed after the fabrication. Creating a ready-to-use cell-laden gel that presents a non-conventional shape is still a challenge. However, this attempt here presented can represent a kickoff to explore a new strategy in this direction.